Abstract

Experiments with ^{87}Rb: Towards Co-trapping ^{88}Sr^{19}F and ^{87}Rb

Yuqi Zhu

2021

Polar molecules can interact via the anisotropic and long-range electric dipole-dipole interaction owing to their large permanent electric dipole moments. Being able to study them in the ultracold temperature regime and at high density would allow us to study strongly correlated physics, and expand the toolbox for quantum computation.

In order to reduce the temperature of SrF beyond the sub-Doppler temperature ($\sim 10\mu$K) achieved with laser cooling by polarization gradients, we hope to implement sympathetic cooling of SrF and Rb. Pursuing this direction requires advancements in experimental capabilities. This thesis describes the experimental efforts towards co-trapping SrF and Rb, which is the starting point of studies of atom-molecule collisions in the ultracold temperature regime. The thesis reports on some technical aspects of conservative trapping: a high-power circuit was developed to facilitate current switching in the context of magnetic quadrupole traps, and depths of optical dipole traps were estimated in anticipation of complexities due to a strongly state-dependent trapping potential. The thesis also details the construction and performance of an apparatus for laser cooling and trapping Rb. The apparatus consists of a 2D MOT that functions as a high-flux beam source of Rb, and an RF MOT. The 2D MOT produces a flux on the order of 10^9 atoms/s with a most probable forward velocity of 30 m/s. With 500-ms loading, the RF MOT is able to collect $\sim 10^9$ atoms at temperatures $\sim$1 mK. Compared to the molecule number typical in an SrF MOT, the atom number in the Rb RF MOT is 10^4 higher, suggesting good prospects of observing atom-molecule collisions in a subsequent conservative trap. In addition, we established a comparison between the dc and RF MOT of Rb in the same apparatus. We found that in an RF MOT, the number is significantly lower and the temperature significantly higher, while the loading time constant and lifetime are similar to those of a dc MOT.

Experiments with ^{87}Rb: Towards Co-trapping ^{88}Sr^{19}F and ^{87}Rb

A Dissertation
Presented to the Faculty of the Graduate School
of
Yale University
in Candidacy for the Degree of
Doctor of Philosophy

by
Yuqi Zhu

Dissertation Director: David DeMille

June 2021

Copyright © 2021 by Yuqi Zhu

All rights reserved.

Acknowledgments

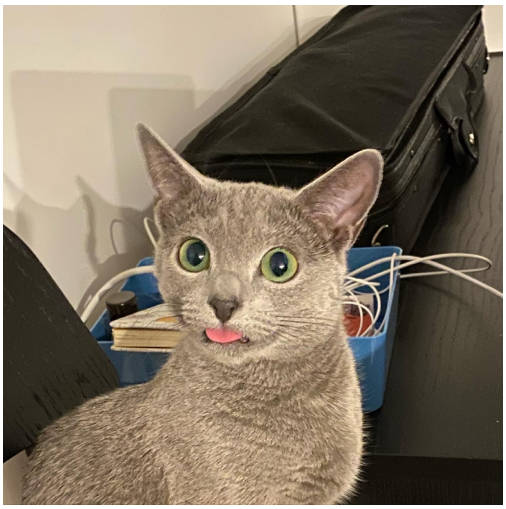
I would like to thank my advisor, Professor Dave DeMille, for offering me opportunities to study atomic physics in his group at Yale.

I spent 6 years in this group, 2015- 2021. In this paragraph, I would like to acknowledge my appreciation to all who contributed this work in chronological order. My first project was building a 980-nm ECDL for the RbCs experiment. It was a good learning experience for me, as I had zero technical skill required for this project and this field. I received a lot of help from Toshi and our visiting professor at the time, Prof. Jin-Tae Kim. I thank them for helping me get started in the lab, and for their patience in teaching me about lasers, electronics, RF circuits, etc. After the ECDL project, I was transferred to the SrF experiment (the Buffer Lab). At that time, around 2016, Danny and Matt were in charge of the experiment, and Eric was graduating. I thank Danny for teaching me everything there was to know about the SrF experiment, even though I ended up working with Rb. He also let me build the circuit for magnetic trapping. I would like to think that what I learned about electronics through this experience was helpful when I needed to fix electrical fences a few years later in Africa. In the summer or fall of 2017, Danny became a professor at UConn after finishing up taking data for our magnetic trap paper. Around this time, I submitted my thesis prospectus, believing that we would at least co-trap SrF and Rb by the time I graduate. Then I started putting together the first version of the 2D MOT with Matt. He is knowledgeable about vacuum technologies and was always willing to comment on my writeups and posters. I also thank him for acknowledging issues in the old ECDL design and for providing low-pass filters to reduce the frequency noise. From 2017 to 2018, we seemed to have everything we needed for the 2D MOT, but nothing really worked out in my opinion. I felt very disappointed by the lack of progress and myself to a point that in 2018, I decided to drop out and find something I could do. I thank all who encouraged me to carry on and shared their stories during this time; I can only hope to pay it forward. Among them, some helped me get hired by the tech company they work for. I feel indebted to them. Even though I did not end up working there, I have made efforts to know and love California since then. Towards the end of 2018, Thomas joined the lab as a postdoc. I am very grateful to him for moving the 2D MOT experiment forward—he convinced Dave of issues with the first 2D MOT setup, and proposed to set up a second 2D MOT in a glass cell. In a year or so, Thomas, Qian and I put together the glasscell 2D MOT and made it work despite the late arrival of the glasscell. In this year, 2019, I actually left my post for a month to attend a neuroscience summer school at Princeton. We only had a preliminary design for the apparatus when I left for the summer school, and I was surprised to see that 80% of the apparatus was ready when I returned. I thank Qian and Thomas for this productive year. In 2020, the plan of integrating the 2D MOT into the main experiment got postponed in order to push forward

in the ODT project that Varun and Thomas set up. I was then assigned to set up a 3D MOT of Rb in SPL 23. Soon after this decision was made, COVID-19 became a bigger problem in life; even the Olympics got postponed. During the lockdown, I spent sometime thinking about Raman sideband cooling and light shifts, some of which ended up in this thesis. I am very grateful to Dave for the valuable comments he made on my writeups, as well as on the rest of my thesis. After Yale reopened in June, I started putting together the 3D MOT apparatus, and spent the next 6 months or so taking data. I thank Eric for providing resources regarding the in-vacuum assembly and Qian for building the bias-T circuit. As I am writing this section after my thesis defense in March 2021, I would like to thank Prof. Nir Navon, Prof. Reina Maruyama, and Prof. Yoram Alhassid for their feedback on my thesis.

Parallel to this timeline, I also received help from outside the SrF cohort. First, I would like to thank Sid. He is never too busy to answer questions or lend a hand, though he is indeed very busy. Over the years, he and Dave raised my awareness around various safety issues, e.g., by reminding me to neutralize acid before pouring it down the drain and to use beam blocks. Second, I thank everyone on the Centrex experiment for lending us equipment at times and for sorting and labelling optics in the RbCs lab. Many of those optics got integrated into the new Rb experiments. Last but not least, I would like to thank Dave Johnson and Craig at the student shop for the tips and tools they offered that made my work easier. They also helped me with problems far beyond me skills, e.g., removing (very) stuck screws/taps and assisting in winding magnetic coils. In addition, I went to the professional machine shop for various jobs: making tunnels for water cooling, brazing, etc. I thank Vinnie for offering advice on designs and practicality.

Anyone who has never made a mistake has never tried anything new. —Albert Einstein



The cat in this photo is Sasha.

Contents

1 Introduction **1**

2 Laser cooling of SrF **4**

2.1 Doppler cooling . . . 4

2.1.1 Laser slowing . . . 6

2.1.2 Radio-frequency magneto-optical trap . . . 7

2.2 Sub-Doppler cooling . . . 9

2.3 Diagnostic techniques . . . 10

2.3.1 Laser induced fluorescence imaging . . . 10

2.3.2 Time-of-flight measurement . . . 10

2.3.3 Scattering rate measurement . . . 11

2.4 Experimental sequence . . . 11

3 Magnetic quadrupole trap **13**

3.1 Summary of results . . . 13

3.2 The switching circuit . . . 16

3.2.1 Simulation and preliminary tests . . . 19

3.2.2 Initial switch-on . . . 24

3.2.3 Thermal dissipation . . . 25

3.2.4 Supplementary . . . 26

4 Two-dimensional magneto-optical trap: a slow beam source of ^{87}Rb **28**

4.1 Introduction . . . 28

4.2 Experiment . . . 29

4.2.1 Rb D_2 laser system . . . 29

4.2.2 2D MOT apparatus . . . 34
4.3 Maximizing the 2D MOT flux . . . 37
4.4 Methods . . . 40
4.4.1 Background subtraction . . . 40
4.4.2 Converting fluorescence signal to atomic flux . . . 41
4.4.3 Calibrating fluorescence to atom number in the 3D MOT . . . 44
4.4.4 Measuring Rb vapor pressure via absorption . . . 46

5 Characterization of a radio frequency magneto-optical trap of ^{87}Rb 49
5.1 Introduction . . . 49
5.1.1 Type-I RF MOT . . . 50
5.2 Experiment . . . 51
5.2.1 Loading from a two-dimensional magneto-optical trap . . . 54
5.3 MOT characterization results . . . 54
5.3.1 Synchronizing switching in RF MOT . . . 55
5.3.2 Optimizing 3D MOT parameters . . . 56
5.3.3 Loading and decay processes . . . 57
5.3.4 Optimized MOT properties . . . 59
5.4 Summary and outlook . . . 61
5.4.1 Sympathetic cooling of SrF and Rb in a magnetic trap . . . 62

6 Optical dipole trap 65
6.1 Light shift . . . 65
6.2 Dipole matrix element . . . 67
6.2.1 Hund's case (a) . . . 68
6.2.2 Hund's case (b) . . . 75
6.2.3 Parity of basis functions and parity eigenstate . . . 78
6.2.4 The effect of hyperfine mixing of J states . . . 81
6.2.5 Atomic case . . . 82
6.2.6 Symmetry and quantum number . . . 83
6.2.7 Vector and rotating frame . . . 85
6.3 Far-detuned dipole traps with linearly polarized light . . . 87
6.3.1 Very far detuned dipole traps . . . 88
6.3.2 Not very far detuned dipole traps . . . 91

6.4 Scalar, vector and tensor light shift . . . 92
6.4.1 Polarizability . . . 97
6.4.2 Linear polarization . . . 102
6.4.3 Elliptical polarization . . . 103
6.5 Polarization-dependent far-detuned dipole traps . . . 106

Appendices

A Properties and spectroscopy data **109**
A.1 SrF properties . . . 109
A.2 $B^2\Sigma^+ - X^2\Sigma^+$ transition . . . 113
A.3 Dipole matrix elements . . . 115
A.4 Rotational branching ratios . . . 116
A.5 Polarizabilities of hyperfine states . . . 118
A.6 Rubidium properties . . . 120

B Technical notes **122**
B.1 Vector space in the complex spherical basis . . . 122
B.2 Resolution test . . . 124

Bibliography **128**

Chapter 1

Introduction

The production of cold molecules ($T < 1$ K) has inspired many interesting experimental and theoretical studies [1], such as the search for the electric dipole moment of the electron [2–4], the measurement of time evolution of the fine structure constant [5], quantum computation with polar molecules [6], and studies of cold chemistry [7]. In experiments where molecules are used as probes, cooling molecules to low temperatures improves the precision of measurements. Cold polar molecules are particularly interesting because of their permanent electric dipole moment, and consequently high sensitivity to external electric fields.

From the perspective of quantum many-body physics, the permanent electric dipole moment also leads to electric dipole-dipole interaction between neutral polarized molecules. This type of interaction is anisotropic, long-range, and tunable. However, compared to studies that mostly rely on the interaction between polar molecules and external electric fields, e.g., in Refs.[3, 5], working in the regime of strongly-correlated many-body systems requires cooling to the ultracold temperature regime, where the inter-particle spacing is sufficiently small. Suppose n is the number density; then for a three-dimensional gas, the average inter-particle spacing is $r = n^{-1/3}$. To quantify how small this inter-particle spacing is, it is natural to compare the average inter-particle spacing to the thermal de Broglie wavelength (λ_{th}). For an ideal gas at temperature T, the thermal de Broglie wavelength is

$$\lambda_{\mathrm{th}} = \sqrt{\frac{2\pi\hbar^2}{mk_{\mathrm{B}}T}}, \tag{1.0.1}$$

where k_{B} is the Boltzmann constant, $\hbar$ is the reduced Planck constant, and m is the mass of an individual particle. The phase-space density, $n\lambda_{\mathrm{th}}^3$, is a quantitative measure of how likely it is for the particles to lie within a de Broglie wavelength of each other. A high phase-space density is crucial for observing novel many-body phenomena, because the strength of interactions, e.g. via magnetic or electric dipole moment, is

inversely proportional to some power of the inter-particle spacing. Furthermore, quantum statistics is also manifested in this regime; in the case of ultracold Bose gases, when $n\lambda_{\rm th}^3 \gtrsim 1$, Bose-Einstein condensation (BEC) can take place [8–10]. Since the achievement of BEC in alkaline atoms (^{87}Rb and ^{23}Na), Bose-Einstein condensates and quantum degenerate Fermi gases have been produced for all stable alkali species and a number of alkaline-earth and rare-earth species. They have served as fruitful platforms for studies of quantum physics, such as quantum phase transitions [11]. In the cases of alkali and alkaline-earth quantum degenerate gasses, ultracold atoms separated by a distance r interact predominantly via isotropic short-range interactions, such as the contact interaction via s-wave scattering, $U \propto \delta(r)$, and the van der Waals interaction, $U \propto r^{-6}$. More recently, studies of ultracold gases have extended to dipolar atoms interacting via magnetic dipole-dipole interactions for both Bosons [12, 13] and Fermions [14–16]. Since the magnetic dipole-dipole interaction depends on θ, which is the angle between the orientation of the dipoles with respect to the inter-particle axis, $U \propto (1-3\cos^2\theta)/r^3$, it is anisotropic and stronger (at larger distances) than the van der Waals interaction. It is however much weaker compared to the electric dipole-dipole interactions between polarized molecules. It follows from dimensional analysis that the ratio of electric to magnetic dipolar coupling strength is on the order of $\frac{e^2 a_0^2}{\epsilon_0 \mu_B^2} \sim \alpha^{-2} \sim 10^4$, with e being the electron charge, a_0 the Bohr radius, μ_B the Bohr magneton, ϵ_0 the vacuum permittivity and $\alpha = 1/137$ the fine structure constant. In summary, studying quantum degenerate gasses of molecules interacting via the electric dipole-dipole interaction would complement prior work on ultracold atomic gasses and potentially open new a frontier for strongly correlated physics.

Since I started graduate school, there has been remarkable progress in bringing molecules into the ultracold temperature regime. To give a few examples, for directly laser-cooled molecules, gray molasses—laser cooling by polarization gradient— has allowed us to reduce the temperatures to $\sim$5 μK [17–19]. For molecules assembled from ultracold atoms at nanokelvin temperatures using magnetoassociation [20], collisional cooling has been demonstrated, e.g., sympathetic cooling via atom-molecule collisions [21] and evaporative cooling of reactive molecules [22]. In addition to the efforts to cool and control molecules, ongoing studies of the quantum degenerate Fermi gas of KRb continue to reveal many unique properties [23–25].

Motivated by the promises of new physics, creating ultracold gases of strontium monofluoride (^{88}Sr^{19}F) with temperatures $T \lesssim 1$ μK is the overarching theme in the experiment I have been involved in. During my time here, I contributed to magnetic trapping of SrF [26], as a demonstration of transferring directly laser-cooled molecules into a conservative trap, by building a circuit to control the current in the magnetic coils. As we later embarked on the plan of applying sympathetic cooling of SrF and ^{87}Rb, I participated in two experiments with Rb: building a two-dimensional magneto-optical trap as a slow beam source of ^{87}Rb and characterizing a radio frequency magneto-optical trap of ^{87}Rb. Last but not least, I considered the

interaction between far off-resonance light and ground state SrF by calculating light shifts in the context of optical dipole traps. Observing strongly state-dependent light shifts (in the calculation) then led me to calculate polarizabilities and look for ways to minimize differential light shifts.

The general outline of this thesis is as follows:

- Chapter 2 gives an overview of preliminary work on laser cooling of strontium monofluoride ($^{88}Sr^{19}F$), including Doppler cooling, polarization-gradient cooling, and diagnostic techniques.
- Chapter 3 presents results from conservative trapping of ground state SrF in a magnetic quadrupole trap, and describes the circuit designed for controlling current in the magnetic coils.
- Chapter 4 describes the apparatus and performance of a two-dimensional magneto-optical trap (MOT) of rubidium (^{87}Rb) as a slow beam source for loading into a three-dimensional MOT.
- Chapter 5 reports the characterization of a radio frequency (RF) magneto-optical trap (MOT) of ^{87}Rb and ends with an outlook for future work, including sympathetic cooling of SrF and Rb.
- Chapter 6 examines some theoretical aspects of optical dipole traps, including the derivation of electric dipole matrix elements for a class of diatomic molecules whose angular momentum coupling scheme is similar to the ground state SrF, and calculation of dynamical polarizability for ground state SrF.

Chapter 2

Laser cooling of SrF

Our lab has focused on producing cold gases of the polar molecule strontium monofluoride (SrF). This chapter is a summary of efforts towards cooling SrF, with focuses on steps after a molecular beam is created, namely, the laser cooling steps. The cryogenic buffer gas beam source had been fully developed before I joined the lab, and its construction and characterization are documented in Ref. [27]. In this chapter, §2.1 is an overview of Doppler cooling techniques applied to SrF—laser radiation pressure slowing and magneto-optical trapping; then §2.2 is on sub-Doppler cooling techniques. §2.3 discusses optical techniques employed to probe the system—to measure temperatures and number densities. As a summary, §2.4 lists the sequence of events within a single repetition of the experimental cycle, with some technical details and timing information. All steps included in this section, buffer-gas cooling and laser cooling steps, have become preparatory work for experimental techniques in later chapters of this thesis such as magnetic trapping (Chapter 3).

2.1 Doppler cooling

Optical cycling is a prerequisite for laser cooling techniques. Owing to its energy level structure, SrF is lucky to be one of the molecules in which optical quasi-cycling is viable. This opens the way for applying Doppler cooling techniques to cool and trap in a single rotational level within the electronic and vibrational ground state $X^2\Sigma^+(v = 0, N = 1)$ with $X^2\Sigma^+$ denoting the electronic ground state, v the vibrational quantum number and N the rotational quantum number.

In applying laser cooling techniques developed for atoms, the challenges stem from added degrees of freedom, namely rotation and vibration in diatomic molecules. These motional degrees of freedom split the ground state degeneracy, adding more decay channels that hinder optical cycling, in a way similar to how spin-coupling interactions generate fine and hyperfine structures, though the energy scales due to

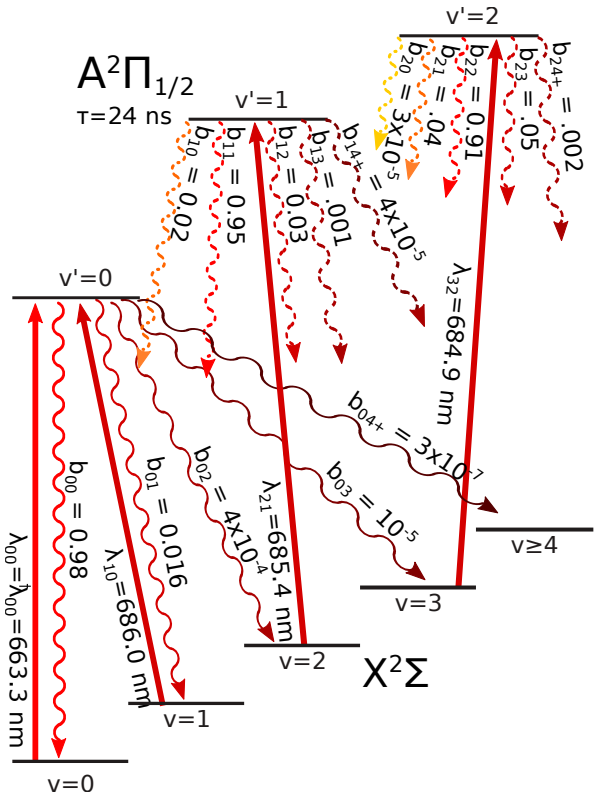


Figure 2.1: Optical cycling scheme in SrF up to the vibrational structure. In addition to a laser with wavelength λ_{00} driving the $X^2\Sigma^+(v=0) - A^2\Pi_{1/2}(v'=0)$ transition. Repump lasers with wavelengths λ_{10}, λ_{21} and λ_{32} address vibrational branching. The vibrational branching ratio ($b_{v'v}$) is the probability of decaying into a ground state with vibrational quantum number v given the excited state vibrational number v' (Figure adapted from Ref. [28]).

vibrational and rotational motions are larger. For example, in $X^2\Sigma^+$, the vibrational splittings are a few hundreds of cm^{-1} (tens of nm), making it impossible to address different vibrational levels with a single laser. Fortunately, in certain diatomic molecules, including monohalides of alkaline earth metals, the probability of changing vibrational number during spontaneous decay is very small [29]. Despite this advantage, in order to put the optical scattering force to use for slowing, cooling, and trapping, vibrational repump lasers are essential. The scattering rate can be on the order of 10^6 photons/s [30] if not higher, implying the leak rate into other vibrational levels is highly nontrivial. The current vibrational repump scheme (Figure 2.1) also creates coherent dark states between $X^2\Sigma^+(v=0)$ and $X^2\Sigma^+(v=1)$. Because both vibrational repump transitions involve the same excited state (with a short lifetime ~ 24 ns), the system evolves into a superposition of the two ground states and then no longer absorbs photons from either repump laser. Using a different electronic state, $B^2\Sigma^+(v'=0)$, to repump $X^2\Sigma^+(v=1)$ has recently become possible. The provisional scheme involving the new excited state is shown in Figure A.5 in Appendix A.2, along with

relevant spectroscopic details.

Rotational branching, in addition to vibrational branching, must be accounted for in optical cycling diatomic molecules. Taking into account parity and angular momentum selection rules, it can be seen that the excited state with positive parity and smallest angular momentum $A^2\Pi_{1/2}(v' = 0, J' = 1/2)$ can only decay to a single rotational level with negative parity $X^2\Sigma^+(v = 0, N = 1)$. Here J' denotes the total angular momentum excluding the nuclear spin of the excited state, $\vec{N} = \vec{J} - \vec{S}$, and the electron spin $S = 1/2$ as indicated by term symbols. Although using an excited state with J' constraints rotational branching without introducing additional technical complexity, the energy level structure of $X^2\Sigma^+(v = 0, N = 1) - A^2\Pi_{1/2}(v' = 0, J' = 1/2)$ makes trapping and cooling intrinsically less effective. Because J' is no greater than J, there are dark states—magnetic sublevels that do not couple to light of a specific polarization and thus are left out of optical cycling.

Despite the difficulties, radiative pressure slowing and magneto-optical trapping of SrF molecules have been demonstrated. In the current experimental sequence, key steps involving optical cycling are slowing molecular beam from a cryogenic buffer gas beam source [30], and loading a radio-frequency (RF) magneto-optical trap (MOT) [31] (Figure 2.2a). Subsequently, the RF MOT is compressed into a compressed RF MOT [32] (Figure 2.3). After optimization, we managed to prepare a sample of SrF molecules at a density of $n = 2.5 \times 10^5$ cm^{-3} and $n\lambda_{\mathrm{dB}}^3 = 6 \times 10^{-14}$ in phase-space density. In terms of molecule number and temperature, this procedure enabled us to collect about 10^4 molecules and to reduce the kinetic temperature to as low as 250 μK.

2.1.1 Laser slowing

The buffer gas beam source produces molecular beams with forward velocities of ≈140 m/s and rotational temperatures of ≈1 K. Laser slowing occurs over a distance of 1.35 m for 32 ms after the molecular beam is produced. It is a crucial step that reduces the forward speed before capturing in an MOT. The frequency profile of the slowing beam is broadened by an Electro-optic modulator (EOM) in order to target as many velocities as possible; hence it is commonly referred to as white-light slowing. With a fiber EOM, the width of frequency profile of the main cycling laser detuned near the $X^2\Sigma^+(v = 0, N = 1) - A^2\Pi_{1/2}(v' = 0, J' = 1/2)$ resonance, is about 300 MHz, corresponding to a velocity range of 200 m/s. The highest frequency in the slowing frequency profile is on resonance with the center of $X^2\Sigma^+(v = 0, N = 1)$. Suppose F and F' are the total angular momentum quantum numbers for ground and excited state, and m_F and m'_F are the Zeeman(magnetic) quantum numbers. With nuclear spin $I = 1/2$ included, only Zeeman sublevels,

$|F, m_F\rangle$ in shorthand, with the same F quantum number are degenerate (in the absence of external fields)*. In this energy level structure (Figure 2.2b), the slowing frequency profile is entirely red detuned to the bottom two hyperfine levels, $|0, m_F\rangle$ and $|1-, m_F\rangle$, and partially red to the top two hyperfine levels, $|1+, m_F\rangle$ and $|2, m_F\rangle$. To deal with the dark states generated during slowing, a co-propagating magnetic field intersects the slowing light polarization at a 45° angle to remix the population via rotational level $N = 0$. More recently, the slowing efficiency has been improved by applying a tapered, as opposed to collimated, slowing beam [32].

2.1.2 Radio-frequency magneto-optical trap

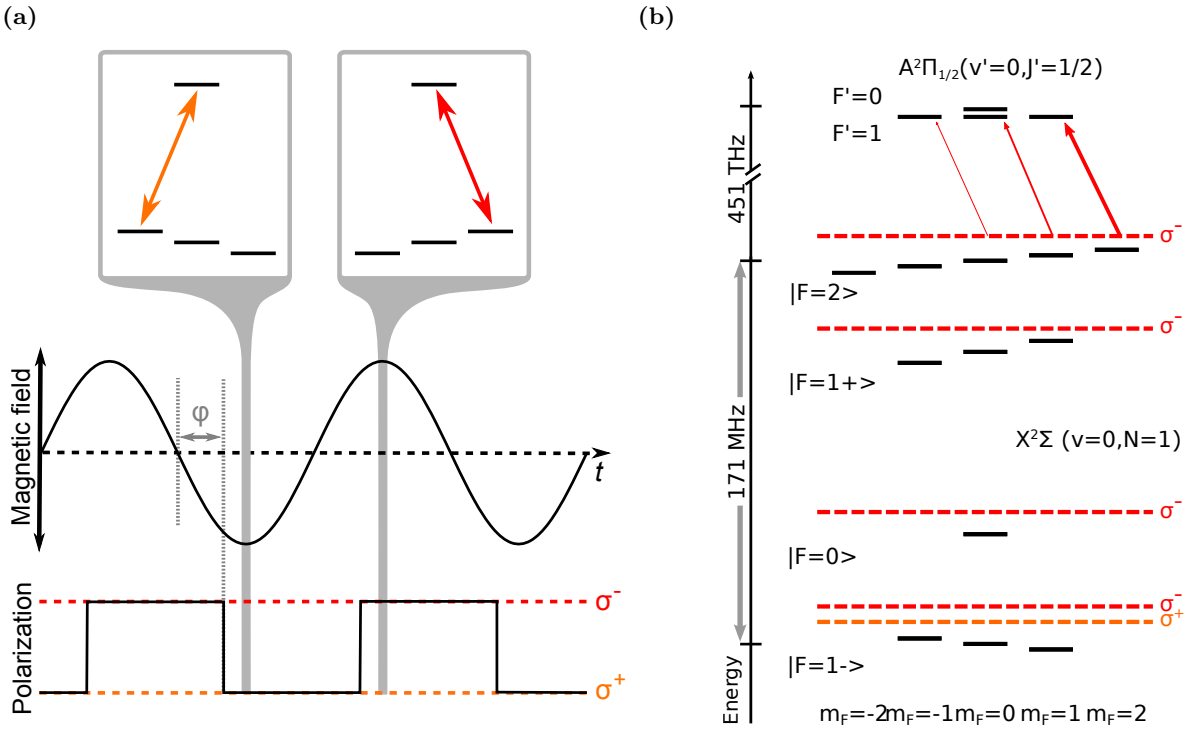


Figure 2.2: (a) RF MOT scheme based on a type II transition. φ is the phase between magnetic field and laser polarization. The trap strength is maximized when $\varphi = 0$. (b) The laser polarization scheme for positive magnetic field gradient. (Figure adapted from Ref. [31])

In the cycling transition, $X^2\Sigma^+(v = 0, N = 1, F) - A^2\Pi_{1/2}(v' = 0, J' = 1/2, F')$, up to hyperfine structure, the ground state has more hyperfine sublevels than the excited state. Therefore, for light of any polarization, there are always dark states. In a MOT, when molecules decay to these dark sublevels during cycling, they do not experience cooling forces due to trap light, so having dark states compromises the average scattering rate. For instance, in Figure 2.2b, Zeeman sublevels $|2, -2\rangle$, $|2, -1\rangle$, $|1+, -1\rangle$ and

*The energy level diagram with more details and the magnetic properties can be found in Figure ?? and Table A.2 in the Appendices.

$|1-,1\rangle$ are dark to σ^- light. To counter issues due to dark Zeeman sublevels, in the RF MOT scheme for trapping $X^2\Sigma^+(v=0, N=1)$ (Figure 2.2a), magnetic field gradient and laser polarization are switched simultaneously at a rate larger than the scattering rate of ground state molecules; dark states are then effectively destabilized. This idea of RF MOT is first realized in 2D [33]. Compared to a standard direct current (dc) MOT, an RF MOT provides larger trapping and damping forces for a system with Zeeman dark states, because the amount of time a molecule spent in dark states is reduced when averaged over a period.

Because the energy splitting between hyperfine levels are larger than the natural linewidth of this transition ($\Gamma = 2\pi \cdot (6.6\text{ MHz})$), sidebands are created with EOM to address individual hyperfine states for trap and repump lasers. The lowest hyperfine manifold, $F = 1-$, has a g-factor whose sign is opposite to the other hyperfine states. Therefore, an additional trap laser (orange in Figure 2.2b) with the complement circular polarization is added.

Despite the RF MOT scheme and frequency sidebands, the SrF MOT is still less effective compared to MOTs whose trapping transition is not compromised by dark states, $F \to F' = F + 1$. In the vicinity of trap center, the spring constant is a measure of restoring force in MOT, and is linear to magnetic field gradient. In the first sodium dc MOT, it is about $1.3 \cdot 10^{-15}$ dynes/cm [34] when the gradient is 5 G/cm, and in an RF MOT, it is 10^{-17} dynes/cm [31] when the gradient is 25 G/cm.

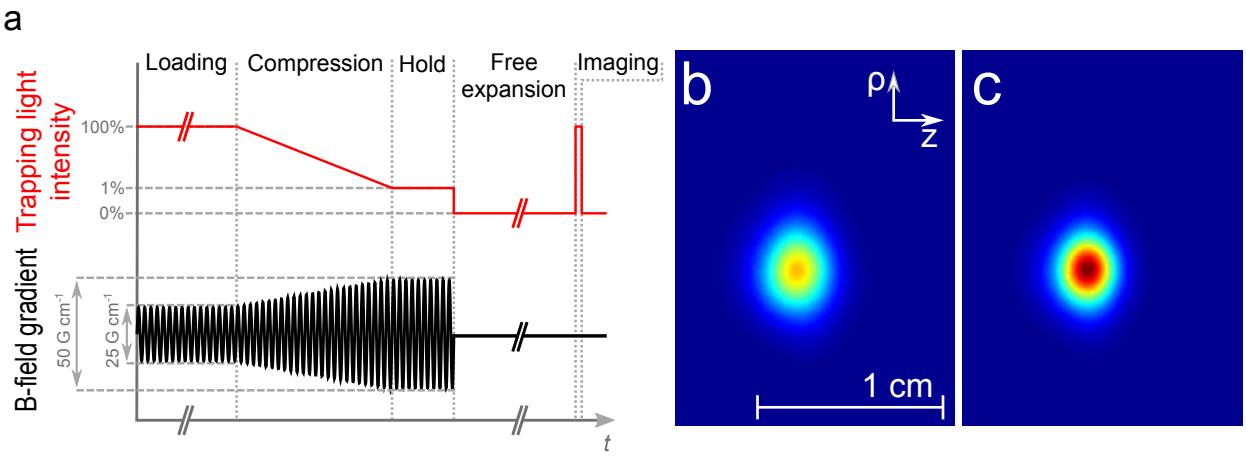


Figure 2.3: (a) Experimental sequence for compressed MOT. (b,c) Comparison of florescence images without (b) and with (c) compression. The detection method is imaging via Laser Induced Florescence (LIF). The higher intensity in (c)—a compressed MOT—corresponds to a higher spatial density, $n = 2.5 \times 10^5$ cm^{-3}. ρ and z denote the radial and axial direction respectively (Figure from Ref. [32]).

After loading an RF MOT with SrF, trapping laser power is reduced and magnetic field gradient is increased. This produces a compressed RF MOT (Figure 2.3) with higher number density—number of molecules per volume. Compared to the same sequence performed without increasing the field gradient amplitude, this compression, by itself, allows for a factor of 2 increase in number density with less than 10%

increase in temperature.

2.2 Sub-Doppler cooling

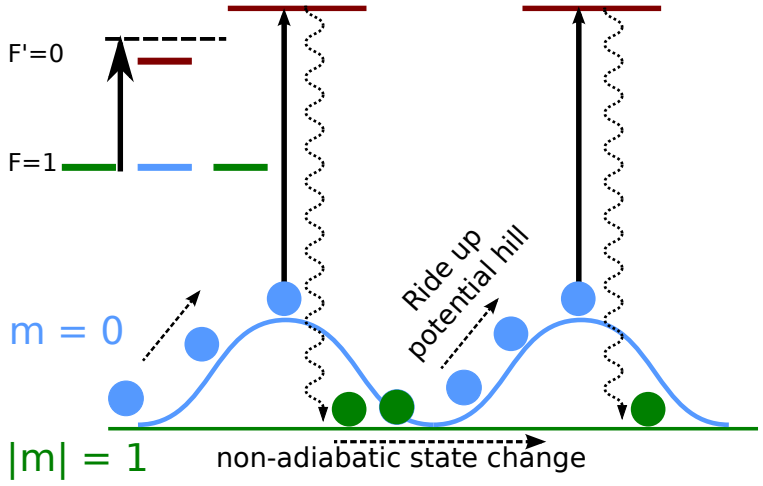


Figure 2.4: Illustration of gray molasses cooling with linear polarization in a $F \rightarrow F' = F - 1$ transition (Figure adapted from Ref. [30]).

In addition to Doppler cooling, the blue-detuned Sisyphus cooling or gray molasses cooling [18, 35, 36] has also been applied, reducing the temperatures to $\approx 50\,\mu$K, below the Doppler temperature limit ($\approx 160\,\mu$K). Unlike optical molasses cooling [37] that works for type-I transitions ($F \rightarrow F' = F + 1$), gray optical molasses cooling makes use of the motion-induced polarization gradient that operates on type-II transitions ($F \rightarrow F' = F - 1$ or $F \rightarrow F' = F$). Due to the presence of dark states in this type of transition, in order to create energy difference between bright and dark states, cooling and repumping lasers are blue-detuned, adding positive light shifts to the bright states. Each pair of counterpropagating laser beams forms a spatial interference pattern with nodes (potential maxima) and antinodes (minima). When a molecule is in a bright state, as it climbs up the optical potential, it is more likely to be optically pumped to an excited state near a potential maximum where it moves with lower velocity. After optical pumping near a node, if it decays to a dark state, its kinetic energy will be reduced by an amount comparable to the light shift of the initial bright state, and as the molecule moves towards the next antinode, the state changes into a bright state non-adiabatically due to motion-induced polarization gradient. To prevent a low-velocity dark state from Lamor precessing into bright states under stray fields including Earth's field, shim coils are necessary for optimizing the molasses temperature [26] (Figure 2.5).

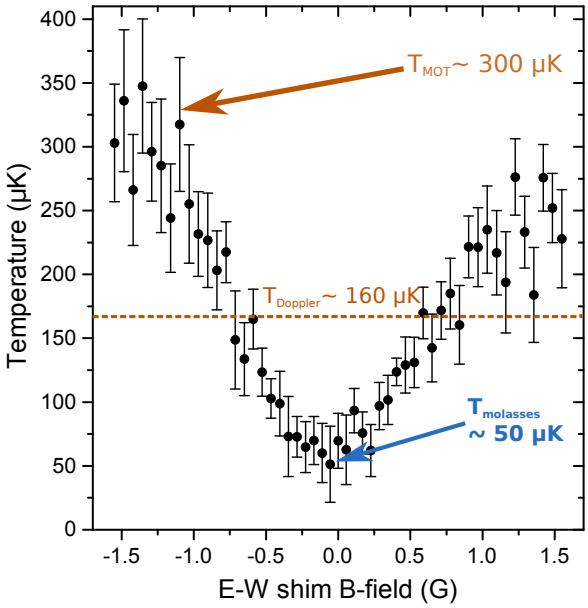


Figure 2.5: Temperature of gray molasses. The lowest temperature is reached after proper cancellation of stray magnetic fields (Figure adapted from Ref. [26]).

2.3 Diagnostic techniques

2.3.1 Laser induced fluorescence imaging

Measuring the number density with absorption is not viable due to the low density, so laser induced fluorescence (LIF) imaging is the primary diagnostic method. After a LIF image is collected on a CCD camera, it can be converted to molecule number based on an established collection efficiency calibration in conjunction with background subtraction* [2]. The spontaneous scattering rate is a necessary parameter in this conversion, and its measurement is described in §2.3.3. For technical simplicity, the frequency profile of the imaging light is identical to that of the RF MOT— with sidebands red detuned to individual hyperfine levels and vibrational repump frequencies for $X^2\Sigma^+(v=1)-A^2\Pi_{1/2}(v'=0)$, $X^2\Sigma^+(v=2)-A^2\Pi_{1/2}(v'=1)$ and $X^2\Sigma^+(v=3)-A^2\Pi_{1/2}(v'=2)$; the polarization of the imaging light is also switched at the same frequency throughout camera's exposure.

2.3.2 Time-of-flight measurement

The time-of-flight technique is a diagnostic method based on LIF, which allows us to infer the initial temperature of a trapped sample. Suppose σ denotes the gaussian rms radius in the axial (or radial)

*A similar procedure is used in characterizing the atomic flux from a 2d MOT in §4.4.2.

dimension, and is a function of time. After the cloud is released from the trap at $\Delta t_{\text{tof}} = 0$, it undergoes free expansion and the expansion rate reflects the kinetic energy along this dimension,

$$\sigma^2(\Delta t_{\text{tof}}) = \sigma^2(\Delta t_{\text{tof}} = 0) + \frac{k_B T}{m}(\Delta t_{\text{tof}})^2; \tag{2.3.1}$$

here, Δt_{tof} is the duration of free/isothermal expansion, T is the kinetic temperature of this dimension, and m is the mass of a particle.

By measuring the cloud size at various time points after the release, the kinetic temperature T can be extrapolated from a linear fit to data,

$$\{y = \sigma^2(|\sqrt{x}|), \quad x = \Delta t_{\text{tof1}}^2, \Delta t_{\text{tof2}}^2, \Delta t_{\text{tof3}}^3, ...\}.$$

2.3.3 Scattering rate measurement

In the context of laser cooling, atoms like rubidium are often de facto two-level systems; even though there are more than one ground state hyperfine levels, the probability of leaking out of the cycling transition is strongly suppressed by a large detuning that equals to the hyperfine splitting; for instance, in cooling ^{87}Rb via $F = 2 \rightarrow F' = 3$ of the D_2 line, the excited state hyperfine splitting is ≈ 270 MHz, and the ground state hyperfine splitting is ≈ 7 GHz. To good approximation, the spontaneous scattering rate can be described by a simple equation based on a two-level system model. This simple model unfortunately does not apply in the case of SrF. Nonetheless, the vibrational structure in molecules allows us to measure lifetime and scattering rate. The rate of leaking into $X^2\Sigma^+(v = 2)$, r_{20}, can be inferred from the exponential decay of LIF signal when the population is optically pumped into $X^2\Sigma^+(v = 2)$; practically, this is achieved by removing the $X^2\Sigma^+(v = 2) - A^2\Pi_{1/2}(v' = 1)$ repump frequency from the default LIF profile for quasi-cycling. The total scattering rate is the reciprocal of vibrational branching ratio multiplied by the measured decay rate, r_{20}/b_{20}.

2.4 Experimental sequence

- Ablation. Ablating a target (made of primarily SrF_2) with a YAG laser creates SrF molecules in the cryogenic buffer gas cell. The width of the ablation pulse is about 5 ns.

- Buffer gas cooling. Collisions with Helium at $\approx 4\,K$ inside the buffer gas cell allows the molecules to thermalize to a lower temperature, thereby suppressing populating higher/more energetic rotational levels. The molecular beam produced has a forward velocity of ≈140 m/s and a rotational temperature

of $\approx$1 K.

- Laser slowing. Laser slowing occurs over a distance of 1.35 m for 32 ms after ablation. The frequency profile, about 300 MHz wide, is created by a fiber EOM via phase modulation at 3.5 MHz.
- Doppler cooling and trapping
  - Loading an RF MOT. RF MOT loading starts as soon as the slowing starts, and it lasts for 35 ms with all trap and repump lasers at maximum intensity. The magnetic field, produced by in-vacuum coils, has a gradient of 25 G/cm in the vicinity of trap center. The switching of polarization and magnetic field occurs at 1.23 MHz.
  - Compressing the RF MOT. After the initial loading is complete, the RF MOT is compressed in 50 ms, by decreasing the intensity to 1% of the maximum level and doubling the magnetic field gradient. Then the low intensity high field configuration continues for 20 ms before the sub-Doppler step.
- Sub-Doppler cooling
  - Gray molasses cooling. Gray molasses cooling is typically applied for 2 ms after the MOT magnetic field is switched off and dc shim fields generated by added coils are switched on.
  - Variation(s) of gray molasses cooling.
- Diagnosis. During a typically LIF imaging process, the imaging light, with both trap and repump frequencies at maximum power, is applied for 2 ms.

Chapter 3

Magnetic quadrupole trap

Trapping SrF in a magnetic trap, or any type of conservative trap, is preliminary to the studies of inter- and intra-species collisions. Steps prior to magnetic trapping are described in Chapter 2. In this chapter, §3.1 discusses the realization of trapping molecules in a weak-field seeking sublevel of the first rotationally excited level in the electronic and vibrational ground state $X^2\Sigma^+(v = 0, N = 1)$, in a magnetic quadrupole trap (MQT). §3.2 describes the switching circuit developed for MQT in detail.

3.1 Summary of results

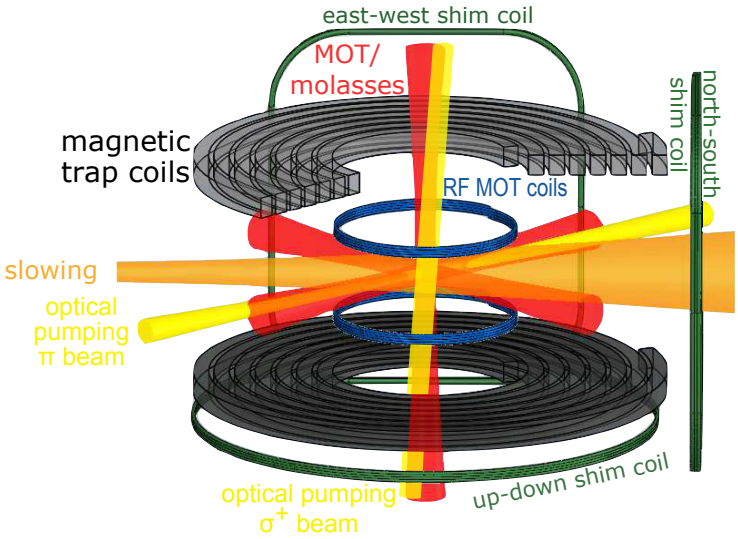


Figure 3.1: Geometry of laser beams and magnetic coils.

In a MQT, the trapping force comes from the interaction with an inhomogeneous magnetic field, $\vec{B}(\vec{r})$, generated by a pair of anti-Helmholtz coils; the gradient along either radial or axial direction is a

linear function of excursion in the vicinity of the trap center. The energy shift for states in the coupled basis depends on the Landé g-factor for the hyperfine state F (g_F), and the component of $\vec{F}$ along the quantization axis defined by the magnetic field (M_F),

$$\Delta E_{\text{Zeeman}}(\vec{r}) = -\mu_B g_F M_F B(\vec{r}). \tag{3.1.1}$$

μ_B is the Bohr magneton; in SI-based atomic units, $\mu_B = -\frac{1}{2}$.

In order to counter gravity, in the case of $|F = 2, M = 2\rangle$ in $X^2\Sigma^+(v = 0, N = 1)$, the axial magnetic field gradient needs to be at least 19 G/cm, which corresponds to 33 A given the coils' geometry. The initial fast switch-on step allows us to reach a gradient of around 32 G/cm within 320 μs. Then this low-gradient trap can be compressed to attain a maximum (power supply limited) gradient of 140 G/cm by ramping up the current (Figure 3.2). In the fully compressed MQT, the $1/e$ lifetime is measured to be on the order of 1 s (Figure 3.3), making it a promising conservative trap for the studies of collisions, and possibly for implementing sympathetic cooling.

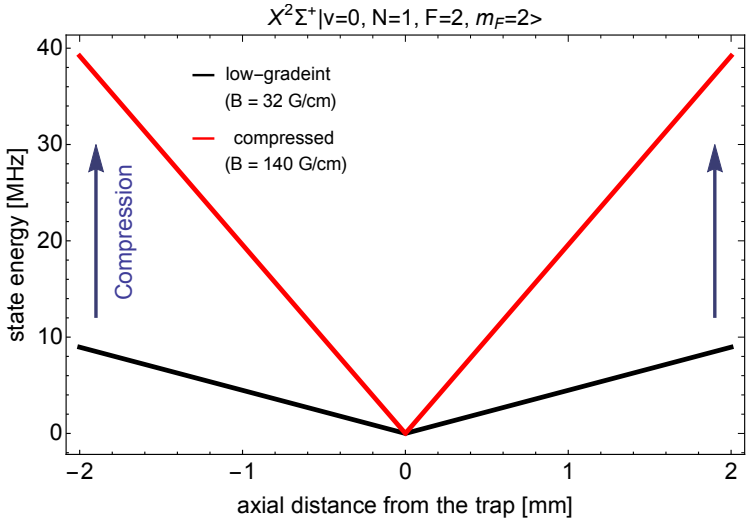


Figure 3.2: Compressing the MQT to increase the number density of the trapped cloud. In the case of adiabatic compression, the probability of undergoing a quantum state transition is minimal and the rise in temperature is as small as thermal dynamics allows.

Prior to magnetic trapping, optical pumping (OP) with σ^+ and π polarizations prepares the majority in a weak-field seeking states within $X^2\Sigma^+(v = 0)$, $|N, J, F, m_F\rangle = |1, 3/2, 2, 2\rangle$ (Figure 3.4a). To confirm, the composition of the trapped sample is measured using the microwave depletion spectroscopy *in situ* (Figure 3.4b). It shows that the majority (over 70%) is initially— in the low-gradient case —pumped into the hyperfine state $|1, 3/2, 2\rangle$, and the rest is in $|1, 3/2, 1\rangle$ and $|1, 1/2, 1\rangle$.

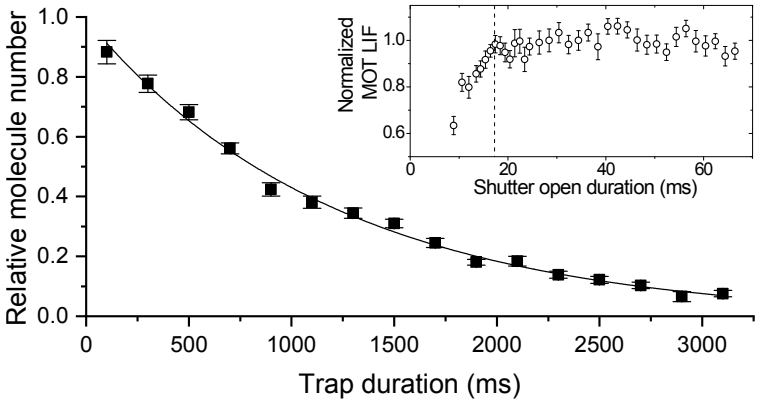


Figure 3.3: Lifetime in MQT. An in-vacuum shutter improves the vacuum condition by increasing the blocking of ballistic helium from the buffer gas beam source. The $1/e$ lifetime is determined by fitting decay of molecule signal to the trap duration. The inset shows that the closing of the shutter at a sufficiently late time (dashed line) has no effect on the MOT loading (Figure from Ref. [26]).

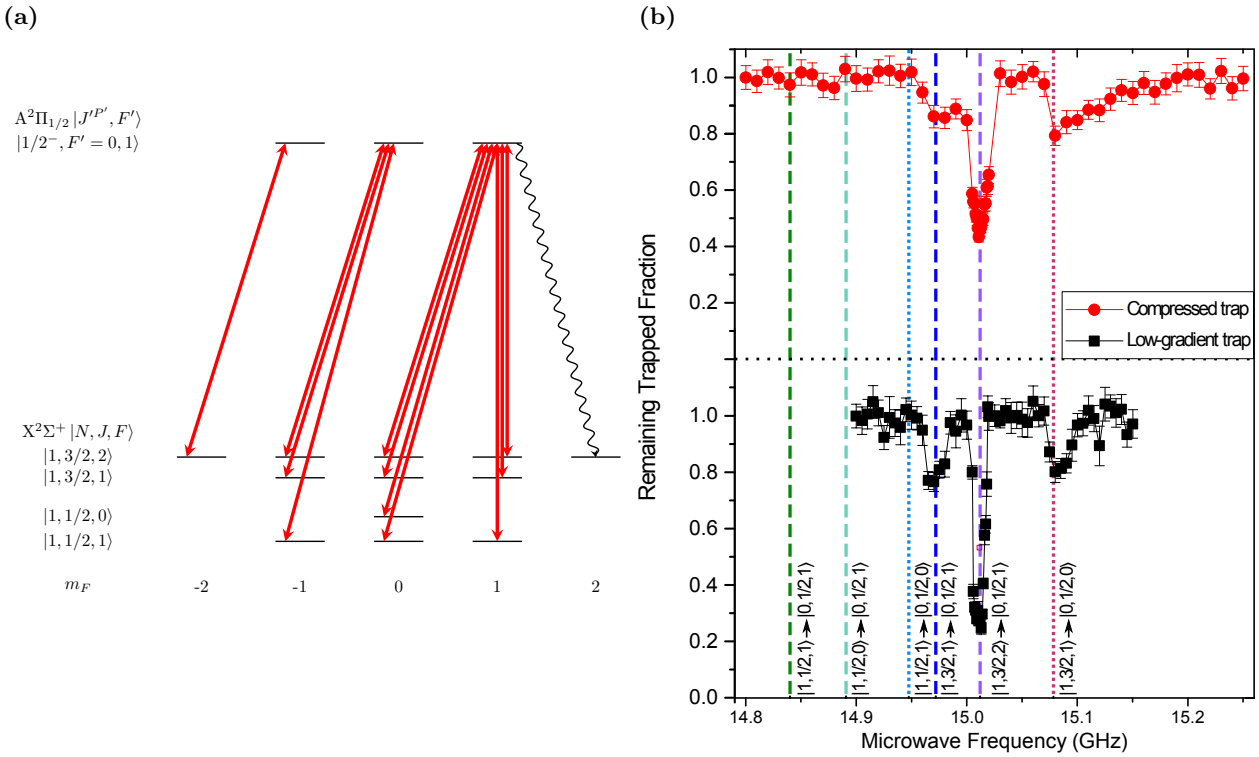


Figure 3.4: (a) Optical pumping prepares the majority o the trapped sample into the weak-field seeking state $|1,3/2,2\rangle$. (b) Microwave depletion spectroscopy depletes the population in the trapped sample within $X^2\Sigma^+(v=0,N=1)$ by driving microwave transitions to a different ground state rotational level $N=0$. Transitions between hyperfine levels are labelled by dashed and dotted vertical lines (Figure from Ref. [26]).

3.2 The switching circuit

A high-power circuit was developed to control the switching of MQT coils, specifically, to switch on and off a large current sufficiently quickly. In order to avoid loss due to gravity during the switch-on and to be compatible with detection methods that require free expansion after molecules are released from the trap, e.g. the time-of-flight method, we wanted to make the switch-on, and respectively, switch-off durations as short as possible. Taking note of other technicalities, such as eddy current in the stainless steel vacuum chamber, we aimed for a sub-millisecond (0.1-1 ms) switch-off time.

Because the low slew rate of the power supply results in a natural (unassisted) switching time is on the order of 100 ms, additional circuitry (Figure 3.5a) is necessary to accomplish these goals. The main current switch is the insulated-gate bipolar transistor (IGBT). It allows us to switch off the current current quickly. When the IGBT is closed/conducting, to switch on current, we can either turn on the power supply to deliver current I or discharge the stored charge in the 10-μF capacitor. The first method, though slow, is the only way to deliver 165 A (the maximum current from the power supply). The second method turns on current in < 1 ms but it only generates a peak current of 40 A when the capacitor is charged by a 1-kV source, in the high-voltage (HV) sub-circuit. The timing of the fast switch-on process is controlled by the silicon controlled rectifier (SCR). To illustrate the relative timing of switching events, Figure 3.5b shows a simplified timing sequence* When the IGBT is conducting, the current flows from either the power supply or the capacitor through the coils and then the IGBT to ground. When a TTL trigger forces the IGBT to become a circuit open, the induced EMF generated by the coils is dissipated in the two parallel chains of transient voltage suppressors (TVSs).

Figure 3.6 is a summary of the circuit's performance in the MQT experiment. The initial switch-on (bottom left) completes in about 320 μs; the switch-off time (bottom right) is sub-millisecond. The initial fast switch-on and switch-off proved sufficiently fast.

The circuit is inspired by a similar circuit designed at the University of Toronto [38]; however, in our case, due to the need to apply higher current and voltage, additional tests were necessary to upgrade the design. §3.2.1 describes how simulation and preliminary tests helped in choosing the configuration that allows us to switch off large current$\sim$ 165 A in the inductive coils sufficiently quickly. §3.2.2 describes the high-voltage sub-circuit (HV) that rapidly switches on $\sim$40 A. §3.2.3 summarizes the cooling methods implemented to deal with power dissipation in individual circuit components. Supplementary materials are in §3.2.4: sub-circuit diagrams, an example of the timing trigger, models/part numbers of circuit components.

*A more detailed version can be found in §3.2.4.

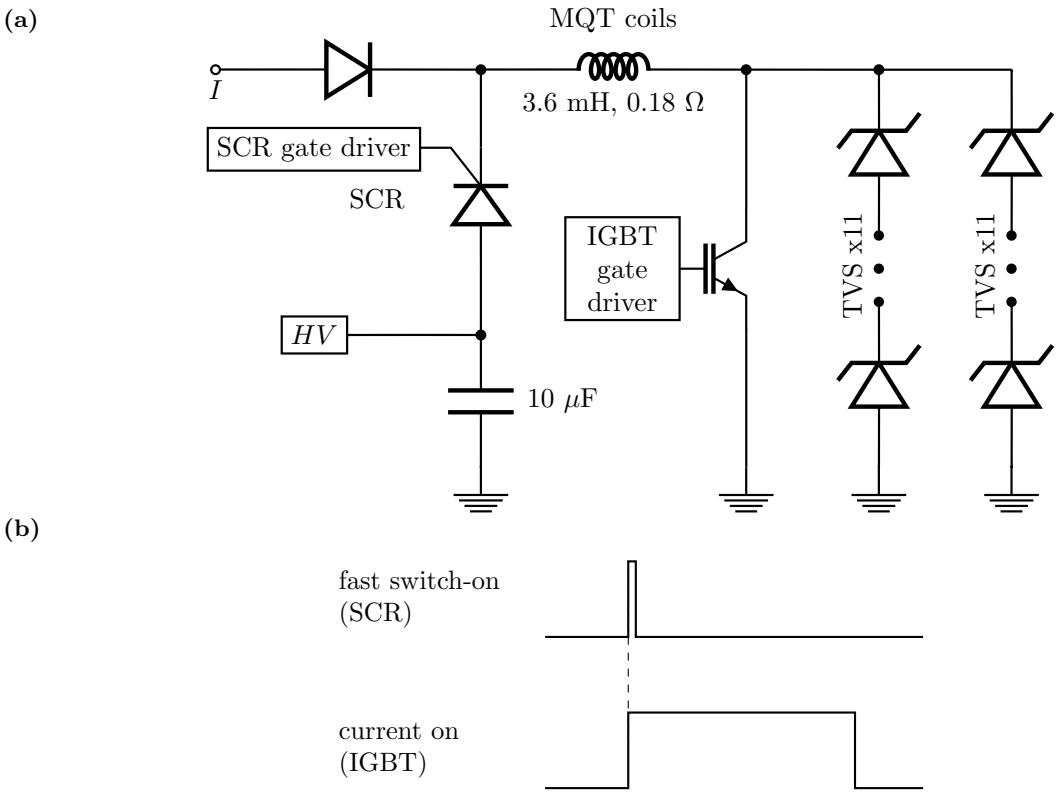


Figure 3.5: (a) Main circuit. IGBT, SCR and HV are controlled by individual timing triggers. The rectangular nodes represent sub-circuits that serve as buffers between the TTL trigger signals and the main circuit. Their circuit diagrams are included in §3.2.4, as those details are not immediate relevant to functions of the main circuit. Nevertheless, they have proven necessary in case of failure in the main circuit. (b) Relative timing of switching events. To switch on current quickly, a pulse trigger is sent the SCR, and a logic high to the IGBT. To switch current off, a logic low is sent to the IGBT.

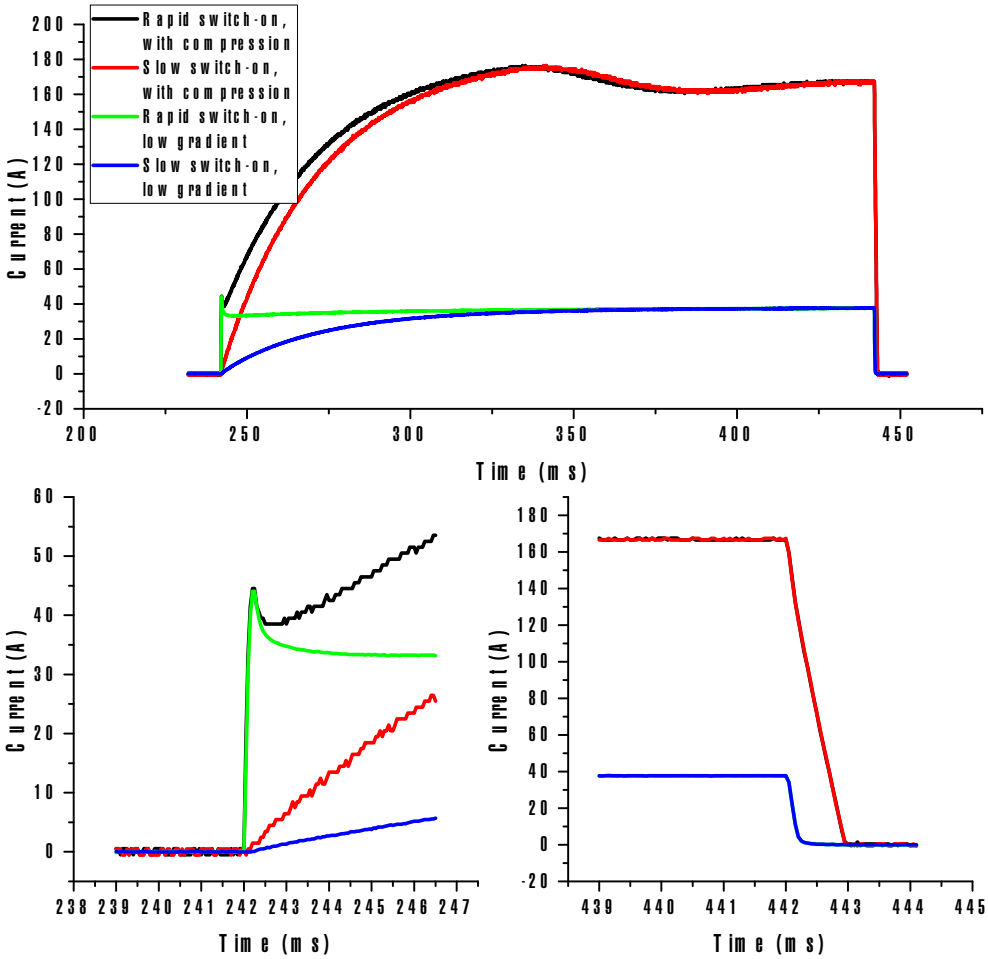


Figure 3.6: Characterization of the MQT switching circuit. Top panel shows the current as a function of time during magnetic trapping, starting at 242 ms in the full experimental cycle, for different switch-on and current settings. Bottom left shows the switch-on step. The rapid switch-on achieved by discharging a charged capacitor is significantly faster than the slow switch-on controlled by the power supply. Bottom right shows the switch-off step. The switch-off time is longer for higher current (in the with-compression cases) but still within a millisecond. The current is measured by a clamp-on Hall probe.

3.2.1 Simulation and preliminary tests

Prior to building and testing the circuit, circuit simulation is carried out to establish a preliminary design in the Simulation Program with Integrated Circuit Emphasis (SPICE). The main goal in the simulation is to work out a feasible configuration to deal with the induced Electromotive Force (EMF) as a result of rapidly switching off the current. To fully understand the challenge—to estimate the magnitude of the induced EMF, it is necessary to mention some features of the IGBT. An IGBT is a power semiconductor switch with higher current and voltage ratings, compared to Metal-Oxide-Semiconductor Field-Effect Transistors (MOSFETs). It combines the input low-impedance feature of MOSFETs with the output characteristics of a bipolar transistor. Unlike MOSFETs, most IGBTs do not have an intrinsic reverse diode; the natural switch-off time of IGBTs with current and voltage ratings sufficient for our purpose is sub-microsecond. This feature of the IGBT has direct implications in this circuit. According to Faraday's law of induction, for a coil with inductance L,

$$\text{EMF} = -L\frac{dI}{dt}. \tag{3.2.1}$$

Given the sub-microsecond switch-off time, the coils' inductance $L = 3.6$ mH, and the steady-state current $I \approx 150$ A (in the compressed MQT), the induced EMF would a few hundreds of kiloVolts. This indeed exceeds the reverse voltage rating of most circuit components including the IGBT itself. The solution is to add TVSs in parallel with the IGBT which effectively increases the switch-off time.

A transient voltage suppressor (TVS) is a Zener diode that suppresses any transient voltage above its stand-off voltage. Usually, in the datasheets provided by manufactures, there is information about the stand-off voltage and the peak pulse power or voltage the device is capable of. To achieve a stand-off voltage over a hundred volts, it is recommended to stack TVSs in series (e.g. in the application note by Vishay [39]). It is however not clear how to estimate the clamping voltage or effective stand-off voltage for a TVS stack from basic information about the stand-off voltage of a single TVS. If the clamping voltage is too high, the induced EMF will find other paths to ground—this defeats the initial objective. If the effective stand-off voltage is too low, the switch-off time will be unnecessarily lengthened. Figure 3.7 shows an intuitive picture of the trade-off between the clamping voltage and the switch-off time. Suppose the transient voltage is clamped to a constant V_{clamp}; according to (3.2.1), the rate of change in current would also be constant, $dI/dt = V_{\text{clamp}}/L$. Therefore, a lower clamping voltage leads to a longer switch-off time. Another idea worth considering is adding TVS stacks in parallel. Provided that the peak power to be absorbed in these TVSs is estimated to be on the order of 100 kW, heating can be nontrivial even if the switch-off duration is sub-millisecond. Therefore, adding multiple stacks of TVSs in parallel can help reduce the current and thus

power dissipated in each TVS.

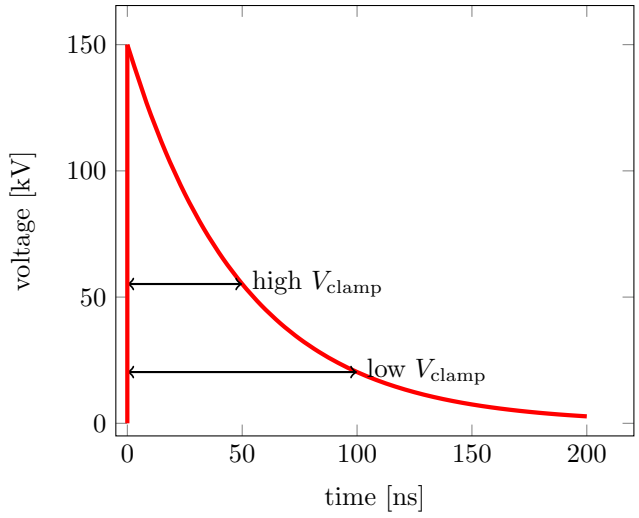


Figure 3.7: Trade-off between the clamping voltage and the switch-off time. The red curve is the (hypothetical) transient voltage induced when a large current $\sim$ 150 A is switched off without any TVSs. The clamping voltage V_{clamp} depends on the configuration of TVSs. A lower V_{clamp} results in a longer switch-off duration.

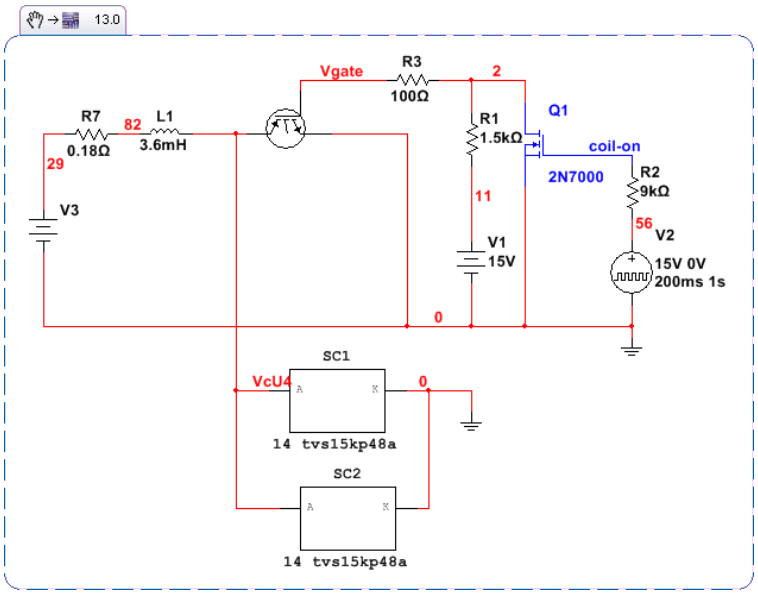


Figure 3.8: An example of circuit diagram in Multisim (an interface for SPICE provided by National Instrument). `SC1` and `SC2` are sub-circuits each consisting of 14 TVSs in series. V2 is a pulse signal that becomes Vgate after a buffer circuit; it ultimately controls the switching of the IGBT.

Motivated by these questions, the simulation investigated switch-off characteristics of different configurations of TVSs, namely, the induced EMF and the switch-off time. In the circuit, the induced EMF after clamping can be measured as the voltage across the IGBT, V_{CE}. C stands for collector, connected to the coils; E stands for emitter, connected to ground. The effective stand-off voltage is estimated as the

maximum of V_{CE}, occurring at the very beginning when the TVSs break down starts. The switch-off time is the time it takes for the current value to change from its maximum to zero. The circuit diagram of one of these configurations investigated in the simulation is shown in Figure 3.8.

Summary of simulation results

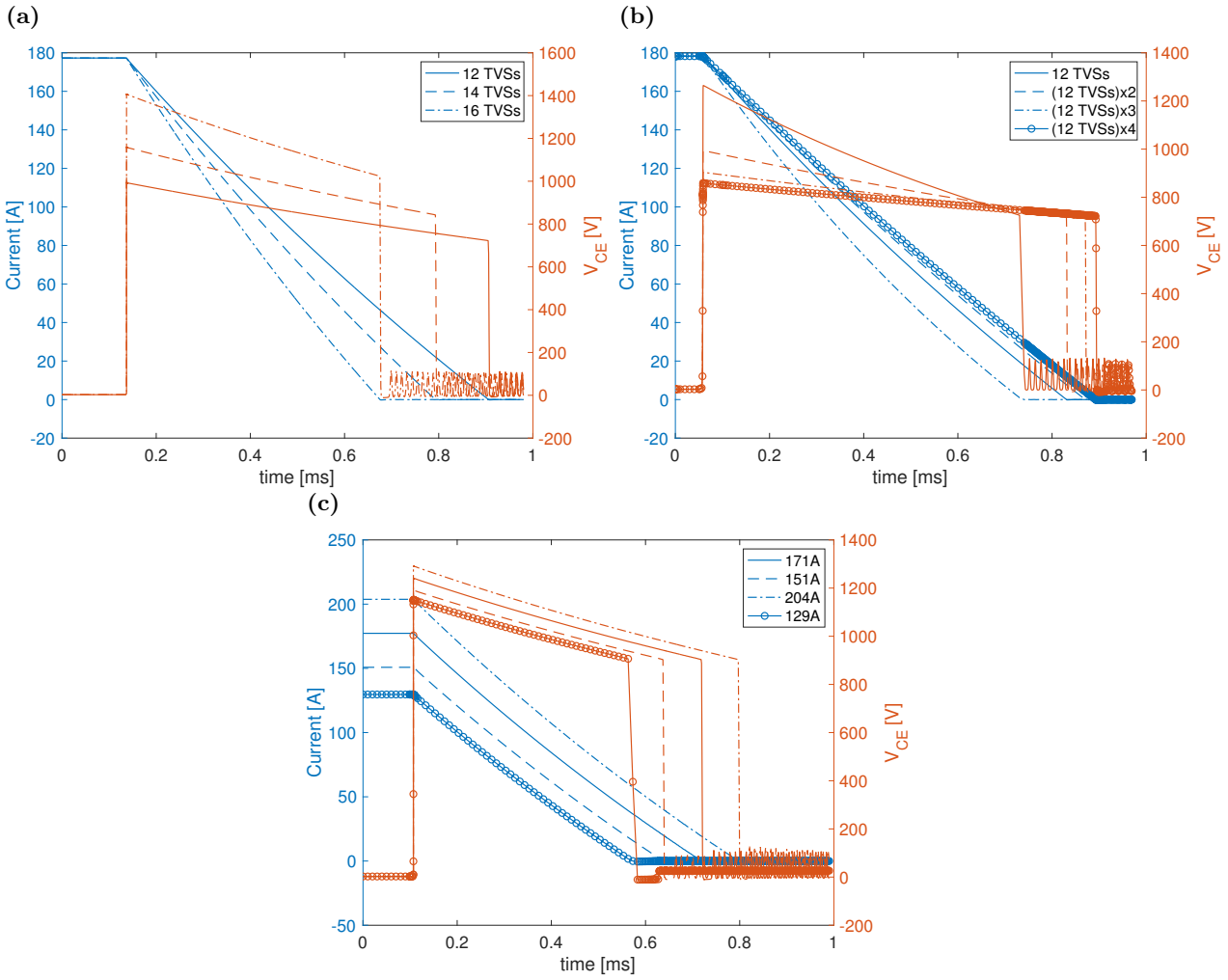


Figure 3.9: Different TVS configurations in SPICE simulation: (a) N TVSs in series and (b) N chains of 12 TVSs in parallel. (c) Current-dependent characteristics in SPICE simulation (15 TVSs in series). Blue lines are current, and red lines are voltage values across the IGBT. Simulation results agree with the intuitive expectations, and finds two chains of 12-TVSs stacks as a good starting point for experiments.

The simulation qualitatively confirmed the intuitive picture* It showed that having more TVSs in series reduces the switch-off time and thereby increases the induced EMF (Figure 3.9a); having TVSs in parallel increases the switch-off time (Figure 3.9b); switching off larger current takes longer time (Figure 3.9c). More

*or in a personal case, it helped establish intuitive understandings as I had not been knowledgeable about Zener diode to begin with.

practically, it suggests that for a TVS model with a stand-off voltage of 48 V, two chains of 12-TVS stacks would be sufficient to clamp the peak voltage to below 1 kV and produce a sub-millisecond switch-off time.

Summary and discussion of preliminary test results

Tests for different TVS configurations shows a linear dependence between switch-off time and current for a wide range of current values (Figures 3.10 and Figure 3.11). In Figure 3.11, characteristics of two models of the TVSs in various arrangements are also compared. 15KP48A has a lower stand-off voltage, 48 V, compared to 15KP60A. The convergence between the simulation and data was not pursued after a promising design was found, even though parameters in the SPICE models for the TVSs and IGBT can be tweaked for this purpose. Two main reasons are as follows. First, the switch-off time depends on both the stand-off voltage and the the temporal width of the induced voltage pulse. The convergence between simulation would require a good SPICE model for not only the TVS but also the IGBT. Second, the best use of such a model would be to predict the circuit characteristics to prevent accidents in the high-current and high-power regime by calibrating to data in the low-current regime. Unfortunately, the characteristics may differ at higher current because of heating: without any fan-cooling, a temperature of over 80°C was measured on TVS's package when switching off only 45 A. Indeed, the linear fits to switch-off time vs current data in the high-current tests are not as good as in the low-current tests. Taking heating into account entails teaching the model about thermal runaway [40], which would involve a new class of technicalities. But more importantly, it is a problem to be dealt with rather than understood, as cooling methods will be mentioned in §3.2.3.

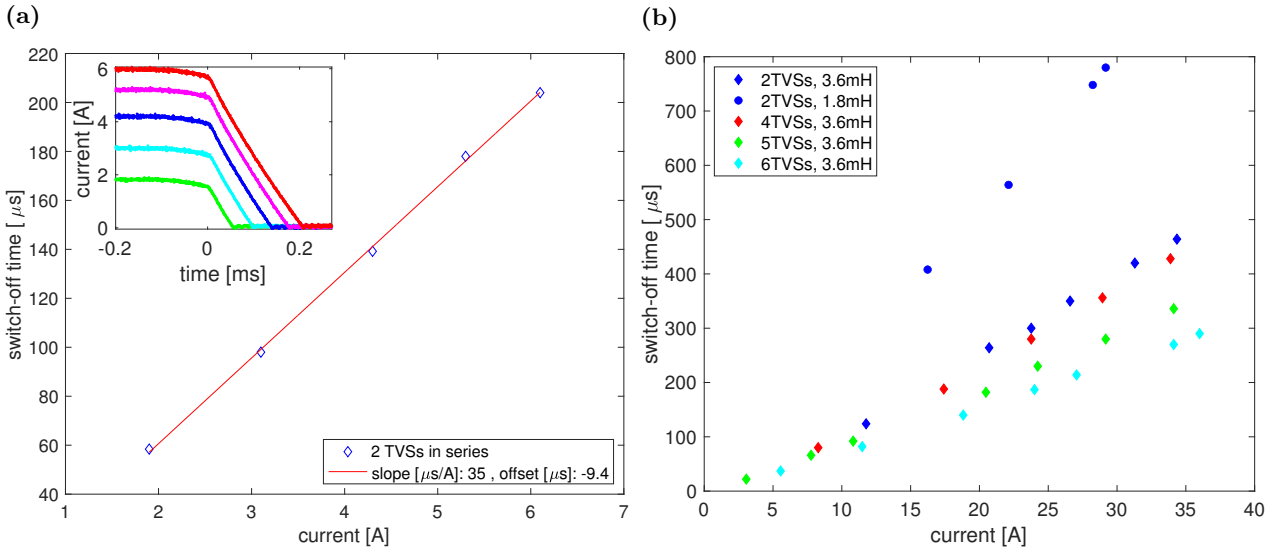


Figure 3.10: Switch-off time vs current in the low-current range. (a) Switch-off time increases linearly with current for 2 TVSs (15KP48A) in series. The inset shows the raw data from which the switch-off times were determined. (b) Switch-off time vs current for different TVS configurations shows adding more TVSs in series reduces the switch-off time.

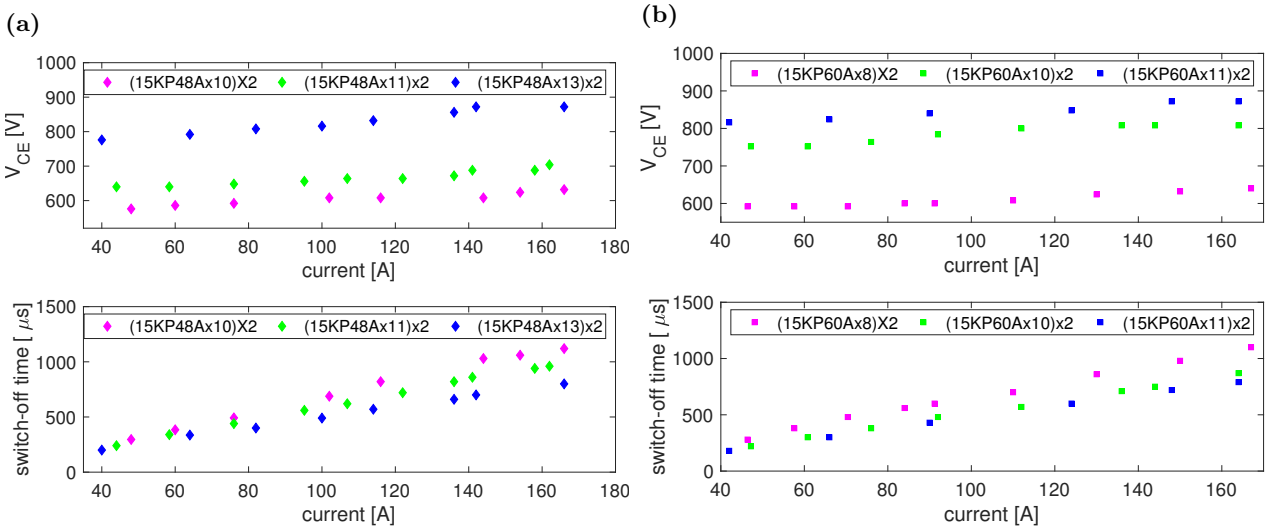


Figure 3.11: Induced EMF and switch-off time for two TVS models, 15KP48A and 15KP60A, in various configurations. Current is measured by a clamp-on hall probe and the voltage across the IGBT (V_{CE}) by a high-voltage oscilloscope probe with range up to 1 kV. Data agrees with simulation results qualitatively. Both V_{CE} and switch-off time are still linear functions of current, though the goodness of fit is not as good as in the low current case. A plausible explanation is thermal effects.

3.2.2 Initial switch-on

To speed up the switch-on of current, the solution is to add a capacitor and make use of LC oscillation. To facilitate this, a high voltage source, which is a dc-dc converter, charges a 10-μF capacitor with high voltage (1 kV). To fully charge the capacitor to 1 kV, the charging duration $\approx$ 560 ms, 7 times the RC constant due to resistors added to limit the charging current, $R \approx 8$ kΩ (Figure 3.16). When the stored charge is discharged from the capacitor into the MQT coil, the initial current is about 40 A and the discharge duration is measured to be $\approx 320\,\mu$s (Figure 3.12). The timing control of the charging process is achieved by sending a TTL to the dc-dc converter. The start of the discharge is controlled by a SCR, a unipolar (anode to cathode only) transistor gated by current triggers. When the trigger voltage is constant, no current flows into the SCR gate and the device remains off in the forward blocking mode. If a rising edge in voltage causes current to flow into the gate and that the gate current is sufficiently large, the SCR latches and becomes conductive. The threshold current for latching depends on the forward voltage— per SCR's IV curve, a lower forward voltage requires a higher gate current. After the capacitor is discharged, the forward voltage drops (and later is reversed during the switch-off) and the SCR remains off in the reverse blocking mode. Its characteristics eliminate the need for a precise pulse width in the trigger signal and minimize interfering with the power supply.

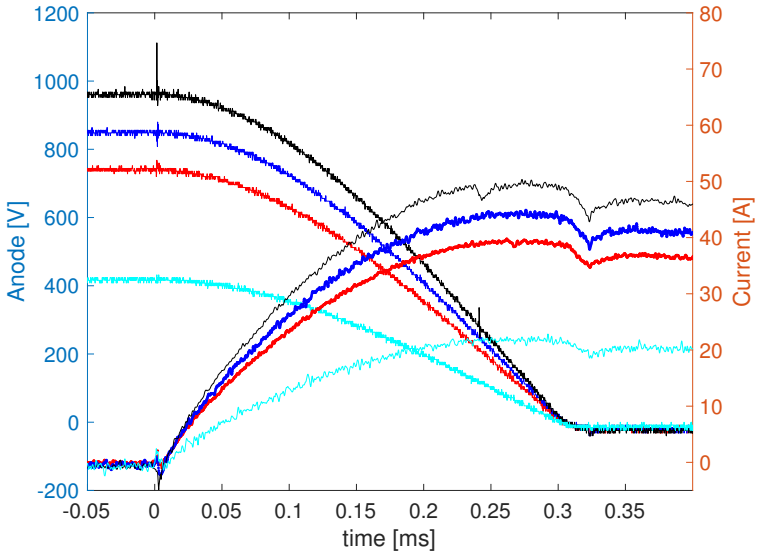


Figure 3.12: Discharging the capacitor. Falling curves are voltage values at SCR's anode (y-axis on the left), relative to ground. Rising curves are current in the coils (y-axis on the right). Curves with the same color are measured simultaneously for the same settings. Different voltages at the SCR anode result in different peak currents, indicated by three different colors, but does not affect the switch-on time.

3.2.3 Thermal dissipation

As heating is prevalent in the entire circuit, the secondary challenge is to regulate the temperatures, especially of active circuit components. Despite the low resistance of most semiconductor devices in the main circuit, heating due to $\approx 160\,A$ is not negligible and can limit the performance of semiconductor devices as per specifications. Direct water cooling is applied to the coils through the central tunnel of the hollow copper tubing used to construct them. The IGBT module is mounted on a water-cooled cold plate. The rectifier diode protecting the power supply is in thermal contact with a heat sink for air cooling. The TVSs diodes are air cooled. Three fans are on included in the box to speed up the air flow. These cooling measures keep the steady-state temperatures below 60°C for a realistic duty cycling (<50%) in the experimental repetition. Figure 3.13 shows the arrangement of fans and their proximity to circuit components and heat sinks.

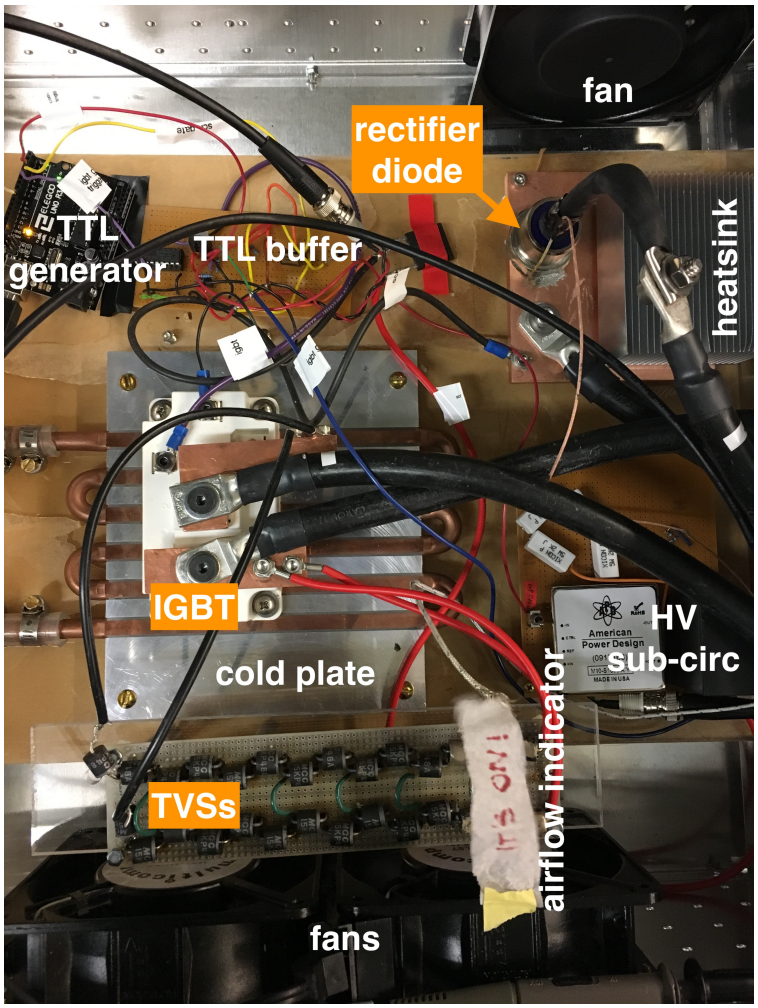


Figure 3.13: Cooling inside the fast switch box. IGBT is cooled by a water-cooled cold plate. TVSs and the power-supply protection diode are cooled by fans.

3.2.4 Supplementary

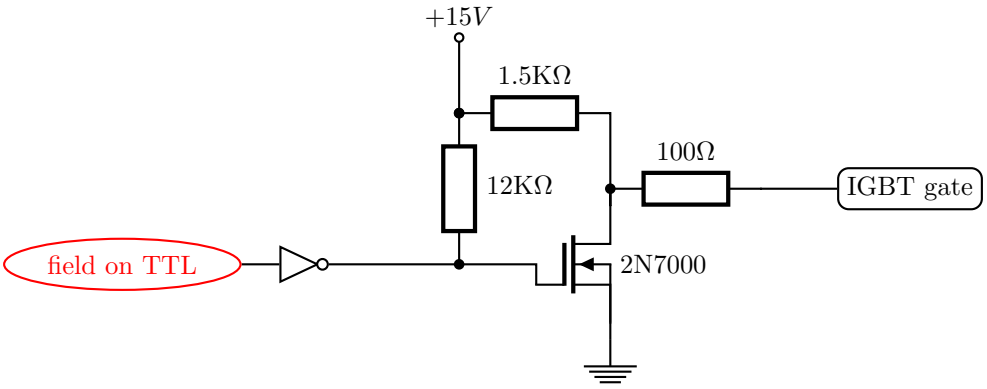


Figure 3.14: IGBT gate driver sub-circuit. This circuit receives a TTL signal that controls the opening and closing of the IGBT.

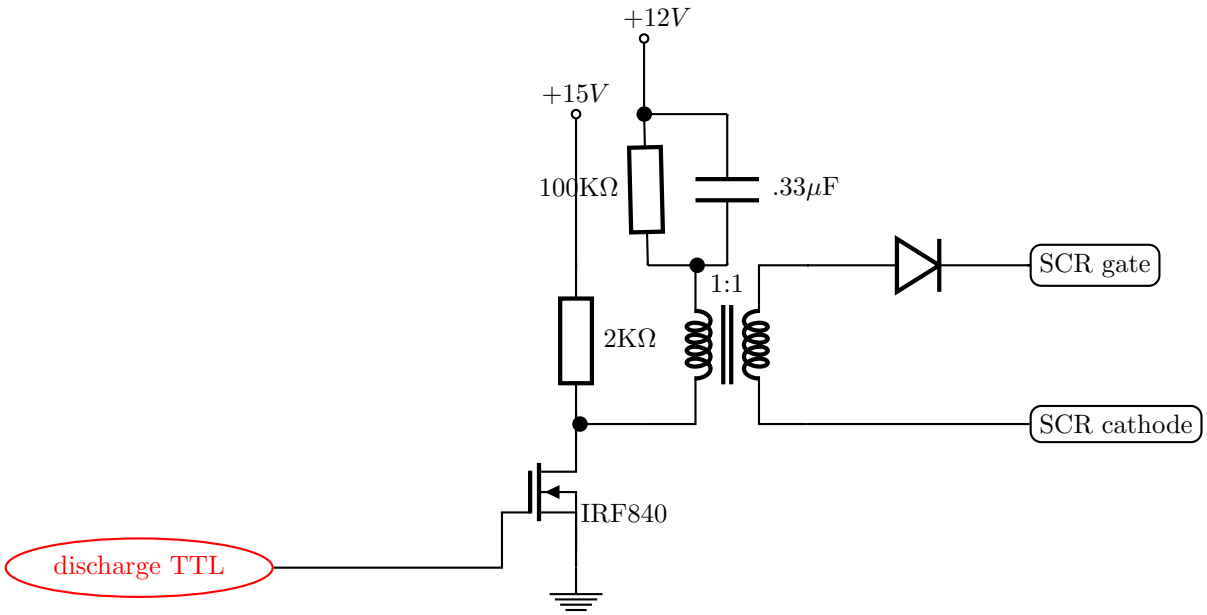


Figure 3.15: SCR gate dirver sub-circuit. This circuit receives a TTL signal that ultimately controls the discharge start of the capacitor. When the TTL changes from low to high, the current flowing from the SCR cathode to its gate triggers SCR to latch (become conductive).

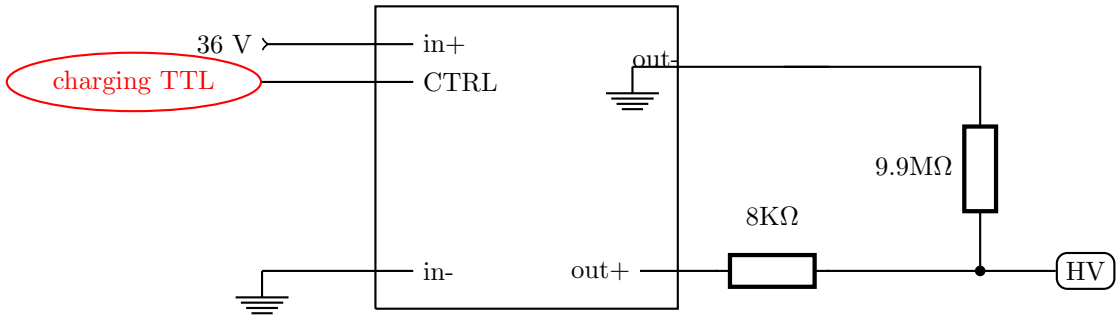


Figure 3.16: HV sub-circuit includes a dc-dc converter and some current-limiting resistors. The charging TTL controls the output voltage (at out+), i.e., when to charge the capacitor.

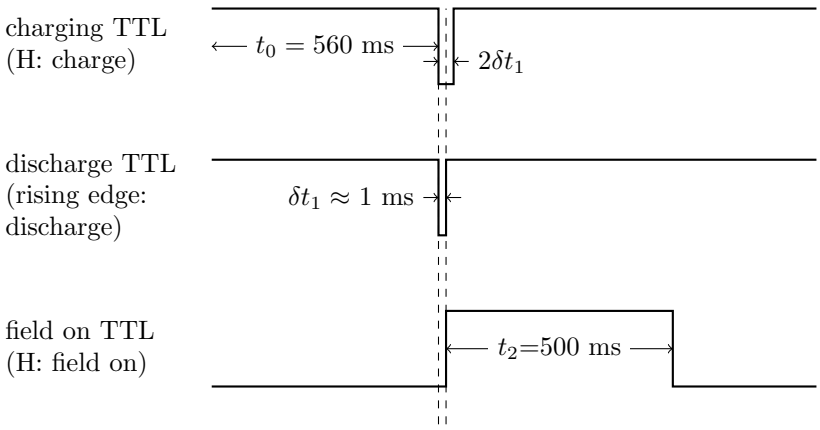


Figure 3.17: An example of trigger signals with typical delay durations (not to scale). The cycle starts by charging the capacitor. t_0 is the charging duration. t_2 is the ON duration of the IGBT. The discharge TTL is a pulse trigger for the SCR with pulse duration δt_1(not critical). Its rising edge generates a current that triggers the SCR to latch. The charging stops during the discharge (about 320 μs) as recommended for the dc-dc converter. The total period is about 1 s.

circuit part	manufacturer	model/part number
insulated-gate bipolar transistor (IGBT)	Microsemi	APTGT600U170D4G
silicon controlled rectifier (SCR)	IXYS	CS 20-22moF1
dc-dc converter	American Power Design	M10S1000A/Y
rectifier diode	GeneSiC Semiconductor	S300Y
unipolar transient voltage suppressor (TVS)	Littelfuse Inc.	15KP48A

Table 3.1: List of circuit components in the switching circuit.

Chapter 4

Two-dimensional magneto-optical trap: a slow beam source of ^{87}Rb

4.1 Introduction

In ultracold quantum gas experiments, the number of atoms is a common and crucial figure of merit. Generally speaking, large atom number allows better signal-to-noise ratios, and greater robustness in day-to-day operation. In connection with the SrF experiment and the long-term goal of implementing sympathetic cooling between Rb and SrF, observing atom-molecule collisions is contingent on loading a large number of Rb in the dual species MOT of SrF and Rb. Naturally, having an intense and slow atomic beam is preliminary to attaining a large atom number. A two-dimensional magneto-optical trap (2D MOT) is a promising solution for creating a slow and intense beam of Rb based on Doppler cooling. It has been shown that the flux out of a 2D MOT can be as high as $10^9 - 10^{11}$ atoms/s [41–43]. Compared to alternatives, including vapor cell [44], Zeeman-slowed beam source [45] and low-velocity intense source [46], the main advantage of a 2D MOT beam source is the ability to produce a higher flux. While the flux of 2D MOTs is, in fact, comparable to that of modern Zeeman slowed beam sources e.g., in Ref.[47], 2D MOTs are more compact. The state-of-the-art Zeeman slower can produce a flux $\sim 10^{12}$ atoms/s [48]. However, because the length of its slowing region is about 1 m, as is typical of Zeeman slowers, integrating it into the current SrF MOT setup would be difficult. In addition to flux and compactness, the range of transverse and longitudinal velocity of 2D MOT atoms suggests good prospects of being captured in a 3D MOT downstream. For instance, in Refs.[41, 42], Rb atoms from a 2D MOT form a collimated atomic beam with a beam divergence of $\sim$40 mrad. From the measured mean forward (or longitudinal) velocity, typically a few tens m/s, the mean transverse velocity is estimated to be less than 1 m/s.

In this chapter, §4.2 describes the experimental setup. §4.3 shows how the maximum flux is determined. §4.4 discusses methods used in characterization, such as the calibration of the flux fluorescence and the determination of Rb vapor pressure via absorption.

4.2 Experiment

§4.2.1 describes the laser system developed for trapping and cooling Rb using the D_2 transition, which is relevant not only to the 2D MOT step but also the 3D MOT in chapter 5. §4.2.2 discusses the rest of 2D MOT apparatus.

4.2.1 Rb D_2 laser system

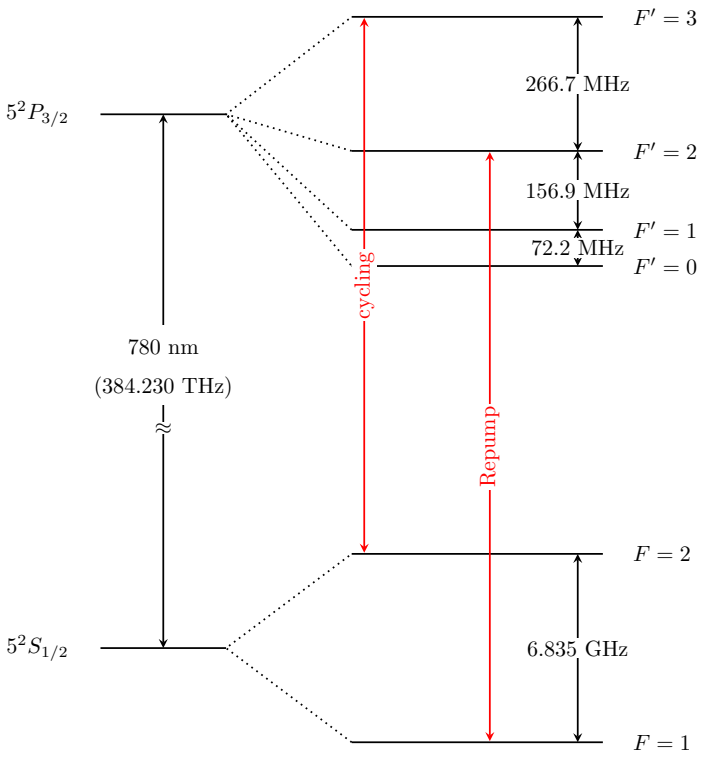


Figure 4.1: D_2 transition and energy level diagram up to the hyperfine structure of ^{87}Rb. Red arrows indicate the cycling and repumping transitions for cooling and trapping.

External cavity diode lasers

Two external cavity diode lasers (ECDLs) are used for laser cooling based on the D_2 transition in ^{87}Rb (Figure 4.1). The cycling/trap ECDL drives the $2 \rightarrow 3$ transition, and the repump ECDL drives the $1 \rightarrow 2$

transition. They are home-built ECDLs in the Littrow configuration [49–51] whose design is detailed in a former graduate student's thesis [27].

In building these ECDLs, we found the frequency profile was very noisy. After a local (and inside the ECDL's housing) low-pass filter circuit was added, the mode quality was significantly improved. Figure 4.2 shows the effectiveness of a low-pass filter with cut-off frequency at $f_c = \frac{1}{2\pi\sqrt{LC}}$ =3.4 kHz. The frequency profiles were randomly sampled at different times under identical conditions, i.e., for the same frequency mode with identical temperature and current set points. With the low-pass filter, the width of each ECDL's frequency profile is typically less than 1 MHz, much smaller than the natural linewidth of the D_2 transition, $\Gamma = 2\pi \cdot (6 \text{ MHz})$. Therefore they are sufficiently coherent for laser cooling.

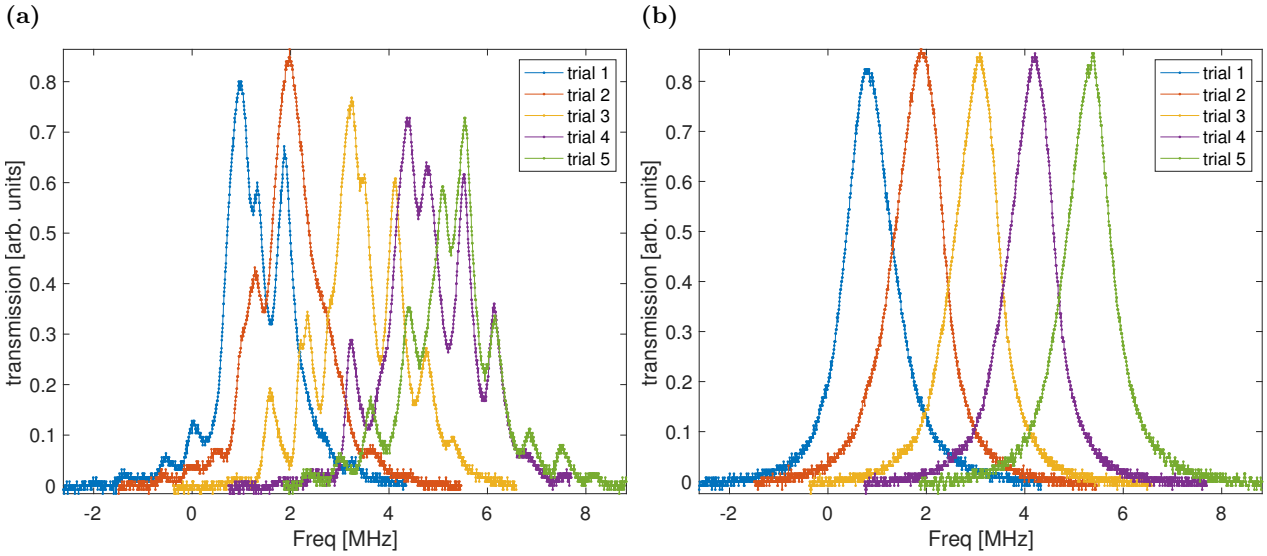


Figure 4.2: Frequency profiles of an ECDL in a Fabry-Pérot cavity (a) before and (b) after a low-pass filter is added. The frequency on the horizontal axis is converted from time, using the scanning time required to a free spectral range. Peaks are shifted arbitrarily for display.

Frequency stabilization

In addition to supplying coherent photons, each ECDL needs to be locked to a useful frequency for laser cooling. The D_2 trap ECDL is locked at a frequency 12 MHz to the red of the $F = 2 \rightarrow F' = 3$ transition, and the D_2 repump ECDL is locked to the $F = 1 \rightarrow F' = 2$ resonance. The transition frequencies are identified via saturated absorption spectroscopy (SAS) in a vapor cell (Figure 4.3).

Then the Cavity Lock, which is a software feedback control program commonly used in this lab [27, 52], stabilizes ECDLs at any desired absolute frequency in the vicinity of the SAS peaks. In the Cavity Lock, the cavity refers to a scanning Fabry-Pérot interferometer built with a pair of confocal mirrors with a piezo attached to one of them. A periodic saw-tooth waveform is applied to the piezo to cover over one free

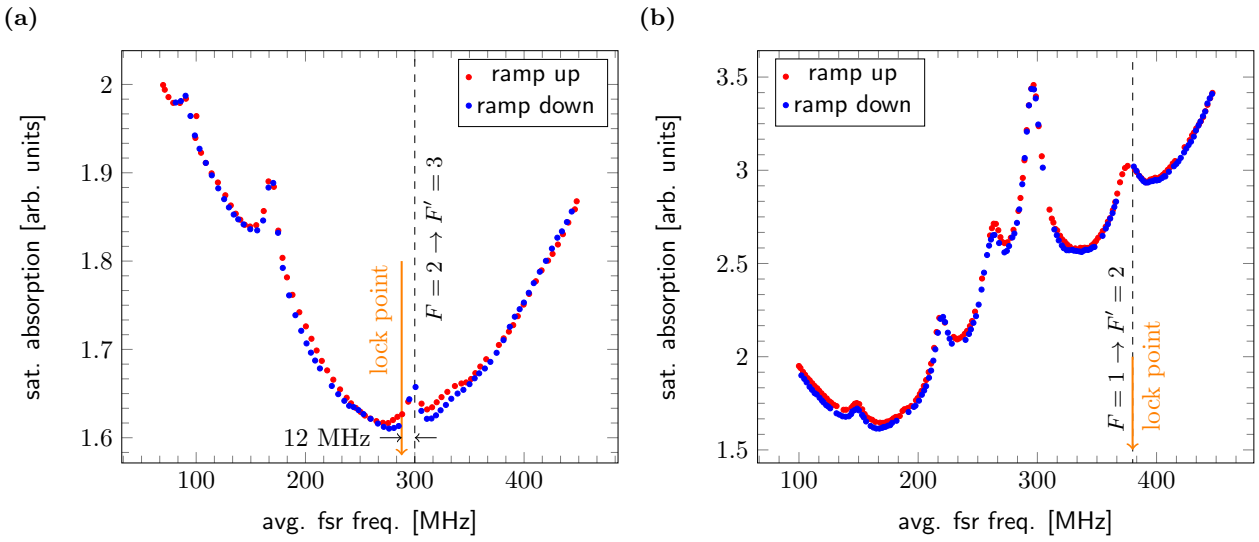


Figure 4.3: Saturated absorption spectroscopy in the vicinity of (a) the cycling transition $F = 2 \to F' = 3$ and (b) the repump transition $F = 1 \to F' = 2$. The horizontal axis shows the frequency defined with respect to the frequency of a stabilized HeNe laser in the same fsr averaged over ∼60 cavity periods. The orange arrow indicates the frequency lock point of each ECDL in the cavity. The splittings in Doppler-free absorption spectrum are as expected, given the excited state energy level structure.

spectral range (fsr) of the cavity, which is 500 MHz in case of the Cavity Lock for the Rb D_2 lasers. In each period (2.5 ms), the Cavity Lock adjusts the offset voltage applied to the piezo to minimize the change in the position of a transmission peak of a commercial stabilized HeNe laser. When the cavity is locked, the cavity error signal can be considered as the relative drift of the HeNe laser line in the cavity. For an ECDL, the error signal is the difference between its real-time frequency mod fsr and its set point. Typically, the root-mean-square (rms) frequency error is 0.5 MHz or less for the cavity, and less than 1 MHz for an ECDL. Figure 4.4 shows the typical size of the frequency error signal while the ECDL is locked by the Cavity Lock. It also shows the closed-loop response to a sudden change in the frequency set point. Compared to the conventional lock based on spectroscopy, the Cavity Lock has a much larger capture range, and lasers can be locked at any arbitrary point within the capture range without the need for additional hardware to offset or modulate the optical frequency.

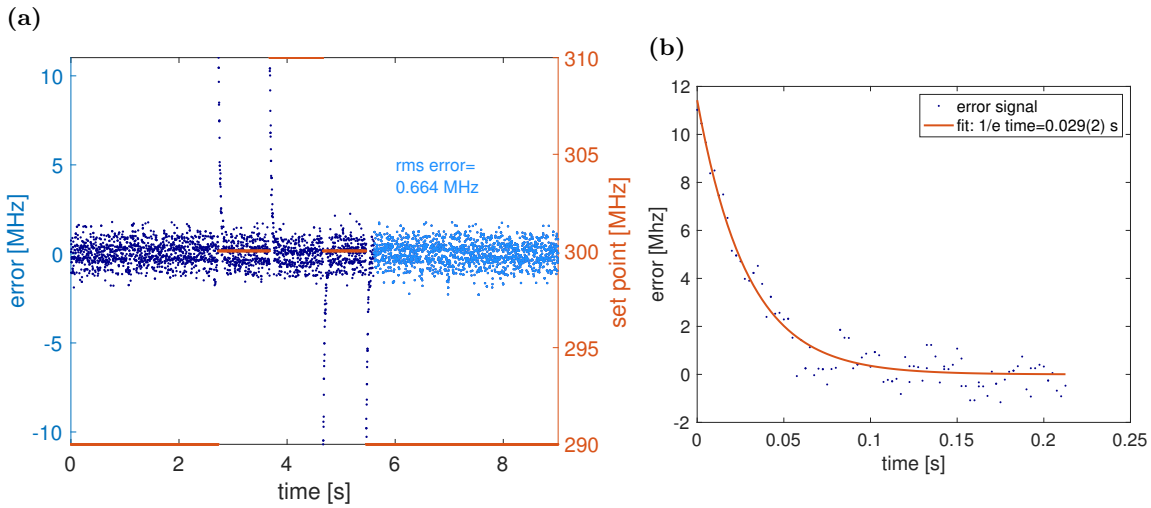


Figure 4.4: Error signal of an ECDL in the Cavity Lock. (a) The steady-state rms error calculated from data points in light blue is less than 1 MHz. Blue points (associated with the y-axis on the left) are rms errors with respect to the red set points (y-axis on the right). (b) Fitting the error signal following a 10-MHz step at time= 0 to an exponential function.

Frequency multiplexing

Since there are multiple laser cooling steps that require different detunings with respect to the cycling transition, acousto-optical modulators (AOMs) in single pass (sp) and double pass (dp) configurations are set up to generate different detunings. In the case of the double-passed AOMs, for changing the intensity and detuning rapidly within one repetition (Figure 4.5). The AOMs are powered by tunable RF sources, which only receive software triggers. By adding RF switches are added between the AOMs and their RF inputs, the AOMs effectively respond to hardware triggers with switching times $\sim \mu$s.

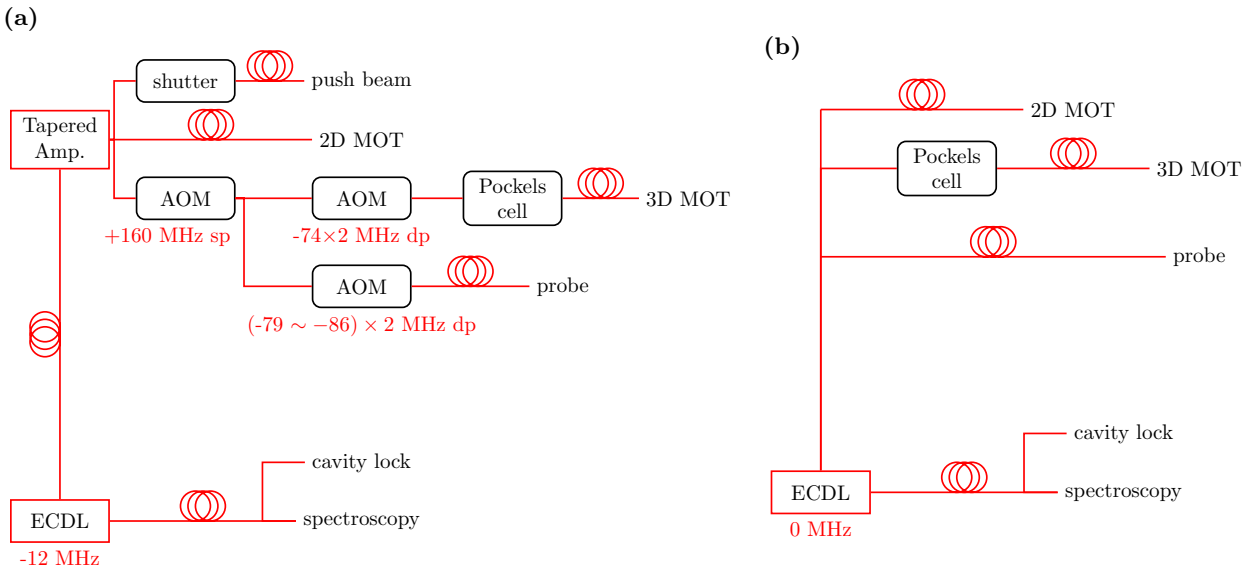


Figure 4.5: Schematic of the D_2 laser system with components addressing (a) the $2 \rightarrow 3$ cycling transition and (b) the $1 \rightarrow 2$ repump transition. Frequencies under the ECDLs indicate where they are locked relative to the resonances, and those under single-pass (sp) and double-pass (dp) AOMs indicate the offsets or the ranges of offset. Components in rounded boxes can receive external hardware triggers. A Pockels cell is used for fast polarization switching at 1.23 MHz in the radio frequency (RF) 3D MOT.

Tapered Amplifier

Each ECDL outputs at most 100 mW optical power at the transition frequency. While this is sufficient for the repump transition, it is not realistic for implementing laser cooling and trapping, due to technicalities such as transmission loss through optical isolators and limited fiber coupling efficiency. To create a high power coherent light source, light from the trap ECDL is used to seed a tapered amplifier (TA) which can generate up much higher optical output (up to 2 W).

$2 \rightarrow 3$	2D MOT	3D MOT
detuning [MHz]	12	24
$1/e^2$ diameter [mm]	(94, 47)	11
power [mW]	130×2	13×3

$1 \rightarrow 2$	2D MOT	3D MOT
detuning [MHz]	0	0
$1/e^2$ diameter [mm]	(94, 47)	11
power [mW]	8×2	2×3

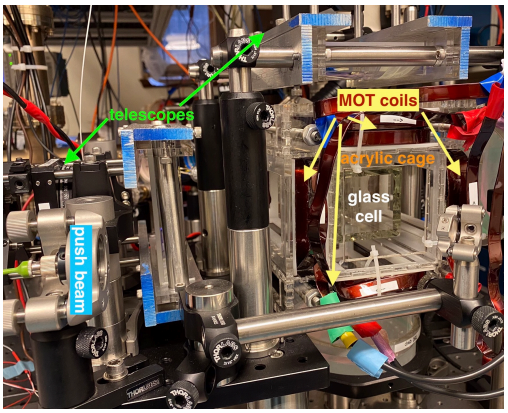
Table 4.1: Detuning and power of trap and repump light. The detuning of the trap light is specified with respect to the cycling transition $F = 2 \rightarrow F' = 3$, and the repump with respect to $F = 1 \rightarrow F' = 2$. The power refers to the power delivered to the experiment after fiber delivery. The multiplying factors in laser power indicate the number of independent laser beams.

Table 4.1 shows the detuning, power, and beam size of light for different purposes. 2D MOT beams are elliptical; the numbers specify the $1/e^2$ diameter along the major and minor axes.

4.2.2 2D MOT apparatus

The 2D MOT apparatus specifically include optics, 2D MOT coils that generate the trapping potential, rubidium dispensers, and vacuum components. Figure 4.6a is a photo of the 2D MOT apparatus, and Figure 4.6b envisions how the 2D MOT can be integrated into the current SrF setup in SolidWorks.

(a)



(b)

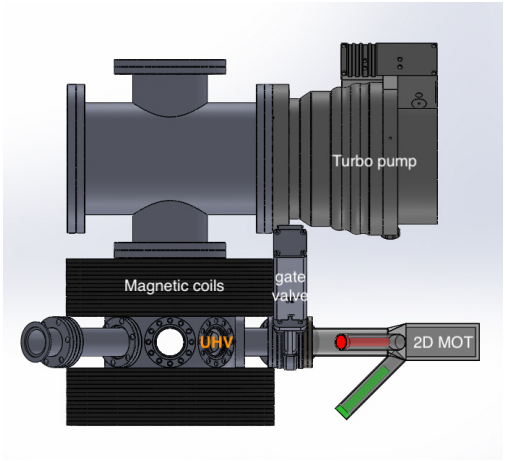


Figure 4.6: (a) 2D MOT apparatus. Two pairs of rectangular anti-Helmholtz coils generate a quadrupole field; they are held in place by an acrylic cage. 2D MOT optics, including two pairs of telescopes, retro-mirrors, and quarter wave plates, produce 4 circularly polarized laser beams intersecting at the trap center. Rb dispensers (not shown) are located inside the glass cell vacuum chamber. (b) Integrating the 2D MOT into the current SrF setup. Main geometric constraints are set by the magnetic trapping coils outside the chamber and the turbopump directly above the 2D MOT apparatus. A gate valve is in between the glass cell and the SrF vacuum system. The 2D MOT is attached to the conflat flange opposing the imaging port, with a gate valve in between the glass cell and the SrF vacuum system.

Optics

Optics for the 2D MOT includes two identical telescopes, quarter-wave plates that circularize linearly polarized light, and retro-mirrors. Each 2D MOT telescope is a Galilean telescope, consisting of a concave lens ($f = -12$ mm) and two cylindrical convex lenses ($f = 75$ mm and $f = 150$ mm). It expands the input circular beam from a fiber collimator with a $1/e^2$ diameter of 7.5 mm by factors of 6.25 and 12.5 anamorphically. The $1/e^2$ diameter is about 94 mm in the longitudinal dimension and 47 mm in the transverse dimension. The longitudinal beam width is very close to the size of the glass cell in this dimension, maximizing the interaction time in the 2D MOT and thus the effect of transverse cooling. Each expanded laser beam is then retro-reflected after traversing the trapping region. Along the longitudinal dimension, the trap beams are collimated so that the entire cooling region is captured; along the transverse dimensions, the beams are slightly convergent to compensate for transmission loss through the glass cell and quarter-wave plates (∼33%

loss without Rb vapor and ∼35% at $2{\cdot}10^{-7}$ mBar).

2D MOT coils

In order to choose the dimensions and the number of turns for the magnetic coils, the analytical expression of the magnetic field generated by a rectangular loop is found by applying the Biot-Savart law. The gradient along each transverse dimension is constant in the vicinity of the trap center. The coils are wound with ribbon wires whose cross section is rectangular and has a large aspect ratio. When stacked in layers, due to the large aspect ratio, ribbon wires can dissipate heat more quickly compared to a bundle of wires with a circular cross-section of the same gauge. When 22 A, the maximum current allowed, is applied with 100% duty cycle, the temperature can reach 70°C, beyond which heating may become a concern for the acrylic cage they are situated in. When the flux is optimized, the current in each coil is not equal, ranging from 15-20 A, producing a transverse magnetic gradient of ∼20 G/cm. Two of the four coils, the top and left coils, are connected in series, and so three power supplies can control the position of field zero in the 2D MOT by applying an arbitrary offset field.

Rubidium dispensers

Dispensers are designed to dispense rubidium atoms (natural abundance) via sublimation and/or vaporization when a heating current is applied. The vapor pressure of rubidium is measured via absorption spectroscopy and determined as a function of the heating current applied to the dispenser (Figure 4.7). Further details— the derivation of absorption cross-section and a comparison to alternative methods for determining Rb vapor pressure—are included in §4.4.4. As the vapor pressure depends exponentially on the heating current, the setpoint for the heating current is digitally controlled for consistency, and the heating current is monitored by a Hall probe.

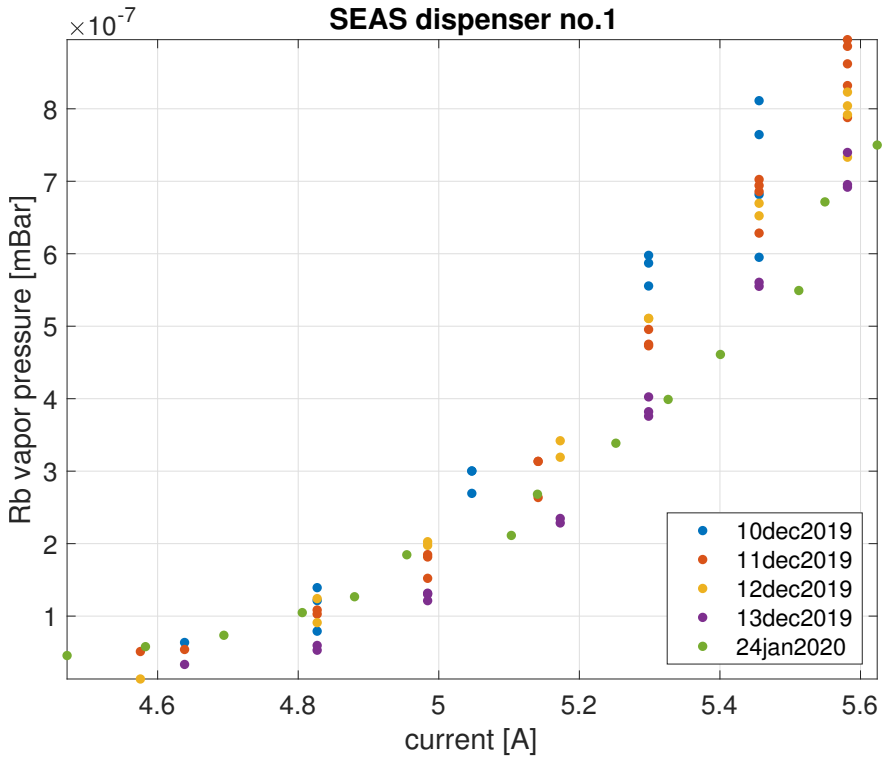


Figure 4.7: Rb vapor pressure vs heating current for a typical dispenser. The vapor pressure stabilizes quickly (within 10 minutes), and is consistent on a daily basis.

Vacuum components

In the latest 2D MOT apparatus (Figure 4.6a), the vacuum chamber is a glass cell with extrusions containing two Non-evaporative getter (NEG) pumps and three Rb dispensers. In addition, there is a gate valve, a differential pumping tube, and some accessories for mounting the differential pumping tube.

Given that all 2D MOT vacuum parts would be baked to reduce outgassing, the pressure in the 2D MOT region ($p_{2\mathrm{D}}$) ought to be primarily due to Rb, $p_{2\mathrm{D}} \approx p_{2\mathrm{D}}(\mathrm{Rb})$. Based on the flux vs vapor pressure curves of Rb 2D MOT and 2D+ MOT (2D MOT with a longitudinal push beam) in Refs.[41, 42], we expect to operate the 2D MOT at $p_{2D}(\mathrm{Rb}) \sim 10^{-7} - 10^{-6}$ mBar. In order to maintain ultra high vacuum (UHV) condition in the 3D MOT region with pressure $p_{\mathrm{UHV}} < 10^{-9}$, differential pumping is necessary to maintain a pressure ratio of $\sim 10^4$. In addition to the conductance (C), the pressure ratio between two vacuum regions also depends on the pumping speed in the UHV region with lower pressure S when there is no pumping in the higher pressure region [53]

$$C = \frac{p_{\mathrm{UHV}}}{p_{2\mathrm{D}}} S. \tag{4.2.1}$$

In our system, the pumping speed from the 3D MOT chamber is the sum of the pumping speed of the turbo (or ion) pump, 700 l/s (40 l/s) and of the stainless steel surfaces which Rb atoms stick to with high

probability ~ 1 [54], $S \sim 1800\, l/s$. The pumping speed of NEG pumps in the 2D MOT region, $\sim 10\, l/s$, is negligible. Given this target pressure ratio and the pumping speed in the UHV region, we aimed to design a differential pumping tube with conductance $\sim 0.1\, l/s$.

In the molecular flow regime, the conductance of a straight tube can be calculated based on geometry, the diameter D and the total length L [53],

$$C_{\text{tube}} = \frac{\pi}{16}\sqrt{\frac{2\pi N_A k_B T}{M}}\frac{D^3}{L}. \tag{4.2.2}$$

Here N_A is the Avogadro constant, T is the temperature, and M is the mass of a gas particle. Given this formula and the desire for a large conductance in a short distance, a small diameter is favorable. On the other hand, for better performance of the 2D MOT beam source, a larger diameter is however preferred to prevent clipping and to maximize the atomic flux.

In the final design, the differential pumping tube is conical— 130 mm long with a 3-mm entrance (on the 2D MOT side) and a 9.5-mm exit. The divergence of the inner cone is about 50 mrad, larger than the divergence of atomic beams reported in literature [42, 55]. Given this geometry, the total conductance is about 0.13 l/s for a Rb gas. In the current Rb 2D MOT setup, the UHV region is pumped by 40 l/s ion pump, so the pressure ratio is only ∼500. Nonetheless, the background pressure, read by the ion pump, in the UHV region is between $10^{-8} - 10^{-9}$ mBar when the Rb vapor pressure is a few 10^{-7} mBar. Because the outer diameter of the differential pumping tube is 19.05 mm, smaller than the inner diameter of the 2.75' conflat flange, we added a copper blank with a hole at the center, and sealed the differential pumping tube to it with indium to ensure its conductance is true to the calculated value. Both the interior of the differential pumping tube and the copper blank are blackened to reduce background noise due to scattered light in fluorescence images of the SrF MOT.

4.3 Maximizing the 2D MOT flux

To measure the 2D MOT flux, a probe beam transverse to the propagation direction of the atomic flux is set up to induce fluorescence (Figure 4.8). The probe beam drives the $2 \to 3$ and $1 \to 2$ transitions on resonance. Its intensity for the $2 \to 3$ transition is typically $> 2I_{\text{sat.}}$, with $I_{\text{sat.}} = 1.67$ mW/cm^2 [56]. Fluorescence of the atomic beam is collected over an exposure time of 1 s.

The flux from a 2D MOT, in general, depends on the alignment of the 2D MOT center with the geometric center (set mainly by the magnetic field zero line, but potentially modified by imbalances in laser radiation pressure), laser power, and detuning ($\delta_{2\to3}$) for the $2 \to 3$ transition, and the Rb vapor pressure.

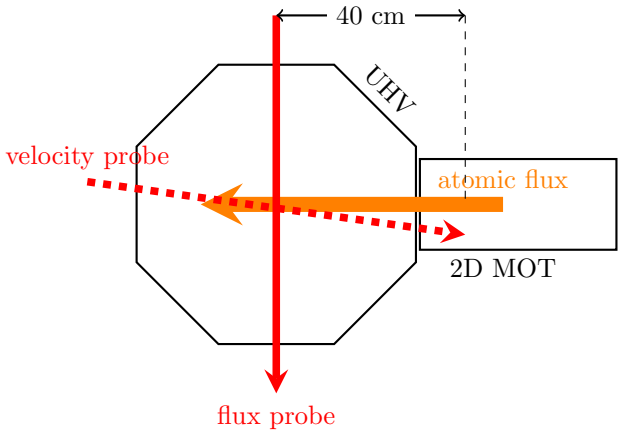


Figure 4.8: Schematic of 2D MOT characterization measurements. In flux measurements, a probe beam (red arrow) transverse to the atomic flux is applied to induce fluorescence. In forward velocity measurements, a probe beam (dashed red arrow) intersects the atomic beam at a small angle ($< 5°$) as shown. The CCD camera and imaging optics that collect the induced fluorescence is directly above the geometric center of the UHV chamber, about 40 cm away from the entrance of the differential pumping tube (not shown), which is also approximately the end of the 2D MOT cooling region.

The magnetic field gradient in the transverse dimension is $\sim$ 20 G/cm with offsets that can be tuned to optimize flux. As for the laser parameters, we choose the trap laser detuning based on the high-flux Rb 2D MOTs in the literature [41, 42], $\delta_{2\to3} = -2\Gamma$. At this detuning, 100 mW power for $2 \to 3$ in each retro-reflected trap beam proves sufficient to saturate the atomic flux (Figure 4.9a). The fluorescence of the atomic beam increases monotonically with Rb vapor pressure (Figure 4.9b). With differential pumping, the UHV pressure is $\sim 10^{-8}$ mBar when the Rb vapor pressure is $4 - 5 \cdot 10^{-7}$ mBar in the 2D MOT region. The uncertainty of each data point is the standard deviation of the mean from three measurements.

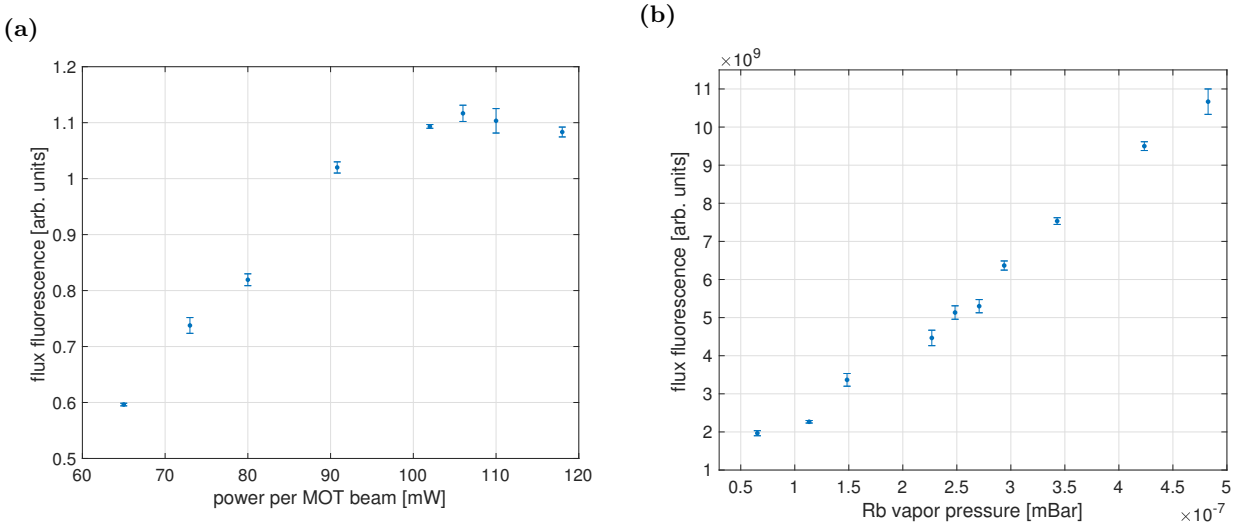


Figure 4.9: (a) Atomic beam fluorescence vs laser power measured at Rb vapor pressure $\sim 2.5 \cdot 10^{-7}$ mBar and (b) Atomic beam fluorescence vs Rb vapor pressure.

In order to determine the atomic flux from the fluorescence signal, the forward velocity and the diameter of the atomic beam must be known. From CCD images, the full width at half maximum (FWHM) of the atomic beam can be found, $D = 17(3)$ mm. Provided the separation from the 2D MOT and the detection region, a divergence of 43(8) mrad is derived. It is comparable to, 50 mrad, the upper limit of the measurable range set by the divergence of the differential pumping tube. In our forward velocity measurements, a velocity probe beam intersecting the atomic beam at a small angle is applied (Figure 4.8). Its detuning with respect to the $2\rightarrow 3$ transition is tuned to probe different forward velocity groups, and the intensity is reduced to $I = I_{\text{sat.}}$ to avoid power broadening while keeping the signal at a detectable level for a wide range of velocities. This method is much more laborious compared to the time-of-flight method used in Refs.[41, 42, 57], but it does not require turning off the 2D MOT or precise control over the time-of-flight duration. In order to estimate the maximum flux at $\sim (2.0-2.5)\cdot 10^{-7}$ mBar, the forward velocity is measured when other 2D MOT parameters are adjusted to maximize the flux (Figure 4.10). By fitting the normalized velocity density distribution to a Maxwell-Boltzmann model, $\phi(v) \propto v^2 e^{-(v/v^p)^2}$, we found the most probable forward velocity to be $v_L^p = 30(2)$ m/s, and the mean forward velocity $\bar{v}_L = \frac{2}{\sqrt{\pi}} v_L^p$=34(3) m/s. For a gaussian model, $\phi(v) \propto e^{-\frac{(v-\bar{v}_g)^2}{2v_{rms}^2}}$, the most probable velocity is the mean velocity. From the fit result, $\bar{v}_L = v_L^p = 32(2)$ m/s, and the rms velocity is 14(2) m/s. The coefficient of determination, R^2, is .80 for the Maxwell-Boltzmann model, and .77 for the gaussian model. The uncertainty in each data point is the standard deviation of the mean from three measurements. The uncertainty in each fit parameter is the half width of the 95% confidence interval from the fit. It is also worth noting that the density function ($\phi(v_L)$) obtained using our method is the density function of atom number in a fixed detection volume whose boundary is defined by the velocity probe beam. Therefore, $\phi(v_L)$ is approximately the volume density (n) integrated over the longitudinal dimension, in units of atom/length^2. This is different from flux as a function of v_L in units of atom/length—atom number integrated over a transverse cross-section as commonly reported in time-of-flight measurements in the 2D MOT literature, such as in Refs.[41, 42].

From the beam divergence and the mean forward velocity, the rms transverse velocity is ∼68 cm/s, corresponding to a Doppler shift of $2\pi\cdot$(890 kHz). This is frequency width can be contained in the power-broadened linewidth, $\Gamma(s) = \Gamma\sqrt{1+s}$, in the flux measurement with $\Gamma(s > 2) > 2\pi \cdot (10 \text{ MHz})$.

In general, both flux and forward velocity can depend on the 2D MOT parameters. Specifically, Ref.[42] showed that the mean and the most probable forward velocities are almost independent of the laser power, but both increase with increased vapor pressure. Though a similar dependence is expected in our case because of similarities in the experimental setup, the dependence of forward velocity on 2D MOT parameters was not investigated. Two methods for converting the fluorescence signal to flux [atom/s] are discussed in §4.4.2

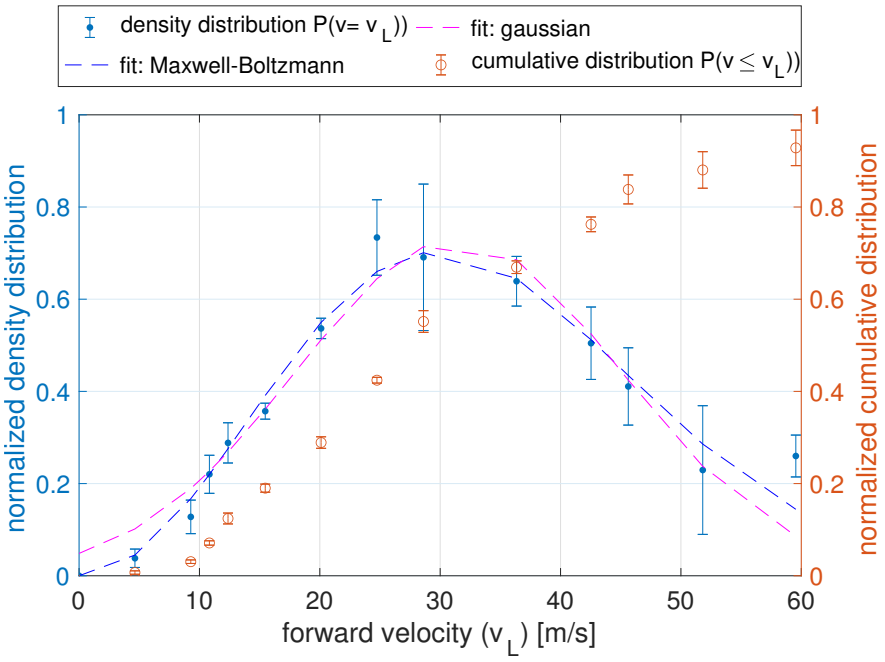


Figure 4.10: Forward velocity distributions when the 2D MOT flux is maximized for Rb vapor pressure $\sim 2 \cdot 10^{-7}$ mBar. The normalized density distribution (left y-axis) is the normalized fluorescence signal. From a fit to a Maxwell-Boltzmann model, the most probable velocity is found to be 30(2) m/s. The normalized distribution (right y-axis) is calculated from the density distribution.

and §4.4.3. Because they both assume a simple linear conversion, the conversion factors are only used to estimate the maximum flux, not for other generic cases.

4.4 Methods

§4.4.1 gives an explanation for background subtraction, which is a first step in any analysis based in fluorescence signals. §4.4.2 discusses how the fluorescence signal is converted to atomic flux with a calibration step. §4.4.3 outlines an alternative conversion method using the absorption in a 3D MOT downstream. §4.4.4 shows how the rubidium vapor pressure is calculated from absorption in the 2D MOT.

4.4.1 Background subtraction

In flux and forward velocity measurements, the fluorescence signal induced by probe beams is collected in the UHV region. It is a measure for the local atom density, contributed by atoms in the beam produced by the 2D MOT, as well as by atoms that effuses from the 2D MOT region. For the purpose of characterizing the 2D MOT flux, we can exclude fluorescence due to this background density of Rb with the background subtraction step. Simply, for a set of atomic beam images, we took a background image when the 2D MOT

flux is extinguished, accomplished by turning off the magnetic field.

4.4.2 Converting fluorescence signal to atomic flux

Calibration: converting camera count to photon number

Given that the energy per photon at 780 nm is $25.4{\cdot}10^{-20}$ J, the optical power P_{calib} [mW] can be converted to the photon flux f_{ph} [photon/ms],

$$f_{\text{ph}} = 3.9 \cdot 10^{12} P_{\text{calib}}. \tag{4.4.1}$$

Then the photon flux multiplied by the exposure time of the CCD camera gives the photon number detected.

In order to convert the number count on the camera to the number of photons, we perform a calibration, similar to the one for molecules in Ref.[28]. First, we set up a diffusive light source to simulate the atomic beam, by back-illuminating a piece of white Delrin with 780 nm light. The front surface of the Delrin is covered except for a 5-mm hole. The optical power transmitted through the Delrin piece is measured by a power meter and later used as P_{calib} to estimate the photon number. Second, we set up the CCD camera and imaging optics (lenses and 780 interference filter) to emulate the realistic geometry in the flux measurement. The imaging lenses, at a distance, h =8(1) cm (measured from the objective lens), were adjusted to focus on the front surface of the Delrin piece. This way, the detection efficiency (η) due to geometry (solid angle ω) and transmission through lenses and to angle-of-incidence dependent transmission through the interference filter are taken into account, when taking images in the calibration setting. The solid angle (ω) in units of steradian (sr) is $\omega \approx \frac{\pi r_L^2}{h^2}$, with r_L=15(1) mm being the radius of the objective lens.

Though the solid angle is the same in calibration and actual measurements, the detection efficiency is halved in actual measurements: in the calibration, the total flux measured by the power meter is distributed over the half sphere facing the camera whose total solid angle is 2π sr; in flux and forward velocity measurements, fluorescence is uniformly* distributed over the full sphere whose solid angle is 4π sr. Therefore, we use an additional factor η_2 to account for the difference in detection efficiency between calibration and measurements. In addition to the factor of 1/2 due to normalization over solid angles, the transmission efficiency, 96%, through the viewport should also be accounted for. As far as we can quantify, $\eta_2 \approx 0.48$.

From the free-space calibration (indicated in the superscript), we found the conversion factor between the camera count (M^{calib}) and the photon number detected ($N_{\text{ph}}^{\text{calib}}\eta$) as $N_{\text{ph}}^{\text{calib}}\eta/M^{\text{calib}} = 3.36 \cdot 10^5$ photon-

*The distance between the imaging optics and the atomic beam (h = 8(1) cm) is much greater than the diameter of the atomic beam (D) and the diameter of the probe beam (w), though both D and w are greater than the diameter of the hole (5 mm) in the calibration. To a good approximation, the illuminated atomic beam is still a point source [58].

s/count. Suppose the photon number emitted in flux measurements is denoted as N_{ph}, and the camera count as M. The conversion between detected photons and camera count is the same, namely, $\frac{N_{\mathrm{ph}}\eta\eta_2}{M} = \frac{N_{\mathrm{ph}}^{\mathrm{calib}}\eta}{M^{\mathrm{calib}}}$. It follows that the conversion rule for photon number and camera signal is

$$N_{\mathrm{ph}} = 7 \cdot 10^5 M. \tag{4.4.2}$$

Converting photon number to atomic flux

The conversion between photon number and the atom number is based on the estimated scattering rate (R_{sc}) and the scattering time in a camera frame. In the atom's rest frame, the scattering rate due to a resonant probe beam depends on the saturation parameter s, the Doppler shift Δ_D and the transition linewidth Γ

$$R_{sc} = \frac{\Gamma}{2}\frac{s}{1+s+4(\Delta_D/\Gamma)^2}. \tag{4.4.3}$$

Since most of the population has a forward velocity (v_L) larger than 10 m/s, the number of photons each atom scatters is limited by the interaction time with the probe beam, namely, $\Delta t_{int} = w/v_L$, provided that the CCD exposure duration is $t_{\mathrm{expo.}} = 1$ s.

The fluorescence signal is integrated over the camera's exposure time and the detection volume, the intersection volume of the atomic beam and the transverse probe beam,

$$N_{\mathrm{ph}} = \int_0^{t_{\mathrm{expo.}}} dt \int_A dA' \int_0^w dz \frac{Dn}{Dt} R_{sc} \Delta t_{int}. \tag{4.4.4}$$

Here n is the density of moving atoms, Dn/Dt is its convective derivative*, z is the longitudinal coordinate (in the lab frame), and A is the cross-section of the intersection in a transverse plane. By approximation, neglecting the divergence over the width of the transverse probe beam (w), the area of cross-section is $A \approx wD$, with w being the diameter of the probe beam and D the width of the atomic beam.

For a continuous flux, assume n and v_L have no explicit time-dependence. On the right-hand side, after applying the chain rule and neglecting the transverse velocity, we find

$$\frac{Dn}{Dt} = (\vec{v}\cdot\nabla)n \approx v_L \frac{dn}{dz}. \tag{4.4.5}$$

With this, the integral over z can be simplified. Moreover, n can be related to the distribution of column/ray

*From the Lagrangian, meaning that we observe while following moving atoms in a volume element, the convective derivative is taken with respect to the moving coordinate system. From the Eulerian view, meaning that we observe at a fixed point in the lab frame and watch atoms move through a volume element, the convective derivative is a sum of temporal change $\partial/\partial t$ and change due to motion $\vec{v}\cdot\nabla$.

density in terms of forward velocity measured previously (Figure 4.10). Then (4.4.4) becomes

$$N_{\text{ph}} \approx \int_0^\infty dv_L v_L \phi(v_L) A R_{sc} \Delta t_{int} t_{\text{expo.}}. \tag{4.4.6}$$

Suppose $\phi(v_L) = \Phi \frac{v_L^2}{(v_L^p)^2} e^{-(v_L/v_L^p)^2}$, with v_L^p from a fit to the Maxwell-Boltzmann model and Φ to be determined. Then the integral of v_L can be carried out. It follows that

$$\Phi = \frac{4}{\sqrt{\pi}} \frac{N_{\text{ph}}}{R_{sc} \times w \times A \times t_{\text{expo.}} \times v_L^P}. \tag{4.4.7}$$

Integrating over a larger volume and all forward velocities, the total flux (F), in units of atom/s, though the geometric center of the UHV chamber is

$$F = \int_{A_2} dA' \int_0^d dz \frac{Dn}{Dt} = \int_{A_2} dA' \int dv_L v_L \phi(v_L) = \frac{2}{\sqrt{\pi}} \frac{d}{w} \frac{N_{\text{ph}} \times A_2 \times v_L^P}{R_{sc} \times w \times A \times t_{\text{expo.}}}. \tag{4.4.8}$$

Here $A_2 = \pi D^2/4$ is the cross-section of the atomic beam at the transverse probe beam about d =40(2) cm away from the 2D MOT.

	w [mm]	D [mm]	d [cm]	v_L^p [m/s]	P_p [mW]	N_{ph}
best value	7.5	17	40	30	2.3	$2.44{\cdot}10^{11}$
uncertainty	0.1_{sys}	3_{stat}	2_{sys}	2_{stat}	$.2_{\text{stat}}$	$0.08 \cdot 10^{11}_{\text{stat}}$
	Δ_D [kHz]	R_{sc} [s^{-1}]	A/A_2			
best value	0	$1.4{\cdot}10^7$	0.6			
uncertainty	890	$0.1{\cdot}10^7$	0.1			

Table 4.2: Best values and uncertainties of the probe beam diameter w, atomic beam diameter D, the distance between the 2D MOT and the geometric center of the UHV chamber d, most probable forward velocity v_L^p, power driving the $2 \to 3$ transition in the probe beam P_p, photon number emitted from the source and integrated over the 1-s exposure time N_{ph}, Doppler shift in the transverse direction Δ_D, scattering rate R_{sc}, the ratio of detection and atomic-beam cross-sections A/A_2. Subscripts in uncertainties of directly measured parameters (first half) indicate whether it is systematic or statistical. Uncertainties of more complex quantities are propagated from their constituents. Systematic uncertainties are due to the resolution of measuring tools.

Using the values of measured parameters in Table 4.2, we found the total flux to be $(3.8 \pm 0.8_{N N_{\text{ph}}} \pm 0.1_{N_{\text{ph}}}) \cdot 10^9$ atoms/s for Rb vapor pressure $p_{2D}(\text{Rb}) \sim 2 - 3 \cdot 10^{-7}$ mBar. The uncertainty due to everything not N_{ph} is about 22% of the mean. The statistical uncertainty in N_{ph} is about 3%. Uncertainties due to calibration and approximations are not accounted for. Some of this, e.g., neglecting the transverse

dimensions, may lead to underestimating the total flux.

4.4.3 Calibrating fluorescence to atom number in the 3D MOT

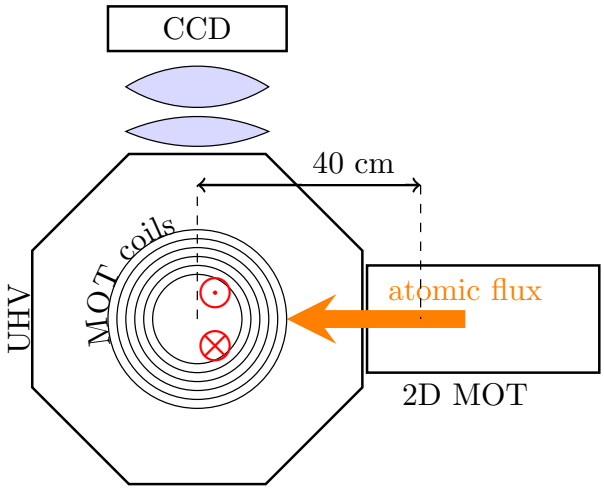


Figure 4.11: Geometry in the alternative flux measurements with a 3D MOT. The vertical retro-reflected beam (red) is used as a resonant probe beam during flux measurements, and as a red-detuned MOT beam during calibration.

Setting up a 3D MOT downstream of the 2D MOT allows us to calibrate the fluorescence signal collected by the camera by comparing fluorescence and absorption images of the 3D MOT. Figure 4.11 shows the geometry in the calibration and flux measurements. The main difference between this method and that in §4.4.2 is the conversion factor between the camera count to photon number. §4.4.3 discusses a calibration based on the atom number from absorption imaging, instead of a laser power measurement as in §4.4.2. The steps subsequent to this calibration are essentially identical to those discussed in §4.4.2. Therefore, they will not be repeated.

Using (4.4.8) and values for relevant parameters in Table 4.3, we have an estimated flux of $F = (3.7 \pm 1_{NN_{\mathrm{ph}}} \pm 0.1_{N_{\mathrm{ph}}}) \cdot 10^9$ atoms/s. The uncertainty due to everything not N_{ph} is about 33% of the mean, and the statistical error in N_{ph} is about 2%.

	w [mm]	D [mm]	d [cm]	v_L^p [m/s]	P_p [mW]	$N_{\rm ph}$
best value	11	17	40	30	17	$2.28{\cdot}10^9$
uncertainty	$1_{\rm sys}$	$3_{\rm stat}$	$2_{\rm sys}$	$2_{\rm stat}$	$2_{\rm sys}$	$0.05{\cdot}10^9_{\rm stat}$
	Δ_D [kHz]	R_{sc} [s^{-1}]	A/A_2			
best value	0	$1.7{\cdot}10^7$	0.8			
uncertainty	890	$0.4{\cdot}10^7$	0.2			

Table 4.3: Best values and uncertainties of the probe beam diameter w, atomic beam diameter D, distance between the 2D MOT and the geometric center of the UHV chamber d, most probable forward velocity v_L^p, power driving the $2 \to 3$ transition in the probe beam P_p, photon number emitted from the source and integrated over the 5-ms exposure time $N_{\rm ph}$, Doppler shift in the transverse direction Δ_D, scattering rate R_{sc}, the ratio of detection and atomic-beam cross-sections A/A_2. The error in P_p is estimated based on the effective transmission loss through viewports $(96\%)^3$.

Calibration: converting camera count to photon number

In this calibration step, the atom number ($N_{\rm a}$) and the photon number emitted by atoms in the MOT ($N_{\rm calib}$) can be determined using absorption imaging and fluorescence image respectively, under nominally identical 3D MOT conditions,

$$N_{\rm calib} = N_a \times R_{\rm calib} \times t_{\rm calib}. \tag{4.4.9}$$

Here $t_{\rm calib} = 80\,\mu$s $\ll$ MOT lifetime) is the camera exposure time and $R_{\rm calib}$ is the scattering rate in the MOT. Suppose the saturation parameter and detuning of 3D MOT light for the $2 \to 3$ transition are $s_{\rm calib}$ and respectively $\delta_{\rm calib} = -3\Gamma$,

$$R_{\rm calib} = \frac{\Gamma}{2}\frac{s_{\rm calib}}{1 + 4\delta_{\rm calib}^2/\Gamma^2 + s_{\rm calib}}. \tag{4.4.10}$$

Suppose the camera count from the fluorescence image of the MOT is $M_{\rm calib}$, we the conversion relation the camera count M and the photo number emitted $N_{\rm ph}$ in flux and velocity measurements,

$$N_{\rm ph} = \frac{N_{\rm calib}\eta}{M_{\rm calib}} M/\eta = 2.7(5) \cdot 10^4 M. \tag{4.4.11}$$

Here η is the collection efficiency due to the solid angle, transmission through imaging optics and the viewport, and $N_{\rm calib}\eta$ is the total number of photons detected during calibration. However, η by itself is not important because it is the same for calibration and actual measurements. It is also worth mentioning that the CCD used in this calibration and the subsequent flux measurements is different from the one referred to in §4.4.2, regarding hardware specifications and the digitization format.

4.4.4 Measuring Rb vapor pressure via absorption

Finding the steady-state pressure p of an ideal gas via absorption requires deriving the number density, n, from Beer's law,

$$p = nk_BT = \frac{k_BT}{l\sigma(\omega)} \log(I_0/I(\omega)), \tag{4.4.12}$$

where $I(\omega)$[arbitrary unit] is the intensity after absorption at frequency ω [rad/s], I_0 is the intensity before without absorption, l[cm] is the interaction length, and $\sigma(\omega)$[cm^{-2}] is the absorption cross-section.

The absorption cross-section is a function of frequency (ω), or equivalently the detuning (Δ) with respect to each transition resonance (ω_0)

$$\sigma(\omega) = \sigma(\Delta + \omega_0) = \sigma_D e^{-(\Delta/\Gamma_D)^2}. \tag{4.4.13}$$

Γ_D is the Doppler width of the ^{87}Rb D_2 line; at room temperature (293 K),

$$\Gamma_D = \sqrt{\frac{2k_BT}{m}}\frac{\omega_0}{c} \approx 2\pi \cdot (303 \text{ MHz}). \tag{4.4.14}$$

σ_D is the resonance cross-section in the presence of Doppler broadening,

$$\sigma_D = \frac{\sqrt{\pi}}{2}\frac{\Gamma}{\Gamma_D}\sigma_0, \tag{4.4.15}$$

where σ_0 is the resonant cross-section without broadening, and $\Gamma/(2\pi)$= 6.07 MHz is the natural linewidth of the 87 D_2 line.

Saturated absorption spectroscopy (such as Figure 4.3, left) suggests the frequency at which the absorption signal attains its minimum is slightly (less than 30 MHz) to the red of the $F = 2 \to F' = 3$ resonance. This allows us to approximate $\log(I_0/I(\omega))$ in (4.4.12) for $\omega = \omega_0^{(23)}$, using the ratio between the maximum transmission I_0 which is attained far off resonance and minimum transmission near the $F = 2 \to F' = 3$ resonance.

Given this Doppler width and the excited state hyperfine splitting, other hyperfine transitions also contribute to absorption when the laser is tuned to the $2 \to 3$ resonance. Therefore in (4.4.12), the cross-section for this frequency should be a sum over all transitions contributing to the overall absorption weighted

by the detuning with respect to an individual transition, denoted by two ordered integers FF',

$$\sigma(\omega) = \sum_{FF'}^{\text{transitions}} \sigma_D^{(FF')} \exp\left[-\left(\frac{\omega - \omega_0^{(FF')}}{\Gamma_D^{(FF')}}\right)^2\right]. \tag{4.4.16}$$

The resonance cross-section of a transition between hyperfine states $F \to F'$ is

$$\sigma_0^{(FF')} = \frac{\lambda^2}{2\pi} \frac{2F'+1}{2F+1} \frac{\Gamma_P^{(FF')}}{\Gamma}, \tag{4.4.17}$$

where $\Gamma_P^{(FF')}$ is the partial linewidth of the hyperfine transition. For a closed transition, e.g., the $F = 2 \leftarrow F' = 3$ transition, $\Gamma_P^{(FF')}/\Gamma$ is the branching ratio of decay from the excited state: for the $F = 2 \leftarrow F' = 2$ transition $\Gamma_P^{(22)}/\Gamma = 1/2$, for the $F = 2 \leftarrow F' = 1$ transition $\Gamma_P^{(21)}/\Gamma = 1/6$. The resonant and the Doppler broadened cross-sections for pumping out from $F = 2$ are summarized in Table 4.4. Substituting them into (4.4.16), we find the total absorption cross-section at $\omega = \omega^{(23)}$ due to ^{87}Rb in hyperfine state $F = 2$ to be

$$\sigma(\omega^{(23)}) = \sigma^{(23)} + \sigma^{(22)} + \sigma^{(21)} \approx 2.83 \cdot 10^{-11} \text{ cm}^2. \tag{4.4.18}$$

	F'=3	F'=2	F'=1
$\sigma_0^{(FF')}$ [cm^2]	$1.4 \cdot 10^{-9}$	$4.8 \cdot 10^{-10}$	$9.7 \cdot 10^{-11}$
$\sigma_D^{(FF')}(T)$ [cm^2]	$2.4 \cdot 10^{-11}$	$8.6 \cdot 10^{-12}$	$1.7 \cdot 10^{-12}$

Table 4.4: Resonant and Doppler broadened cross-sections for hyperfine transitions $F = 2 \to F'$ at $T = 293$ K.

Evaluating (4.4.12) using this absorption cross-section, we have the vapor pressure of ^{87}Rb in a ground state hyperfine level $5S_1/2(F = 2)$, denoted as $\tilde{p}$. For comparison to vapor pressures quoted in the 2D MOT literature and for vacuum-related considerations, we calculate the effective vapor pressure of rubidium p(Rb) by taking into account the natural abundance of the 87 isotope (f_A=27.83% [59]) and the the fraction of population in the correct ground state hyperfine level $5S_1/2(F = 2)$ ($f_B = 5/8$),

$$p(\text{Rb}) = \frac{\tilde{p}}{f_A f_B}. \tag{4.4.19}$$

In Table 4.5, the total Rb vapor pressure calculated from absorption data is compared to estimates based on empirical formulae.

p_1(Rb) [mBar]	p_2(Rb) [mBar]	p(Rb) [mBar]
$2.99 \cdot 10^{-7}$	$2.29 \cdot 10^{-7}$	$2.80 \cdot 10^{-7}$

Table 4.5: Vapor pressures of Rb in a vapor cell are evaluated at $T = 293$ K using different methods. p_1 is calculated using a formula and coefficients from section 4 of the CRC handbook [59, 60], p_2 from Ref.[61], and p from our data in an absorption scan.

Chapter 5

Characterization of a radio frequency magneto-optical trap of ^{87}Rb

5.1 Introduction

The radio frequency (RF) magneto-optical trap (MOT) proves a useful tool for molecular species whose energy level structure allows for the direct application of laser cooling, such as SrF [31], CaF [17] and YO [62]. In these species with type-II cycling transitions ($F \rightarrow F' = F - 1$ or $F' = F$), the rapid switching in an RF MOT is crucial due to the presence of polarization dark states. Under typical MOT conditions, with high laser power, a polarization bright state is optically pumped into a polarization dark state in about 2 excited state lifetimes. To overcome this problem, rapid switching allows the particle to scatter photons in each RF cycle, therefore producing stronger damping and confining forces, compared to the average forces in the dc case [63].

In order to study atom-molecule collisions in a conservative trap, and possibly implement sympathetic cooling of SrF and ^{87}Rb [64], we put together an experiment in a separate setup to trap Rb atoms in an RF MOT, very similar to the RF MOT of SrF in Ref.[31]. Using the type-I transition ($F \rightarrow F' = F + 1$) based on the ^{87}Rb D_2 line, we aim to trap as many as possible atoms in an RF MOT, before further phase-space compression, e.g., by applying optical molasses, and transfer into any conservative traps. Therefore, the performance of an Rb RF MOT is characterized. Additionally, this setup allows us to compare the direct current (dc) and RF MOT operating on a type-I transition, and consequently to gain perspective in the cooling and trapping mechanism in an RF MOT. §5.1.1 gives a simple description of the type-I RF MOT, as well as some results from simulations. The discussion of mechanism in a type-II RF MOT of SrF is reproduced from Ref.[31] in §2.1.2 of chapter 2.

In the rest of this chapter, §5.2 describes the experiment, including the apparatus and detection techniques, and §5.3 presents MOT characterization results— optimization of 3D MOT parameters, characterization of loading and decay processes and of other MOT properties under typical conditions.

5.1.1 Type-I RF MOT

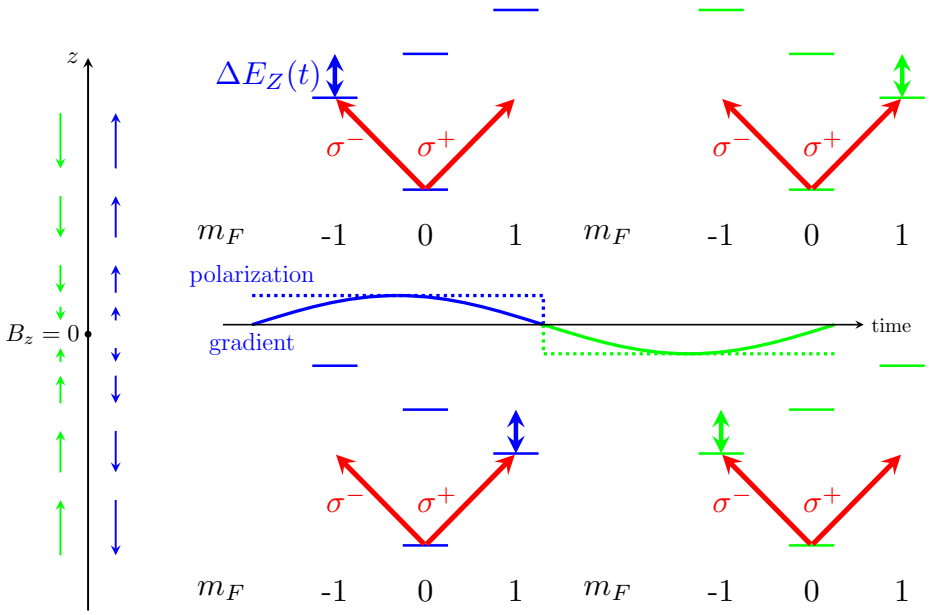


Figure 5.1: RF MOT scheme for a single ground state hyperfine sublevel in one dimension on both sides of the trap center ($B_z = 0$). Two phases defined by the sign of the magnetic field gradient are indicated by the color, blue or green. In this description, the direction of the quantization axis z (indicated by the black arrow on the left) remains constant during switching, provided that the magnetic field gradient (solid sine wave) and light polarization (dotted square wave) switch synchronously. The excited state Zeeman shifts ($\Delta E_Z(t)$) vertical double arrows) are relative to unperturbed levels when no magnetic field is applied. In an RF MOT, these Zeeman shifts depend on not only position, as in a dc MOT, but also time. When the Doppler shift is comparable to $\Delta E_Z(t)$, same as in a dc MOT, an RF MOT exerts confining and damping forces as the particle goes through $\sigma^{\pm}$ transitions.

Cooling, trapping and detection in both dc and RF configuration make use of optical cycling on the $F = 2 \rightarrow F' = 3$ transition (with repumping on the $F = 1 \rightarrow F' = 2$ transition). Figure 5.1 shows the RF MOT schemes on a type-I transition for a single ground state hyperfine sublevel in one dimension. A particle cycling on a type-I transition can continuously scatter off photons in either RF or dc MOT. In a type-I dc MOT, there is also sub-Doppler (polarization gradient) cooling due to the nonadiabatic coupling between Zeeman sublevels undergoing different light shifts in the particle's moving rotating frame [37]. For multilevel atoms, the effect of sub-Doppler cooling is more pronounced when the optical-pumping time (τ_P), is longer than the excited state lifetime τ, in regions of low laser intensity. In a type-I RF MOT, Figure 5.1 shows that the optical pumping scheme changes in each RF cycle, on the order of an excited state lifetime.

Therefore, we qualitatively anticipated that the temperature in an RF MOT would be higher than in a dc MOT.

We note that an alternating current (ac) MOT based on type-I transitions in atoms has been demonstrated [65, 66]. However, in Ref. [65], the ac MOT switching occurs at a few kHz, much lower than the optical pumping rate. It is likely that due to this key difference, the kHz ac MOT appears to be as effective as the dc MOT. As far as we know, no direct comparison between type-I dc and RF MOT has been made in the regime with the mechanisms described above.

5.2 Experiment

A schematic of the experimental apparatus is shown in Figure 5.2. The 3D MOT in the octagon region is loaded from a 2D MOT in the rectangular region, which is a high-flux beam source that allows us to collect a large number of atoms while maintaining ultra high vacuum (UHV) pressures, $p_{UHV} \sim 10^{-9}$ mBar in the 3D MOT region. More details on the beam source 2D MOT can be found in §5.2.1 and in Chapter 4.

The laser system, relevant to the 3D MOT and in general to laser cooling Rb, is described in §4.2.1 of Chapter 4. In the case of an RF MOT, the polarization switching is enabled by a Pockels cell, which rapidly rotates the linear polarization by 90 degrees before it is turned into circular by quarterwave plates. The optics for the 3D MOT includes three identical Galilean telescopes (f =-18 mm and f =60 mm), six quarterwave plates that change the polarization between circular and linear, and a few mirrors for MOT beam alignment. Each telescope expands the input beam from a fiber collimation package with a $1/e^2$ diameter of $\sim$ 4 mm into a MOT beam with a $1/e^2$ diameter of $\sim$11 mm. The imaging optics includes variable magnification lenses and an interference filter placed between the lenses and the CCD chip. The lenses are adjusted to maximize the resolution at a working distance of 25 cm. The pixel density turns out to be 10 pixels per mm.

The 3D MOT magnetic fields are created by anti-Helmholtz coils in vacuum. The setup for the RF MOT, including the in-vacuum assembly (Figure 5.3) and the resonant circuit for efficient RF coupling at 1.23 MHz, is largely similar to the setup in Ref.[31]. The RF current can be switched on and off within tens of microseconds with a triggerable RF switch. In order to apply static current in the case of dc MOT, a dc power supply and a MOSFET-based switching circuit are connected in parallel with the RF resonant circuit. In fact, the RF resonant circuit and the dc switching circuit are borrowed from a bias tee circuit intended for seamless and rapid switching between the dc and RF MOT. Because of an additional inductor in the bias tee circuit, the rise and fall time of dc current is $\sim$2 ms. If the dc fall time is critical, for instance in temperature measurements via the time-of-flight method, this extra inductor in the bias tee circuit can be disconnected or replaced by an inductor with lower inductance to reduce the dc current fall time to less

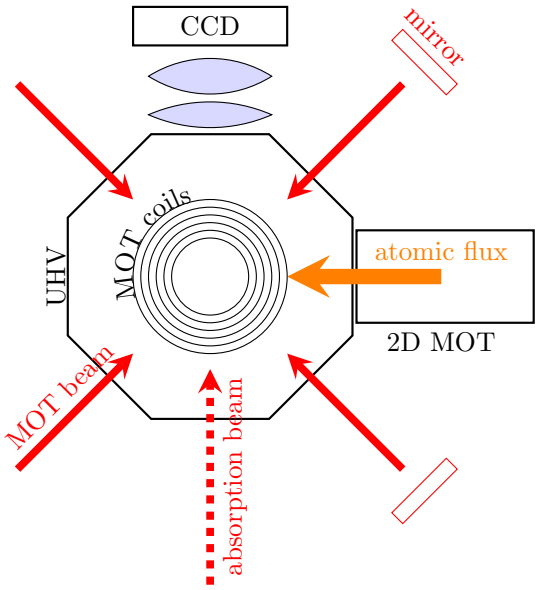


Figure 5.2: Experimental setup. Laser beams for cooling and trapping in the 3D MOT, trap and repump frequencies combined (780 nm), are shown by red arrows. The MOT beam in each dimension is independent and retro-reflected (vertical MOT beams not shown). The atomic flux from the 2D MOT is represented by the orange arrow. Detection via fluorescence or absorption imaging is facilitated by a CCD camera and imaging lenses. A weak absorption beam (dashed arrow) propagates through the geometric center into the camera.

than 1 ms.

In order to investigate properties such as temperatures and lifetime, interval durations in the timing sequence sent to various devices are varied; an example of timing sequence used for fluorescence imaging is shown in Figure 5.4a. For absorption imaging, the absorption probe beam which is controlled by an AOM receives the same timing trigger as the CCD camera. In each repetition, a background and a signal image are taken, from which the net fluorescence due to atoms captured by the MOT is isolated from the background due to scattered laser light by subtracting the background from the signal image. This way fluorescence due to effusive atoms from the 2D MOT beam source, which is not the subject of interest and would likely add noise, is also removed. Similarly, in absorption imaging, background and signal images are taken in each cycle.

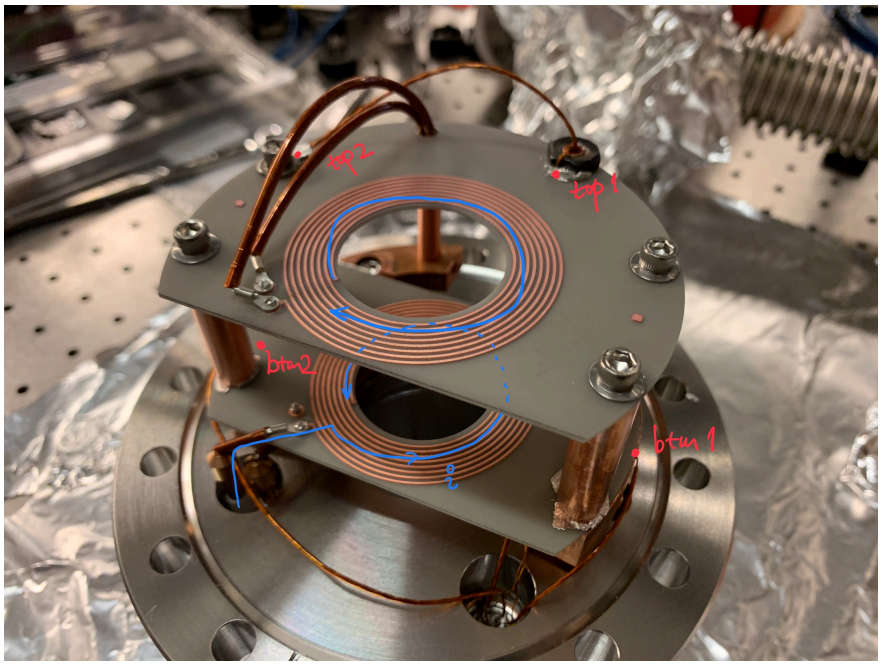
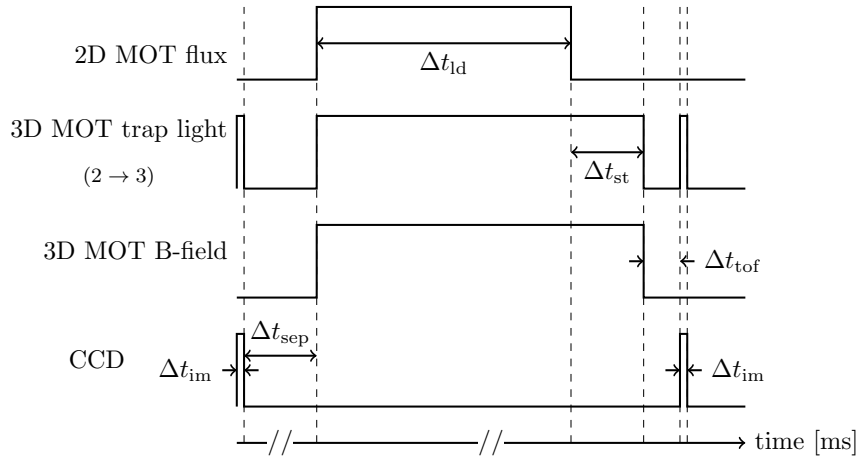


Figure 5.3: Fully assembled in-vacuum MOT coils. The MOT coils are connected in series, and the direction of current is indicated by the blue arrows. Different from the setup in the SrF experiment, current carrying wires have crimped ring terminals and are secured to the MOT boards by 00-90 screws and nuts. Temperatures of MOT boards are measured by K-type thermocouples at 4 points (red).

(a)



(b)

measurement type	variable
loading time constant	Δt_{ld}
lifetime	Δt_{st}
temperature	Δt_{tof}

Figure 5.4: (a) Timing sequence for fluorescence imaging. Δt_{ld} is the 3D MOT loading time; Δt_{st} is the 3D MOT storage time, and $\Delta t_{\mathrm{st}} = 0$ in all measurements except the lifetime measurement; Δt_{tof} is the time of flight between turning off the trap and imaging; Δt_{im} is the camera exposure duration, by default $\Delta t_{\mathrm{im}} = 100\,\mu$s; Δt_{sep} is the time between taking the background image and starting to load the MOT. The period is typically $\sim$1 s. The time axis at the bottom is not to scale. (b) The list of measurement types and their control variables.

5.2.1 Loading from a two-dimensional magneto-optical trap

The 2D-MOT setup is similar to those in Refs.[41–43], in terms of geometry, 2D MOT parameters, and the pressure ratio between the 2D MOT and UHV 3D trapping region. In our setup, the current in four 2D MOT coils can be controlled independently to maximize the flux and turned off to stop the flux after loading the 3D MOT. It can be converted to a 2D+ MOT by adding a push beam, which is only present during 3D MOT loading for a duration of Δt_{ld} and controlled by a mechanical shutter. When the Rb vapor pressure in the 2D MOT region is $2.5 \cdot 10^{-7}$ mBar, the flux of ^{87}Rb from a 2D MOT is on the order of $10^9 - 10^{10}$ atoms/s (cf. Chapter 4). With a low intensity linearly polarized push beam along the longitudinal direction, the flux can be enhanced by a factor of 3.

5.3 MOT characterization results

This section reports on MOT characterization results using detection methods based on absorption imaging and fluorescence imaging (Figure 5.5). §5.3.1 illustrates the synchronization of polarization and magnetic gradient in an RF MOT. §5.3.2 shows how the 3D MOT parameters are adjusted to maximize the atom number, from which the typical 3D MOT parameters are chosen. Under these conditions, time constants in the loading and decay process are determined in §5.3.3, and other properties, namely, temperatures, cloud sizes, and calculated trap frequency, in §5.3.4.

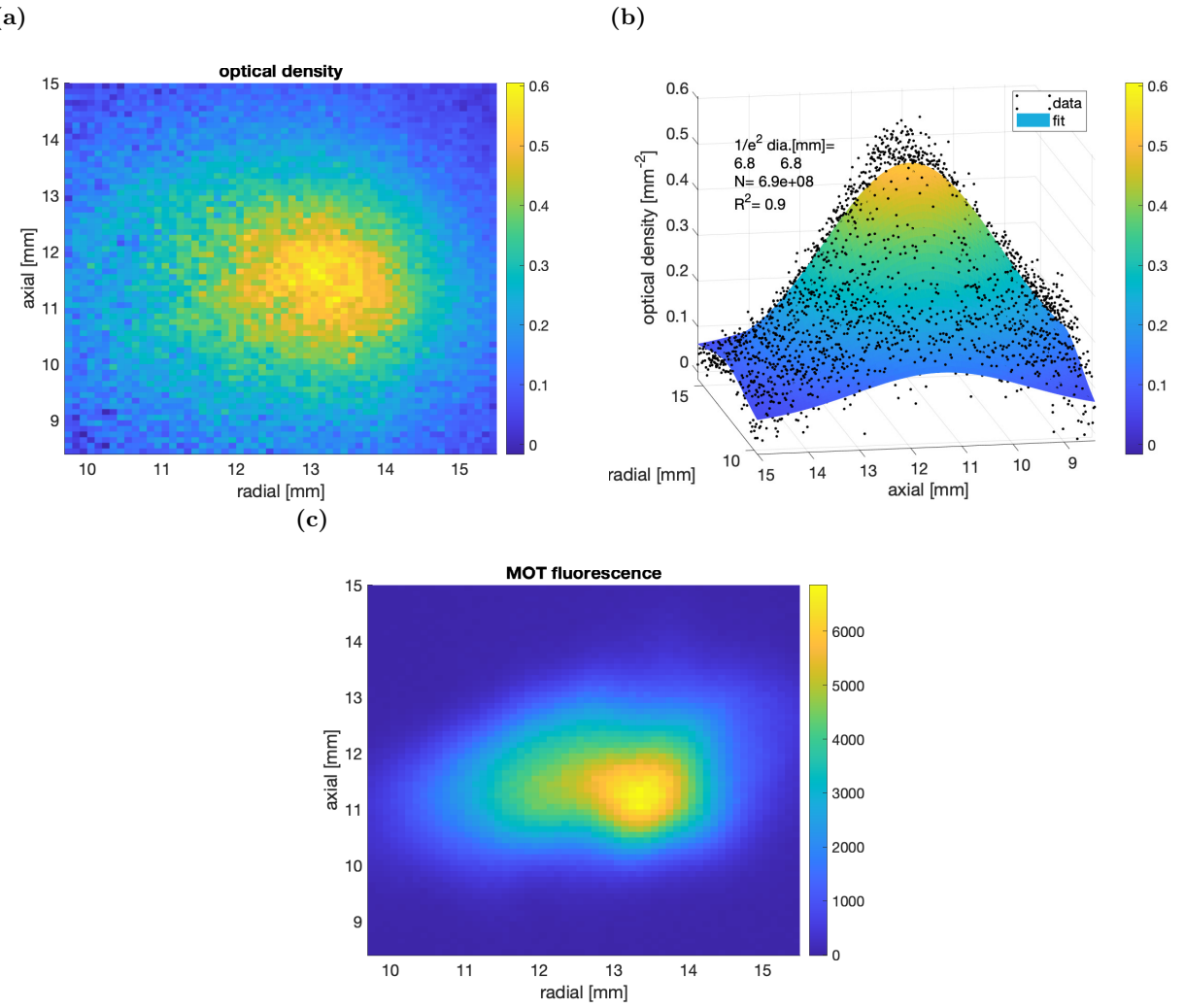


Figure 5.5: (a) Absorption image of an RF MOT. The z-axis and color map show the optical density integrated along the absorption path. The detuning of the absorption beam is -14 MHz (default). (b) A 2D gaussian fit to the optical density in (a) gives information about the cloud sizes and atom number (N). R^2, the coefficient of determination, is a measure for the goodness of this gaussian fit. Absorption images are typically taken 3 ms after the magnetic field and MOT light are switched off. (c) Fluorescence image of an RF MOT *in situ*.

5.3.1 Synchronizing switching in RF MOT

As expected from the intuitive description in Figure 5.1, and observed in several molecular RF MOTs [31, 67], we found that the RF MOT signal is sensitive to the relative phase between gradient and polarization switching (Figure 5.6). The MOT signal (y-axis) is the total fluorescence, which is proportional to the number of atoms in the MOT. In this plot, it is normalized to the highest value achieved while varying the relative phase. Uncertainties in measured quantities in Figure 5.6, and in the rest of this section, are statistical and show the standard error in the mean; uncertainties in fitting parameters are the half width of the 95%

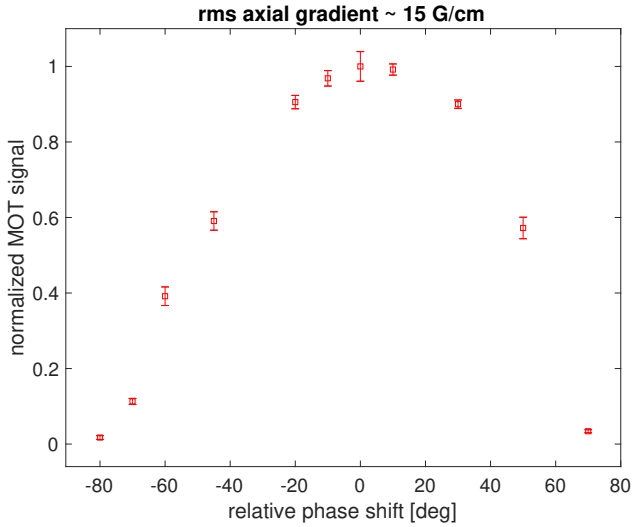


Figure 5.6: RF MOT signal vs relative phase between polarization and RF current switching. The optimum is attained when they are in phase.

confidence interval. The relative phase is fixed to be near optimum in all RF MOT measurements hereafter. Under this condition, the scattering rate in an RF MOT, estimated from the ratio of MOT fluorescence to the atom number determined by absorption, is identical to that in a dc MOT to within our uncertainties of $\sim \pm 6\%$ for a wide range of 3D MOT parameters—namely, the magnetic field gradient, laser intensity and cycling laser detuning.

5.3.2 Optimizing 3D MOT parameters

For the purpose of maximizing the atom number in the 3D MOT, the dependence of MOT signal on 3D MOT parameters— the magnetic gradient at the trap center (quoted as the axial dc gradient $\partial B_z/\partial z$ or the rms axial gradient of the RF magnetic field), laser power ($\bar{P}_{2\to3}$, the average laser power in a single beam) and detuning ($\delta_{2\to3}$) for the cycling transition $2 \to 3$— were investigated while the loading parameters were kept constant. The parameters are relatively independent, and the optimization process is iterative. Figure 5.7 shows the MOT signal as a function of each 3D MOT parameter when others are near optimum. In Figure 5.7a, the MOT signal (y-axis) refers to the total fluorescence; in Figure 5.7c and 5.7b, it is the atom number from absorption imaging. Based on the dependence of normalized MOT signal on the gradient at fixed power ($\bar{P}_{2\to3} \approx$14 mW) and detuning ($\delta_{2\to3} = -4\Gamma$) (Figure 5.7a), the axial dc and rms gradient of the RF magnetic field was set to be $\partial B_z/\partial z \approx 15$ G/cm. Given the MOT signal vs magnetic field gradient at fixed power ($\bar{P}_{2\to3} \approx$14 mW) and for several detuning (Figure 5.7b), the detuning $\delta_{2\to3} = -4\Gamma$ was chosen, with $\Gamma = 2\pi \cdot (6\text{ MHz})$ being the natural linewidth. Under these conditions ($\delta_{2\to3} = -4\Gamma$, $\partial B_z/\partial z \approx 15$G/cm), 14 mW in a single beam for the $2 \to 3$ transition proved sufficient, given the MOT signal vs laser power curve in

Figure 5.7c. For this laser power, the total laser intensity in the center of the MOT is 84 mW/cm^2=50$I_{\text{sat.}}$, with $I_{\text{sat.}}$=1.67 mW/cm^2 being the saturation intensity for circularly polarized light [56].

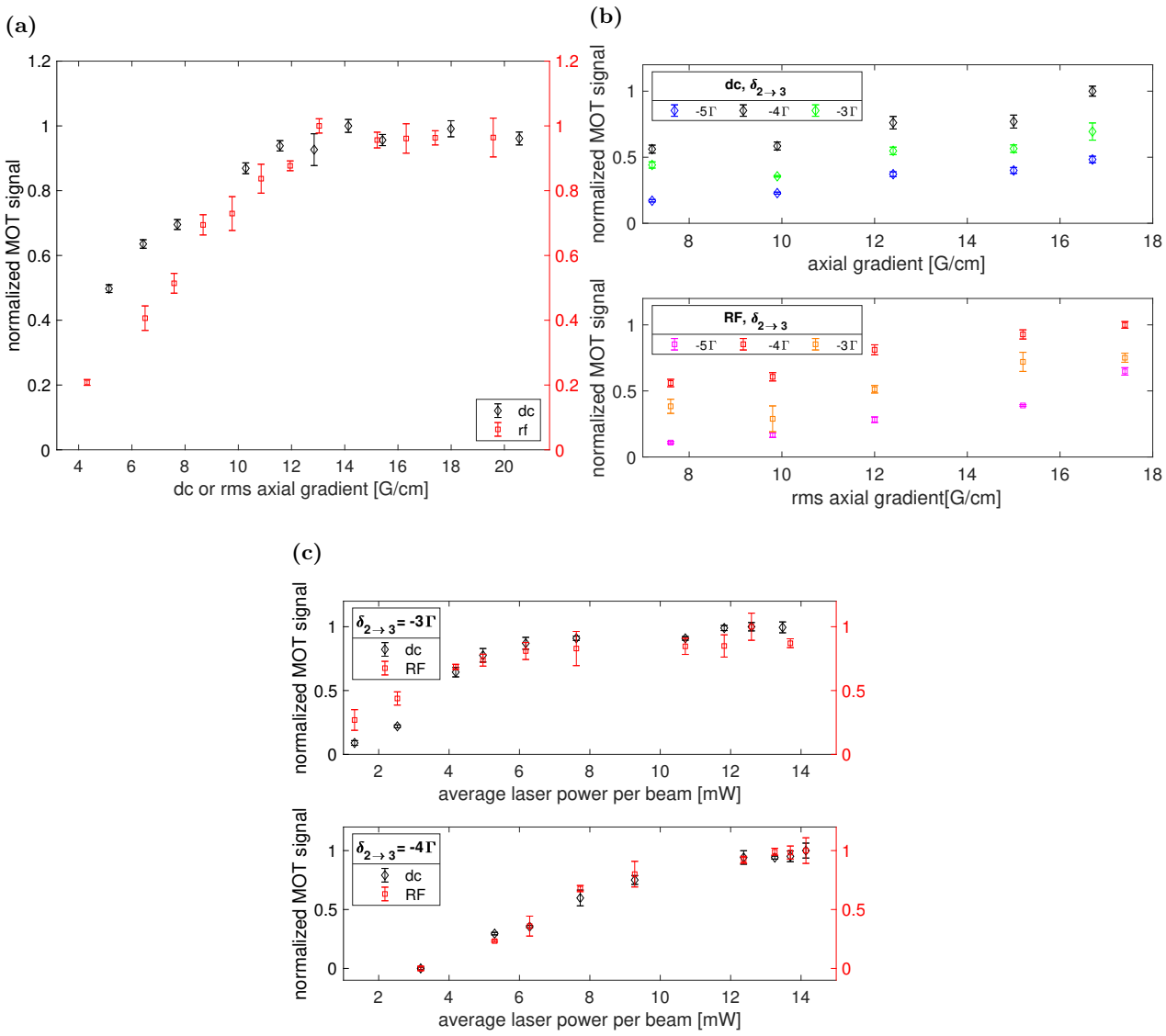


Figure 5.7: (a) MOT signal vs magnetic field gradient ($\partial B_z/\partial z$). Note that the x-axis refers to either the dc field gradient or the rms gradient of the oscillating RF magnetic field, inferred from direct measurements of the dc or RF current. (b) Atom number vs magnetic field gradient for several different detunings ($\delta_{2\to3}$) with fixed input laser power ($\bar{P}_{2\to3}$ ≈14 mW). (c) Atom number vs laser power per beam ($\bar{P}_{2\to3}$) for two detunings at fixed gradient ($\partial B_z/\partial z$ ≈15 G/cm).

5.3.3 Loading and decay processes

In addition to the 3D MOT parameters, the atom number also depends on the atomic flux from the 2D MOT beam source and the 3D MOT lifetime. In a 2D MOT (or pure 2D MOT), the flux depends on

the Rb vapor pressure in the 2D MOT region (p_{2D}(Rb)) for given values of the other 2D MOT parameters such as the 2D MOT magnetic field. In a 2D+ MOT, the flux generally depends on the push beam power and detuning. For technical convenience, we apply a linearly polarized push beam with the same detuning as that of other 2D MOT beams (-2Γ), and switch it off with a shutter after loading. At any given vapor pressure, adding a push beam typically increases the atom number in a 3D MOT by a factor of 2-3. The optimal power is around 400 μW, which corresponds to a push beam intensity of 22 mW/cm^2 $\approx 13 I_{\text{sat.}}$ (Table 5.1). We found, only after setting up a 3D MOT downstream, that applying higher power (> 1 mW) push beam reduces the 3D MOT signal significantly even though the flux is larger.

push beam power	atom number	
(P_{push}) [μW]	dc MOT	RF MOT
0	$1.3(1)\cdot 10^9$	$.49(3)\cdot 10^9$
200	$1.6(2)\cdot 10^9$	$.82(3)\cdot 10^9$
400	$2.3(2)\cdot 10^9$	$.90(2)\cdot 10^9$
600	$1.9(1)\cdot 10^9$	$.90(6)\cdot 10^9$

Table 5.1: Atom number vs push beam power (P_{push}). dc and RF MOT are loaded for 500 ms from a 2D+ MOT with $p_{2D}(\text{Rb}) \approx 2.5 \cdot 10^{-7}$ mBar.

To measure the loading time constant, the loading time (Δt_{ld} in Figure 5.4) is varied to produce a plot of fluorescence vs Δt_{ld} (e.g., in Figure 5.8a), from which the $1/e$ loading time constant (τ_{ld}) can be found from an exponential fit. Using this method, the loading process in a dc and an RF MOT for a few vapor pressures and two 2D MOT configurations, 2D MOT and 2D+ MOT, were studied, under the optimal conditions found in the previous subsections §5.3.1 and §5.3.2. The comparison in Table 5.2 shows that the loading time constants are similar in dc and RF MOT when loading from the same beam source, but the atom number loaded into an RF MOT is lower by a factor of 2-3. Comparing loading at different vapor pressure, we found that there is an optimum vapor pressure for loading, in the vicinity of $p_{2D}(\text{Rb}) \approx 2 \cdot 10^{-7}$ mBar for both 2D MOT and 2D+ MOT. Though a longer loading time can increase the atom number significantly, we chose 500 ms as the default loading time, and used it in all measurements except the loading characterization, because 500 ms is comparable to the loading duration of the molecular MOT in the current SrF experiment. It is worth noting, as it is not shown in Figure 5.4, that a 3 ms delay is padded between trigger for 2D MOT flux start and 3D MOT start to ensure that the 2D MOT flux has reached a steady state when the 3D MOT begins loading. Therefore transient behavior is not expected.

To determine the MOT lifetime under conditions optimized thus far, the MOT fluorescence signal is recorded as a function of storage time (Δt_{st} in Figure 5.4), with the loading time is fixed at 500 ms. The $1/e$ lifetimes (decay constants) are 3.6(1) s in a dc MOT and 3.6(4) s in an RF MOT.

		dc MOT			RF MOT		
p_{2D}(Rb) [mBar]	P_{push} [mW]	τ_{ld} [s]	$N(t_{ld}$ =500 ms)	$\tilde{N}(t_{ld} \to \infty)$	τ_{ld} [s]	$N(t_{ld}$ =500 ms)	$\tilde{N}(t_{ld} \to \infty)$
$1.4{\cdot}10^{-7}$	0	1.1(3)	$.70(7){\cdot}10^9$	$2.0(3){\cdot}10^9$	1.2(6)	$.45(4){\cdot}10^9$	$1.4(4){\cdot}10^9$
	.4	.16(4)	$1.7(2){\cdot}10^9$	$1.9(1){\cdot}10^9$	.19(6)	$.75(3){\cdot}10^9$	$.81(4){\cdot}10^9$
$2.0{\cdot}10^{-7}$	0	1.0(2)	$1.1(5){\cdot}10^9$	$2.9(3){\cdot}10^9$	.9(4)	$.52(7) \cdot 10^9$	$1.3(3){\cdot}10^9$
	.4	.21(5)	$2.8(4){\cdot}10^9$	$3.2(2){\cdot}10^9$	.20(6)	$.91(8){\cdot}10^9$	$1.0(1){\cdot}10^9$
$2.5{\cdot}10^{-7}$	0	.8(3)	$.87(1){\cdot}10^9$	$2.0(3){\cdot}10^9$	.6(3)	$.48(3){\cdot}10^9$	$.9(4){\cdot}10^9$
	.4	.26(7)	$1.7(4){\cdot}10^9$	$2.1(1){\cdot}10^9$	.24(9)	$.78(4) \cdot 10^9$	$.9(1){\cdot}10^9$

Table 5.2: Loading process in dc and RF MOT for different 2D MOT vapor pressure (p_{2D}(Rb)) and push beam power (P_{push}). The loading time constant (τ_{ld}) is the $1/e$ filling time from an exponential fit, $N(t_{ld} =$ 500 ms) is the atom number measured after 500 ms loading, and $\tilde{N}(t_{ld} \to \infty)$ is the asymptotic value of the atom number from the fit.

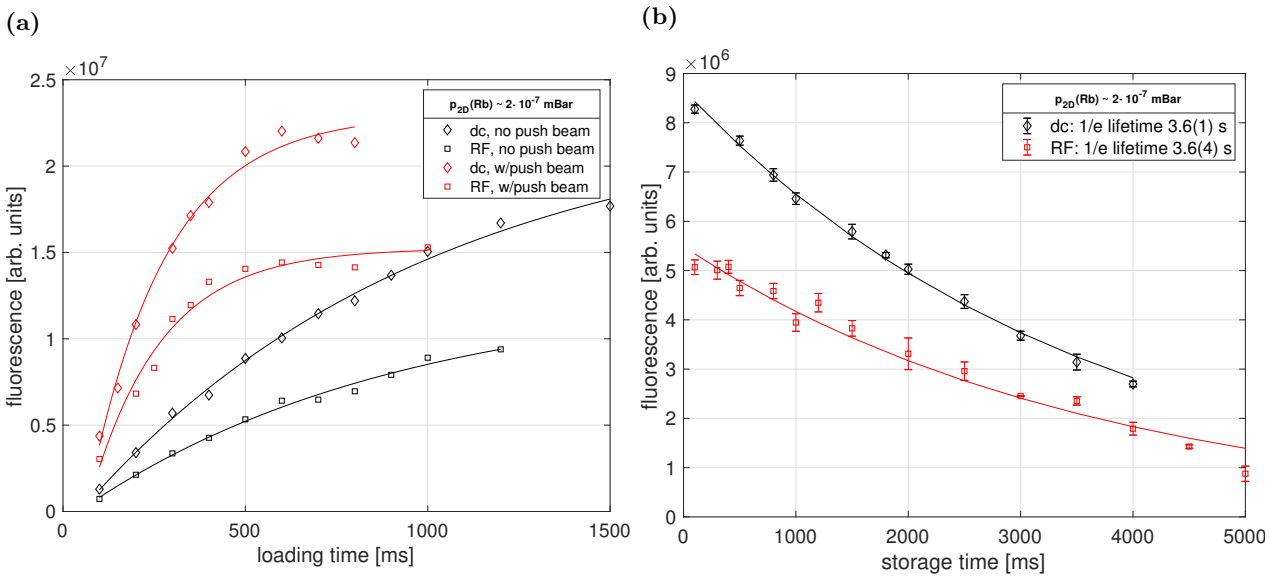


Figure 5.8: (a) Loading the dc and RF MOT from a 2D and 2D+ MOT. Each curve is an exponential fit to the fluorescence data, and yields the loading time constant τ_{ld} for scenarios indicated in the plot legend. (b) MOT fluorescence vs storage time following 500 ms loading from a 2D MOT with Rb vapor pressure $p_{2D}(\text{Rb}) \approx 2 \cdot 10^{-7}$ mBar. Each curve is an exponential fit that yields the MOT $1/e$ decay time constant τ_{MOT} for RF and dc MOT

5.3.4 Optimized MOT properties

Under these conditions that optimize the atom number, other MOT properties have been investigated; specifically, the MOT temperature (T) and the cloud size (σ) are determined using the time-of-flight technique (Figure 5.9).

First, fluorescence images of a free expanding cloud at different time-of-flight (Δt_{tof}) are fitted to 2D

Gaussian surfaces which give the axial and radial gaussian rms radii as functions of the time-of-flight. Then the temperature and the gaussian rms radius at $\Delta t_{\rm tof} = 0$ of each dimension is inferred from fitting to the relation between σ and $\Delta t_{\rm tof}$ given in (2.3.1). The gaussian rms radii from this analysis are consistent with the full widths at half maximum (FWHMs) of the MOT determined from fluorescence imaging *in situ*. In general, temperature, size, and number density depend on the 3D MOT parameters. Under nominally identical 3D MOT conditions (i.e. laser power, magnetic field, etc), Table 5.3 gives dc and RF MOT properties for two detunings.

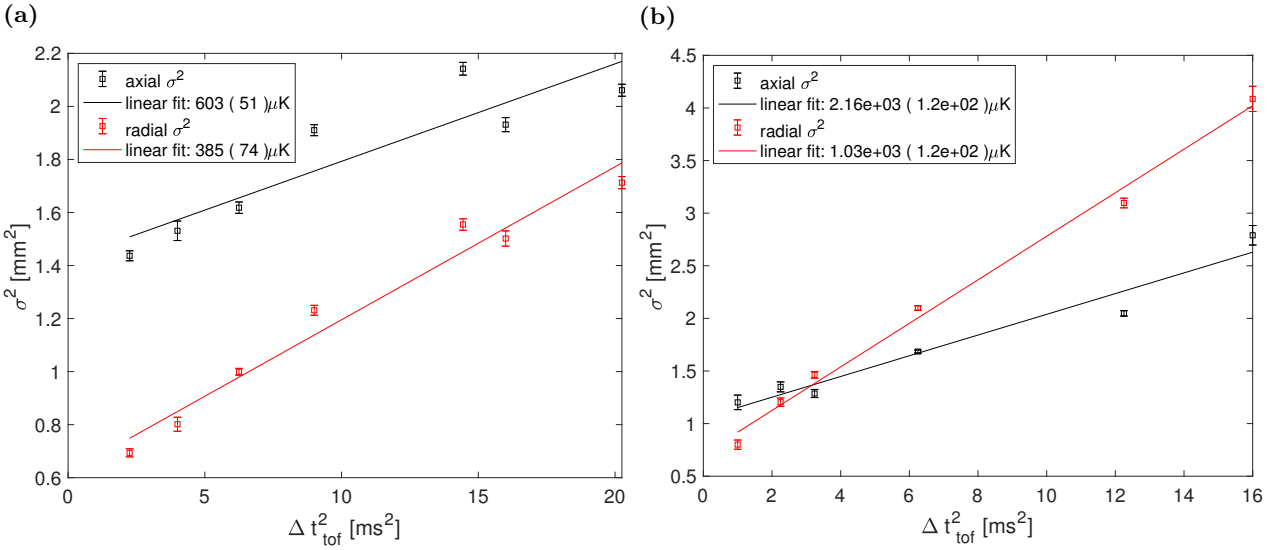


Figure 5.9: (a) dc and (b) RF MOT temperatures measured by the time-of-flight method. In measuring the dc MOT temperatures, the earliest time-of-flight is 2 ms, limited by the switching time of the magnetic field.

	dc MOT			RF MOT		
$\delta_{2\to3}$	(σ_a, σ_r) [mm]	(T_a, T_r) [mK]	N	(σ_a, σ_r) [mm]	(T_a, T_r) [mK]	N
-4Γ	0.79(4),1.19(4)	0.60(5),0.39(7)	$6.8(2)\cdot10^8$	0.84(6),1.03(5)	2.2(1),1.0(1)	$4.3(2)\cdot10^8$
-3Γ	0.84(8),1.17(7)	1.3(1), 1.4(2)	$5.4(4)\cdot10^8$	0.88(5),1.38(4)	3.4(1),1.8(2)	$4.1(4)\cdot10^8$
	$(\omega_a, \omega_r)/(2\pi)$ [Hz]	n [cm^{-3}]	PSD	$(\omega_a, \omega_r)/(2\pi)$ [Hz]	n [cm^{-3}]	PSD
-4Γ	48(5), 26(5)	$3.9(3)\cdot10^{10}$	$2.6(5)\cdot10^{-8}$	87(13), 48(9)	$3.1(4)\cdot10^{10}$	$4.2(6)\cdot10^{-9}$
-3Γ	67(13), 49(9)	$3.0(5)\cdot10^{10}$	$3.8(9)\cdot10^{-9}$	103(6), 47(4)	$1.6(2)\cdot10^{10}$	$1.0(2)\cdot10^{-9}$

Table 5.3: 3D MOT properties: gaussian rms radius (σ), temperature (T), atom number (N), trap frequency (ω), peak density (n) and phase-space density (PSD). Properties in the first half are determined from time-of-flight measurements and absorption, and those in the second half are calculated from the first half. Subscripts a and r indicate axial and radial respectively.

From the cloud sizes and temperatures, assuming the trapping potential is harmonic, the effective linear trap frequency (ω) for each trapping dimension can be inferred using the equipartition theorem, $\omega = \sqrt{\frac{k_B T}{m\sigma^2}}$,

with k_B being the Boltzmann constant and m the mass of the atom.

From the atom number and cloud sizes *in situ*, the peak number density (n) can be calculated, $n = N/((2\pi)^{3/2}\sigma_z\sigma_r^2)$. To compare the separation between atoms and the thermal de Broglie wavelength, $\lambda_{\mathrm{th}} = \sqrt{\frac{2\pi\hbar^2}{mk_BT}}$, the phase-space density (PSD) is defined as PSD$= n(\lambda_{\mathrm{th}})_a(\lambda_{\mathrm{th}})_r^2$, with subscripts a and r indicating axial and radial.

5.4 Summary and outlook

We have quantitatively characterized the differences between dc and RF MOTs operating on a type-I transition under nominally identical conditions. The dc and RF MOT show similar properties in terms of the loading time constant and lifetime. The loading time constants agree for various 2D MOT conditions, and the shortest loading time constant is .2 s, achieved with a push beam when the Rb vapor pressure is around $2{\cdot}10^{-7}$ mBar. The lifetime is 3.6 s. In terms of atom number and temperatures, for a range of 3D MOT parameters, the atom number is significantly lower in an RF MOT than in a dc MOT, and the temperatures significantly higher.

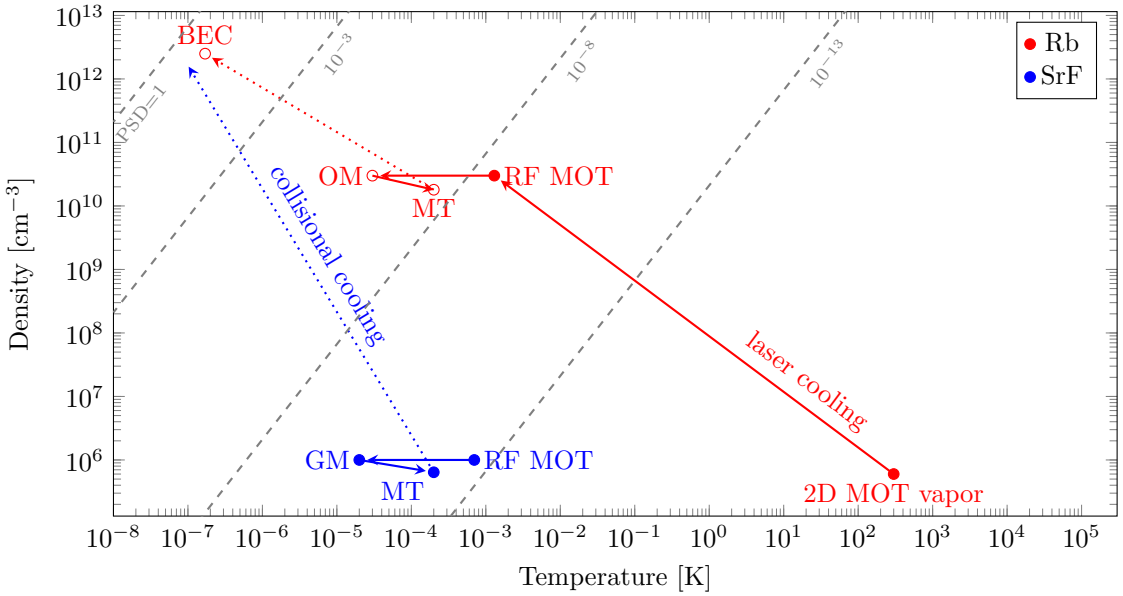


Figure 5.10: Outlook on the path to quantum degeneracy for SrF. The plot shows density and temperature at selected stages of a typical process for cooling to quantum degeneracy. Solid dots are recent results from our lab, and circles are expectations based on the literature on ultracold Rb. Specifically, the temperature after molasses is estimated to be 30 μK [68], the transfer efficiency from molasses into a magnetic trap (MT) $\sim 60\%$ [26] and a final temperature in MT $\sim$200 μK, the density $n \sim 2.5 \cdot 10^{12}$ cm^{-3} and temperature ~ 170 nK in a Bose-Einstein condensate (BEC) [9]. Laser cooling steps are indicated by red solid arrows, and collisional cooling steps by dotted arrows. PSD contours (dashed lines) are calculated for ^{88}Sr^{19}F.

In addition to the comparison, we demonstrated the capability of trapping a substantial number of Rb

atoms, $\sim 10^8 - 10^9$, in an RF MOT. Not only is it preliminary to further phase-space compression of Rb atoms, e.g., via optical molasses (OM) or gray molasses (GM) and evaporative cooling, but ultimately it also opens up the path for phase-space compression of SrF via collisional cooling (Figure 5.10). For molecules, given the densities in MOTs and subsequent conservative traps [26, 69–71], e.g., $n \sim 8 \cdot 10^7$ cm^{-3} and PSD $\sim 2 \cdot 10^{-9}$ in Ref.[69], evaporative cooling is not immediately applicably because it requires a much higher PSD, e.g., PSD $\sim 10^{-3}$ for ^{161}Dy and ^{40}K in Ref.[72]. By comparison, sympathetic cooling via atom-molecule collisions, which does not require a high initial density or PSD of molecules, is one of the common methods for increasing the PSD prior to evaporative cooling via molecule-molecule collisions. Applying sympathetic cooling is also one of the incentives for studying atom-molecule collisions [21, 73–76]. For instance, Ref.[21] shows that sympathetic cooling between Na and NaLi increased the PSD of molecules by a factor of 20, producing a temperature ~ 220 nK. For SrF, in §5.4.1, the possibility of sympathetic cooling of SrF and Rb in a magnetic trap is considered. There are a few advantages of using Rb: first, calculation of the scattering cross-sections of Rb and SrF in specific quantum state shows good prospects of interspecies cross-section [64]; second, the mass of Rb (87 amu) is similar to the mass of SrF (107 amu); last but not least, cooling Rb—by laser cooling and evaporative cooling—is straightforward.

5.4.1 Sympathetic cooling of SrF and Rb in a magnetic trap

Suppose SrF and ^{87}Rb prepared in $|N = 0, F = 1, m_F = 1\rangle$ and respectively, $|F = 1, m_F = -1\rangle$, are co-trapped in a magnetic quadrupole trap (Figure 5.11). The trapping potential of molecules is deeper than that of Rb atoms, allowing for a good overlap of cold molecules with colder atoms. When the trap depth is large, the loss of molecules or atoms due to inelastic collisions (that does not induce internal transitions) is small. The success of sympathetic cooling is contingent on the cross-species thermalization. This thermalization process is often simulated based on a differential equation for $\Delta T = T_{\mathrm{SrF}} - T_{\mathrm{Rb}}$ [21, 72, 77, 78],

$$\frac{1}{\Delta T}\frac{d(\Delta T)}{dt} = -\Gamma_{\mathrm{th}}(T, t), \tag{5.4.1}$$

with $\Gamma_{\mathrm{th}}(T, t)$ being the thermalization rate that depends on temperatures, and other time-dependent parameters, e.g., atom numbers and trap frequencies. When the atom number is much larger than the molecule number, the increase in T_{Rb} ought to be much smaller than to the decrease in T_{SrF}. In a mass-imbalanced system with a mass-dependent reduction factor $\xi = 4m_{\mathrm{Rb}}m_{\mathrm{SrF}}/(m_{\mathrm{Rb}} + m_{\mathrm{SrF}})^2 \approx 0.99$, the thermalization

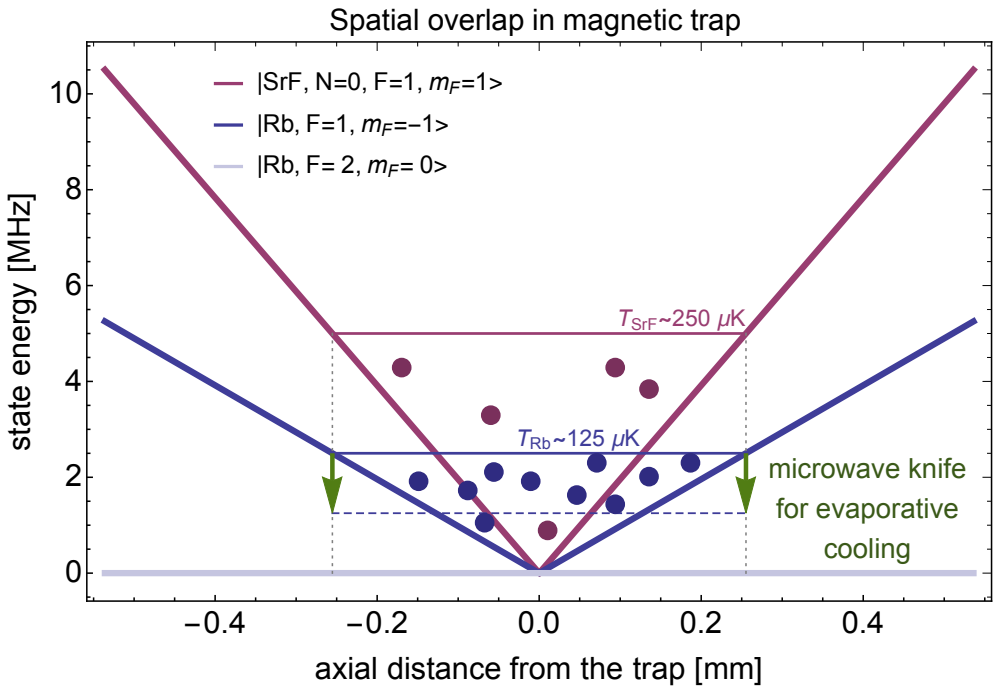


Figure 5.11: Sympathetic cooling in a magnetic trap. As sympathetic cooling progresses, the Rb temperature (T_{Rb}) is reduced by microwave induced evaporative cooling via the hyperfine transition in Rb $|F=1, m_F=-1\rangle \rightarrow |F=0, m_F=0\rangle$.

rate can be estimated as [21, 72, 77, 78]

$$\Gamma_{\mathrm{th}} \approx \frac{n_{\mathrm{RbSrF}} \sigma_{\mathrm{el}} v_{\mathrm{rel}}}{3/\xi}, \tag{5.4.2}$$

where n_{RbSrF} is the overlap density— the density the average density of Rb seen by SrF, σ_{el} is the interspecies elastic scattering cross-section, $v_{\mathrm{rel}} = \sqrt{\frac{8k_B}{\pi}\left(\frac{T_{\mathrm{Rb}}}{m_{\mathrm{Rb}}} + \frac{T_{\mathrm{SrF}}}{m_{\mathrm{SrF}}}\right)}$ is the mean relative velocity, and $3/\xi$ is the approximate average number of collisions per particle required for thermalization. The overlap density can be estimated based on trap frequencies, temperatures and densities of both species [21, 72, 77]. As the trap properties may be experimentally difficult to measure precisely and cause a large uncertainty, we consider a similar interpretation, treating the overlap density as a product of the Rb atom number and an overlap function, $n_{\mathrm{RbSrF}} = N_{\mathrm{Rb}} f_{\mathrm{RbSrF}}$ [78]. In Ref.[78], $f_{YbRb} \approx 50 \cdot 10^{10}$ m^{-3} in a hybrid system with ^{87}Rb in a magnetic trap and ^{176}Yb in a bichromatic dipole trap. Insofar as scattering cross-sections are concerned, the *ab initio* quantum scattering calculation of ground state SrF molecules and Rb atoms in magnetic traps in Ref. [64] suggests an elastic cross-section $\sigma_{\mathrm{el}} \sim 10^4$ Å^2. For starting temperatures in Figure 5.11, at the beginning of sympathetic cooling, $v_{\mathrm{rel}} = 0.28$ m/s. Suppose the volume occupied by Rb atoms is $\sim 5 \cdot 10^{-12}$ m^3 and that atoms are perfectly overlapped with SrF; then $n_{\mathrm{RbSrF}} \sim 10^8/(5 \cdot 10^{-12})$ m^{-3}. For initial conditions depicted in Figure 5.11 and $\sigma_{\mathrm{el}} \sim 10^4$ Å^2, the estimated thermalization rate is $\Gamma(t=0) \sim 1900$/s.

Concurrent with the thermalization process via elastic collisions, there are also inelastic collisions causing loss. In a magnetic trap, there is spin relaxation driven by the magnetic dipole-dipole interaction between the electronic spins of Rb and SrF. This loss mechanism due to inelastic collisions ultimately limits the efficiency of sympathetic cooling. In regard to this issue, the paper suggests the possibility to suppress the magnetic-field-dependent inelastic cross-section in the ultracold s-wave regime. Given the good prospects of interspecies thermalization, i.e., the elastic-to-inelastic collision ratio is much greater than 1, sympathetic cooling to below 1 μK seems plausible.

Chapter 6

Optical dipole trap

The interaction between coherent light and neutral particles leads to an optically induced shift, known as light shift (or ac Stark shift), and there are a number of ideas for using it to trap neutral particles [79]. In this chapter, §6.1 reviews, for neutral particles in general, the prospect of conservative trapping with off-resonance light based on perturbation theory. §6.2 derives expressions for the matrix elements of the electric dipole operator for molecules and relates them to experimental parameters and data. Thereby, for individual hyperfine magnetic levels, the energy shift due to far-detuned monochromatic light can be easily calculated. With certain assumptions about the intensity of trap light, §6.3 gives two examples in which trap depths for hyperfine magnetic levels due to far-detuned linearly polarized light are estimated. §6.4 discusses an alternative view for light shifts that improves intelligibility and thereby allows us to separate the dependence of energy shift on the frequency and on the polarization of trap light. Based on results in §6.4, §6.5 discusses the polarization dependence of trapping potentials due to far-detuned light in two specific examples.

6.1 Light shift

The effect of off-resonance laser light can be treated as a perturbation due to the interaction Hamiltonian,

$$H_1 = -\vec{\mu} \cdot \vec{\mathcal{E}}(\omega, \vec{r}), \tag{6.1.1}$$

where $\vec{\mu} = -e\vec{r}(e > 0)$ is the electric dipole operator and $\vec{\mathcal{E}}$ is the light field that has some spatial dependence $\vec{r}$, a well-defined frequency ω, and polarization $\hat{e}$ (unit vector)

$$\vec{\mathcal{E}}(\omega, \vec{r}) = \hat{e}\mathcal{E}(\vec{r})e^{-i\omega t} + c.c. \tag{6.1.2}$$

When considering the interaction with laser light, it is useful to work in the dressed state picture. In the simplest nontrivial case, suppose light, $|n\rangle$, interacts via H_1 (6.1.1) with a two-level system where the excited state $|\mathfrak{e}\rangle$ and the ground state $|g\rangle$ are separated by $\hbar\omega_0$, $\{|\psi_i\rangle\} = \{|\mathfrak{e}\rangle, |g\rangle\} \otimes \{|n\rangle\}$. The unperturbed energy $E^{(0)}_{\psi_i}$ includes the energy of both photons in the light field and the quantum system, such as a two-level system and a molecule. The ground state can absorb a photon from the light field out of a total of n photons, in which case the unperturbed energy changes from $E^{(0)}_{\psi_i} = n\hbar\omega$ to $E^{(0)}_{\psi_j} = \hbar\omega_0 + (n-1)\hbar\omega$.

Applying nondegenerate time-independent perturbation theory, to leading order, the energy shift of state $|\psi_i\rangle$ with unperturbed energy $E^{(0)}_{\psi_i}$ is given by

$$E^{(2)}_{\psi_i} = \sum_{\psi_i \neq \psi_j} \frac{|\langle\psi_j|H_1|\psi_i\rangle|^2}{E^{(0)}_{\psi_i} - E^{(0)}_{\psi_j}}. \tag{6.1.3}$$

Despite absorption, for $n \gg 1$, the total energy of light field is assumed to be unchanged; hence to the same order, $E^{(2)}_g \approx E^{(2)}_{\psi_i}$. Suppose the detuning is defined as $\Delta = \omega - \omega_0$, and the polarization of the photon is $\hat{e}$. With the rotating wave approximation, the ground state is shifted by,

$$E^{(2)}_g = \frac{|\langle g|\vec{\mu}\cdot\vec{\mathcal{E}}|\mathfrak{e}\rangle|^2}{\Delta}. \tag{6.1.4}$$

Apart from the detuning, other quantities on the right-hand side can be experimentally measured or controlled as well. The strength of the light field is most commonly characterized by its intensity

$$I = 2c\epsilon_0|\mathcal{E}(\vec{r})|^2. \tag{6.1.5}$$

It is well-known (by way of a semiclassical approach) that the dipole matrix elements of a two-level system can be related to the natural linewidth of the excited state Γ (or equivalently the reciprocal of lifetime) via [79]

$$\Gamma = \frac{\omega_0^3}{3\pi\epsilon_0\hbar c^3} \sum_{\{\hat{e}^p\}} |\langle g|\vec{\mu}\cdot\hat{e}^p|\mathfrak{e}\rangle|^2. \tag{6.1.6}$$

The polarization of the photon emitted in a spontaneous emission is unconstrained, so the sum accounts for different polarizations, for example, in the Cartesian coordinate, $p = x, y, z$. A superscript/subscript p denotes the p-component of a vector/covector. In summary,

$$E^{(2)}_g = \frac{3\pi c^2}{2\omega_0^3} I \frac{\Gamma}{\Delta}. \tag{6.1.7}$$

For red detunings, $\Delta < 0$, the ground state light shift is negative, $E_g^{(2)} < 0$, creating a trapping potential for the ground state.

This solution can be generalized to a more realistic system with multiple excited and ground states, denoted as $\{|\mathfrak{e}_i\rangle\}$ and respectively $\{|g_j\rangle\}$, with degeneracy due to angular momentum. Suppose each transition has a distinct detuning Δ_{ij}; then the light shift for ground state $|g_j\rangle$ excited with laser light of polarization $\hat{e}^p$ is given by

$$E_{g_j}^{(2)} = \sum_{i,p} \frac{|\langle g_j|\vec{\mu}\cdot\hat{e}^p|\mathfrak{e}_i\rangle|^2}{\Delta_{ij}} |\hat{e}_p\cdot\vec{\mathcal{E}}|^2. \tag{6.1.8}$$

To evaluate this expression, it is necessary to calculate the squared norm of the dipole matrix element $\langle g_j|\vec{\mu}\cdot\hat{e}^p|\mathfrak{e}_i\rangle$ between individual pair of states where a dipole transition is allowed for polarization $\hat{e}^p$. The details of this calculation and how to relate the dipole matrix element to the transition linewidth in a multilevel system with angular momentum will be discussed in §6.2.

6.2 Dipole matrix element

The goal of this section is to derive the analytical expression of a matrix element for a p-dipole transition with p labeling the polarization of emitted or absorbed photon in a space-fixed axis system (lab frame),

$$\langle\eta|\vec{\mu}\cdot\hat{e}^p|\eta'\rangle\,. \tag{6.2.1}$$

Here η and η' denote the set of quantum numbers for the ground and excited states respectively; they will be asserted in each subsequent subsection.

The logic of the first three subsections is to decouple angular momenta from the matrix element using spherical tensor algebra, and eventually obtain a quantity that only depends on the radial solution to the Schrödinger equation and can be deduced from the natural linewidth and frequency of a transition. §6.2.1 outlines steps for deriving the dipole matrix element in the Hund's case (a) basis. §6.2.2 shows a similar derivation in the Hund's case (b) basis. After the Hund's case basis functions are introduced, §6.2.3 and §6.2.4 discuss superpositions of Hund's case basis functions with practical relevance, §6.2.3 on the very fundamental question in regard to parity (space-fixed inversion symmetry) in retrospect, and §6.2.4 on the effect of hyperfine mixing of J states that leads to a modification of states in matrix elements with a more precise description of constituent angular momentum J. §6.2.5 shows the derivation for ground state rubidium atoms, which is well-known. The formalism for the spherical tensor algebra used here is outlined

in Chapter 5 of the book by Brown and Carrington, *Rotational Spectroscopy of Diatomic Molecules* [80]; the equations cited are from this reference unless otherwise specified. In the derivation, $\overset{\text{(eq.)}}{=}$ indicates the equation or theorem above the equal sign is invoked in this step, and that its proof may not be immediately obvious.

§6.2.6 is on quantum numbers and symmetries in the case of diatomic molecules; it is an attempt to explain the terminology of spectroscopy of diatomic molecules by giving a hand-waving justification to quantum numbers that are asserted. §6.2.7 is on the treatment for finite rotations in the angular momentum formalism as a supplement to some algebraic tools used earlier in the derivation. A summary of dipole matrix elements derived for different bases and branching ratios are included in the Appendix A.3 and A.4.

(6.2.1) is a component of the dipole matrix element in the space-fixed axis system with p indexing coordinate components, since it is most convenient to discuss the polarization of photons in the space-fixed axis system (space-fixed frame). Before applying any parity selection rule and spherical tensor algebra to the matrix element of $\vec{\mu}\cdot\hat{e}^p$, it is useful to establish the coordinate system using basis vectors that corresponds to the polarization of light, $p=0,\pm1$. To transform from the Cartesian coordinate system where $p=x,y,z$,

$$\hat{e}^1=-\frac{1}{\sqrt{2}}(\hat{e}^x+i\hat{e}^y),\quad \hat{e}^0=\hat{e}^z,\quad \hat{e}^{-1}=\frac{1}{\sqrt{2}}(\hat{e}^x-i\hat{e}^y). \tag{6.2.2}$$

Insofar as the dipole matrix elements are concerned, in this coordinate system, $\mu_p=\vec{\mu}\cdot\hat{e}^p$ is the p^{th} component of the dipole covector operator. A more detailed discussion of notations and vector space in the complex spherical basis can be found in Appendix B.1.

6.2.1 Hund's case (a)

Preliminaries

In diatomic molecules, multiple angular momentum vectors are necessary to fully specify the state, and their relations are defined as

$$\vec{F}=\vec{I}+\vec{J},\quad \vec{J}=\vec{N}+\vec{S},\quad \vec{N}=\vec{R}+\vec{L}. \tag{6.2.3}$$

$\vec{F}$ is the grand total angular momentum, $\vec{J}$ the total angular momentum excluding the nuclear spin $\vec{I}$, $\vec{N}$ the total angular momentum excluding the nuclear spin $\vec{I}$ and the electron spin $\vec{S}$. In the absence of spherical symmetry in diatomic molecules, there are two axes the electron can orbit around. $\vec{N}$ accounts for both rotation in the plane orthogonal to the internuclear axis ($\hat{n}$) due to the bare nuclei ($\vec{R}$) and orbital angular

momentum of the electron around the center of mass of the molecule ($\vec{L}$). The definition of these angular momentum operators is consistent for different Hund's cases.

The set of good quantum numbers* in Hund's case (a) is

$$\{\eta\} = \xi, \Lambda, v, \Omega, \Sigma, S, J, M. \tag{6.2.4}$$

Hund's cases (a) and (b) both neglect the nuclear spin, and therefore F. Here M is the projection of $\vec{J}$ in the space-fixed axis system along $\hat{e}^z$ by convention. ξ is a label for a particular electronic state, v the vibrational quantum number, Λ the projection of $\vec{L}$ on the internuclear axis, Σ the projection of $\vec{S}$ on the internuclear axis, and Ω projection of $\vec{J}$ on the internuclear axis. The relation between component quantum numbers in the body-fixed frame (attached to the molecule) is given by

$$\Omega = \Lambda + \Sigma. \tag{6.2.5}$$

In a term symbol such as $\xi^{2S+1}|\Lambda|_{|\Omega|} = A^2\Pi_{1/2}$, the sign of Λ and Ω are unspecified—Π denotes $|\Lambda| = 1$ and the subscript denotes $|\Omega| = 1/2$.

In the Dirac notation,

$$|\eta\rangle = |\xi, \Lambda; v; S, \Sigma; J, \Omega, M\rangle\,. \tag{6.2.6}$$

$|\eta\rangle$ is a product of the electronic orbital function $|\xi, \Lambda\rangle$, the vibrational wavefunction $|v\rangle$, the electron spin wavefunction $|S, \Sigma\rangle$, and the rotational function $|J, \Omega, M\rangle$. The semicolon here can be replaced by $\otimes$ indicating a tensor product of wavefunctions.

When projections of angular momenta onto the internuclear axis are included in the basis, writing the dipole operator in the body-fixed frame is necessary for decoupling the angular dependence from the matrix element. The treatment is to write each vector component of the dipole operator in the space-fixed frame (indexed by p) in terms of the dipole operator in the body-fixed frame (indexed by q) via

$$\mu_p \overset{(5.144)}{=} \sum_q \mathfrak{D}^{(1)}_{pq}(\omega_E)^* \mu_q, \tag{6.2.7}$$

where ω_E is a shorthand for the set of Euler angles in a finite rotation that allows the space-fixed frame to overlap with the body-fixed frame and $\mathfrak{D}^{(1)}_{pq}(\omega_E)^*$ is the complex conjugate of the pq element of a rank-1

*These quantum numbers correspond to eigenvalues of particular operators, and a detour to discussing symmetries and quantum numbers can be found in §6.2.6.

Wigner rotation matrix $\mathfrak{D}^{(1)}(\omega_E)$ that relates finite rotations of a rank-1 operator (e.g. μ_p) to infinitesimal rotations*. As far angular momentum conservation in a dipole transition is concerned, if the dipole operator is indexed by q, it imposes selection rules on component quantum numbers defined in the body-fixed frame, such as Λ, Σ, Ω. From the perspective of frame transformation, including quantum number defined in the molecule-fixed frame in the basis function enforces the consideration of the relative orientation between the space-fixed axes and the body-fixed axes, because the parametrization of component quantum numbers depends on the angles between the angular momentum vector, a physical quantity that should be independent of parametrization, and the axes (in Euclidean space).

Dipole matrix element in Hund's case (a) basis

Using the Hund's case (a) basis and algebraic tools discussed in the preliminaries, the dipole matrix element can be simplified

$$\begin{aligned}\langle \eta|\mu_p|\eta'\rangle &= \sum_q \langle \xi,\Lambda; v; S,\Sigma; J,\Omega,M|\mathfrak{D}^{(1)}_{pq}(\omega_E)^*\mu_q|\xi',\Lambda'; v'; S',\Sigma'; J',\Omega',M'\rangle \\ &= \sum_q \langle J,\Omega,M|\mathfrak{D}^{(1)}_{pq}(\omega)^*|J',\Omega',M'\rangle \langle \xi,\Lambda; v'; S,\Sigma|\mu_q|\xi',\Lambda'; v'; S',\Sigma'\rangle . \end{aligned} \tag{6.2.8}$$

The first braket can be simplified

$$\begin{aligned}&\langle J,\Omega,M|\mathfrak{D}^{(1)}_{pq}(\omega_E)^*|J',\Omega',M'\rangle \\ &\overset{(5.185)}{=} (-1)^{J-M}\langle J,\Omega||\mathfrak{D}^{(1)}_{.q}(\omega_E)^*||J',\Omega'\rangle \begin{pmatrix} J & k=1 & J' \\ -M & p & M' \end{pmatrix}\end{aligned} \tag{6.2.9}$$

where

$$\langle J,\Omega||\mathfrak{D}^{(1)}_{.q}(\omega_E)^*||J',\Omega'\rangle \overset{(5.186)}{=} (-1)^{J-\Omega}\sqrt{(2J+1)(2J'+1)}\begin{pmatrix} J & k=1 & J' \\ -\Omega & q & \Omega' \end{pmatrix}. \tag{6.2.10}$$

$\langle J,\Omega||\mathfrak{D}^{(1)}_{.q}(\omega_E)^*||J',\Omega'\rangle$ is a reduced matrix element that is independent of the component (or magnetic) quantum numbers in the space-fixed frame, and thus the orientation of the space-fixed frame.The subscript of the Wigner rotation matrix, $.q$, indicates that it depends only on the orientation of the body-fixed frame.

As for the second term in the sum (6.2.8), corresponding to the matrix element of the q-component of

*Detail on Wigner rotation matrices and Euler rotations that are not immediately relevant to the derivation in this subsection can be found in §6.2.7.

the dipole operator in the body-fixed frame, because the electric dipole operator does not change the electron spin or its projection, we can write

$$\langle \xi, \Lambda; v; S, \Sigma | \mu_q | \xi', \Lambda'; v'; S', \Sigma' \rangle = \langle \xi, \Lambda; v | \mu_q | \xi', \Lambda'; v' \rangle \, \delta_{\Sigma'\Sigma} \delta_{S'S}. \tag{6.2.11}$$

The sum in (6.2.8) over q is simplified as we recognize, from (6.2.9), that the only nontrivial term is contributed by $q = \Omega - \Omega'$. This is then replaced by $\Lambda - \Lambda'$, because $\Sigma = \Sigma'$. $\Lambda = 0$ in the ground state $X^2\Sigma^+$. If the final state is $A^2\Pi_{|\Omega'|}$, $\Lambda' = \pm 1$ and $\Omega - \Omega' = \mp 1$; if it is $B^2\Sigma^+$, $\Lambda' = 0$ and $\Omega - \Omega' = 0$.

Within this electronic and vibrational transition, i.e. the electronic state and the vibrational number of both initial and final states are known, $\{\xi', \Lambda', v'\}$ and $\{\xi, \Lambda, v\}$, an excited state with rotational quantum numbers Ω' and total angular momentum J' can decay into ground states with any Ω, J as far as the triangle inequality is satisfied. The branching ratio between decays to levels with distinct Ω, J quantum numbers follows from (6.2.9), after all the decay channels for different polarizations and component quantum numbers M are accounted for,

$$\begin{aligned} BR(\Omega, J) &= \sum_{p,M} |\, \langle J, \Omega, M | \mathfrak{D}^{(1)}_{pq}(\omega_E)^* | J', \Omega', M' \rangle \,|^2 \\ &= (2J+1) \begin{pmatrix} J & k=1 & J' \\ -\Omega & \Lambda - \Lambda' & \Omega' \end{pmatrix}^2 . \end{aligned} \tag{6.2.12}$$

As for normalization within an electronic and vibrational transition, for an arbitrary excited state with Ω' and J',

$$\sum_{J,\Omega} BR(\Omega, J) = 1. \tag{6.2.13}$$

The rotational branching ratios for the $A^2\Pi_{|\Omega|} - X^2\Sigma^+$ transitions can be found in Table A.6, A.8 in §A.4.

To summarize, the norm squared of a dipole matrix element can be decomposed into a radial matrix element, rotational branching ratio, and transition strength,

- electronic matrix element:

$$\langle \xi, \Lambda; v | \mu_{\Lambda - \Lambda'} | \xi', \Lambda'; v' \rangle \, \delta_{\Sigma'\Sigma} \delta_{S'S} \tag{6.2.14}$$

- rotational branching ratio:

$$(2J+1)\begin{pmatrix} J & k=1 & J' \\ -\Omega & \Lambda-\Lambda' & \Omega' \end{pmatrix}^2 \tag{6.2.15}$$

- transition strength:

$$(2J'+1)\begin{pmatrix} J & k=1 & J' \\ -M & p & M' \end{pmatrix}^2 \tag{6.2.16}$$

The square norm of a dipole matrix element is now factored in to functions each with fewer variables than all of $\{\eta, \eta'\}$,

$$|\langle\eta|\mu_p|\eta'\rangle|^2 = \text{electronic matrix element}^2 \times \text{rotational branching ratio} \times \text{transition strength}. \tag{6.2.17}$$

Vibrational branching

The radial matrix element in (6.2.14) can be written as a product of integrals in the coordinate representation such that each individual integral only depends on either vibrational numbers or electron orbitals. In the Dirac notation, (6.2.14) can be factored into the Franck-Condon factors (FCF) that only depends on the vibrational quantum numbers, and a matrix element that only depends on the electron orbitals,

$$|\langle\xi,\Lambda;v|\mu_{\Lambda-\Lambda'}|\xi',\Lambda';v'\rangle|^2 = FCF(v,v')|\langle\xi,\Lambda|\mu_{\Lambda-\Lambda'}|\xi',\Lambda'\rangle|^2. \tag{6.2.18}$$

The Franck-Condon factors are normalized for each excited state vibrational number,

$$\sum_v FCF(v,v') = 1. \tag{6.2.19}$$

Dipole matrix elements and transition linewidth

The sum of the squared norms of dipole matrix elements over quantum numbers $\{v, J, M, \Omega, S, \Sigma\}$ for all allowed transitions effectively describes the strength of the electronic transition coupling the ground state labelled by $\{\xi, \Lambda\}$ and excited state $\{\xi', \Lambda'\}$*. With (6.2.17), we can simplify the sum using orthogonal

*In labelling the transition with only the electronic orbital quantum numbers, the energy splittings due to vibrational and rotational motions, spin rotation coupling, and to the nuclear spin are neglected. In SrF, they are much smaller compared to the energy splitting between electronic states.

relations of Wigner $3J$ symbols [81],

$$\begin{aligned}
&\sum_{v}\sum_{J,p,M,\Omega,S,\Sigma} |\langle J,\Omega,M;\xi,\Lambda;v;S,\Sigma|\mu_p|J',\Omega',M';\xi',\Lambda';v';S',\Sigma'\rangle|^2 \\
&= \sum_{J,p,M,\Omega,\Sigma}(2J+1)(2J'+1)\begin{pmatrix} J & k=1 & J' \\ -\Omega & \Lambda-\Lambda' & \Omega' \end{pmatrix}^2\begin{pmatrix} J & 1 & J' \\ -M & p & M' \end{pmatrix}^2\delta_{SS'}\delta_{\Sigma\Sigma'} \\
&\quad\times|\langle\xi,\Lambda|\mu_{\Lambda-\Lambda'}|\xi',\Lambda'\rangle|^2 \\
&= \sum_{J,\Omega}(2J+1)\begin{pmatrix} J & k=1 & J' \\ -\Omega & \Lambda-\Lambda' & \Omega' \end{pmatrix}^2|\langle\xi,\Lambda|\mu_{\Lambda-\Lambda'}|\xi',\Lambda'\rangle|^2 \\
&= |\langle\xi,\Lambda|\mu_{\Lambda-\Lambda'}|\xi',\Lambda'\rangle|^2. \qquad (6.2.20)
\end{aligned}$$

It turns out to only depend on the electronic orbital wavefunctions of the ground and excited state, as Λ is the orbital angular momentum projected on the internuclear axis. As the electronic quantum numbers, ξ and Λ, are not summed over, it is implied that single-photon decay from $|\xi',\Lambda'\rangle$ into electronic states other than $|\xi,\Lambda\rangle$ is not accounted for. However, in general, since dipole transition can occur between electronically excited states, decay via all possible electronic transitions amount to the total linewidth, with one exception—when $|\xi',\Lambda'\rangle$ is the lowest electronic excited state, the electron can only end up in the ground state*. In spite of this, the partial linewidth of the higher excited state is approximately equal to the total linewidth because the branching ratio between decay into different electronic states is roughly proportional to the cube of the ratio of transition frequencies. Therefore this sum is equivalent, up to the dimensional factor, to the partial width of this excited state, and to a good approximation, the total linewidth.

Suppose Γ and ω_0 are the linewidth and frequency of a transition labelled by $\{\xi,\Lambda,\xi',\Lambda'\}$. Then it follows from (6.1.6) the expression for the linewidth of a two-level system that

$$\Gamma = \frac{\omega_0^3}{3\pi\epsilon_0\hbar c^3}|\langle\xi,\Lambda|\mu_{\Lambda-\Lambda'}|\xi',\Lambda'\rangle|^2. \qquad (6.2.21)$$

This equation allows us to solve for the matrix element in (6.2.14) from experimental measurements of ω_0 and Γ.

*Given the possibility of dipole transitions between excited states, the contrary mechanism, cascading from higher excited states, would bias the lifetime/linewidth measurement of a lower excited state. The linewidths for various excited states used and cited are clear of such systematics from either direction. For example, in Ref.[82] where the lifetimes of A states are determined via fluorescence decay, cascading from higher excited states should not contribute to the measured lifetime.

$$|\langle \xi, \Lambda | \mu_{\Lambda-\Lambda'} | \xi', \Lambda' \rangle|^2 = \frac{3\pi\epsilon_0\hbar c^3}{\omega_0^3}\Gamma. \tag{6.2.22}$$

For future reference, the right-hand side is defined as a function of experimental parameters

$$f(\Gamma, \omega_0) = \frac{3\pi\epsilon_0\hbar c^3}{\omega_0^3}\Gamma. \tag{6.2.23}$$

With (6.2.14), (6.2.16) and (6.2.18), the squared norm of a matrix element can be evaluated

$$\begin{aligned}|\langle \eta | \mu_p | \eta' \rangle|^2 = f(\Gamma, \omega_0) \times FCF(v, v') \times \text{rotational branching ratio} \\ \times \text{transition strength.}\end{aligned} \tag{6.2.24}$$

Hyperfine structure

The nuclear spin I leads to hyperfine structure in both ground and excited states. This can be treated by introducing the grand total angular momentum F to the Hund's case (a) basis,

$$|\eta\rangle = |\xi, \Lambda; v; S, \Sigma; J, I, \Omega, F, M\rangle\,. \tag{6.2.25}$$

With (6.2.7), quantum numbers defined with respect to the space-fixed frame and the body-fixed frame can be separated,

$$\langle \eta | \mu_p | \eta' \rangle = \sum_q \langle J, I, \Omega, F, M | \mathfrak{D}^{(1)}_{pq}(\omega_E)^* | J', I', \Omega', F', M' \rangle \langle \xi, \Lambda; v; S, \Sigma | \mu_q | \xi', \Lambda'; v'; S', \Sigma' \rangle\,. \tag{6.2.26}$$

The first braket depends on the space-fixed axis system, in the sense that M depends on the angle between $\vec{F}$ and the z-axis, $M = F\cos\theta$. Applying the Wigner-Eckart theorem allows us to obtain a reduced matrix element that is independent of this relative orientation; a term in the sum of (6.2.26) becomes

$$\begin{aligned}&\langle J, I, \Omega, F, M | \mathfrak{D}^{(1)}_{pq}(\omega_E)^* | J', I', \Omega', F', M' \rangle \\ &= (-1)^{F-M} \begin{pmatrix} F & k=1 & F' \\ -M & p & M' \end{pmatrix} \langle J, I, \Omega, F || \mathfrak{D}^{(1)}_{\cdot q}(\omega_E)^* || J', I', \Omega', F' \rangle\,.\end{aligned} \tag{6.2.27}$$

Because the nuclear spin is a conserved quantity in a dipole transition, the spectator theorem (5.136) allows us to decouple the nuclear spin I from F in the reduced matrix element. Applying it to the braket on the

right-hand side,

$$\begin{aligned}
&\langle J, I, \Omega, F||\mathfrak{D}^{(1)}_{.q}(\omega_E)^*||J', I', \Omega', F'\rangle \\
&\overset{(5.157)}{=} (-1)^{I+k+F+J'}\sqrt{(2F+1)(2F'+1)}\begin{Bmatrix} J & F & I \\ F' & J' & k=1 \end{Bmatrix} \\
&\times \langle J, \Omega, F||\mathfrak{D}^{(1)}_{.q}(\omega_E)^*||J', \Omega', F'\rangle\, \delta_{II'}.
\end{aligned} \tag{6.2.28}$$

After substituting (6.2.28) into (6.2.26), the matrix element looks more similar to (6.2.8), and so the subsequent arguments for simplifying the sum apply.

In summary, the dipole matrix elements in the Hund's case (a) basis with and without the hyperfine structure can be written in a factored form and related to observables that can be determined experimentally, and the expression can be found in the Appendix A.3, (A.3.1) and (A.3.2).

6.2.2 Hund's case (b)

The matrix element in the Hund's case (b) basis is relevant to the dipole transition between $X^2\Sigma^+$ and $B^2\Sigma^+$. In Hund's case (b), the good quantum numbers are

$$\{\eta\} = \xi, v, \Lambda, S, N, J, M. \tag{6.2.29}$$

In the Dirac notation,

$$|\eta\rangle = |\xi, \Lambda; v; S, N, J, M\rangle\,. \tag{6.2.30}$$

Suppose M_S and M_N are the projections of $\vec{S}$ and $\vec{N}$ along $\hat{e}^z$; it follows from a relation defined in (6.2.3) that $M = M_S + M_N$. Provided that the electron spin $S = 1/2$, J can only take two values, and the coupled basis is a direct sum of $\{|J, M\rangle\}$ for the two possible J's,

$$\{|S, M_S\rangle\} \otimes \{|N, M_N\rangle\} = \{|J = N + S, M\rangle\} \oplus \{|J = N - S, M\rangle\}. \tag{6.2.31}$$

The notation for vector $\vec{J}$ in the coupled basis is $|S, N, J, M\rangle\,.$

To deal with component quantum numbers in both space-fixed and body-fixed frames, we substitute

(6.2.7) into the matrix element,

$$\begin{aligned}\langle\eta|\mu_p|\eta'\rangle &= \sum_q \langle\eta|\mathfrak{D}^{(1)}_{pq}(\omega_E)^*\mu_q|\eta'\rangle \\ &= \sum_q \langle\Lambda,S,N,J,M|\mathfrak{D}^{(1)}_{pq}(\omega_E)^*|\Lambda',S',N',J',M'\rangle\,\langle\xi',\Lambda';v'|\mu_q|\xi',\Lambda';v'\rangle\,. \end{aligned} \tag{6.2.32}$$

In the body-fixed frame, Λ by definition is the projection of $\vec{L}$ on the internuclear axis, and it is equal to the projection of $\vec{N}$ on the internuclear axis. Λ in the first braket corresponds to the projection of N along the internuclear axis, as it is a part of the symmetric top wavefunction for this case, $|N,\Lambda,M\rangle$, that is acted on by the Wigner rotation matrix $\mathfrak{D}^{(1)}(\omega_E)^*$.

In the first matrix element, the pq^{th} component of a Wigner rotation matrix only acts on the part of the basis wavefunction with angular dependence; it can be reduced and become independent of the orientation in the space-fixed frame by applying the Wigner-Eckart theorem,

$$\begin{aligned}&\langle\Lambda,S,N,J,M|\mathfrak{D}^{(1)}_{pq}(\omega_E)^*|\Lambda',S',N',J',M'\rangle \\ &= (-1)^{J-M}\begin{pmatrix} J & k=1 & J'' \\ -M & p & M'' \end{pmatrix}\langle\Lambda,S,N,J||\mathfrak{D}^{(1)}_{.q}(\omega_E)^*||\Lambda',S',N',J'\rangle\,. \end{aligned} \tag{6.2.33}$$

In the remaining reduced matrix element on the right-hand side, the electron spin can be decoupled from J,

$$\begin{aligned}&\langle\Lambda,S,N,J||\mathfrak{D}^{(1)}_{.q}(\omega_E)^*||\Lambda',S',N',J'\rangle \\ &= (-1)^{S+J'+1}\,\langle\Lambda,N||\mathfrak{D}^{(1)}_{.q}(\omega_E)^*||\Lambda',N'\rangle\,\sqrt{(2J+1)(2J'+1)}\begin{Bmatrix} N & J & S \\ J' & N' & k=1 \end{Bmatrix}\delta_{SS'}. \end{aligned} \tag{6.2.34}$$

It can then be fully reduced to combinatorial factors, provided a property of the case (b) symmetric top wavefunction,

$$\langle\Lambda,N||\mathfrak{D}^{(1)}_{.q}(\omega_E)^*||\Lambda',N'\rangle = (-1)^{N-\Lambda}\sqrt{(2N+1)(2N'+1)}\begin{pmatrix} N & 1 & N' \\ -\Lambda & q & \Lambda' \end{pmatrix}. \tag{6.2.35}$$

This shows that the first matrix element in (6.2.32) is only nonzero when $q = -\Lambda' + \Lambda$, thereby simplifying terms in the sum over q.

In the second braket appeared in the sum of (6.2.32), μ_q only acts on the quantum numbers relevant in the body-fixed frame, so the sum can be further simplified invoking the orthonormality of basis wavefunctions.

Similar to (6.2.12), a rotational branching ratio between case (b) levels with different rotational levels within the same electronic and vibrational transition can be found by summing over all decay channels,

$$\begin{aligned} BR(N) &= \sum_{p,M,J,S} |\left\langle \Lambda, S, N, J, M|\mathfrak{D}^{(1)}_{pq}(\omega_E)^*|\Lambda', S', N', J', M'\right\rangle|^2 \\ &= (2N+1)\begin{pmatrix} N & k=1 & N' \\ -\Lambda & \Lambda-\Lambda' & \Lambda' \end{pmatrix}^2 . \end{aligned} \tag{6.2.36}$$

The resulting rotational branching ratios for the $B^2\Sigma^+ - X^2\Sigma^+$ transition are given in Table A.11.

In considering the transition labelled by $\{\xi, \Lambda\}$ and $\{\xi', \Lambda'\}$, to account for all allowed dipole transitions, the transition linewidth should not depend on the polarization of the photon emitted, parametrization in the space-fixed and body-fixed frames, as well as finer energy structures such as vibrational and rotational structures. To remove the dependence, we can sum over all possible photon polarizations, orientations of both space-fixed and body-fixed axes and quantum numbers corresponding to finer structures,

$$\begin{aligned} \sum_{v,S,N,\Lambda,J,p,M} |\left\langle \eta|\mu_p|\eta'\right\rangle|^2 &= \sum_{N,\Lambda} |\left\langle \xi, \Lambda|\mu_{\Lambda-\Lambda'}|\xi', \Lambda'\right\rangle|^2 (2N+1)\begin{pmatrix} N & k=1 & N' \\ -\Lambda & \Lambda-\Lambda' & \Lambda' \end{pmatrix}^2 \\ &= |\left\langle \xi, \Lambda|\mu_{\Lambda-\Lambda'}|\xi', \Lambda'\right\rangle|^2. \end{aligned} \tag{6.2.37}$$

As already mentioned earlier, Λ is equal to the projection of $\vec{N}$ on the internuclear axis. Hence the sum over Λ accounts for all possible orientations of the body-fixed frame. The sum, after simplification, only depends on the electron orbital configurations of the ground and excited state. The relation between linewidth, frequency, and the reduced matrix element is essentially the same as (6.2.21) from the previous subsection,

$$|\left\langle \xi, \Lambda|\mu_{\Lambda-\Lambda'}|\xi', \Lambda'\right\rangle|^2 = f(\Gamma, \omega_0). \tag{6.2.38}$$

To account for the effect of hyperfine structure on dipole transitions, suppose we use the coupled basis,

$$|\eta\rangle = |\xi, \Lambda; v; S, N, J, I, F, M\rangle . \tag{6.2.39}$$

Following similar steps outlined in §6.2.1, we obtain an expression for the dipole matrix element in its factored form (A.3.4). Without the hyperfine structure, the dipole matrix elements in the Hund's case (b) basis are given by (A.3.3).

6.2.3 Parity of basis functions and parity eigenstate

Under parity/space-fixed inversion P,

$$P : \mu^p \hat{e}^p \to -\mu^p \hat{e}^p, \quad (p \in \{x, y, z\}) \tag{6.2.40}$$

so the dipole transition can only occur between states with opposite parity, and parity selection should constrain the matrix element calculation; in hindsight, the space-fixed inversion symmetry should manifest. Apparently, neither the case (a) nor the case (b) basis function is an eigenstate of the space-fixed inversion operator due to component quantum numbers in the molecule-fixed frame and symmetric top wavefunctions being part of the basis functions, more specifically,

$$P\,|J, \Omega, M; \xi, \Lambda; v; S, \Sigma\rangle \overset{(6.231)}{=} (-1)^{J-S}\,|J, -\Omega, M; \xi, -\Lambda; v; S, -\Sigma\rangle\,, \tag{6.2.41}$$

$$\text{and } P\,|J, M, S, N; \xi, \Lambda; v\rangle \overset{(6.233)}{=} (-1)^{N}\,|J, M, S, N; \xi, -\Lambda; v\rangle\,. \tag{6.2.42}$$

For Hund's case (a), a parity eigenstate can be written as a superposition of case (a) basis functions, according to (6.234),

$$\begin{aligned} &|J^{\pm}, M; \xi, |\Lambda|; v; S, |\Sigma|\rangle \\ &= \frac{1}{\sqrt{2}}\,|J, \Omega, M; \xi, \Lambda; v; S, \Sigma\rangle \pm (-1)^{J-S}\frac{1}{\sqrt{2}}\,|J, -\Omega, M; \xi, -\Lambda; v; S, -\Sigma\rangle\,; \end{aligned} \tag{6.2.43}$$

similarly, for case (b), it follows from (6.233) that

$$|J, M, S, N^{\pm}; \xi, |\Lambda|; v\rangle = \frac{1}{\sqrt{2}}\,|J, M, S, N; \xi, \Lambda; v\rangle \pm (-1)^{N}\frac{1}{\sqrt{2}}\,|J, M, S, N; \xi, -\Lambda; v\rangle\,. \tag{6.2.44}$$

Given these parity combinations of basis function, naturally, a brute-force method would work; it entails calculating four matrix elements that arise from the parity combinations and making use of results derived previously. And yet we also recall, irrelevant to the choice of wavefunctions, how a component of

the dipole operator transforms under space-fixed inversion,

$$P^\dagger \mu_p P = -\mu_p. \tag{6.2.45}$$

Insofar as dipole matrix elements for SrF are concerned, provided (6.2.41) and suppose $|J, \Omega, M\rangle$ is a shorthand for the case (a) basis function, it follows that

$$\begin{aligned}\langle J, \Omega, M|\mu_p|J', \Omega', M'\rangle &= -\langle J, \Omega, M|P^\dagger \mu_p P|J', \Omega', M'\rangle \\ &= -(-1)^{J'-S'+J-S} \langle J, -\Omega, M|\mu_p|J', -\Omega', M'\rangle ,\end{aligned} \tag{6.2.46}$$

and

$$\begin{aligned}&\langle J, \Omega, M|\mu_p P|J', \Omega', M'\rangle = -\langle J, \Omega, M|P^\dagger \mu_p|J', \Omega', M'\rangle \\ \Rightarrow\ &(-1)^{J'-S'} \langle J, \Omega, M|\mu_p|J', -\Omega', M'\rangle = -(-1)^{J-S} \langle J, -\Omega, M|\mu_p|J', \Omega', M'\rangle .\end{aligned} \tag{6.2.47}$$

Suppose $S = S' = 1/2$ (as in the case of SrF), the possible values for J and J' are $\{\frac{4k+1}{2}, \frac{4k+3}{2}\}_{k=0,1,\ldots}$. When $J, J' \in \{\frac{4k+1}{2}\}$ or $J, J' \in \{\frac{4k+3}{2}\}$, $(-1)^{J-S} = (-1)^{J'-S'}$; otherwise, $(-1)^{J-S} = -(-1)^{J'-S'}$.

Similar results hold for dipole matrix elements between Hund's case (a) states and between different case (a) and (b) states since this is argued based on the operators.

The matrix elements between parity eigenstates can then be simplified, for example, between case (a) parity eigenstates with opposite parity,

$$\begin{aligned}&\langle J^+, M|\mu_p|J'^-, M'\rangle \\ &= \frac{1}{2}\langle J, \Omega, M|\mu_p|J', \Omega', M'\rangle - (-1)^{J+J'-1}\frac{1}{2}\langle J, -\Omega, M|\mu_p|J', -\Omega', M'\rangle \\ &+ (-1)^{J-S}\frac{1}{2}\langle J, -\Omega, M|\mu_p|J', \Omega', M'\rangle - (-1)^{J'-S'}\frac{1}{2}\langle J, \Omega, M|\mu_p|J', -\Omega', M'\rangle \\ &= \langle J, \Omega, M|\mu_p|J', \Omega', M'\rangle + (-1)^{J-S}\langle J, -\Omega, M|\mu_p|J', \Omega', M'\rangle .\end{aligned} \tag{6.2.48}$$

Similarly, it is easy to show that the matrix element between states with the same parity is zero. In the context of spontaneous decay, $|J', \Omega', M'\rangle$ contains equal compositions of $|J'^-, M'\rangle$ and $|J'^+, M'\rangle$. (6.2.48) confirms that $\langle J^+, M|\mu_p|J'^-, M'\rangle$ account for half of the decay events from $|J', \Omega', M'\rangle$. In another example,

the dipole matrix element between case (a) and case (b) parity eigenstates can be simplified

$$\begin{aligned}
&\langle N^+, J, M|\mu_p|J'^-, M'\rangle \\
&= \frac{1}{2}\langle N, J, M, \Lambda|\mu_p|J', M', \Omega\rangle - (-1)^{J'-S'+N}\frac{1}{2}\langle N, J, M, -\Lambda|\mu_p|J', M', -\Omega\rangle \\
&- (-1)^{J'-S'}\frac{1}{2}\langle N, J, M, \Lambda|\mu_p|J', M', -\Omega\rangle + (-1)^N\frac{1}{2}\langle N, J, M, -\Lambda|\mu_p|J', M', \Omega\rangle \\
&= \langle N, J, M, \Lambda|\mu_p|J', M', \Omega\rangle + (-1)^N\langle N, J, M, -\Lambda|\mu_p|J', M', \Omega\rangle\,. \qquad (6.2.49)
\end{aligned}$$

To evaluate a matrix elements between case (a) and case (b) states, changing basis is necessary. With (23a) of Ref.[83] or (29) of Ref.[84]*,

$$|\xi, \Lambda; N, S, J\rangle = \sum_{\Sigma,\Omega}(-1)^{J+\Omega}\sqrt{2N+1}\begin{pmatrix} J & S & N \\ -\Omega & \Sigma & \Lambda \end{pmatrix}|\xi, \Lambda; S, \Sigma; J, \Omega\rangle\,, \qquad (6.2.50)$$

we can write the final state in the case (a) basis,

$$\begin{aligned}
&\langle \xi', \Lambda'; v'; S', \Sigma'; J', \Omega', M'|\mu_p|\xi, \Lambda; v; S, N, J, M\rangle = \sum_{\Sigma,\Omega}(-1)^{J+\Omega}\sqrt{2N+1} \\
&\times\begin{pmatrix} J & S & N \\ -\Omega & \Sigma & \Lambda \end{pmatrix}\langle \xi', \Lambda'; v'; S', \Sigma'; J', \Omega', M'|\mu_p|\xi, \Lambda; v; S, \Sigma; J, \Omega, M\rangle\,, \qquad (6.2.51)
\end{aligned}$$

and then make use of expressions derived in §6.2.1. Note that the case (a) (case (b)) basis is nothing but a uncoupled (coupled) basis in the body-fixed frame for three angular momenta, $\vec{N} = \vec{J} + (-\vec{S})$. This process of changing basis is seemly intricate, but ultimately it deals with a familiar problem—finding equivalent representations between two Hilbert spaces with superpositions and coefficients

$$\{|J, \Omega\rangle\} \otimes \{|S, \Sigma\rangle\} = \{|N = \max(0, J-S), \Lambda\rangle\} \oplus \cdots \{|N = J+S, \Lambda\rangle\}.$$

As far as the rotational branching ratio is concerned (Table A.7 and A.9), the branching ratios between case (a) and case (b) states can be determined from rotational branching ratios between case (a) states (6.2.15) (or case (b) states (6.2.36)), in conjunction with simple arguments based on the triangle inequality, $\max(0, J-S) \le N \le J+S$, and parity. The rotational branching ratio and transition strength for different

*There is an error in (6.149) of Ref. [80].

cases produce consistent physical results

In conclusion, insofar as the calculation of dipole matrix elements is concerned, the lack of caution has no consequences beyond notation thanks to this formalism.

6.2.4 The effect of hyperfine mixing of J states

When the nuclear spin I is neglected, J commutes with the Hamiltonian that includes a spin-rotation coupling term $\gamma\vec{S}\cdot\vec{N}$. In §6.2.1 and §6.2.2, when the nuclear spin is dealt with by adding the grand total angular momentum F into either basis, the nuclear spin coupling is neglected such that J and the new Hamiltonian with nuclear spin included are still simultaneously diagonalizable. However, the nuclear spin couples to the electron spin S via $b\vec{I}\cdot\vec{S}$. In this picture, F and N are preferred over J because F commutes with the full Hamiltonian and rotational motion quantified by N makes a larger contribution to the state energy. Furthermore, because $S = I = 1/2$, when $F = N$, J can take two values. The J-mixing ratios can be obtained by diagonalizing $b\vec{I}\cdot\vec{S}$ in the J-state basis $\{|X,\Lambda;v;S,I,M_F,N,F,J\rangle\}$. The coupling strength constants, b and γ, depend on the electronic state, vibrational and rotational quantum numbers; for the electronic and vibrational ground state of SrF, the J-mixing ratios have been worked out [27, 85],

$$|N^P = 1^-, F = 1, +\rangle = 0.8880\,|1^-, F, J = 3/2\rangle + 0.4598\,|1^-, F, J = 1/2\rangle \tag{6.2.52a}$$

$$|N^P = 2^+, F = 2, +\rangle = 0.9569\,|2^+, F, J = 5/2\rangle + 0.2903\,|2^+, F, J = 3/2\rangle \tag{6.2.52b}$$

$$|N^P = 3^-, F = 3, +\rangle = 0.9776\,|3^-, F, J = 7/2\rangle + 0.2107\,|3^-, F, J = 5/2\rangle \tag{6.2.52c}$$

$$|N^P = 4^+, F = 4, +\rangle = 0.9908\,|4^+, F, J = 9/2\rangle + 0.1354\,|4^+, F, J = 7/2\rangle\,. \tag{6.2.52d}$$

Here $|N^P, F, +\rangle$ has a larger expected value of J compared to its orthogonal complement $|N^P, F, -\rangle$ with the same constituents $|N^P, F, J\rangle$; $\pm$ superscript for N denotes the state's parity. Other quantum numbers are not included in the kets since they are the same for kets on both sides of the equations $|X, \Lambda = 0; v = 0; S, I, M_F\rangle$.

When the dipole matrix element involved a ground state with $F = N$, J-mixing should be taken into account for accuracy. For example, the matrix elements for energy levels with $F = N = 1$ (in the shorthand notation) are given by

$$\langle N, F, +|\mu_p|\eta'\rangle = 0.888\,\langle N, F, J = \frac{3}{2}|\mu_p|\eta'\rangle + 0.4598\,\langle N, F, J = \frac{1}{2}|\mu_p|\eta'\rangle\,, \tag{6.2.53}$$

$$\langle N, F, -|\mu_p|\eta'\rangle = -0.4598\,\langle N, F, J = \frac{3}{2}|\mu_p|\eta'\rangle + 0.8880\,\langle N, F, J = \frac{1}{2}|\mu_p|\eta'\rangle\,, \tag{6.2.54}$$

with $|\eta'\rangle$ denoting the excited state in a basis.

In summary, J-mixing arises from a spin coupling mechanism that is not accounted for in the basic Hund's coupling cases (a and b). However, as it directly affects the ground state whose light shift we aim to calculate, this complexity cannot be avoided. It can be dealt with by creating superpositions of Hund's case basis

6.2.5 Atomic case

In the case of atoms such as rubidium, the coupling scheme of angular momentum is given by

$$\vec{F} = \vec{I} + \vec{J}, \quad \vec{J} = \vec{L} + \vec{S}; \tag{6.2.55}$$

$\vec{F}$ is the total angular momentum, $\vec{J}$ is the total angular momentum excluding the nuclear spin I, and $\vec{L}$ the orbital angular momentum. Suppose we use a couple basis

$$|\eta\rangle = |L, S, I, J, F, m\rangle \tag{6.2.56}$$

It follows from the steps outlined in the previous subsections that the norm square of the dipole matrix element is given by

$$|\langle \eta|\mu_p|\eta'\rangle|^2 = \text{reduced matrix element}^2 \times \text{ transition strength}$$

- reduced matrix element*:

$$\langle L, S, J||\mu||L', S', J'\rangle \tag{6.2.57}$$

- transition strength:

$$(2F+1)(2F'+1)\begin{Bmatrix} J & F & I \\ F' & J' & k=1 \end{Bmatrix}^2 \begin{pmatrix} F & k=1 & F' \\ -m & p & m' \end{pmatrix}^2 \delta_{II'}. \tag{6.2.58}$$

*Although the reduced matrix element can be further reduced to be independent of J and J', given the large energy splitting due to fine structure, e.g. 238 cm^{-1} separation between the D_1 and D_2 lines in ^{87}Rb, they are treated separately.

When the ground state quantum numbers and photon polarizations are summed over, using the orthogonality relations of Wigner $3J$ and $6J$ symbols, the sum takes a very simple form,

$$\sum_F \sum_{S,I,m,p} |\langle F, m, J, I, S, L|\mu_p|F, m', J', I', S', L'\rangle|^2 = \frac{1}{2J'+1}|\langle L, S, J||\mu||L', S', J'\rangle|^2. \tag{6.2.59}$$

In relation to the linewidth and frequency, Γ and ω_0, of the D_i transition ($i = 1, 2$), where D_i is the short-hand notation for the transition labelled by quantum number L and J in the ground and excited states,

$$\Gamma = \frac{\omega_0^3}{3\pi\epsilon_0\hbar c^3}\frac{|\langle L, S, J||\mu||L', S', J'\rangle|^2}{2J'+1}, \tag{6.2.60}$$

$$\Rightarrow |\langle L, S, J||\mu||L', S', J'\rangle|^2 = (2J'+1)f(\Gamma, \omega_0). \tag{6.2.61}$$

6.2.6 Symmetry and quantum number

Calculating the dipole matrix element requires only some knowledge of the angular momentum theory, and does not involve the molecular Hamiltonian directly. However, quantum numbers in a braket such as $|F, m_F, J, I, L, S\rangle$ in the atomic case are physical observables necessary to uniquely specify the system.
In order to choose good quantum numbers, the knowledge of the Hamiltonian and spectroscopy is imperative. In fact, Hund's coupling cases are invented to deal with various coupling schemes of angular momentum in molecules. My working knowledge of Hund's cases is most relevant to the states involved in laser cooling of SrF. Hund's case (b) applies to $X^2\Sigma^+$ and $B^2\Sigma^+$, and Hund's case (a) to $A^2\Pi_{|\Omega|}$.

How to get by with limited knowledge of spectroscopy? Here the goal is to justify the choice of quantum numbers necessary to form a complete basis, $\{\eta\}$, based on symmetry as well as the lack of symmetry in diatomic molecules. Having a symmetry, by Noether's theorem, implies a trivial commutation relation between the Hamiltonian and certain physical observables. Such observables constitute the complete set of commuting observables (CSCO). On the other hand, the lack of certain symmetry implies a nontrivial commutation relation. When breaking a symmetry lifts certain degeneracy, it gives rise to energy splitting in spectroscopy, and as far as the following discussion is concerned, it creates the need for new quantum numbers that distinguish different configurations. Good quantum numbers usually refer to the ones that break the rotational symmetry most effectively by coupling with others, especially with conserved quantities in CSCO, such as the electron and nuclear spins. They lead to large scale energy structures, and hence are useful in dealing with patterns in spectroscopy data.

Although SrF as a diatomic molecule has two constituent atoms, under the Born-Oppenheimer approximation, the nuclear and electronic motions are separated. The Schrödinger equation of its electron

can be solved using separation of variables, similar to the atomic case. The solution can be factored into functions with only radial or angular dependence. Therefore it is natural to start with the set of quantum numbers for an atomic system, as it reflects the rotational symmetry in the presence of other conserved angular momenta—the electron spin S and the nuclear spin I,

$$\{\xi, F, J, M, S, I, N, R, L\}. \tag{6.2.62}$$

Apart from ξ the label for an electronic state, the other quantum numbers are angular momenta introduced to deal with coupling of angular momentum such as $\vec{J} \cdot \vec{S}$; their relations are defined in (6.2.3).

Given the definitions, (6.2.62) is not the unique set of quantum numbers necessary to specify the system. The projection of at least one angular momentum should be included in $\{\eta\}$. In (6.2.62), M is a projection of J (or F or N) in the space-fixed frame.

Although the atomic basis is a starting point, there are key distinctions between atoms and diatomic molecules. From the perspective of symmetries, having an internuclear axis implies that the molecular Hamiltonian does not commute with arbitrary rotation. This axis is defined by $\vec{R}$; given the cylindrical symmetry in diatomic molecules, $\vec{R}$ is sufficient to define the plane that is uniquely defined by the internuclear axis. However, the more common approach is to define the projection of quantum numbers with respect to the internuclear axis,

$$\{\Lambda, \Sigma, \Omega\}, \tag{6.2.63}$$

as in Hund's case bases (6.2.4) and (6.2.30).

In addition to rotating in the plane defined by the internuclear axis, the vibrational motion of nuclei along the internuclear axis should also be considered, because it is a perturbation to the trapping potential the electron is situated in. Therefore, a vibrational quantum number, v, is necessary to specify the wavefunction. Since this can be considered as a perturbation to the Coulomb potential, this quantum number is only relevant to the radial solution of the Schrödinger equation. Vibration is independent of rotation and thus does not have any angular dependence.

To close, I should acknowledge that all this has been said over and over. I am limiting myself to making a rapid revelation and to pointing out these obvious themes that are particularly useful in asserting intuition when faced with the field of spectroscopy and their classifications.

6.2.7 Vector and rotating frame

An angular momentum vector $\vec{J}$ is often parametrized by the subtended angle between $\vec{J}$ and an arbitrary axis; conventionally, the angle between $\vec{J}$ and the z-axis in the space-fixed frame is denoted as θ_p, and its component quantum number along this axis is given by

$$M = J\cos\theta_p, \tag{6.2.64}$$

with J being the length of the vector (L-2 norm in an Euclidean space), and θ_p defined in the range of $[0, \pi]$.

Though parametrization is instrumental in describing, and thus probing a vector quantity such as angular momentum, as a physical quantity, angular momentum should be independent of this arbitrary parametrization despite how natural and convenient it is. Another way to see the component quantum number M in the notation for an angular momentum eigenfunction $|J, M\rangle$ is that it encodes information about this parametrization. Given M, we can infer the relative orientation between the angular momentum vector and the space-fixed frame,

$$\theta_p = \arccos\frac{M}{J}. \tag{6.2.65}$$

It is clear that only one polar angle is encoded in this notation, which is sufficient when provided spherical symmetry. However, diatomic molecules do not possess spherical symmetry because of the internuclear axis, and the orientation of the body-fixed frame, whose z-axis is defined (up to a sign) by the internuclear axis, is unknown to experimenters in the lab frame in the absence of external fields.

How to encode the orientations of the second frame into a wavefunction? An intuitive solution is to add at least one component quantum number defined in the body-fixed frame, or more specifically with respect to the internuclear axis, such as Ω and Λ. In the formalism of spherical tensor algebra in conjunction with the Dirac representation, this is dealt with by introducing normalized symmetric top wavefunctions and Wigner rotation matrices. In the Hund's case (a) basis, the symmetric top wavefunction is given by

$$|J, \Omega, M\rangle \overset{(5.145)}{=} \sqrt{\frac{(2J+1)}{8\pi^2}}\mathfrak{D}^{(J)}_{M\Omega}(\omega_E)^*; \tag{6.2.66}$$

similarly, in Hund's case (b),

$$|N, \Lambda, M\rangle \overset{(5.181)}{=} \sqrt{\frac{(2N+1)}{8\pi^2}}\mathfrak{D}^{(N)}_{M\Lambda}(\omega_E)^*. \tag{6.2.67}$$

In (6.2.66) and (6.2.67), ω_E is a shorthand for angles (ϕ, θ, χ) in a series of rotations that generates the

body-fixed axes starting with the space-fixed axes*. The Wigner rotation matrices $D^{(J)}_{M\Omega}(\omega_E)$ and $\mathfrak{D}^{(N)}_{M\Lambda}(\omega_E)$ come from applying the finite rotation operator to the eigenfunction an angular momentum operator,

$$R(\omega_E)\,|j,m\rangle \overset{(5.44)}{=} \sum_{m'} |j,m'\rangle\, \mathfrak{D}^{(j)}_{m'm}(\omega_E). \tag{6.2.68}$$

$R(\omega_E) = R(\phi,\theta,\chi)$ rotates an angular momentum eigenstate by the Euler angles in the argument. As far as orthogonality is concerned,

$$\int d\omega_E \mathfrak{D}^{(J)}_{M\Omega}(\omega_E)^* \mathfrak{D}^{(J')}_{M'\Omega'}(\omega_E) \overset{(5.99)}{=} \frac{8\pi^2}{2J+1}\delta_{JJ'}\delta_{MM'}\delta_{\Omega\Omega'}, \tag{6.2.69}$$

where $d\omega_E = d\theta \sin\theta d\phi d\chi$ and $\int d\omega_E = 8\pi^2$. With this normalization convention, the eigenfucntions of angular momentum as well as basis functions of Hund's case (a) and (b) are normalized, and the rotation operator is unitary.

How to know the orientation of the internuclear axis? Fortunately, the orientation of the body-fixed frame has direct impacts on the energy structure, and the energy spectrum is often labeled by good component quantum numbers defined in the body-fixed frame, such as Ω and Λ; thereby the orientation of the internuclear axis can be inferred from state energy. For Hund's case (a) and (b), because either basis includes at least one projection on the internuclear axis and one on the space-fixed frame.

To highlight the convenience of this notation in the context of spontaneous decay, it allows for an easy generalization from the atomic case with spherical symmetry to the diatomic case. In relating dipole matrix elements to the transition linewidth, in the atomic case, (6.2.59), the sum over p accounts for allowed dipole transitions for any polarizations, and the sums over other ground state quantum numbers effectively collapse all finer energy structures and allows us to apply the equation derived for a two-level system in which lifetime/linewidth only depends on the radial wavefunctions of the initial and final state. Without any external fields, the sum over m would seem unnecessary because the magnetic sublevels are already degenerate. The sum over m is equivalent to a sum over θ_p (6.2.65) that accounts for different ways to parameterize $\vec{F}$ as a result of having different orientations of the space-fixed frame. In the diatomic case, for Hund's case (a) in (6.2.20), the sum over Ω effectively is a sum over the angle between $\vec{J}$ and the internuclear

*Suppose, in a space-fixed frame, ϕ and θ are spherical polar angles used to describe the orientation of the internuclear axis (z-axis in the body-fixed frame), and χ is the angle between the space-fixed z-axis and the body-fixed axis. Starting in the space-fixed frame, the body-fixed frame can be generated by three rotations in the following order:

1. a rotation through χ about the space-fixed z-axis
2. a rotation through θ about the space-fixed y-axis
3. a rotation through ϕ about the space-fixed z-axis

axis,

$$\theta_{q,a} = \arccos \frac{\Omega}{J}. \tag{6.2.70}$$

For Hund's case (b) in (6.2.37), orientations of the body-fixed frame can be accounted by summing over the angle defined by $\vec{N}$ and the internuclear axis,

$$\theta_{q,b} = \arccos \frac{\Lambda}{N}. \tag{6.2.71}$$

6.3 Far-detuned dipole traps with linearly polarized light

Recall that (6.1.8) gives the general expression for energy shifts due to far-detuned light; in this section, the discussion is limited to far-detuned light with linear polarization,

$$E_\eta^{(2)} = \sum_{\eta'} \frac{|\langle \eta' | \mu_0 | \eta \rangle|^2 |\mathcal{E}|^2}{\Delta_{\eta\eta'}}. \tag{6.3.1}$$

When applying this formula to estimate trap depths, spectroscopic information about optical transitions and parameters of the trap laser are necessary in addition to the expressions for $|\langle \eta' | \mu_p | \eta \rangle|^2$ (Appendix A.3). Latest spectroscopy data for SrF are reproduced in Table A.3, from which a comparison of energy scales can be established:

$$\begin{aligned} &\text{electronic energy } (T_e) \gg \text{vibrational energy } (\omega_e, \omega_e\chi_e) \gg \text{rotational energy } (B_e) \\ &\gg \text{spin-rotation coupling } (\gamma) \approx \text{nuclear spin coupling } (b). \end{aligned} \tag{6.3.2}$$

The energy level structure of SrF is well-known and yet complex, implying that including all the excited states $\{\eta'\}$ and accounting for energy structures to the finest scale in detunings ($\Delta_{\eta\eta'}$) is feasible but laborious.

Then two cases with practical relevance are discussed: in §6.3.1, the detuning is large compared to all energy structures; in §6.3.2, trap laser's detuning is large compared to the spin-rotational and hyperfine structures but comparable to the rotational splitting. In either case, we choose a laser intensity such that a trap depth around 1 mK is attained, which is much greater than typical ensemble temperatures after sub-Doppler cooling.

6.3.1 Very far detuned dipole traps

We consider the case where a trap laser (1064 nm) is very far detuned from all electronic transitions. Only three low-lying electronic excited states are included in the sum (6.3.1), and detunings are only distinguished between different electronic transitions ($\Delta_{\eta\eta'} = \Delta_{\xi\xi'}$)*,

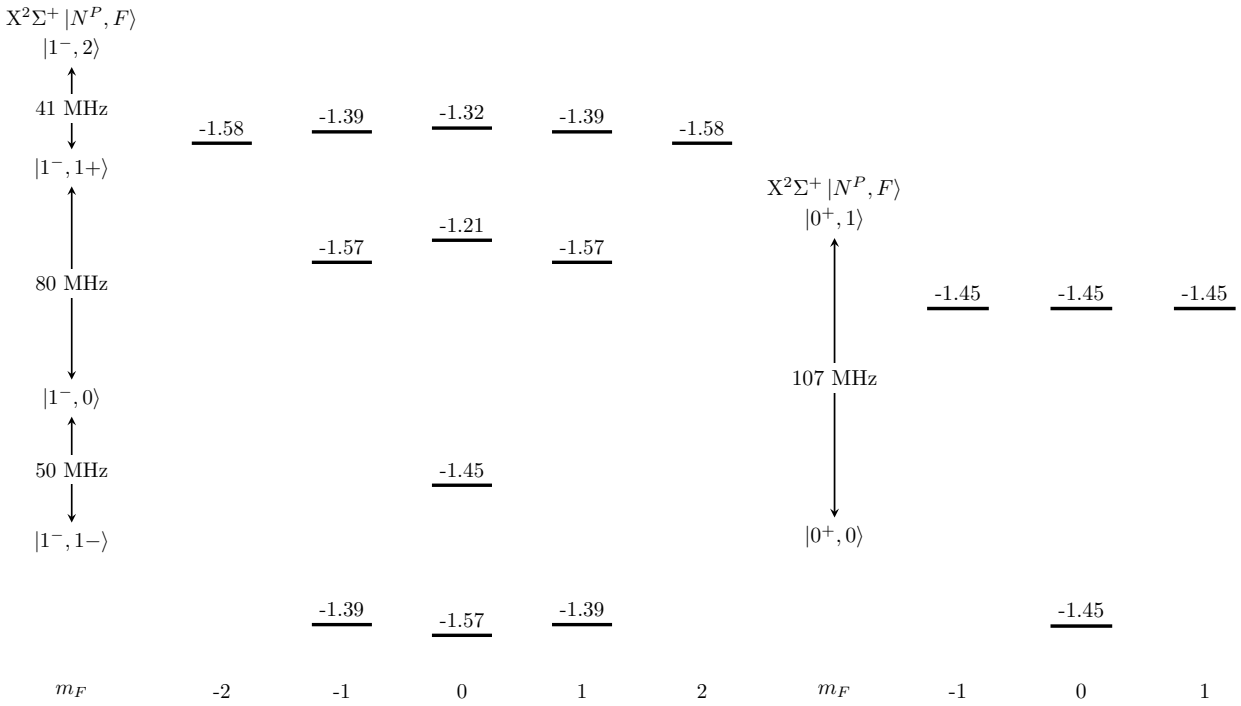
$$E_\eta^{(2)} \approx \sum_{\xi',\Lambda'} \frac{|\mathcal{E}|^2}{\Delta_{\xi\xi'}} \sum_{\substack{v', S', N' \\ I', F', M'}} |\langle \xi', \Lambda'; v'; S', N', J', I', F', M' | \mu_p | \xi, \Lambda; v; S, N, J, I, F, M \rangle|^2, \tag{6.3.3}$$

$$\text{where} \quad \{\xi', \Lambda'\} = \{A^2\Pi_{1/2}, A^2\Pi_{3/2}, B^2\Sigma^+\}.$$

Detunings with respect to transitions between $X^2\Sigma^+(v = 0)$ and the vibrational ground state of different electronic excited states†, calculated based on spectroscopy data in Table A.3 are as follows:

$\{\xi'\} - \{\xi\}$	$\Delta_{\xi\xi'}/(2\pi)$
$A^2\Pi_{1/2} - X^2\Sigma^+$	-169.98 THz
$A^2\Pi_{3/2} - X^2\Sigma^+$	-178.39 THz
$B^2\Sigma^+ - X^2\Sigma^+$	-235.90 THz

1064 nm is detuned to the next electronic transition $C^2\Pi_{1/2} - X^2\Sigma^+$ by -539.192 THz, roughly twice compared to the $B^2\Sigma^+ - X^2\Sigma^+$ detuning, so light shifts due to higher electronic states are neglected. The energy shifts due to vibrational, rotational and hyperfine structures are neglected. To justify this simplification, let us consider the vibrational constant which creates the largest energy splitting within each electronic level. For the A state, the vibrational constant $\omega_e \approx 15$ THz, is small compared to the detuning, $\frac{\omega_e}{178\ \text{THz}} \approx 0.09$. Other spectroscopy constants (6.3.2) are only smaller, and $X^2\Sigma^+(N = 1)$ mostly and most strongly couples to the lowest energy levels in those electronic bands because the $N = 1$ rotational level consists of states with small angular momentum $J \leq 3/2$.



(a) $X^2\Sigma^+(N=1,F,M)$ **(b)** $X^2\Sigma^+(N=0,F,M)$

Figure 6.1: Trap depths [mK] due to 100 W trap light at 1064 nm with linear polarization and a $1/e^2$ radius of 30 μm. The spacings reflect energy shifts due to fine/hyperfine structure and trap light. The position of each state label reflects its energy level unperturbed by trap light. Both hyperfine structure and J-mixing of the ground state due to the nuclear spin are included in the calculation.

Trap depth estimates

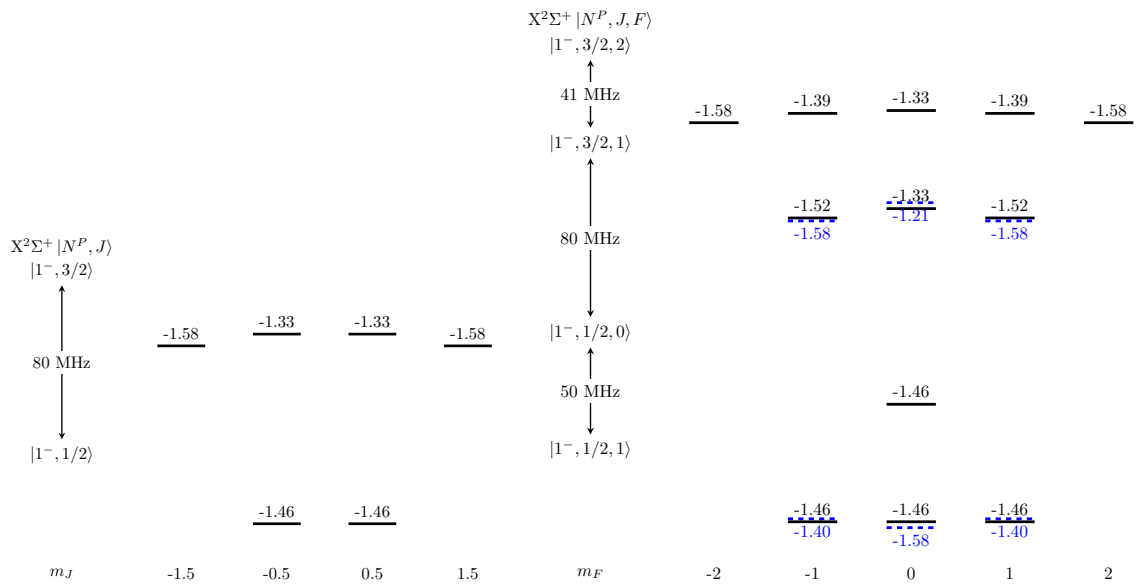
Assuming the trap laser supplies 100 W in a single mode at 1064 nm with linear polarization and a $1/e^2$ radius of 30 μm at the beam waist, the estimated trap depth for each hyperfine magnetic level and J-mixing included of $X^2\Sigma^+(N=1,F,M)$ and $X^2\Sigma^+(N=0,F,M)$ are shown in Figure 6.1a and Figure 6.1b. The trap depth is uniform for all magnetic levels in $X^2\Sigma^+(N=0)$; by contrast, the trap depth has a quadratic dependence on M in $X^2\Sigma^+(N=1)$. The differential energy shift between magnetic sublevels is as large as 30% ($F=1+$).

Trap depths for different eigenstate composition

To illustrate how the use of different eigenstate composition affects the trap depths for the very far detuned linearly polarized case, Figure 6.2a and 6.2b gives trap depths for spin-rotation levels and for hyperfine

*Although both ξ and Λ are used to label an electronic state, $\xi\xi'$ is a unique label for any electronic transition in SrF, since $\xi \mapsto \Lambda$ is injective.

†Excited or ground states in this subsection have vibrational number $v' = v = 0$ unless specified otherwise. In shorthand notation with term symbol, e.g. $X^2\Sigma^+|N,F,M_F\rangle$, the vibrational number, as well as conserved spin quantum numbers (S and I), are left out.



(a) $X^2\Sigma^+(N=1,J,I=0,M)$ **(b)** $X^2\Sigma^+(N=1,J,F,M)$

Figure 6.2: Trap depths [mK] due to 100 W trap light at 1064 nm with linear polarization and a $1/e^2$ radius of 30 μm estimated with different basis functions. (a) shows estimates for the fictitious case where there is no hyperfine structure in the X state. (b) shows the effect of J-mixing when the hyperfine structure is accounted for. Black and blue lines mark the energy shifts due to far-detuned light before and after adding J-mixing.

levels without and with J-mixing. Within both hyperfine subspaces of $\{|F=1+,M\rangle\}$ and $\{|F=1-,M\rangle\}$, J-mixing increases the differential shifts between magnetic levels.

Naturally, including J-mixing or not changes both energy and the dipole matrix elements that enter the expression (6.3.3) for the light shift; it effectively changes the internal state Hamiltonian that accounts for the energy structures without the far-detuned field. In this case, where trap laser detuning is about 10^6 times larger than the spin-rotational structure, the contribution due to differences in energy structures should be minimal. Regardless of the angular momentum composition, the quadratic dependence in M is present for states with a constituent angular momentum of $J > 1/2$, and the differential shift is significant ($\approx$14%). This marks a qualitative difference compared to the alkaline case where the ground state orbital angular momentum is L =0, less than any excited states it can interact with. In the case of SrF, L, the electron orbital around the center of mass is not conserved/well-defined in the electronic states, but its projection on the internuclear axis is. So the angular momentum of the bare nucleus, highly correlated to the internuclear axis, becomes important in describing the electron's orbital motion. If we consider the electron orbital as the zeroth order interaction and other spin couplings as perturbations, which is fair judging by their interaction strengths, we see that a Hund's case (b) molecule with $N \geq 1$ in its electronic ground state is fundamentally different a ground state alkaline atom, insofar as the light shift is concerned.

Heating due to spontaneous scattering

Despite the large detuning ($\hbar\Delta \gg \vec{\mu}\cdot\vec{\mathcal{E}}$), there is still spontaneous scattering. Following the discussion of the heating mechanism in the Ref.[79], we estimate the heating power to be

$$P = 2E_{\mathrm{rec}}\bar{\Gamma}_{\mathrm{sc}}, \tag{6.3.4}$$

where E_{rec} is the recoil energy and $\bar{\Gamma}_{\mathrm{sc}}$ the average photon scattering rate. The average scattering rate in a 3d harmonic trap in terms of the maximum dipole potential ($U_0 < 0$), transition linewidth (Γ), detuning (Δ) and average kinetic energy (k_BT) is given by (29) in Ref.[79],

$$\bar{\Gamma}_{\mathrm{sc}} = \frac{\Gamma}{\hbar\Delta}\left(U_0 + \frac{3}{2}k_BT\right); \tag{6.3.5}$$

$U_0 + \frac{3}{2}k_BT$ here is the average trapping potential experienced by trapped molecules. In this case, $U_0/k_B \approx -1.5$ mK, and the nearest transition $A^2\Pi_{1/2} - X^2\Sigma^+$ is $\Delta_{A^2\Pi_{1/2}} = -2\pi(170\ \mathrm{THz})$ away, so

$$\bar{\Gamma}_{\mathrm{sc}} \approx \left(\frac{2\pi(6.6\ \mathrm{MHz})}{\hbar|\Delta_{A^2\Pi_{1/2}}|}\right)(1.5\ \mathrm{m}K)k_B \approx 7.5/s, \tag{6.3.6}$$

assuming $T \approx 10\,\mu$K, which is typical after sub-Doppler cooling.

6.3.2 Not very far detuned dipole traps

We now consider a case where the detuning of the trap laser is larger than the spin-rotational splitting in both ground and excited states, but smaller than or comparable to the rotational energy; numerically, tens of GHz red to the lowest excited state $A^2\Pi_{1/2}$. The excited states included are identical to (6.3.3), though the energy shift is mostly due to the $A^2\Pi_{1/2} - X^2\Sigma^+$ transition. The contribution to the total light shift of each optical transition depends on the angular momenta quantum numbers, for the sake of argument, I compare, in Table 6.1, the contributions due to each optical transition to the total light shift of $X^2\Sigma^+(N = 1, J = 1/2, F = 1-)$ in a very far-detuned case and in a not very far-detuned case. The

	$A^2\Pi_{1/2} - X^2\Sigma^+$	$A^2\Pi_{3/2} - X^2\Sigma^+$	$B^2\Sigma^+ - X^2\Sigma^+$
663.7 nm	99%	0.8%	0.09%
1064 nm	39%	37%	24%

Table 6.1: Contributions of optical transitions to the total light shift of $X^2\Sigma^+(N = 1, J = 1/2, F = 1-)$ in a very far-detuned trap vs. in a not very far-detuned trap.

comparison implies that a good approximation can be obtained by only including the $A^2\Pi_{1/2}$ state in the estimation, which can simplify the calculation.

It is also perceivable that in not very far-detuned traps, the energy shifts are more susceptible to other perturbations, such as the spin-rotational and hyperfine interactions. Suppose the trap laser is red detuned to the $A^2\Pi_{1/2}(J'^{P'} = 1/2^+, F') - X^2\Sigma^+(N^P = 1^-, F = 1-)$ transition by $\Delta(< 0)$. Then the detunings with respect to transitions between hyperfine levels, $F \to F'$, can be easily determined from relevant energy level diagrams (Figure A.2 and A.1). In the very far-detuned traps, the trap depths estimated in the absence of the nuclear spin (Figure 6.2a) are already less than 10% from the estimates when all spin interactions are included (Figure 6.1a). As far as the numerics and coding are concerned, including energy level to the hyperfine scale increases the number of transitions to calculate by a factor of 2 due to ground state multiplicity and another factor of 4 to 6 due to excited states multiplicity: adding hyperfine quantum number increases the total ground states from 2 to 4, and each ground state hyperfine level couples to 4 hyperfine levels*, and 6 for ground state levels with J-mixing.

In terms of physics, one advantage for choosing a not very far detuned dipole trap is that a large trap depth can be attained with relatively low optical power. When $\Delta = -60$ GHz, trap depths comparable to that in §6.3.1, ~ 1 mK, are achieved with a few hundred times lower optical intensity, 200 mW and a $1/e^2$ radius of 30 μm. On account of a smaller detuning, heating due to off-resonance photon scattering occurs at a higher rate in a not very far detuned dipole trap. Assuming the same maximum trap depth ($U_0/k_B = -1.5$ mK) and kinetic energy ($T = 10\,\mu$K) and applying (6.3.5), we estimate the spontaneous scattering rate to be

$$\bar{\Gamma}_{\text{sc}} \approx \left(\frac{2\pi(6.6\text{ MHz})}{\hbar|\Delta|}\right)(1.5\text{ m}K)k_B \approx 2.1 \cdot 10^4/s, \tag{6.3.7}$$

which is much higher (2800 times) compared to the estimation in (6.3.6).

6.4 Scalar, vector and tensor light shift

The numerical estimates in §6.3 are very interesting in that with linearly polarized trap light, light shifts of magnetic levels within the same hyperfine manifold are not identical, making it qualitatively different from the well-known alkaline case where trap depths are identical to a good approximation. The light shift appears to have a quadratic dependence on the component quantum number M. It is then natural to decompose the energy shift due to linearly polarized light into a scalar light shift with no dependence on M, and a tensor light shift with quadratic dependence on M.

*Even if the excited state hyperfine splitting is very small, the transitions connecting degenerate excited state hyperfine levels are distinguishable by their matrix elements and thus the transition strengths.

In calculating the energy shift for ground state $|g_j\rangle$ due to H_1 (6.1.1), the leading order energy shift is second order in perturbation theory. To separate the scalar and tensor shifts, we return to the general expression (after making the rotating wave approximation) for the light shift in (6.1.8) and write it, using the vector notation defined and described previously in (B.1.2)–(B.1.5), as

$$\begin{aligned}\langle g_j|H_1|g_j\rangle &= \sum_{i,p,p'} \frac{\langle g_j|(-1)^p \mu_p \mathcal{E}^{-p}|\mathfrak{e}_i\rangle \left(\langle g_j|(-1)^{p'} \mu_{p'} \mathcal{E}^{-p'}|\mathfrak{e}_i\rangle\right)^\dagger}{\Delta_{ij}} \\ &= \sum_{p,p'} (-1)^{p+p'} \langle g_j|\, \mu_p \mathcal{P} \mu^*_{p'}\, |g_j\rangle\, \mathcal{E}^{-p'*} \mathcal{E}^{-p} \\ &\overset{(B.1.5)}{=} \sum_{p,p'} \langle g_j|\, \mu_p \mathcal{P} \mu^{p'}\, |g_j\rangle\, \mathcal{E}_{-p'} \mathcal{E}^{-p}, \end{aligned} \tag{6.4.1}$$

$$\text{where we have defined } \mathcal{P} = \sum_i \frac{|\mathfrak{e}_i\rangle\langle\mathfrak{e}_i|}{\Delta_{ij}}. \tag{6.4.2}$$

The second order energy shift due to H_1 can be seen as the first order shift due to another operator

$$H_2 = H_1 \mathcal{P} H_1 = \sum_{p,p'} \mu_p \mathcal{P} \mu^{p'} \mathcal{E}_{-p'} \mathcal{E}^{-p}. \tag{6.4.3}$$

H_2 can then be expanded into parts associated with a scalar operator ($H_2^{(0)}$), a vector operator ($H_2^{(1)}$) and a tensor operator ($H_2^{(2)}$),

$$H_2 = H_2^{(0)} + H_2^{(1)} + H_2^{(2)}. \tag{6.4.4}$$

The rank-1 operator is included in the expansion to be general, though it plays no role in the nonuniformity of energy shift due to linearly polarized light observed previously. It proves important for elliptically polarized light, to be discussed later.

Proceeding to define each term, we construct rank-K spherical tensors from each vector and then calculate the scalar product between spherical tensors, using (2.10-2.15) of Ref.[86],

$$\begin{aligned} H_2^{(K)} &= \{\vec{\mu}, \mathcal{P}\vec{\mu}\}^K \cdot \{\vec{\mathcal{E}}, \vec{\mathcal{E}}\}^K \\ &= \sum_{Q=K}^{-K} (-1)^Q \{\vec{\mu}, \mathcal{P}\vec{\mu}\}^K_Q \{\vec{\mathcal{E}}, \vec{\mathcal{E}}\}^K_{-Q}. \end{aligned} \tag{6.4.5}$$

We denote the Q^{th} term in the sum as $(H_2)^{(K)}_Q$. The Q^{th} component of a rank-K spherical tensor constructed

from two vectors is

$$\{\vec{A},\vec{B}\}_Q^K = \sum_{p,p'} \langle 11pp'|11KQ\rangle\, A_p B^{p'}, \tag{6.4.6}$$

with B^p being the p^{th} component of the vector $\vec{B}$, A_p the p^{th} component of $\vec{A}^\dagger$ (the covector of $\vec{A}$ in the complex spherical coordinate system (B.1.3)), and $\langle 11pp'|11KQ\rangle$ a Clebsch-Gordan coefficient.

Note that because $\mathcal{P} = \mathcal{P}^\dagger$ from the definition (6.4.2), $\{\vec{\mu},\mathcal{P}\vec{\mu}\}^K = \{\vec{\mu}\mathcal{P},\vec{\mu}\}^K$. $\mathcal{P}\vec{\mu}$ or $\vec{\mu}\mathcal{P}$ can be seen as a dipole operator with additional weights that depend on relative detunings (under the rotating wave approximation). In another popular notation for spherical tensors [80],

$$H_2^{(K)} = T^K(\vec{\mu},\mathcal{P}\vec{\mu})\cdot T^K(\vec{\mathcal{E}},\vec{\mathcal{E}}),$$

and the expression for each tensor (T^K) is given by (5.109) in Ref.[80].

The expressions of scalar ($K=0$), vector ($K=1$) and tensor ($K=2$) contributions to the light shift follow from (6.4.5) and (6.4.6):

$$\begin{aligned} H_2^{(0)} &= \{\vec{\mu},\mathcal{P}\vec{\mu}\}^0\cdot\{\vec{\mathcal{E}},\vec{\mathcal{E}}\}^0 \\ &= \frac{1}{\sqrt{3}}(\mu_1\mathcal{P}\mu^{-1} - \mu_0\mathcal{P}\mu^0 + \mu_{-1}\mathcal{P}\mu^1)\frac{1}{\sqrt{3}}(\mathcal{E}_1\mathcal{E}^{-1} - \mathcal{E}_0\mathcal{E}^0 + \mathcal{E}_{-1}\mathcal{E}^1) \\ &= \frac{1}{\sqrt{3}}(\mu_1\mathcal{P}\mu^{-1} - \mu_0\mathcal{P}\mu^0 + \mu_{-1}\mathcal{P}\mu^1)\frac{-1}{\sqrt{3}}|\mathcal{E}|^2 \end{aligned} \tag{6.4.7}$$

$$\begin{aligned} H_2^{(1)} &= \{\vec{\mu},\mathcal{P}\vec{\mu}\}^1\cdot\{\vec{\mathcal{E}},\vec{\mathcal{E}}\}^1 \\ &= -\frac{\mu_1\mathcal{P}\mu^0 - \mu_0\mathcal{P}\mu^1}{\sqrt{2}}\frac{\mathcal{E}_0\mathcal{E}^{-1} - \mathcal{E}_{-1}\mathcal{E}^0}{\sqrt{2}} \\ &+ \frac{\mu_1\mathcal{P}\mu^{-1} - \mu_{-1}\mathcal{P}\mu^1}{\sqrt{2}}\frac{|\mathcal{E}^1|^2 - |\mathcal{E}^{-1}|^2}{\sqrt{2}} - \frac{\mu_0\mathcal{P}\mu^{-1} - \mu_{-1}\mathcal{P}\mu^0}{\sqrt{2}}\frac{\mathcal{E}_1\mathcal{E}^0 - \mathcal{E}_0\mathcal{E}^1}{\sqrt{2}} \end{aligned} \tag{6.4.8}$$

$$
\begin{aligned}
H_2^{(2)} &= \{\vec{\mu}, \mathcal{P}\vec{\mu}\}^2 \cdot \{\vec{\mathcal{E}}, \vec{\mathcal{E}}\}^2 \\
&= \left(\mu_1 \mathcal{P} \mu^1\right)\left(\mathcal{E}_{-1}\mathcal{E}^{-1}\right) - \frac{1}{\sqrt{2}}\left(\mu_1 \mathcal{P}\mu^0 + \mu_0 \mathcal{P}\mu^1\right)\frac{1}{\sqrt{2}}\left(\mathcal{E}_0\mathcal{E}^{-1} + \mathcal{E}_{-1}\mathcal{E}^0\right) \\
&+ \left(\frac{\mu_1 \mathcal{P}\mu^{-1}}{\sqrt{6}} + \sqrt{\frac{2}{3}}\mu_0\mathcal{P}\mu^0 + \frac{\mu_{-1}\mathcal{P}\mu^1}{\sqrt{6}}\right)\left(\frac{\mathcal{E}_1\mathcal{E}^{-1}}{\sqrt{6}} + \sqrt{\frac{2}{3}}\mathcal{E}_0\mathcal{E}^0 + \frac{\mathcal{E}_{-1}\mathcal{E}^1}{\sqrt{6}}\right) \\
&- \frac{1}{\sqrt{2}}\left(\mu_0\mathcal{P}\mu^{-1} + \mu_{-1}\mathcal{P}\mu^0\right)\frac{1}{\sqrt{2}}\left(\mathcal{E}_1\mathcal{E}^0 + \mathcal{E}_0\mathcal{E}^1\right) + \left(\mu_{-1}\mathcal{P}\mu^{-1}\right)\left(\mathcal{E}_1\mathcal{E}^1\right) \\
&= \left(\mu_1 \mathcal{P} \mu^1\right)\left(\mathcal{E}_{-1}\mathcal{E}^{-1}\right) - \frac{1}{\sqrt{2}}\left(\mu_1 \mathcal{P}\mu^0 + \mu_0 \mathcal{P}\mu^1\right)\frac{1}{\sqrt{2}}\left(\mathcal{E}_0\mathcal{E}^{-1} + \mathcal{E}_{-1}\mathcal{E}^0\right) \\
&+ \left(\frac{\mu_1 \mathcal{P}\mu^{-1}}{\sqrt{6}} + \sqrt{\frac{2}{3}}\mu_0\mathcal{P}\mu^0 + \frac{\mu_{-1}\mathcal{P}\mu^1}{\sqrt{6}}\right)\left(-\frac{|\mathcal{E}|^2}{\sqrt{6}} + \frac{3}{\sqrt{6}}\mathcal{E}_0\mathcal{E}^0\right) \\
&- \frac{1}{\sqrt{2}}\left(\mu_0\mathcal{P}\mu^{-1} + \mu_{-1}\mathcal{P}\mu^0\right)\frac{1}{\sqrt{2}}\left(\mathcal{E}_1\mathcal{E}^0 + \mathcal{E}_0\mathcal{E}^1\right) + \left(\mu_{-1}\mathcal{P}\mu^{-1}\right)\left(\mathcal{E}_1\mathcal{E}^1\right). \qquad (6.4.9)
\end{aligned}
$$

For convenience, suppose a ground state level $|\zeta F M\rangle$ couples to excited states $\{|\zeta' F' M'\rangle\}$ via H_1 and that the detuning depends on the hyperfine energy levels defined by $\{\zeta, F, \zeta', F'\}$,

$$
\mathcal{P} = \sum_{\zeta' F' M'} \frac{|\zeta' F' M'\rangle \langle \zeta' F' M'|}{\Delta_{\zeta F \zeta' F'}}. \qquad (6.4.10)
$$

Nonetheless, the same derivation applies when a different basis is chosen, e.g. $\{|\zeta J M\rangle\}$ with the nuclear spin neglected.

In this basis, the Wigner-Eckart theorem can by applied to any component of the rank-K tensor

$$
\langle \zeta F M|(H_2)_Q^{(K)}|\zeta F \tilde{M}\rangle = (-1)^{F-M+Q}\begin{pmatrix} F & K & F \\ -M & Q & \tilde{M}\end{pmatrix}\langle \zeta F||\{\vec{\mu}, \mathcal{P}\vec{\mu}\}^K||\zeta F\rangle\, \{\vec{\mathcal{E}}, \vec{\mathcal{E}}\}^K_{-Q}. \qquad (6.4.11)
$$

$\langle \zeta F M|(H_2)_Q^{(K)}|\zeta F \tilde{M}\rangle$ is now factored: the $3J$ symbol depends on the component quantum number and hence on orientation, $\{\vec{\mathcal{E}}, \vec{\mathcal{E}}\}^K_{-Q}$ on the polarization and amplitude of the field and on orientation, $\langle \zeta F||\{\vec{\mu}, \mathcal{P}\vec{\mu}\}^K||\zeta F\rangle$ on the laser frequency and the overall strength of optical transitions. The reduced matrix element of a tensor product is a composite rank-K tensor and can then be related to the reduced matrix elements of constituent

tensors according (5.142) or (5.177) in Ref.[80],

$$\begin{aligned}
&\langle \zeta F||\{\vec{\mu},\mathcal{P}\vec{\mu}\}^K||\zeta F\rangle \\
&\overset{(5.177)}{=} \sum_{\zeta'' F''} \langle \zeta F||\mu^\dagger||\zeta'' F''\rangle \langle \zeta'' F''||\mathcal{P}\mu||\zeta F\rangle \sqrt{(2K+1)}(-1)^{2F+K} \begin{Bmatrix} 1 & 1 & K \\ F & F & F'' \end{Bmatrix} \\
&= \sum_{\zeta' F'} \frac{\langle \zeta F||\mu^\dagger||\zeta' F'\rangle \langle \zeta' F'||\mu||\zeta F\rangle}{\Delta_{\zeta F \zeta' F'}} \sqrt{(2K+1)}(-1)^{2F+K} \begin{Bmatrix} 1 & 1 & K \\ F & F & F' \end{Bmatrix}. \qquad (6.4.12)
\end{aligned}$$

The reduced matrix element of the dipole operator can be easily related to previously derived results $|\langle \eta|\mu_p|\eta'\rangle|^2$ in Appendix A.3 via the Wigner-Eckart theorem; for instance, when the nuclear spin is neglected, $F \mapsto J$,

$$\begin{aligned}
&\langle \zeta J||\mu^\dagger||\zeta' J'\rangle \langle \zeta' J'||\mu||\zeta J\rangle = (-1)^{J'-J} |\langle \zeta' J'||\mu||\zeta J\rangle|^2 \\
&= (-1)^{J'-J} f(\Gamma,\omega_0) FCF(v,v')(2J'+1)(2J+1) \begin{pmatrix} J & k=1 & J' \\ -\Omega & \Lambda-\Lambda' & \Omega' \end{pmatrix}^2.
\end{aligned}$$

It is presumed that $\langle \zeta J||\mu^\dagger||\zeta' J'\rangle = (-1)^{J'-J} \langle \zeta' J'||\mu||\zeta J\rangle^*$; this can be shown by applying properties of the

$3J$ symbols

$$\begin{aligned}
\langle \zeta' J' || \mu || \zeta J \rangle^* &= \sum_{MM'p} (-1)^{J'-M'} \begin{pmatrix} J' & k=1 & J \\ -M' & p & M \end{pmatrix} \langle \zeta' J' M' | \mu_p | \zeta J M \rangle^* \\
&= \sum_{MM'p} (-1)^{J'-M'} \begin{pmatrix} J' & k=1 & J \\ -M' & p & M \end{pmatrix} \langle \zeta J M | \mu_p^\dagger | \zeta' J' M' \rangle \\
&\overset{\substack{\text{swap col. 1 and 3} \\ \text{negate bottom row}}}{=} \sum_{MM'p} (-1)^{J'-M'} \begin{pmatrix} J & k=1 & J' \\ -M & -p & M' \end{pmatrix} \langle \zeta J M | \mu_p^\dagger | \zeta' J' M' \rangle \,, \\
\langle \zeta J || \mu^\dagger || \zeta' J' \rangle &= \sum_{MM'p} (-1)^{J-M} \begin{pmatrix} J & k=1 & J' \\ -M & p & M' \end{pmatrix} \langle \zeta J M | \mu_p^\dagger | \zeta' J' M' \rangle \,. \qquad (6.4.13)
\end{aligned}$$

In comparing them, see that in both cases, the sum over p is only nontrivial under equivalent conditions, when the bottom row of the $3J$ symbols adds to zero.

In light of this factorization, §6.4.1 is about the frequency dependence of energy shift due to H_2, and §6.4.2 and §6.4.3 about the polarization dependence.

6.4.1 Polarizability

After $(H_2)^{(K)}_Q$ (6.4.11) is factored, remarkably, the factor $\langle \zeta J || \{\vec{\mu}, \mathcal{P}\vec{\mu}\}^K || \zeta J \rangle$ is independent of orientation of either the polarization or the quantization axis. For terminology and the ease of comparison, we define the scalar, vector, and tensor polarizabilities based on (11) in Ref.[87] after applying the rotating wave approximation,

$$\alpha^s_{\zeta J}(\omega) = \frac{1}{\sqrt{3(2J+1)}} \langle \zeta J || \{\vec{\mu}, \mathcal{P}\vec{\mu}\}^0 || \zeta J \rangle \qquad (6.4.14a)$$

$$\alpha^v_{\zeta J}(\omega) = -\sqrt{\frac{2J}{(J+1)(2J+1)}} \langle \zeta J || \{\vec{\mu}, \mathcal{P}\vec{\mu}\}^1 || \zeta J \rangle \qquad (6.4.14b)$$

$$\alpha^t_{\zeta J}(\omega) = -\sqrt{\frac{2J(2J-1)}{3(J+1)(2J+1)(2J+3)}} \langle \zeta J || \{\vec{\mu}, \mathcal{P}\vec{\mu}\}^2 || \zeta J \rangle \,. \qquad (6.4.14c)$$

In the SI system, the atomic unit of electric polarizability is $\left[\frac{e^2 a_0^2}{E_h}\right]$; in cgs system, the volume polarizability

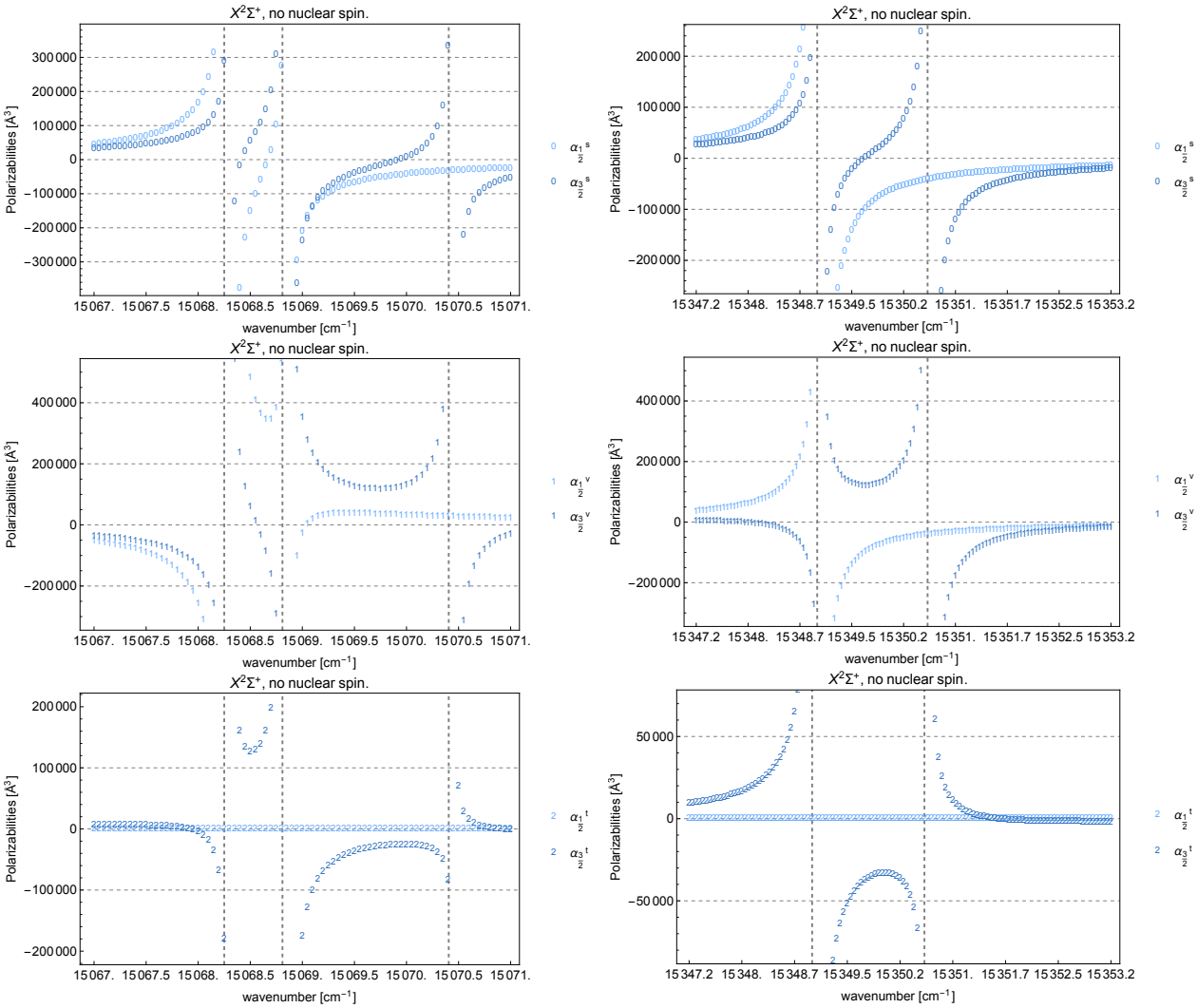
$$\tilde{\alpha} = \frac{1}{4\pi\epsilon_0}\alpha, \tag{6.4.15}$$

has the unit of $[\text{Å}^3]$ or $[a_0^3]$.

Figure 6.3a, 6.3b, 6.4a and 6.4b show that resonant singularities in polarizabilities occur in the vicinities of optical resonances. Figure 6.5 shows the signed log plot over a broad range, $\text{sign}(\tilde{\alpha})\text{Log}_{10}(|\tilde{\alpha}|)$. In making these plots, $A^2\Pi$, $B^2\Sigma^+$, $C^2\Pi$ and $D^2\Sigma^+$ are taken into account. Relevant spectroscopy data can be found in the Table A.3 and A.4. For $J = 1/2$ and 0, the tensor polarizability is always zero. This stems from properties of the $6J$ symbol in (6.4.12) and is made more obvious in (6.4.14c).

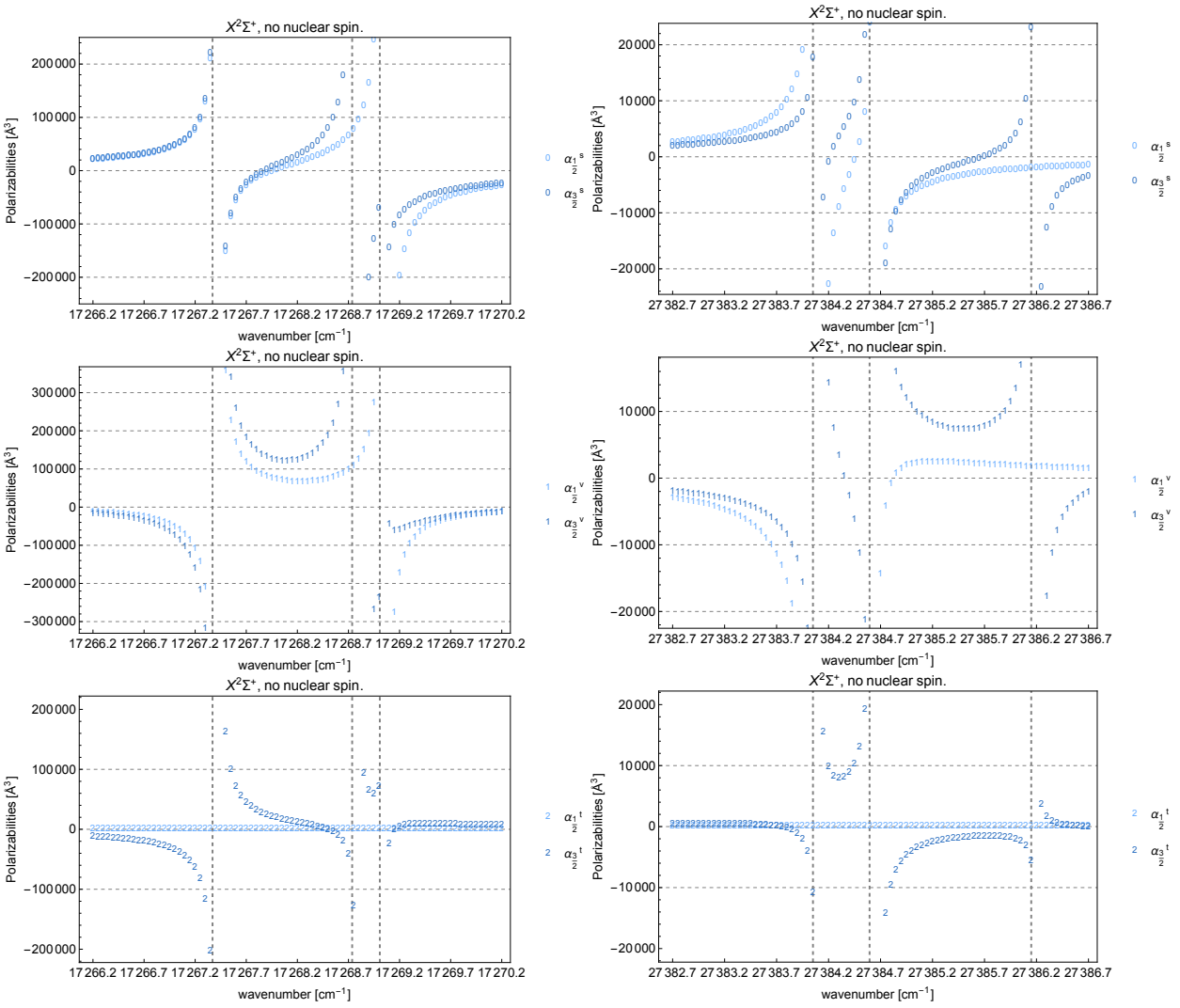
In choosing experimental parameters for conservative trapping, a large detuning is advantageous in suppressing spontaneous scattering (6.3.5). Figure 6.5 shows that, when the trap light is far detuned from optical resonances, the scalar polarizability is much larger than the tensor or vector polarizability. Therefore, its sign has practical relevance to the trap geometry, magnitude to laser power. In a simple case— trapping with a single laser beam, when $\alpha^s_{\zeta J} > 0$, a gaussian beam (assumed in §6.3) is suitable for conservative trapping; when $\alpha^s_{\zeta J} < 0$, light in a Laguerre-Gaussian mode (e.g. a hollow-beam trap in Ref.[88]) can create the same trap depth with $e^2 \sim 7$ times higher laser power.

The following discussion on the polarization dependence of light shift will be limited to the simple case without any hyperfine structure. Plots of the polarizabilities of hyperfine states including J-mixing can be found in Appendix A.5. When the nuclear spin is taken into account, naturally the hyperfine interaction splits the energy levels. The hyperfine energy splittings are much smaller than the detuning (in the far-detuned traps), so it does not have much significance in the numerics other than increasing the number of states to compute. Nonetheless, the hyperfine interaction also mixes J eigenstates when $F = N = 1$ as mentioned in §6.2.4, and it has been shown with numerics (Figure 6.2b) that this causes nontrivial shifts even when the laser is very far off resonance. Consequently, in the presence of the nuclear spin $I = 1/2$, polarizabilities and thus light shifts to become even more complex and less uniform within the rotational level $X^2\Sigma^+(N = 1)$.



(a) $A^2\Pi_{1/2}(J') - X^2\Sigma^+$ **(b)** $A^2\Pi_{3/2}(J') - X^2\Sigma^+$

Figure 6.3: Scalar, vector and tensor polarizabilities of $X^2\Sigma^+(v = 0, N = 1, J)$ as functions of trap frequency in the vicinity of the $A^2\Pi(J') - X^2\Sigma^+$ resonances.



(a) $B^2\Sigma^+(J') - X^2\Sigma^+$ **(b)** $C^2\Pi_{1/2}(J') - X^2\Sigma^+$

Figure 6.4: Scalar, vector and tensor polarizabilities of $X^2\Sigma^+(v = 0, N = 1, J)$ as functions of trap frequency in the vicinity of the $B^2\Sigma^+(J') - X^2\Sigma^+$ and $C^2\Pi_{1/2}(J') - X^2\Sigma^+$ resonances.

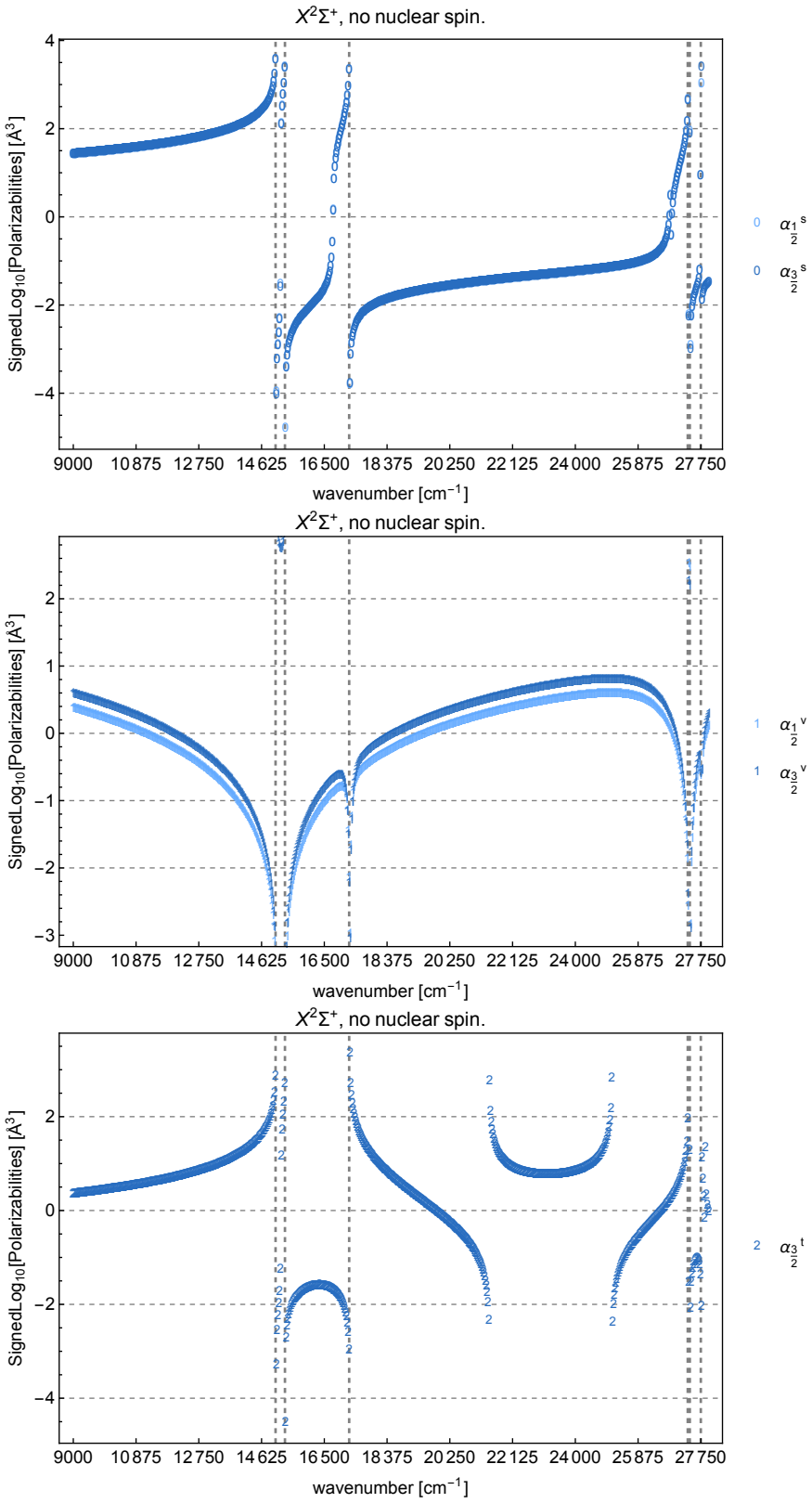


Figure 6.5: SignedLog function of polarizabilities $\text{sign}(\tilde{\alpha})\text{Log}_{10}(|\tilde{\alpha}|)$. All the optical resonances $A^2\Pi$, $B^2\Sigma^+$, $C^2\Pi$ and $D^2\Sigma^+$ are labelled by vertical dashed lines. The extra resonances in the tensor polarizability plot are artifacts due to its value crossing zero.

6.4.2 Linear polarization

Suppose the polarization vector is $\hat{e}^z = \hat{e}^0$, $|\mathcal{E}|^2 = \mathcal{E}_0\mathcal{E}^0$,

$$\{\vec{\mathcal{E}},\vec{\mathcal{E}}\}_0^0 = \frac{-|\mathcal{E}|^2}{\sqrt{3}}, \quad \{\vec{\mathcal{E}},\vec{\mathcal{E}}\}_0^2 = \frac{2|\mathcal{E}|^2}{\sqrt{6}}, \quad \text{otherwise } \{\vec{\mathcal{E}},\vec{\mathcal{E}}\}_Q^K = 0. \tag{6.4.16}$$

We choose to work in a basis $\{|\zeta FM\rangle\}_{M=-F,\dots,F}$ where M is the eigenvalue of F_z. Then the basis' quantization axis is aligned with the symmetry axis of H_2, i.e. $[H_2, F_z] = 0$. With the Wigner-Eckart theorem, the matrix elements of each rank-K operator can be evaluated using algebra. The matrix elements of $H_2^{(0)}$ are independent of M,

$$\langle \zeta FM|H_2^{(0)}|\zeta F\tilde{M}\rangle = \frac{\langle \zeta F||\{\vec{\mu},\mathcal{P}\vec{\mu}\}^K||\zeta F\rangle\,\{\vec{\mathcal{E}},\vec{\mathcal{E}}\}_0^0}{\sqrt{2F+1}}\delta_{\tilde{M}M}. \tag{6.4.17}$$

This expression agrees with the expression derived earlier ((6.3.1) with $p = 0$). For $(H_2)_Q^{(2)}$, we write its components with (6.4.12) and find it to be nontrivial for $Q = 0$ due to (6.4.16). Then in the H_2 operator becomes

$$\begin{aligned}
\langle \zeta FM|H_2|\zeta F\tilde{M}\rangle &= \frac{-|\mathcal{E}|^2}{\sqrt{3(2F+1)}}\,\langle \zeta F||\{\vec{\mu},\mathcal{P}\vec{\mu}\}^0||\zeta F\rangle\,\delta_{\tilde{M}M} \\
&- \frac{F^2+F-3M^2}{\sqrt{F(F+1)(2F+3)(2F+1)(2F-1)}}\frac{2}{\sqrt{6}}|\mathcal{E}|^2\,\langle \zeta F||\{\vec{\mu},\mathcal{P}\vec{\mu}\}^2||\zeta F\rangle\,\delta_{\tilde{M}M} \\
&= \begin{cases} -|\mathcal{E}|^2\alpha_{\zeta F}^s(\omega)\delta_{\tilde{M}M}, & F = 0, 1/2; \\ -|\mathcal{E}|^2\alpha_{\zeta F}^s(\omega)\delta_{\tilde{M}M} + |\mathcal{E}|^2\alpha_{\zeta F}^t(\omega)\frac{F^2+F-3M^2}{F(2F-1)}\delta_{\tilde{M}M}, & \text{otherwise.} \end{cases}
\end{aligned} \tag{6.4.18}$$

Here the quadratic dependence of light shift on M is evident.

To summarize, in this subsection, we show the new calculation routine involving H_2 reproduces identical results to those using the second order perturbation theory (6.3.1). For purely linear polarization, there exists a representation of energy eigenfunctions, in which H_2 is diagonal, $(H_2)_{Q\neq 0}^{(K>0)}$. It is straightforward in this case because we set up the problem, by choosing a basis whose quantization axis aligns with the symmetry axis of the operator H_2 for the chosen polarization. In the degenerate subspace of energy eigenfunctions $\{|\zeta FM\rangle\}_{M=-F,\dots,F}$, $(H_2)^{(2)}$ is diagonal, and yet lifts the degeneracy between levels with different $|M|$. In other words, it is straightforward because we set up the problem based on the intuition that the CSCO is $\{H_0, H_2, F, F_z\}$ with H_0 being the operator that gives rise to all the internal energy structures. If we choose the same basis when the symmetry axis of the operator and $\hat{e}^z$ subtend a nontrivial angle θ, $[H_2, F_z] \neq 0$, it can be shown directly with algebra that the resulting matrix of H_2 in has the same eigenvalues. This is

consistent with the intuition that physical situations are identical, and that CSCO $= \{H_0, H_2, F, R^{-1}F_zR\}$ with R being an Euler rotation (6.2.68) with $\omega_E = (0, \theta, 0)$.

6.4.3 Elliptical polarization

Suppose light propagates along $\hat{e}^z$ and that the polarization is

$$\begin{aligned}\hat{e}(\beta) &= \cos\beta\hat{e}^x + i\sin\beta\hat{e}^y = \frac{\cos\beta}{\sqrt{2}}\hat{e}^{-1} - \frac{\cos\beta}{\sqrt{2}}\hat{e}^1 + \frac{\sin\beta}{\sqrt{2}}\hat{e}^1 + \frac{\sin\beta}{\sqrt{2}}\hat{e}^{-1} \\ &= \sin\left(\beta + \frac{\pi}{4}\right)\hat{e}^{-1} + \cos\left(\beta + \frac{\pi}{4}\right)\hat{e}^1. \end{aligned} \tag{6.4.19}$$

The nonzero components of the field tensor are

$$\begin{gathered}\{\vec{\mathcal{E}}, \vec{\mathcal{E}}\}_0^0 = \frac{-|\mathcal{E}|^2}{\sqrt{3}}, \quad \{\vec{\mathcal{E}}, \vec{\mathcal{E}}\}_0^1 = \frac{-\sin 2\beta|\mathcal{E}|^2}{\sqrt{2}}, \quad \{\vec{\mathcal{E}}, \vec{\mathcal{E}}\}_0^2 = \frac{-|\mathcal{E}|^2}{\sqrt{6}}, \\ \text{and } \{\vec{\mathcal{E}}, \vec{\mathcal{E}}\}_{\pm 2}^2 = \frac{-\cos 2\beta|\mathcal{E}|^2}{2}. \end{gathered} \tag{6.4.20}$$

The diagonal matrix elements are due to $(H_2)^{(0)}$, $(H_2)_0^{(1)}$ and $(H_2)_0^{(2)}$,

$$\begin{aligned}&\langle \zeta FM|(H_2)_0|\zeta FM\rangle = \frac{-|\mathcal{E}|^2}{\sqrt{3(2F+1)}}\langle \zeta F||\{\vec{\mu}, \mathcal{P}\vec{\mu}\}^0||\zeta F\rangle \\ &+ \frac{M}{\sqrt{F(F+1)(1+2F)}}\frac{-\sin 2\beta|\mathcal{E}|^2}{\sqrt{2}}\langle \zeta F||\{\vec{\mu}, \mathcal{P}\vec{\mu}\}^1||\zeta F\rangle \\ &- \frac{F^2+F-3M^2}{\sqrt{F(F+1)(2F+3)(2F+1)(2F-1)}}\left(-\frac{|\mathcal{E}|^2}{\sqrt{6}}\right)\langle \zeta F||\{\vec{\mu}, \mathcal{P}\vec{\mu}\}^2||\zeta F\rangle \\ &= -|\mathcal{E}|^2\alpha_{\zeta F}^s + \frac{M\sin 2\beta}{2F}|\mathcal{E}|^2\alpha_{\zeta F}^v - \frac{F^2+F-3M^2}{2F(2F-1)}|\mathcal{E}|^2\alpha_{\zeta F}^t; \end{aligned} \tag{6.4.21}$$

the off-diagonal matrix elements (for $F \geq 2(3/2)$) are due to $(H_2)_{\pm 2}^{(2)}$,

$$\begin{aligned}&\langle \zeta FM|(H_2)_{\pm 2}^{(2)}|\zeta F\tilde{M}\rangle = (-1)^{F-M+2}\begin{pmatrix} F & 2 & F \\ -M & \pm 2 & \tilde{M}\end{pmatrix}\left(\mathcal{E}_{\mp 1}\mathcal{E}^{\mp 1}\right)\langle \zeta F||\{\vec{\mu}, \mathcal{P}\vec{\mu}\}^2||\zeta F\rangle \\ &\overset{(6.4.23)}{=} \sqrt{\frac{3}{2}}\sqrt{\frac{(2+F\mp M)(1+F\mp M)(-1+F\pm M)(F\pm M)}{F(F+1)(2F+3)(2F+1)(2F-1)}} \\ &\quad\times\left(\frac{-|\mathcal{E}|^2}{2}\cos 2\beta\right)\langle \zeta F||\{\vec{\mu}, \mathcal{P}\vec{\mu}\}^2||\zeta F\rangle\,\delta_{\tilde{M},M\mp 2} \\ &= \frac{3}{2}\frac{\sqrt{(2+F\mp M)(1+F\mp M)(-1+F\pm M)(F\pm M)}}{2F(2F-1)}\frac{|\mathcal{E}|^2\cos 2\beta}{2}\alpha_{\zeta F}^t\delta_{\tilde{M},M\mp 2}. \end{aligned} \tag{6.4.22}$$

In simplifying the sign in this expression, we have used

$$(F \mp F - M \pm M) \equiv 0 \mod 2. \tag{6.4.23}$$

To see why this holds when F is an half-integer, suppose $F, M \in \{\frac{4n+1}{2}, \frac{4n+3}{2}\}_{n=\ldots,0,1,\ldots}$. It follows that $2F$ and $2M$ are always 1 or 3 modulo 4, and therefore $2F - 2M \equiv 0 \mod 2$. F can only be an integer or half-integer, so the other cases are trivial.

Most relevant to calculating light shifts for $\zeta \mapsto X^2\Sigma^+(N=1)$, $F \mapsto J = 1/2, 3/2$, the off-diagonal matrix elements are zero for in the subspace of $J = 1/2$; in the $J = 3/2$ subspace M and $M \pm 2$ sublevels are coupled by the rank-2 operator,

$$H_2 = -|\mathcal{E}|^2 \alpha^s_{\zeta J} \mathbb{I} + |\mathcal{E}|^2 \begin{bmatrix} -\frac{\alpha^v_{\zeta J}}{2}\sin 2\beta + \frac{\alpha^t_{\zeta J}}{2} & & \frac{\sqrt{3}\alpha^t_{\zeta J}}{4}\cos 2\beta & \\ & -\frac{\alpha^v_{\zeta J}}{6}\sin 2\beta - \frac{\alpha^t_{\zeta J}}{2} & & \frac{\sqrt{3}\alpha^t_{\zeta J}}{4}\cos 2\beta \\ \frac{\sqrt{3}\alpha^t_{\zeta J}}{4}\cos 2\beta & & \frac{\alpha^v_{\zeta J}}{6}\sin 2\beta - \frac{\alpha^t_{\zeta J}}{2} & \\ & \frac{\sqrt{3}\alpha^t_{\zeta J}}{4}\cos 2\beta & & \frac{\alpha^v_{\zeta J}}{2}\sin 2\beta + \frac{\alpha^t_{\zeta J}}{2} \end{bmatrix}, \tag{6.4.24}$$

The energy eigenvalues are

$$\begin{aligned} ee_{1,2} &= |\mathcal{E}|^2 \left(-\alpha^s_{\zeta J} - \frac{\alpha^v_{\zeta J}}{6}\sin 2\beta \mp x(\alpha^v_{\zeta J}, \alpha^t_{\zeta J}, -\beta) \right), \\ \text{and } ee_{3,4} &= |\mathcal{E}|^2 \left(-\alpha^s_{\zeta J} + \frac{\alpha^v_{\zeta J}}{6}\sin 2\beta \mp x(\alpha^v_{\zeta J}, \alpha^t_{\zeta J}, \beta) \right), \\ \text{with } x &= \frac{\sqrt{2}}{24}\sqrt{99(\alpha^t_{\zeta J})^2 + 16(\alpha^v_{\zeta J})^2 + (27(\alpha^t_{\zeta J})^2 - 16(\alpha^v_{\zeta J})^2)\cos 4\beta + 96\alpha^t_{\zeta J}\alpha^v_{\zeta J}\sin 2\beta}. \end{aligned} \tag{6.4.25}$$

With linearly polarized trap light, i.e. when $\beta = \beta_l \in \{0, \pi/4, \pi/2\}$,

$$\begin{aligned} ee_1(\beta_l) = ee_3(\beta_l) &= |\mathcal{E}|^2 \left(-\alpha^s_{\zeta J} - \frac{\sqrt{7}}{4}\alpha^t_{\zeta J} \right) = \langle \zeta \tfrac{3}{2}, \pm\tfrac{3}{2} | H_2 | \zeta \tfrac{3}{2}, \pm\tfrac{3}{2} \rangle, \\ ee_2(\beta_l) = ee_4(\beta_l) &= |\mathcal{E}|^2 \left(-\alpha^s_{\zeta J} + \frac{\sqrt{7}}{4}\alpha^t_{\zeta J} \right) = \langle \zeta \tfrac{3}{2}, \pm\tfrac{1}{2} | H_2 | \zeta \tfrac{3}{2}, \pm\tfrac{1}{2} \rangle; \end{aligned} \tag{6.4.26}$$

The energy eigenvalues are exactly the diagonal matrix elements in (6.4.21), and the eigenstates are exactly the magnetic sublevels.

When $\beta \neq \beta_l$, and in general when $\alpha^{s,v,t}_{\zeta J} \neq 0$, energy eigenvalues of H_2 are not degenerate. Furthermore, the energy eigenstates are mixtures of magnetic sublevels couples by its rank-2 component, in a basis whose quantization axis is $\hat{e}^z$. The entangled magnetic levels can be problematic, e.g. in optical pumping and when there is an external magnetic field. Then it is worth mentioning that the problem is avoided when $\alpha^t_{\zeta J} = 0$. Under this condition, for arbitrary β, the energy eigenvalues are equal to the diagonal matrix elements

$$\begin{aligned} ee_{1,2}(\alpha^t_{\zeta J} = 0) &= |\mathcal{E}|^2 \left(-\alpha^s_{\zeta J} - \frac{\alpha^v_{\zeta J}}{6} \sin 2\beta \mp \frac{|\alpha^v_{\zeta J}|}{3} |\sin 2\beta| \right), \\ ee_{3,4}(\alpha^t_{\zeta J} = 0) &= |\mathcal{E}|^2 \left(-\alpha^s_{\zeta J} + \frac{\alpha^v_{\zeta J}}{6} \sin 2\beta \mp \frac{|\alpha^v_{\zeta J}|}{3} |\sin 2\beta| \right). \end{aligned} \tag{6.4.27}$$

and the eigenstates have well-defined magnetic quantum numbers. For β defined on $[0, \pi/2)$, the eigenstates can be associated to magnetic sublevels by comparing the expressions to (6.4.24),

$$ee_1 = \begin{cases} \langle \zeta \tfrac{3}{2}, -\tfrac{3}{2} | H_2 | \zeta \tfrac{3}{2}, -\tfrac{3}{2} \rangle, & \alpha^v_{\zeta J} > 0 \\ \langle \zeta \tfrac{3}{2}, \tfrac{1}{2} | H_2 | \zeta \tfrac{3}{2}, \tfrac{1}{2} \rangle, & \alpha^v_{\zeta J} \leq 0 \end{cases}, \quad ee_2 = \begin{cases} \langle \zeta \tfrac{3}{2}, \tfrac{1}{2} | H_2 | \zeta \tfrac{3}{2}, \tfrac{1}{2} \rangle, & \alpha^v_{\zeta J} > 0 \\ \langle \zeta \tfrac{3}{2}, -\tfrac{3}{2} | H_2 | \zeta \tfrac{3}{2}, -\tfrac{3}{2} \rangle, & \alpha^v_{\zeta J} \leq 0 \end{cases},$$

$$ee_3 = \begin{cases} \langle \zeta \tfrac{3}{2}, -\tfrac{1}{2} | H_2 | \zeta \tfrac{3}{2}, -\tfrac{1}{2} \rangle, & \alpha^v_{\zeta J} > 0 \\ \langle \zeta \tfrac{3}{2}, \tfrac{3}{2} | H_2 | \zeta \tfrac{3}{2}, \tfrac{3}{2} \rangle, & \alpha^v_{\zeta J} \leq 0 \end{cases}, \quad ee_4 = \begin{cases} \langle \zeta \tfrac{3}{2}, \tfrac{3}{2} | H_2 | \zeta \tfrac{3}{2}, \tfrac{3}{2} \rangle, & \alpha^v_{\zeta J} > 0 \\ \langle \zeta \tfrac{3}{2}, -\tfrac{1}{s} 2 | H_2 | \zeta \tfrac{3}{2}, -\tfrac{1}{2} \rangle, & \alpha^v_{\zeta J} \leq 0 \end{cases}.$$

In terms of polarizabilites (6.4.15) and intensity (6.1.5), the H_2 operator in this basis is

$$\begin{aligned} &\langle \zeta J M | H_2 | \zeta J \tilde{M} \rangle \\ &= \frac{2\pi I}{c} \left(-\tilde{\alpha}^s_{\zeta J}(\omega) + \frac{M}{J} \frac{\sin 2\beta}{2} \tilde{\alpha}^v_{\zeta J}(\omega) - \frac{J^2 + J - 3M^2}{2J(2J-1)} \tilde{\alpha}^t_{\zeta J}(\omega) \right) \delta_{\tilde{M} M} \\ &+ \frac{2\pi I}{c} \frac{3}{2} \frac{\sqrt{(2 + J \mp M)(1 + J \mp M)(-1 + J \pm M)(J \pm M)}}{2J(2J-1)} \frac{\cos 2\beta}{2} \tilde{\alpha}^t_{\zeta J}(\omega) \delta_{\tilde{M}, M \pm 2}. \end{aligned} \tag{6.4.28}$$

For $J = 1/2$ levels, the energy eigenvalues are exactly the diagonal elements; for $J = 3/2$, they are given by (6.4.25) with substitution, $|\mathcal{E}|^2 \mapsto \frac{2\pi I}{c}$ and $\alpha \mapsto \tilde{\alpha}$.

If in (6.4.19), i is replaced by 1, i.e. the polarization is linear, the nonzero components of the field tensor are

$$\{\vec{\mathcal{E}}, \vec{\mathcal{E}}\}^0_0 = \frac{-|\mathcal{E}|^2}{\sqrt{3}}, \quad \{\vec{\mathcal{E}}, \vec{\mathcal{E}}\}^2_0 = \frac{-|\mathcal{E}|^2}{\sqrt{6}}, \quad \text{and } \{\vec{\mathcal{E}}, \vec{\mathcal{E}}\}^2_{\pm 2} = \frac{e^{\pm i 2\beta} |\mathcal{E}|^2}{2}. \tag{6.4.29}$$

The H_2 operator in the angular momentum basis becomes

$$\begin{aligned}
&\langle \zeta JM|H_2|\zeta J\tilde{M}\rangle \\
&= \frac{2\pi I}{c}\left(-\tilde{\alpha}^s_{\zeta J}(\omega) - \frac{J^2+J-3M^2}{2J(2J-1)}\tilde{\alpha}^t_{\zeta J}(\omega)\right)\delta_{\tilde{M}M} \\
&+ \frac{2\pi I}{c}\frac{3}{2}\frac{\sqrt{(2+J\mp M)(1+J\mp M)(-1+J\pm M)(J\pm M)}}{2J(2J-1)}\frac{e^{\pm 2i\beta}}{2}\tilde{\alpha}^t_{\zeta J}(\omega)\delta_{\tilde{M},M\pm 2}.
\end{aligned} \tag{6.4.30}$$

The eigenvalues for $J = 3/2$ obtained by diagonalization, are identical to those given by (6.4.26) for a linear polarization.

6.5 Polarization-dependent far-detuned dipole traps

To investigate the polarization dependence of energy shifts, the effect of ellipticity β in (6.4.19), we want to fix the frequency of the trap light. In the first example, we choose $\omega = \omega_L$ such that $\tilde{\alpha}^t_{\zeta J}(\omega_L) = 0$ and so the energy eigenstates shifted by H_2 are simultaneous eigenstates of the magnetic quantum number. Figure 6.6 shows that this condition can be fulfilled around $\omega_L/(2\pi c) = 15214.25\,\mathrm{cm}^{-1}$ ($2\pi c/\omega_L = 657.3$ nm). At $\omega = \omega_L$, the polarizabilities are estimated as follows:

$$\begin{aligned}
\tilde{\alpha}^s_{\zeta 1/2}(\omega_L) &= 58\,\text{Å}^3, \quad \tilde{\alpha}^v_{\zeta 1/2}(\omega_L) = 910\,\text{Å}^3, \\
\tilde{\alpha}^s_{\zeta 3/2}(\omega_L) &= 52\,\text{Å}^3, \quad \tilde{\alpha}^v_{\zeta 3/2}(\omega_L) = 540\,\text{Å}^3.
\end{aligned} \tag{6.5.1}$$

Figure 6.7a shows the trap depth as a function of β for each energy eigenstate $|\zeta JM\rangle$, assuming an intensity of $1.4{\cdot}10^5$ W/cm^2, coming from 4 W trap light focused to a beam waist ($1/e^2$ radius) of 30 μm in a single-pass configuration. At this trap frequency, the state-dependent difference is minimized when $\beta = 0$ or $\pi/2$

$$\hat{e}(\beta = 0) = \hat{e}^x, \quad \hat{e}(\beta = \pi/2) = i\hat{e}^y.$$

The trap potentials for $\zeta \mapsto X^2\Sigma^+(v = 0, N = 1)$ levels are

$$\langle \zeta\frac{1}{2}M|H_2|\zeta\frac{1}{2}M\rangle \approx -120\,\mu K, \quad \text{and } \langle \zeta\frac{3}{2}M|H_2|\zeta\frac{3}{2}M\rangle \approx -110\,\mu K.$$

There is no differential shift within the spin-rotational subspace labelled by ζ and J. The difference in light shift is entirely due to the difference in scalar polarizability, which is about 5.6 Å^3. The fractional difference in scalar polarizability, 11%, is consistent with the fractional difference in light shift, and the

absolute difference between J levels scales linearly with intensity.

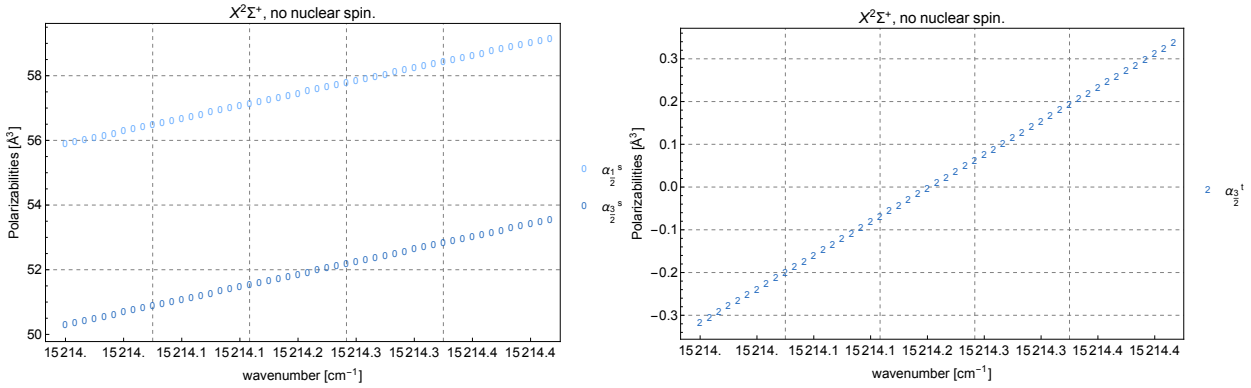
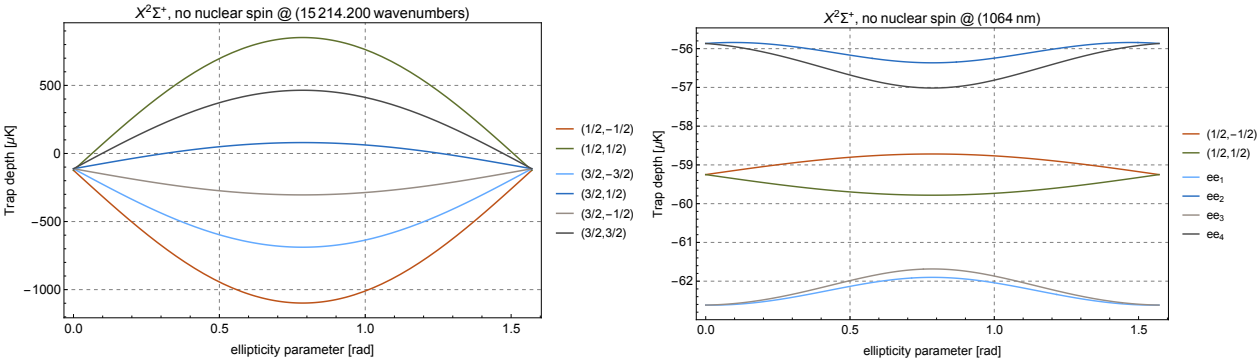


Figure 6.6: Scalar (L) and tensor (R) polarizabilities near $\omega_L/(2\pi c)$ =15214.25 cm^{-1} where the tensor polarizability vanishes for $J = 3/2$.



(a) $\omega_L/(2\pi c) = 15214.25$ cm^{-1} **(b)** $2\pi c/\omega'_L$ =1064 nm

Figure 6.7: Trap depths as functions of the ellipticity parameter (β) at fixed frequencies, assuming 4 W trap light with a beam waist ($1/e^2$ radius) of 30 μm in a single-pass configuration.

For comparison, we consider the polarization dependence at a different frequency; at $2\pi c/\omega'_L$ =1064 nm ($\omega'_L/(2\pi c) = 9398.5$ cm^{-1}),

$$\tilde{\alpha}^s_{\zeta 1/2}(\omega'_L) = 28\ \text{Å}^3, \quad \tilde{\alpha}^v_{\zeta 1/2}(\omega'_L) = -.50\ \text{Å}^3, \quad \tilde{\alpha}^t_{\zeta 1/2}(\omega'_L) = 0\ \text{Å}^3,$$
$$\tilde{\alpha}^s_{\zeta 3/2}(\omega'_L) = 28\ \text{Å}^3, \quad \tilde{\alpha}^v_{\zeta 3/2}(\omega'_L) = -.30\ \text{Å}^3, \quad \tilde{\alpha}^t_{\zeta 3/2}(\omega'_L) = 2.4\ \text{Å}^3. \tag{6.5.2}$$

Assuming the intensity is the same as in the previous case, trap depths as functions of ellipticity are plotted in Figure 6.7b. In this scenario, when $\beta = \pi/4$, the energy eigenstates also have well-defined projection quantum number in a basis with its quantization axis being $\hat{e}^z$, but the shifts for levels with different $|M|$ are no longer equal. When $\beta = \pi/4$, the difference in energy shifts of energy eigenstates is minimized. Since the differential energy light shift is due to a large nonzero tensor polarizability $\alpha^t_{\zeta 3/2}$, the absolute difference

scales linearly with trap intensity and therefore trap depths. The absolute difference is about 5 μK in the plot and would be doubled if the trap depth is about 100 μK, comparable to that in the previous case $2\pi c/\omega_L$ =657.3 nm.

Provided the estimates in the first example and typical temperatures after sub-Doppler cooling, we assume that the maximum potential energy $U_0/k_B \approx -120\,\mu$K and the average kinetic energy $T \approx 10\,\mu$K. Then the scattering rate due to $A^2\Pi_{1/2} - X^2\Sigma^+$ (145 cm^{-1} below the trap wavelength) and $A^2\Pi_{3/2} - X^2\Sigma^+$ (136 cm^{-1} above) can be estimated using (6.3.5),

$$\begin{aligned}\bar{\Gamma}_{\rm sc} &= \frac{\Gamma}{\hbar\Delta}\left(U_0 + \frac{3}{2}k_BT\right)\\ &\approx \left(\frac{2\pi(6.6\text{ MHz})}{\hbar|\Delta_{A^2\Pi_{1/2}}|} + \frac{2\pi(7\text{ MHz})}{\hbar|\Delta_{A^2\Pi_{3/2}}|}\right)(105\,\mu K)k_B\\ &= 2\pi(7.1\text{ Hz}) = 45/s.\end{aligned}$$

In the second case where $2\pi c/\omega_L'$ =1064 nm, the scattering rate for $U_0/k_B \approx -50\,\mu$K is

$$\bar{\Gamma}_{\rm sc} \approx \left(\frac{2\pi(6.6\text{ MHz})}{\hbar|\Delta_{A^2\Pi_{1/2}}|}\right)(35\,\mu K)k_B = 2\pi(28\text{ mHz}) = 0.18/s.$$

Appendix A

Properties and spectroscopy data

A.1 SrF properties

transition frequency (ν_0)	451.97 THz [89, 90]
natural linewidth (Γ)	$2\pi\cdot$ (6.6 MHz) [82]
recoil energy	$k_B\cdot$ (406.8 nK)
recoil velocity (v_r)	5.62 mm/s
maximum Doppler shift due to recoil ($\nu_0 \frac{v_r}{c}$)	8.48 kHz
Doppler temperature	157.4 μK

Table A.1: SrF $A^2\Pi_{1/2} - X^2\Sigma^+$ transition data.

nuclear spin (I)	1/2
nuclear g-factor	5.586
nuclear moment (μ_N)	1/1836 μ_B
$X^2\Sigma^+(N=1)$ hyperfine g-factors (g_F)	$g_2 = 0.4997$
	$g_{1+} = 0.9716$
	$g_{1-} = -0.4716$
$A^2\Pi_{1/2}(J=1/2)$ hyperfine g-factors (g_F)	$g_1 = -0.3352$
$X^2\Sigma^+(N=0)$ hyperfine g-factors (g_F)	$g_1 = 1$

Table A.2: SrF properties data

Excited state	T_e [cm^{-1}]	ω_e [cm^{-1}]	$\omega_e\chi_e$ [cm^{-1}]	B_e [cm^{-1}]
$A^2\Pi_{1/2}$	15068.9 [91]	507.9 [92]	2.21 [92]	0.2528335(37) [93]
$A^2\Pi_{3/2}$	15348.9 [91]	507.3 [92]	2.18 [92]	
$B^2\Sigma^+$	17267.4465(26) [94]	495.8(7) [95]	2.34(21) [95]	0.24961(9) [90]
$C^2\Pi_{1/2}$	27384.1 [89]	454.2245 [96]	1.6532 [96]	0.2462110(39) [93]
$C^2\Pi_{3/2}$	27445 [89]			
$D^2\Sigma^+$	27773.8168(42) [93]	552.1 [91]	2.15 [92]	0.2627533(42)[93]

Table A.3: Spectroscopy data for excited states SrF based on latest experimental data. T_e: minimal electronic energy relative to $X^2\Sigma^+$, ω_e: vibrational constant–first term, $\omega_e\chi_e$: vibrational constant–second term.

Electronic transition	Natural Linewidth (Γ) [MHz]	Lifetime [ns]	Transition dipole moment
$A^2\Pi_{1/2} - X^2\Sigma^+$	$2\pi\cdot$ (6.6)	24.1(2.0) [82]	$2.45ea_0$
$A^2\Pi_{3/2} - X^2\Sigma^+$	$2\pi\cdot$ (7.0)	22.6(4.7) [82]	$2.46ea_0$
$B^2\Sigma^+ - X^2\Sigma^+$	$2\pi\cdot$ (6.3)	25.4(0.8) [97]	$1.94ea_0$
$C^2\Pi_{1/2} - X^2\Sigma^+$	$2\pi\cdot$ (1.7)	66.3 [98]	$0.60ea_0$
$C^2\Pi_{3/2} - X^2\Sigma^+$	$2\pi\cdot$ (2.4)	66.3 [98]	$0.60ea_0$
$D^2\Sigma^+ - X^2\Sigma^+$	$2\pi\cdot$ (0.73)	219 [98]	$0.32ea_0$

Table A.4: Natural linewidth transitions connecting to the ground state. Natural linewidths and transition dipole moments of the A and B states are calculated based on mean values of lifetime data in Ref.[82] and Ref.[97] respectively. For the $C^2\Pi - X^2\Sigma^+$ and $D^2\Sigma^+ - X^2\Sigma^+$ transitions, linewidths are calculated from theoretical values in Ref.[98].

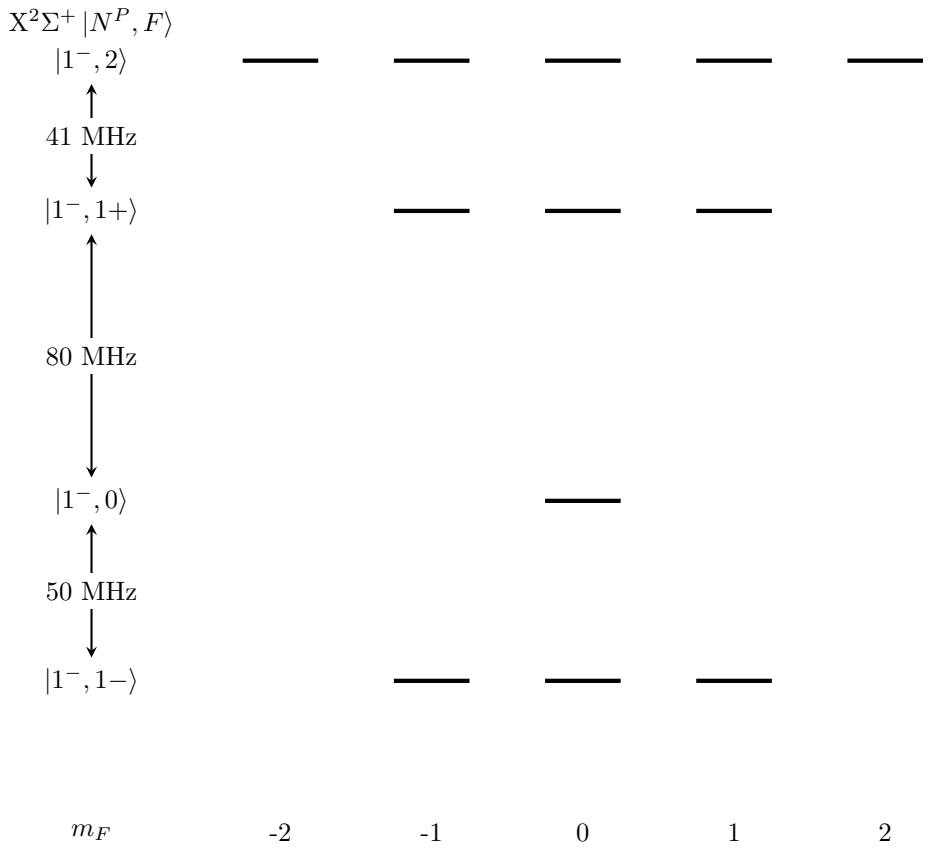


Figure A.1: Energy level diagram of ground state $X^2\Sigma^+(v = 0, N = 1)$.

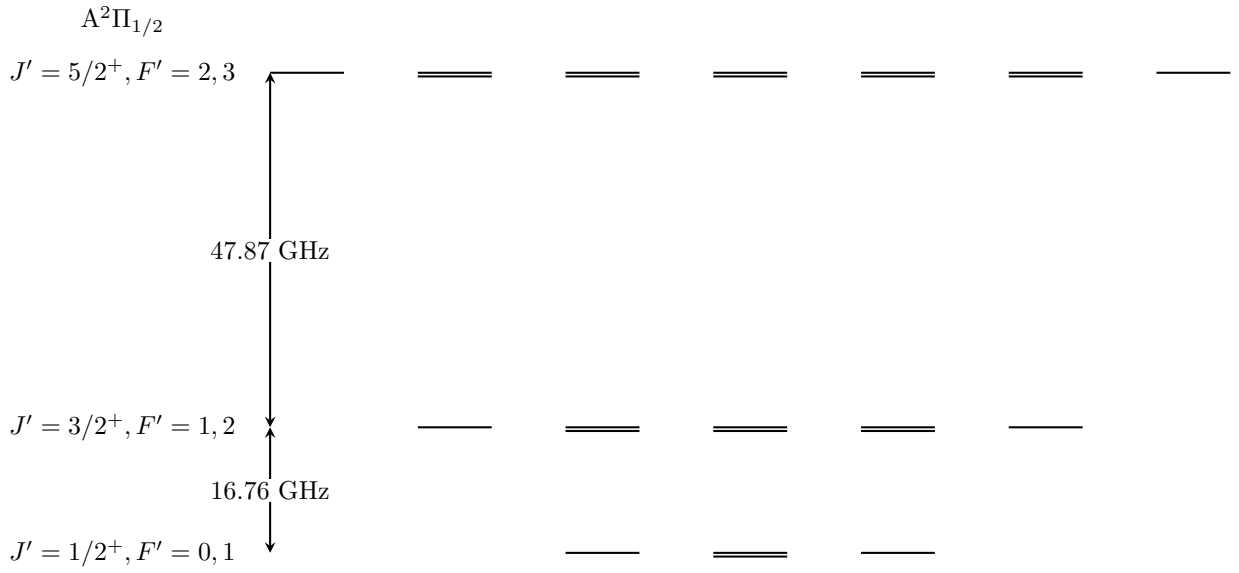


Figure A.2: Energy level diagram of $A^2\Pi_{1/2}(v = 0)$ with positive parity. Rotational splittings calculated based on measured spectroscopy constant B_e [93]. The hyperfine splitting is small, ≈ 3 MHz.

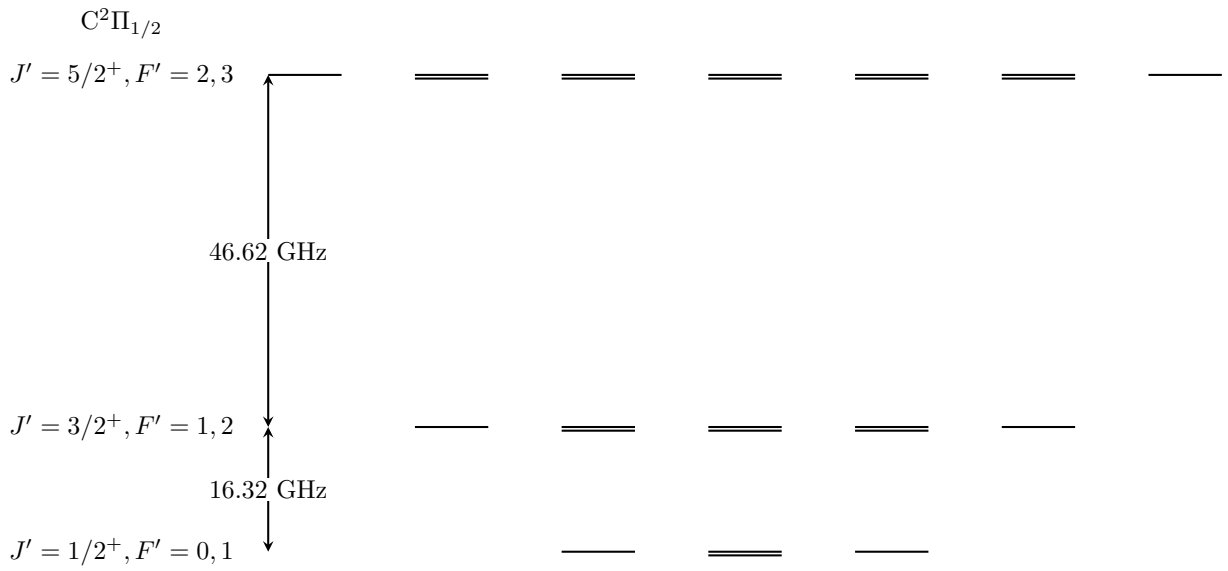


Figure A.3: Energy level diagram of $C^2\Pi_{1/2}(v = 0)$ with positive parity. Rotational splittings calculated based on measured spectroscopy constant B_e [93].

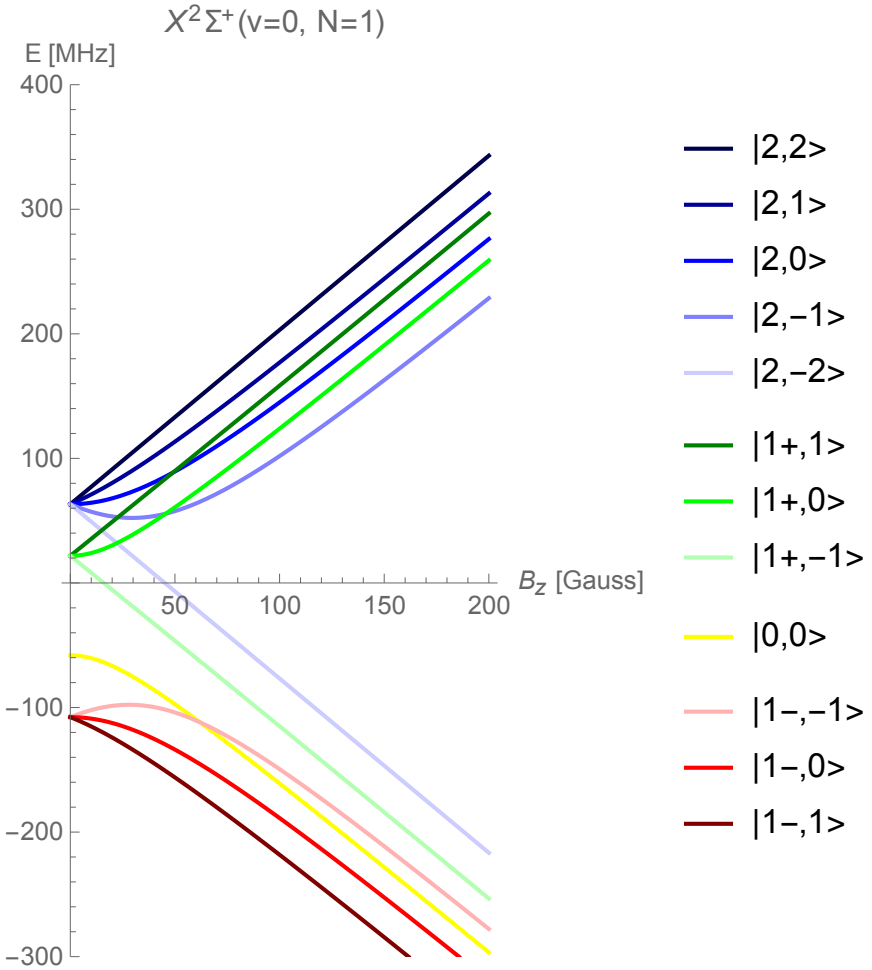


Figure A.4: Breit-Rabi diagram of $X^2\Sigma^+(v = 0, N = 1)$

A.2 $B^2\Sigma^+ - X^2\Sigma^+$ TRANSITION

With a frequency-doubling crystal, using a higher electronic state, $B^2\Sigma^+$ for optical cycling has become viable. It is realistic to use the $B^2\Sigma^+ - X^2\Sigma^+$ transition as the vibrational repump for $X^2\Sigma^+(v=1)$, replacing the current repump line $A^2\Pi_{1/2}(v'=0) - X^2\Sigma^+(v=1)$. This change is beneficial as it the coherent dark states (Λ-systems) created by the main cycling laser $A^2\Pi_{1/2}(v'=0) - X^2\Sigma^+(v=0)$ and the repump laser $A^2\Pi_{1/2}(v'=0) - X^2\Sigma^+(v=1)$ would be suppressed.

This section summarizes spectroscopy details on this electronic transition, and calculates the energy splittings for experimentally measured spectroscopy constants.

In the Hund's case (b) basis with nuclear spin (6.2.30), the scalar product of the Hamiltonian is given by

$$\langle H\rangle = T_e + \omega_e\left(v+\frac{1}{2}\right) - \omega_e\chi_e\left(v+\frac{1}{2}\right)^2 + B_v N(N+1) + \langle H_{\mathrm{sr/hfs}}\rangle\,, \tag{A.2.1}$$

where v is the vibrational quantum number, N is the rotational quantum number, and $H_{\mathrm{sr/hfs}}$ denotes the spin-rotation and hyperfine coupling Hamiltonian

$$H_{\mathrm{sr/hfs}} = \gamma_v \vec{S}\cdot\vec{N} + b_{vN}\vec{I}\cdot\vec{S} + c_{vN}I_zS_z + C_{I,N}\vec{I}\cdot\vec{N}. \tag{A.2.2}$$

The other symbols denote the spectroscopic constants whose definition can be found on the NIST Chemistry WebBook [99]: electronic energy (T_e), vibrational constants ($\omega_e, \omega_e\chi_e$), rotational constant (B_v), spin-rotational (γ_v), hyperfine constants (b_{vN} and c_{vN}), and nuclear spin-rotation constant ($C_{I,N}$).

Experimental measurements of relevant spectroscopic constants used in this calculation are given in Table A.5*, and c_{vN} and $C_{I,N}$ are small enough to be neglected. With these data, the $B^2\Sigma^+$ state potential curve and the Franck-Condon factors (FCFs) can be calculated using specialized programs, RKR [101] and LEVEL [102] respectively. Then the vibrational branching ratios are derived using

$$b_{v'v} = \frac{FCF_{v'v}\omega_{v'v}^2}{\sum_w FCF_{v'w}\omega_{v'w}^2}, \tag{A.2.3}$$

where $FCF_{v'v}$ is the Franck-Condon factor between excited vibrational level v' and ground state vibrational level v, and $\omega_{v'v}$ is the frequency of this transition.

*In the case multiple measured results are reported, the consistency between measurements is considered,

- B_v and γ_v of [94] are calculated from on Dunham coeff.'s, and are consistent with results in [90, 95, 100]
- T_e and B_v in [94] and [95] are not consistent

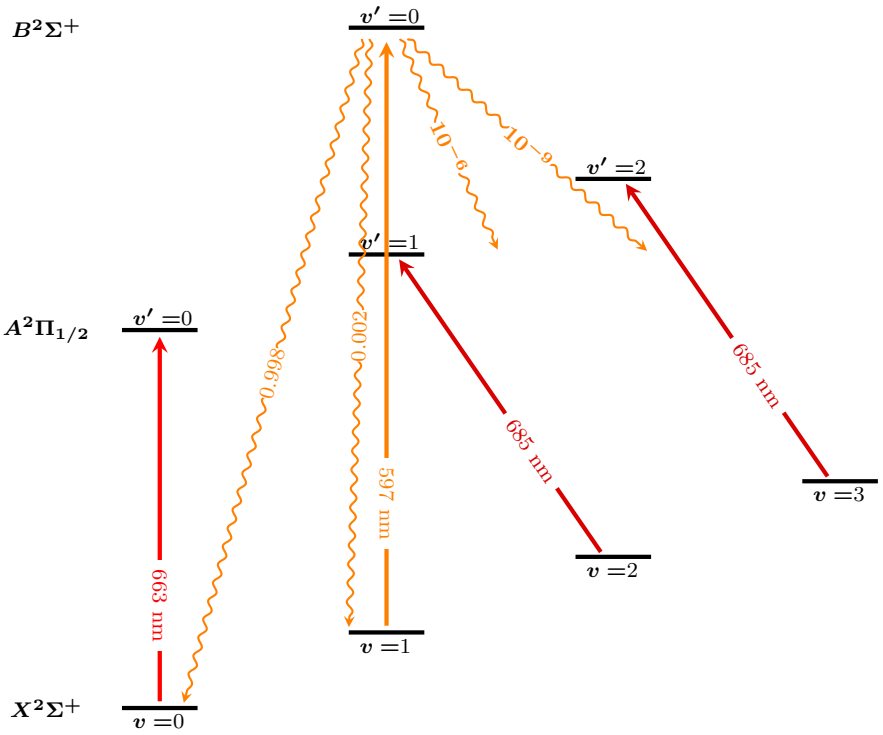


Figure A.5: Repump scheme using the $B^2\Sigma^+(v'=0) - X^2\Sigma^+(v=1)$ transition. Spontaneous decays (wavy arrows) from $B^2\Sigma^+(v'=0)$ end up in the vibrational ground state of $X^2\Sigma^+$ with over 99% probability.

$B^2\Sigma^+(v'=0)$		$X^2\Sigma^+(v=1)$	
B_0 =.248617(4) cm^{-1}	[94]	B_1 =.248212(1) cm^{-1}	[94]
γ_0 =– 0.135229(78) cm^{-1}	[94]	γ_1 =.0024804(128) cm^{-1}	[94]
b_{0N} = 14.0 (4.6) MHz	[103]	b_{1N} = 95.9155(22) MHz	[100]

Table A.5: Spectroscopic constants relevant to the $B^2\Sigma^+(v=0) - X^2\Sigma^+(v=1)$ transition

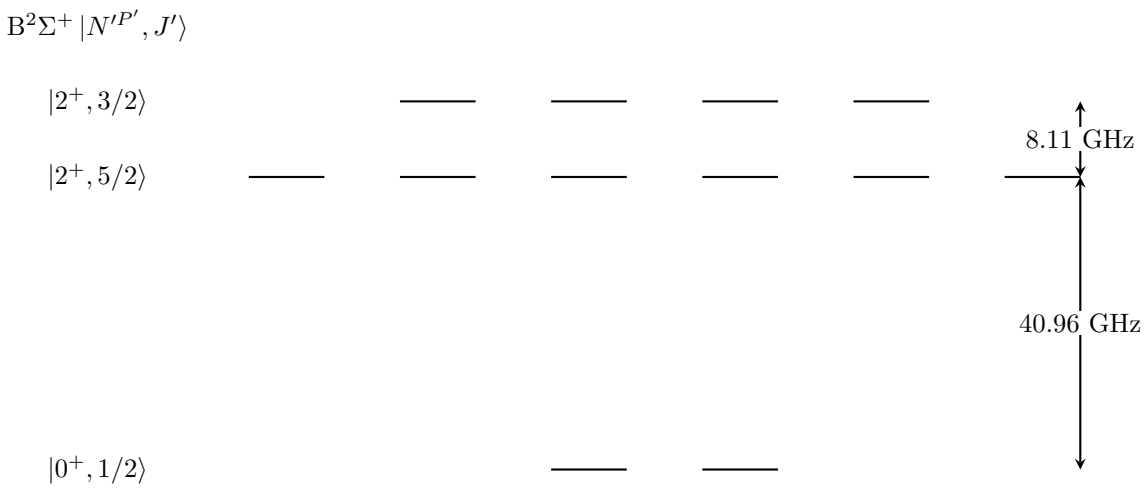


Figure A.6: Energy level diagram of low-lying rotational levels with positive parity in $B^2\Sigma^+(v'=0)$. Spacings are calculated based on constants from Table A.5.

A.3 Dipole matrix elements

Suppose $\langle\eta|\mu_p|\eta'\rangle$ denotes the matrix element of a p-dipole transition with $p \in \{-1, 0, 1\}$ being an index of the complex spherical coordinate (6.2.2), represented in the basis $\{|\eta\rangle\}$ (to be specified individually), the general expressions are as follows:

- Hund's case (a) $|\eta\rangle \mapsto$ (6.2.6)

$$\langle\eta|\mu_p|\eta'\rangle = (-1)^{2J-M-\Omega}\sqrt{f(\Gamma,\omega_0)FCF(v,v')}\sqrt{(2J'+1)(2J+1)} \times \begin{pmatrix} J & k=1 & J' \\ -\Omega & \Lambda-\Lambda' & \Omega' \end{pmatrix} \begin{pmatrix} J & 1 & J' \\ -M & p & M' \end{pmatrix} \delta_{\Sigma\Sigma'}\delta_{SS'} \tag{A.3.1}$$

- Hund's case (a) with hyperfine and no J-mixing $|\eta\rangle \mapsto$ (6.2.25)

$$\langle\eta|\mu_p|\eta'\rangle = (-1)^{F-M+J-\Omega}(-1)^{F+I+1+J'}\sqrt{f(\Gamma,\omega_0)FCF(v,v')} \times\sqrt{(2J'+1)(2J+1)} \begin{pmatrix} J & k=1 & J' \\ -\Omega & \Lambda-\Lambda' & \Omega' \end{pmatrix} \times\sqrt{(2F+1)(2F'+1)} \begin{Bmatrix} J & F & I \\ F' & J' & k=1 \end{Bmatrix} \begin{pmatrix} F & k=1 & F' \\ -M & p & M' \end{pmatrix} \delta_{\Sigma\Sigma'}\delta_{SS'}\delta_{II'} \tag{A.3.2}$$

- Hund's case (b) $|\eta\rangle \mapsto$ (6.2.30)

$$\langle\eta|\mu_p|\eta'\rangle = (-1)^{J-M+N-\Lambda}(-1)^{S+J'+1}\sqrt{f(\Gamma,\omega_0)FCF(v,v')} \times\sqrt{(2J+1)(2J'+1)} \begin{pmatrix} J & k=1 & J' \\ -M & p & M' \end{pmatrix} \times\sqrt{(2N+1)(2N'+1)} \begin{Bmatrix} N & J & S \\ J' & N' & k=1 \end{Bmatrix} \begin{pmatrix} N & k=1 & N' \\ -\Lambda & \Lambda-\Lambda' & \Lambda' \end{pmatrix} \delta_{SS'} \tag{A.3.3}$$

- Hund's case (b) with hyperfine and no J-mixing $|\eta\rangle \mapsto$ (6.2.39)

$$\langle\eta|\mu_p|\eta'\rangle = (-1)^{F-M+N-\Lambda}(-1)^{S+J'+1}(-1)^{F+I+1+J'}\sqrt{f(\Gamma,\omega_0)FCF(v,v')}$$
$$\times\sqrt{(2J+1)(2J'+1)}\begin{Bmatrix} N & J & S \\ J' & N' & k \end{Bmatrix}\sqrt{(2N+1)(2N'+1)}\begin{pmatrix} N & 1 & N' \\ -\Lambda & \Lambda-\Lambda' & \Lambda' \end{pmatrix}$$
$$\times\sqrt{(2F+1)(2F'+1)}\begin{Bmatrix} J & F & I \\ F' & J' & k=1 \end{Bmatrix}\begin{pmatrix} F & k=1 & F' \\ -M & p & M' \end{pmatrix}\delta_{SS'}\delta_{II'} \tag{A.3.4}$$

- atomic case with hyperfine $|\eta\rangle \mapsto$ (6.2.56)

$$\langle\eta|\mu_p|\eta'\rangle = (-1)^{F-M}(-1)^{F+I+1+J'}\sqrt{f(\Gamma,\omega_0)}\sqrt{(2J'+1)(2F+1)(2F'+1)}$$
$$\times\begin{Bmatrix} J & F & I \\ F' & J' & k=1 \end{Bmatrix}\begin{pmatrix} F & k=1 & F' \\ -M & p & M' \end{pmatrix}\delta_{SS'}\delta_{II'} \tag{A.3.5}$$

In addition to angular momentum quantum numbers in the cases, $f(\Gamma,\omega_0)$, defined in (6.2.23), is a function of transition linewidth Γ and transition ω_0,

$$f(\Gamma,\omega_0) = \frac{3\pi\epsilon_0\hbar c^3}{\omega_0^3}\Gamma.$$

$FCF(v,v')$ denotes a Franck-Condon factor whose numerical value can be determined experimentally.

A.4 Rotational branching ratios

$A^2\Pi_{1/2}(J') \to X^2\Sigma^+(J)$	$J'=1/2$	$J'=3/2$	$J'=5/2$
$J=1/2$	$\frac{2}{3}$	$\frac{1}{6}$	
$J=3/2$	$\frac{1}{3}$	$\frac{8}{15}$	$\frac{1}{5}$
$J=5/2$		$\frac{3}{10}$	$\frac{18}{35}$
$J=7/2$			$\frac{2}{7}$

Table A.6: Branching ratios of $A^2\Pi_{1/2}(J') \to X^2\Sigma^+(J)$ transitions with initial and final states represented in the Hund's case (a) basis.

$J' \to N$	$J' = 1/2^+$	$J' = 1/2^-$	$J' = 3/2^+$	$J' = 3/2^-$	$J' = 5/2^+$	$J' = 5/2^-$
$N = 0^+$		$\frac{2}{3}$		$\frac{1}{6}$		
$N = 1^-$	1		$\frac{7}{10}$		$\frac{1}{5}$	
$N = 2^+$		$\frac{1}{3}$		$\frac{5}{6}$		$\frac{5}{7}$
$N = 3^-$			$\frac{3}{10}$		$\frac{4}{5}$	
$N = 4^+$						$\frac{2}{7}$

Table A.7: Branching ratios of $A^2\Pi_{1/2}(J'^{P'}) \to X^2\Sigma^+(N^P)$ transitions with initial and final states represented in the Hund's case (a) parity eigenstates and respectively (b) basis.

$A^2\Pi_{3/2}(J') \to X^2\Sigma^+(J)$	$J' = 3/2$	$J' = 5/2$
$J = 1/2$	$\frac{1}{2}$	
$J = 3/2$	$\frac{2}{5}$	$\frac{2}{5}$
$J = 5/2$	$\frac{1}{10}$	$\frac{16}{35}$
$J = 7/2$		$\frac{1}{7}$

Table A.8: Branching ratios of $A^2\Pi_{3/2}(J') \to X^2\Sigma^+(J)$ transitions with initial and final states represented in parity combinations of Hund's case (a) basis.

$J' \to N$	$J' = 3/2^+$	$J' = 3/2^-$	$J' = 5/2^+$	$J' = 5/2^-$
$N = 0^+$		$\frac{1}{2}$		
$N = 1^-$	$\frac{9}{10}$		$\frac{2}{5}$	
$N = 2^+$		$\frac{1}{2}$		$\frac{6}{7}$
$N = 3^-$	$\frac{1}{10}$		$\frac{3}{5}$	
$N = 4^+$				$\frac{1}{7}$

Table A.9: Branching ratios of $A^2\Pi_{3/2}(J'^{P'}) \to X^2\Sigma^+(N^P)$ transitions, with initial and final states represented in the Hund's case (a) parity eigenstates and respectively (b) basis.

$B^2\Sigma^+(J') \to X^2\Sigma^+(J)$	$J' = 1/2$	$J' = 3/2$	$J' = 5/2$
$J = 1/2$	$\frac{1}{3}$	$\frac{1}{3}$	
$J = 3/2$	$\frac{2}{3}$	$\frac{1}{15}$	$\frac{2}{5}$
$J = 5/2$		$\frac{3}{5}$	$\frac{1}{35}$
$J = 7/2$			$\frac{4}{7}$

Table A.10: Branching ratios of $B^2\Sigma^+(J') \to X^2\Sigma^+(J)$ transitions with initial and final states represented in the Hund's case (a) basis.

$B^2\Sigma^+(N') \to X^2\Sigma^+(N)$	$N'=0^+$	$N'=1^-$	$N'=2^+$
$N=0^+$		$\frac{1}{3}$	
$N=1^-$	1		$\frac{2}{5}$
$N=2^+$		$\frac{2}{3}$	
$N=3^-$			$\frac{3}{5}$

Table A.11: Branching ratios of $B^2\Sigma^+(N'^{P'}) \to X^2\Sigma^+(N^P)$ transitions with initial and final states represented in the Hund's case (b) basis.

A.5 Polarizabilities of hyperfine states

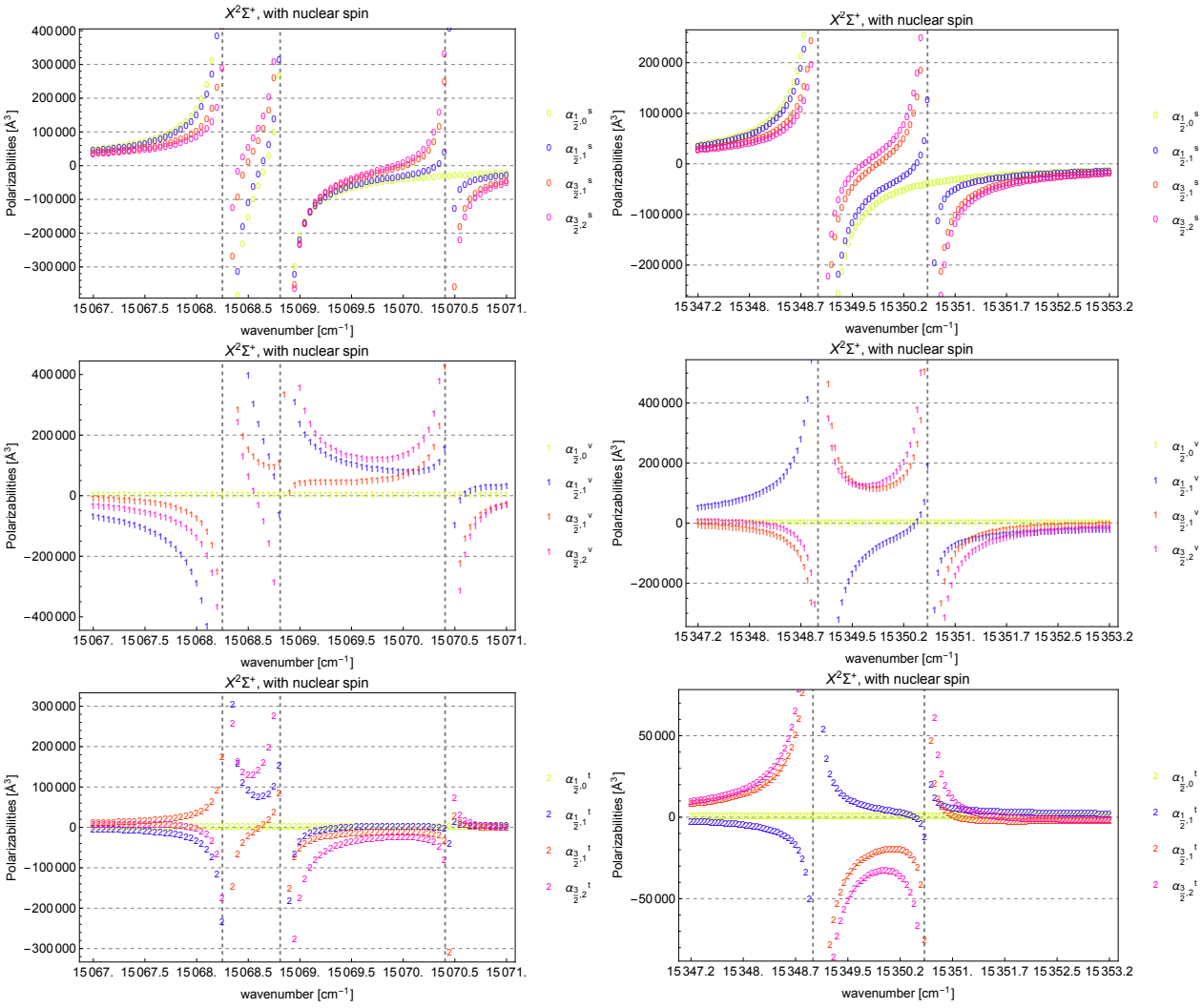
The definitions of polarizabilities for hyperfine states follow from (B.36) in Ref.[87],

$$\alpha^s_{\zeta F}(\omega) = \frac{1}{\sqrt{3(2F+1)}} \langle \zeta F || \{\vec{\mu}, \mathcal{P}\vec{\mu}\}^0 || \zeta F \rangle \tag{A.5.1}$$

$$\alpha^v_{\zeta F}(\omega) = -\sqrt{\frac{2F}{(F+1)(2F+1)}} \langle \zeta F || \{\vec{\mu}, \mathcal{P}\vec{\mu}\}^1 || \zeta F \rangle \tag{A.5.2}$$

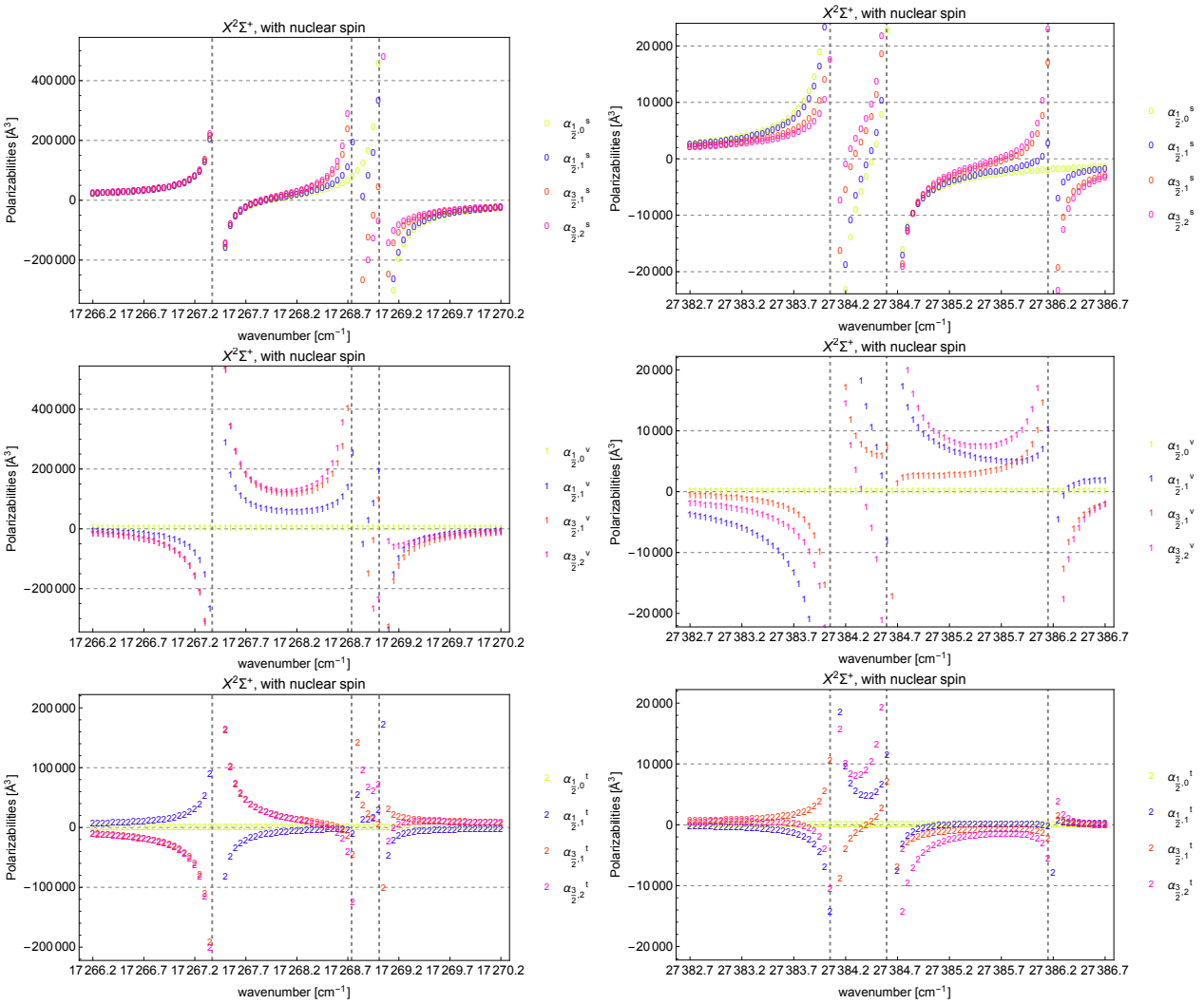
$$\alpha^t_{\zeta F}(\omega) = -\sqrt{\frac{2F(2F-1)}{3(F+1)(2F+1)(2F+3)}} \langle \zeta F || \{\vec{\mu}, \mathcal{P}\vec{\mu}\}^2 || \zeta F \rangle \,. \tag{A.5.3}$$

They are identical to (6.4.14c) with substitution $J \mapsto F$.



(a) $A^2\Pi_{1/2}(J') - X^2\Sigma^+$ **(b)** $A^2\Pi_{3/2}(J') - X^2\Sigma^+$

Figure A.7: Scalar, vector and tensor polarizabilities of $X^2\Sigma^+(v = 0, N = 1, J, F)$ as functions of trap frequency in the vicinity of the $A^2\Pi(J') - X^2\Sigma^+$ resonances.



(a) $B^2\Sigma^+(J') - X^2\Sigma^+$ **(b)** $C^2\Pi_{1/2}(J') - X^2\Sigma^+$

Figure A.8: Scalar, vector and tensor polarizabilities of $X^2\Sigma^+(v = 0, N = 1, J, F)$ as functions of trap frequency in the vicinity of the $B^2\Sigma^+(J') - X^2\Sigma^+$ and $C^2\Pi_{1/2}(J') - X^2\Sigma^+$ resonances. For $B^2\Sigma^+ - X^2\Sigma^+$, the hyperfine mixing of J in the excited state is not taken into account.

A.6 Rubidium properties

transition frequency (ν_0)	384.23 THz
natural linewidth (Γ)	$2\pi\cdot$ (6.06 MHz)
recoil energy	$k_B\cdot$ (361.6 nK)
recoil velocity (v_r)	5.88 mm/s
maximum Doppler shift due to recoil ($\nu_0 \frac{v_r}{c}$)	7.53 kHz
Doppler temperature	145.6 μK

Table A.12: Rubidium 87 isotope D_2 line data [56]

nuclear spin (I)	3/2
nuclear g-factor	-0.000995
$5^2S_{1/2}$ hyperfine g-factors (g_F)	$g_2 = 1/2$
	$g_1 = -1/2$
	$g_3 = 2/3$
$5^2P_{3/2}$ hyperfine g-factors (g_F)	$g_2 = 2/3$
	$g_1 = 2/3$
singlet scattering length (a_S)	90 a_0
triplet scattering length (a_T)	106 a_0
$\|1,-1\rangle$ scattering length	103 a_0

Table A.13: Rubidium 87 isotope properties [104, 105] .

Appendix B

Technical notes

B.1 Vector space in the complex spherical basis

Given the basis vectors in the spherical coordinate system (6.2.2),

$$\hat{e}^1 = -\frac{1}{\sqrt{2}}(\hat{e}^x + i\hat{e}^y), \quad \hat{e}^0 = \hat{e}^z, \quad \hat{e}^{-1} = \frac{1}{\sqrt{2}}(\hat{e}^x - i\hat{e}^y),$$

the unit vectors in this complex coordinate system still form an orthonormal basis; the complex conjugate (denoted by $*$) of a unit vector is given by

$$\hat{e}^{p*} = (-1)^p \hat{e}^{-p}; \tag{B.1.1}$$

the orthonormality of basis vectors manifests as

$$\hat{e}^p \cdot \hat{e}^{p'} = \hat{e}^{p\dagger}\hat{e}^{p'} = (-1)^p \delta_p^{p'}, \tag{B.1.2}$$

where the superscript $\dagger$ denotes the Hermitian transpose (complex conjugate transpose), T the transpose—lowering the index, and $\delta_p^{p'}$ the Kronecker delta function.

Suppose A^p is the p^{th} component in the complex spherical coordinate system of vector $\vec{A}$ in the complex vector space V, and A_p denotes the same component of its covector $\vec{A}^\dagger$ in the dual space $V^\dagger$, which is defined by taking the complex conjugate transpose of every vector in V ($\dagger : V \to V^\dagger$),

$$\dagger : \quad \vec{A} = \sum_p A^p \hat{e}^p \mapsto \vec{A}^\dagger = \sum_p A_p \hat{e}_p. \tag{B.1.3}$$

Applying † twice maps $\vec{A}$ back to itself, so the mapping is bijective. In the standard notation,

$$\dagger : \begin{bmatrix} \hat{e}^{-1} & \hat{e}^{0} & \hat{e}^{1} \end{bmatrix} \begin{bmatrix} A^{-1} \\ A^{0} \\ A^{1} \end{bmatrix} \mapsto \begin{bmatrix} -A^{1*} & A^{0*} & -A^{-1*} \end{bmatrix} \begin{bmatrix} \hat{e}_{-1} \\ \hat{e}_{0} \\ \hat{e}_{1} \end{bmatrix} . \tag{B.1.4}$$

Here A^p is a component of vector $\vec{A}$ in V, so it is a complex number (operator) whose transpose is itself, $A_p^\dagger = A_p^*$. The sign and non-cyclic permutation are due to (B.1.1), $\dagger : \hat{e}^p \mapsto (-1)^p \hat{e}_{-p}$. Suppose the ordering of coordinate indices remain the same, i.e. $p = -1$ is the first/rightmost index in the covector, components of covectors in the dual space can be related to components of vectors in the primary space,

$$A_p = (-1)^p A^{-p*}. \tag{B.1.5}$$

Given the well-defined mapping between the primal and dual vector spaces, I define a dot product (interchangeable with scalar product) as an operation that takes two vectors from the primal space and returns a scalar quantity, $\cdot : V \to \text{Complex}$,

$$\begin{aligned} \cdot : \{\vec{A}, \vec{B}\} \in V \mapsto \vec{A} \cdot \vec{B} = \sum_{p,p'} (A^p \hat{e}^p)^\dagger (B^{p'} \hat{e}^{p'}) &\overset{(B.1.3)}{=} \sum_{p,p'} A_p B^{p'} \hat{e}^{p\dagger} \hat{e}^{p'} \\ &\overset{(B.1.2)}{=} \sum_{p} (-1)^p A_p B^{-p}. \end{aligned} \tag{B.1.6}$$

$(-1)^p$ in the definition follows from orthonormality (B.1.2). Though the scalar quantity is in general complex, the L-2 norm of any vector is non-negative for the dot product defined here,

$$\begin{aligned} \vec{A} \cdot \vec{A} = (-1)^p A_p A^{-p} &= -A_1 A^{-1} + A_0 A^0 - A_{-1} A^1 \\ &= A^{-1} A^{-1*} + A^0 A^{0*} + A^1 A^{1*}. \end{aligned}$$

Suppose the dot product is also symmetric under the exchange of arguments,

$$\vec{A}\cdot\hat{e}^p = \hat{e}^p\cdot\vec{A}$$

$$rhs = \hat{e}^p\cdot\left(\sum_{p'}A^{p'}\hat{e}^{p'}\right)\overset{(B.1.2)}{=}(-1)^pA^p$$

$$lhs = \left(\sum_{p'}A^{p'}\hat{e}^{p'}\right)\cdot\hat{e}^p = \left(\sum_{p'}A^{p'}\hat{e}^{p'}\right)^\dagger\hat{e}^p\overset{(B.1.2)}{=}(-1)^pA_p\overset{(B.1.5)}{=}A^{-p*};$$

consequently, this constraint leads to

$$(-1)^pA^p = A^{-p*}. \tag{B.1.7}$$

In another common notation used in Ref. [80], the scalar product is defined arbitrarily in (5.111),

$$T^k(\vec{\mu})\cdot T^k(\vec{\mathcal{E}}) = \sum_p(-1)^pT^k_p(\vec{\mu})T^k_{-p}(\vec{\mathcal{E}})$$

with which the form in (B.1.6) agrees to some extent.

B.2 Resolution test

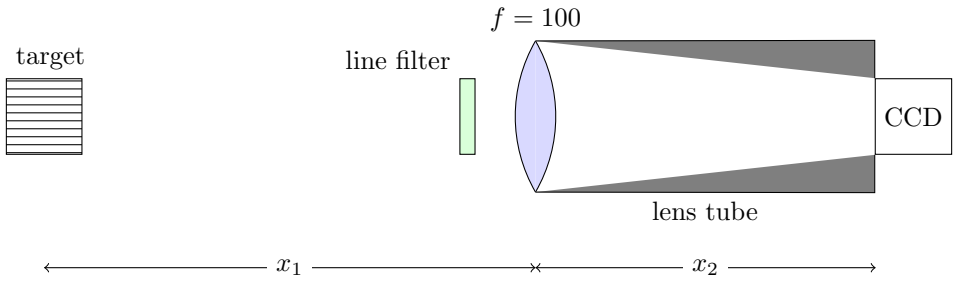


Figure B.1: Experimental setup. In the resolution test, an Air Force target (from Thorlabs) is back-illuminated by monochromatic light at 780 nm. The 2" lens with a focal length $f = 100$ mm is mounted to the camera with a black lens tube, and a line-filter is placed before the lens to prevent stray light from reaching the CCD camera. x_1 is the separation between the target and the lens, and x_2 is the separation between the lens and the imaging chip on the CCD camera.

Figure B.1 shows the setup in the resolution test for an imaging system with a single lens. This is a prototype for an imaging system in the SrF experiment with improved resolution. In this system, the focal length, and the distance between the lens and the object, x_1, and distance between the lens and the image x_2 follow a simple formula,

$$\frac{1}{f} = \frac{1}{x_1} + \frac{1}{x_2}. \tag{B.2.1}$$

In a realistic scenario, x_1 is usually constrained by geometry, e.g., the distance from a viewport to the center of the chamber. x_2 needs to be adjusted, by optimizing the imaging resolution by eye. when x_1 and f are fixed. In this test, $x_1 = 137(2)$ mm. After manual focusing, $x_2 = 370(15)$ mm. The magnification is therefore

$$m = \frac{x_2}{x_1} = 2.7(2). \tag{B.2.2}$$

The target consists of multiple groups of line patterns, the resolution in unit of line pairs per mm is known

$$R[\text{lp/mm}] = 2^{\text{group}+\frac{\text{element}-1}{6}}. \tag{B.2.3}$$

Using R as the figure of merit, the goal here is to determine the resolution of this imaging setup. To begin with, we consider the highest resolution possible for this camera, supposing the optics are ideal and cause no diffraction. In this case, the resolution would be limited by the pixel size of the CCD camera, 6.45 μm. According the the Nyquist-Shannon (NS) theorem, the smallest feature we wish to record must be greater than twice the pixel width to avoid aliasing,

$$\text{linewidth} > \frac{12.9}{m}\ \mu m. \tag{B.2.4}$$

From the magnification factor m and the pixel size, the NS limit for resolvable linewidth on the target is 4.7(3) μm. This suggests sampling is only sufficient for elements before group 6 element 5, with a line with of 4.92 μm.

It is worth noting that the quality of the lens matters in reality. Figure B.2 shows a comparison between images taken by a high-precision CNC polished aspheric lens and by a molded aspheric lens, with nominally identical illumination and magnification conditions.

For a more qualitative analysis, the contrast for selected line groups on the target is calculated (Table B.1). The contrast is defined as the ratio of the maximum intensity to the minimum intensity, summed over the dimension perpendicular to lines. The uncertainties quoted in Table B.1 are standard errors of the average over 3 random line profiles. Figure B.3 shows one of these sub-images cropped out from the CCD image, and 3 line profiles. The sub-images for other elements are cropped out from the same CCD image, so the illumination and magnification conditions are nominally identical. With the high-precision lens, the imaging system is able to resolve lines with width larger than 6.96 μm, very close to the NS sampling limit (Figure B.4).

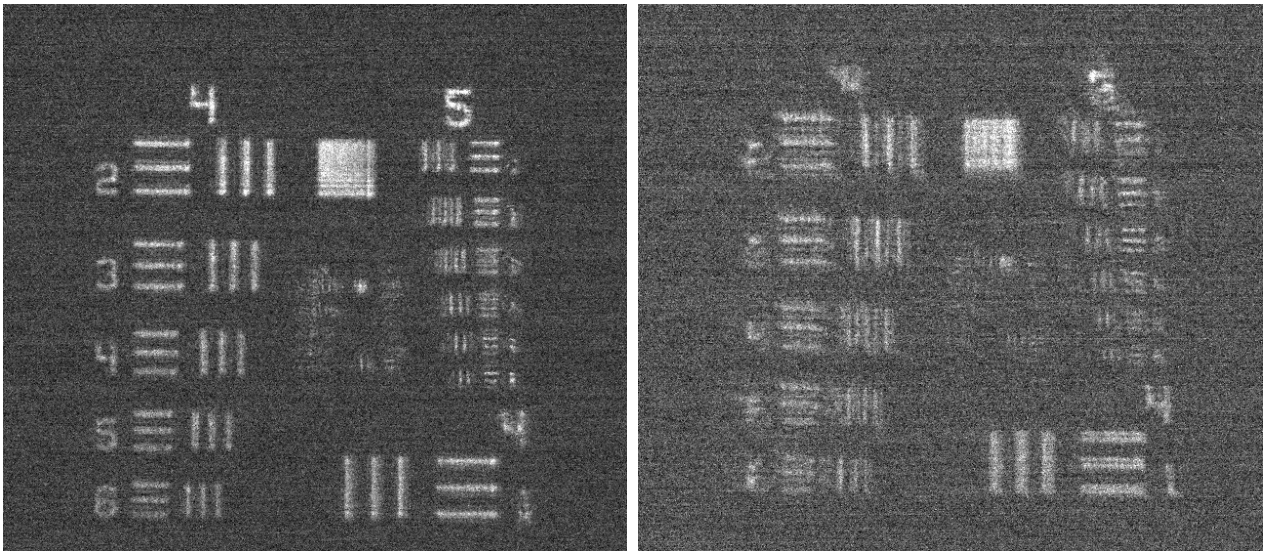


Figure B.2: High-precision aspheric (L) vs molded aspheric lens (R).

group.element	R [lp/mm]	linewidth [μm]	contrast
3.4	11.30	44.19	.76(2)
4.2	17.95	27.84	.69(2)
5.1	32.00	15.63	.625(3)
6.2	71.8	6.96	.92(1)

Table B.1: Resolutions and contrasts of elements analyzed in the test with a high-precision aspheric lens. The linewidth quoted is the width of each bright/transmission line.

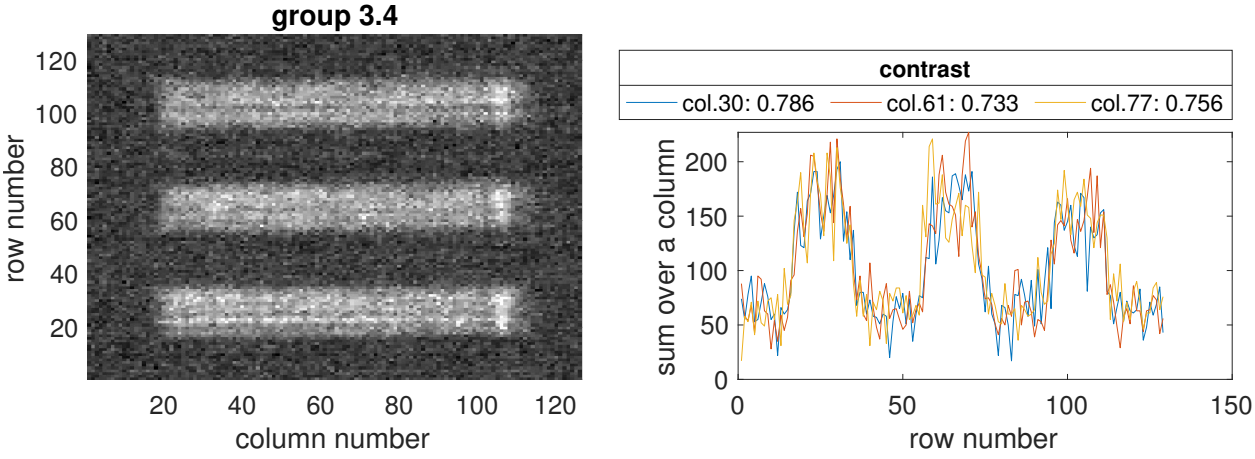


Figure B.3: Resolving a group 3 element 4 on the Air Force target test with a high-precision aspheric lens ($f = 100$ mm).

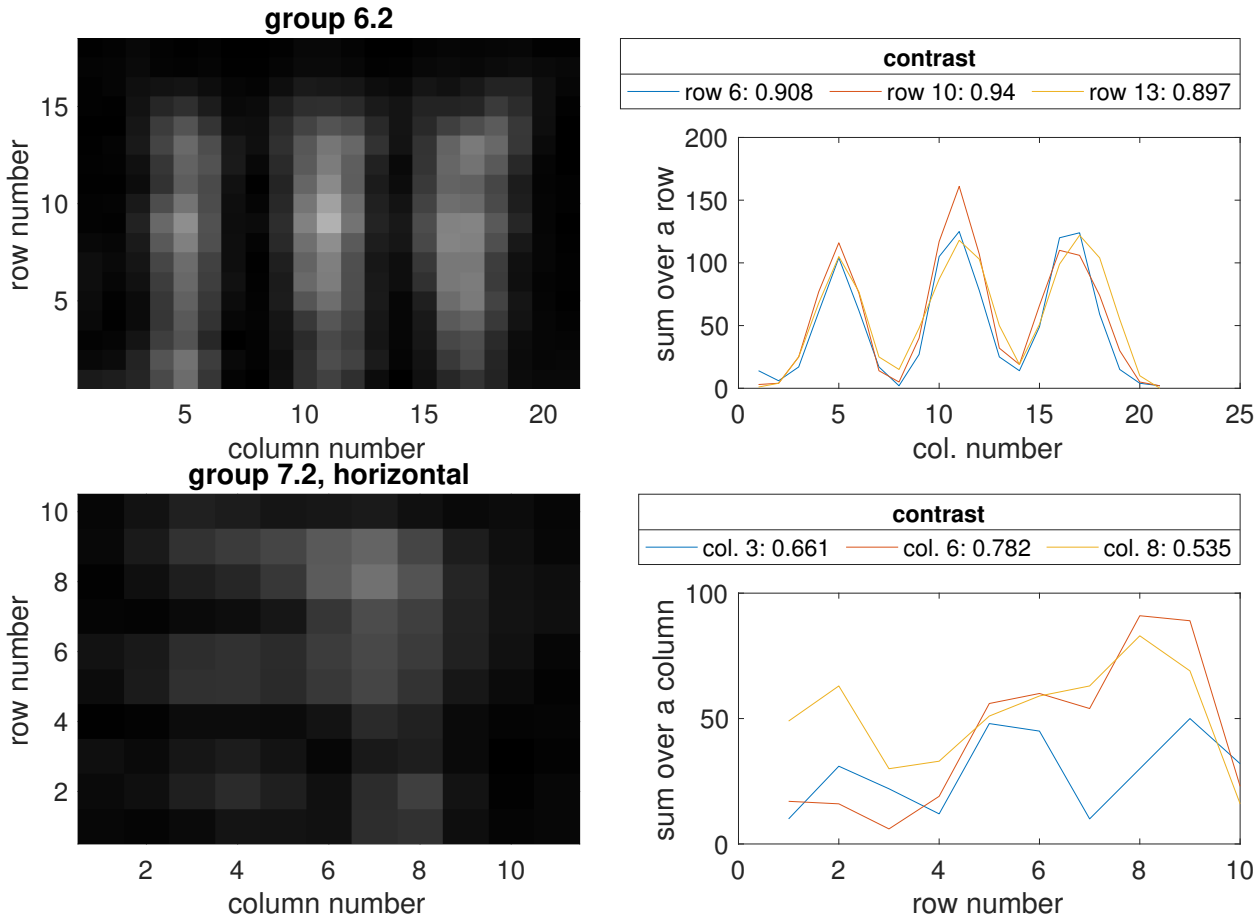


Figure B.4: Resolved vs not resolved.

Bibliography

1. Carr, L. D., DeMille, D., Krems, R. V. & Ye, J. Cold and ultracold molecules: Science, technology and applications. *New J. Phys.* **11** (2009).
2. Baron, J. *et al.* Order of Magnitude Smaller Limit on the Electric Dipole Moment of the Electron. *Science* **343,** 269–272 (2014).
3. Andreev, V. *et al.* Improved limit on the electric dipole moment of the electron. *Nature* **562,** 355–360 (Oct. 2018).
4. Yu, P. & Hutzler, N. R. Probing Fundamental Symmetries of Deformed Nuclei in Symmetric Top Molecules. *Physical Review Letters* **126** (2021).
5. Hudson, E. R., Lewandowski, H. J., Sawyer, B. C. & Ye, J. Cold Molecule Spectroscopy for Constraining the Evolution of the Fine Structure Constant. *Phys. Rev. Lett.* **96,** 143004 (14 2006).
6. DeMille, D. Quantum Computation with Trapped Polar Molecules. *Phys. Rev. Lett.* **88,** 067901 (2002).
7. Krems, R. V. Cold controlled chemistry. *Phys. Chem. Chem. Phys.* **10,** 4079–4092 (28 2008).
8. Davis, B., Mewes, M.-o., Joffe, M. A., Andrews, M. R. & Ketterle, W. Evaporative Cooling of Sodium Atoms. *Phys. Rev. Lett.* **74,** 5202–5205 (1995).
9. Anderson, M. H., Ensher, J. R., Matthews, M. R., Wieman, C. E. & Cornell, E. A. Observation of Bose-Einstein Condensation in a Dilute Atomic Vapor. *Science* **269,** 198–201 (1995).
10. Bradley, C. C., Sackett, C. A., Tollett, J. J. & Hulet, R. G. Evidence of Bose-Einstein condensation in an atomic gas with attractive interactions. *Phys. Rev. Lett.* **75,** 1687–1690 (1995).
11. Greiner, M., Mandel, O., Esslinger, T., Haensch, T. & Bloch, I. Quantum phase transition from a superfluid to a Mott insulator in a gas of ultracold atoms. *Nature* **415,** 39–44 (Feb. 2002).
12. Aikawa, K. *et al.* Bose-Einstein Condensation of Erbium. *Phys. Rev. Lett.* **108,** 210401 (21 2012).
13. Petter, D. *et al.* Probing the Roton Excitation Spectrum of a Stable Dipolar Bose Gas. *Phys. Rev. Lett.* **122,** 183401 (18 2019).

14. Lu, M., Burdick, N. Q. & Lev, B. L. Quantum Degenerate Dipolar Fermi Gas. *Phys. Rev. Lett.* **108,** 215301 (21 2012).

15. Maier, T. *et al.* Emergence of Chaotic Scattering in Ultracold Er and Dy. *Physical Review X* **5** (2015).

16. Bismut, G. *et al.* Collective Excitations of a Dipolar Bose-Einstein Condensate. *Phys. Rev. Lett.* **105,** 040404 (4 2010).

17. Anderegg, L. *et al.* Radio Frequency Magneto-Optical Trapping of CaF with High Density. *Phys. Rev. Lett.* **119,** 103201 (10 2017).

18. Truppe, S. *et al.* Molecules cooled below the Doppler limit. *Nat. Phys.* **357,** 372–375 (2017).

19. Ding, S., Wu, Y., Finneran, I. A., Burau, J. J. & Ye, J. Sub-Doppler Cooling and Compressed Trapping of YO Molecules at K Temperatures. *Physical Review X* **10** (2020).

20. Chin, C., Grimm, R., Julienne, P. & Tiesinga, E. Feshbach resonances in ultracold gases. *Rev. Mod. Phys.* **82,** 1225–1286 (2 2010).

21. Son, H., Park, J. J., Ketterle, W. & Jamison, A. O. Collisional cooling of ultracold molecules. *Nature* **580,** 197–200 (2020).

22. Valtolina, G. *et al.* Dipolar evaporation of reactive molecules to below the Fermi temperature. *Nature* **588,** 239243 (2020).

23. Ni, K. *et al.* A High Phase-Space-Density Gas of Polar Molecules. *Science* **322,** 231–235 (2008).

24. De Marco, L. *et al.* A degenerate Fermi gas of polar molecules. *Science* **363,** 853856 (2019).

25. Sonderhouse, L. *et al.* Thermodynamics of a deeply degenerate SU(N)-symmetric Fermi gas. *Nature Physics* **16,** 12161221 (2020).

26. McCarron, D. J., Steinecker, M. H., Zhu, Y. & DeMille, D. Magnetic Trapping of an Ultracold Gas of Polar Molecules. *Phys. Rev. Lett.* **121,** 013202 (2018).

27. Barry, J. F. *Laser cooling and slowing of a diatomic molecule* PhD thesis (2013).

28. Barry, J. F., McCarron, D. J., Norrgard, E. B., Steinecker, M. H. & DeMille, D. Magneto-optical trapping of a diatomic molecule. *Nature* **512,** 286–289 (2014).

29. Di Rosa, M. D. Laser-cooling molecules. *Eur. Phys. J. D - At. Mol. Opt. Plasma Phys.* **31,** 395–402 (2004).

30. Barry, J. F., Shuman, E. S., Norrgard, E. B. & DeMille, D. Laser Radiation Pressure Slowing of a Molecular Beam. *Phys. Rev. Lett.* **108,** 103002 (2012).

31. Norrgard, E. B., McCarron, D. J., Steinecker, M. H., Tarbutt, M. R. & DeMille, D. Submillikelvin Dipolar Molecules in a Radio-Frequency Magneto-Optical Trap. *Phys. Rev. Lett.* **116,** 1–6 (2016).

32. Steinecker, M. H., McCarron, D. J., Zhu, Y. & DeMille, D. Improved Radio-Frequency Magneto-Optical Trap of SrF Molecules. *ChemPhysChem* **17,** 3664–3669 (2016).

33. Hummon, M. T. *et al.* 2D Magneto-Optical Trapping of Diatomic Molecules. *Phys. Rev. Lett.* **110,** 143001 (14 2013).

34. Raab, E. L., Prentiss, M., Cable, A., Chu, S. & Pritchard, D. E. Trapping of Neutral Sodium Atoms with Radiation Pressure. *Phys. Rev. Lett.* **59,** 2631–2634 (1987).

35. Grynberg, G & Courtois, J.-Y. Proposal for a Magneto-Optical Lattice for Trapping Atoms in Nearly-Dark States. *Eur. Lett.* **27,** 41–46 (1994).

36. Fernandes, D. R. *et al.* Sub-Doppler laser cooling of fermionic ^{40}K atoms in three-dimensional gray optical molasses. *Europhys. Lett.* **100,** 63001 (2012).

37. Dalibard, J. & Cohen-Tannoudji, C. Laser cooling below the Doppler limit by polarization gradients: simple theoretical models. *J. Opt. Soc. Am. B* **6,** 2023 (1989).

38. *BEC Coil Driver* https://www.physics.utoronto.ca/~astummer/Archives/2004%20BEC%20Coil%20Driver%20%27Mag-O-Matic%27/BEC_coils.html.

39. Hartwig, B. Series Stacking of TVS for Higher Voltages and Power. *Application Notes by Vishay General Semiconductor* (2007).

40. Horowitz, P. & Hill, W. *The Art of Electronics* (Cambridge University Press, New York, 2015).

41. Dieckmann, K., Spreeuw, R., Weidemüller, M. & Walraven, J. Two-dimensional magneto-optical trap as a source of slow atoms. *Phys. Rev. A* **58,** 3891–3895 (1998).

42. Schoser, J. *et al.* An Intense Source of Cold Rb Atoms from a Pure 2D-MOT. *Phys. Rev. A* **66,** 1–10 (2002).

43. Catani, J., Maioli, P., Sarlo, L. D., Minardi, F. & Inguscio, M. Intense slow beams of bosonic potassium isotopes. *Phys. Rev. A,* 1–9 (2006).

44. H., L. Simplified System for Creating a BoseEinstein Condensate. *J. Low Temp. Phys.* **132,** 309 (2003).

45. Phillips, W. D. & Metcalf, H. Laser Deceleration of an Atomic Beam. *Phys. Rev. Lett.* **48,** 596–599 (9 1982).

46. Lu, Z. T. *et al.* Low-Velocity Intense Source of Atoms from a Magneto-optical Trap. *Phys. Rev. Lett.* **77,** 3331–3334 (16 1996).

47. Streed, E. W. *et al.* Large atom number Bose-Einstein condensate machines. *Review of Scientific Instruments* **77,** 023106 (2006).

48. Slowe, C., Vernac, L. & Hau, L. V. High flux source of cold rubidium atoms. *Review of Scientific Instruments* **76,** 103101 (2005).

49. Ricci, L *et al.* A compact grating-stabilized diode laser system for atomic physics. *Opt. Commun.* **117,** 541–549 (1995).

50. Hawthorn, C. J., Weber, K. P. & Scholten, R. E. Littrow configuration tunable external cavity diode laser with fixed direction output beam. *Review of Scientific Instruments* **72,** 4477–4479 (2001).

51. MacAdam, K. B., Steinbach, A & Wieman, C. A narrowband tunable diode laser system with grating feedback, and a saturated absorption spectrometer for Cs and Rb. *Am. J. Phys.* **60,** 1098–1111 (1992).

52. Zhao, W. Z., Simsarian, J. E., Orozco, L. A. & Sprouse, G. D. A computer-based digital feedback control of frequency drift of multiple lasers. *Review of Scientific Instruments* **69,** 3737–3740 (1998).

53. Chambers, A. *Modern Vacuum Physics* (Boca Raton: CRC Press, 2004).

54. Baglin, V. *Cold / sticky system* (Feb. 2006).

55. Dieckmann, K. *Bose-Einstein Condensation with High Atom Number in a Deep Magnetic Trap* PhD thesis (2001).

56. Steck, D. A. Rubidium 87 D Line Data. *J. Geophys. Res.* **2009,** 31 (2010).

57. Catani, J. *A NEW APPARATUS FOR ULTRACOLD K-RB BOSE-BOSE ATOMIC MIXTURES* PhD thesis (2006).

58. Keitz, H. *Light Calculations and Measurements* (MACMILLAN and CO LTD, 1971).

59. *CRC Handbook of Chemistry and Physics, 101st Edition (Internet Version 2020)* (ed Rumble, J. R.) (CRC Press/Taylor & Francis, 2020).

60. Alcock, C. B., Itkin, V. P. & Horrigan, M. K. Vapour Pressure Equations for the Metallic Elements: 2982500K. *Canadian Metallurgical Quarterly* **23,** 309–313 (1984).

61. Nesmeyanov, A. N. *Vapor Pressure of the Chemical Elements* (Elsevier, 1963).

62. Collopy, A. L. *et al.* 3D Magneto-Optical Trap of Yttrium Monoxide. *Physical Review Letters* **121** (2018).

63. Tarbutt, M. R. Magneto-optical trapping forces for atoms and molecules with complex level structures. *New Journal of Physics* **17,** 015007 (2015).

64. Morita, M., Kosicki, M. B., uchowski, P. S. & Tscherbul, T. V. Atom-molecule collisions, spin relaxation, and sympathetic cooling in an ultracold spin-polarized $Rb(^2S) - SrF(^2\Sigma^+)$ mixture. *Physical Review A* **98** (2018).

65. Harvey, M. & Murray, A. J. Cold Atom Trap with Zero Residual Magnetic Field: The ac Magneto-Optical Trap. *Phys. Rev. Lett.* **101,** 173201 (17 2008).

66. Chae, E. *Laser Slowing of CaF Molecules and Progress towards a Dual-MOT for Li and CaF* PhD thesis (2015).

67. Stuhl, B. K., Sawyer, B. C., Wang, D. & Ye, J. Magneto-optical trap for polar molecules. *Phys. Rev. Lett.* **101,** 1–4 (2008).

68. Lett, P. D. *et al.* Observation of Atoms Laser Cooled below the Doppler Limit. *Phys. Rev. Lett.* **61,** 169–172 (2 1988).

69. Anderegg, L. *et al.* Laser cooling of optically trapped molecules. *Nat. Phys.* **14,** 890–893 (2018).

70. Zirbel, J. J. *et al.* Heteronuclear molecules in an optical dipole trap. *Physical Review A* **78** (2008).

71. Caldwell, L. *et al.* Deep Laser Cooling and Efficient Magnetic Compression of Molecules. *Phys. Rev. Lett.* **123,** 033202 (3 2019).

72. Ravensbergen, C. *et al.* Production of a degenerate Fermi-Fermi mixture of dysprosium and potassium atoms. *Phys. Rev. A* **98,** 063624 (6 2018).

73. Fitch, N. J., Parazzoli, L. P. & Lewandowski, H. J. Collisions between ultracold atoms and cold molecules in a dual electrostatic-magnetic trap. *Phys. Rev. A* **101,** 032703 (3 2020).

74. Hummon, M. T. *et al.* Cold **N**+NH Collisions in a Magnetic Trap. *Phys. Rev. Lett.* **106,** 053201 (5 2011).

75. Akerman, N. *et al.* Trapping of Molecular Oxygen together with Lithium Atoms. *Phys. Rev. Lett.* **119,** 073204 (7 2017).

76. Jurgilas, S. *et al.* Collisions Between Ultracold Molecules and Atoms in a Magnetic Trap. arXiv: 2101.01580 [physics.atom-ph] (2021).

77. Mosk, A. *et al.* Mixture of ultracold lithium and cesium atoms in an optical dipole trap. *Applied Physics B* **73,** 791799 (2001).

78. Tassy, S *et al.* Sympathetic cooling in a mixture of diamagnetic and paramagnetic atoms. *Journal of Physics B: Atomic, Molecular and Optical Physics* **43,** 205309 (2010).

79. Grimm, R, Weidemüller, M & Ovchinnikov, Y. Optical dipole trap for neutral atoms. *Adv. At. Mol. Opt. Phys.* **42,** 95 (2000).

80. Brown, J. M. & Carrington, A. *Rotational Spectroscopy of Diatomic Molecules* (Cambridge University Press, 2003).

81. *Wigner 3j-Symbol —Wolfram MathWorld* http://mathworld.wolfram.com/Wigner3j-Symbol.html.

82. Dagdigian, P. J., Cruse, H. W. & Zare, R. N. Radiative lifetimes of the alkaline earth monohalides. *The Journal of Chemical Physics* **60,** 2330–2339 (1974).

83. Brown, J. M. & Howard, B. J. An approach to the anomalous commutation relations of rotational angular momenta in molecules. *Mol. Phys.* **31,** 1517–1525 (1976).

84. Watson, J. K. Hönl-London factors for multiplet transitions in Hunds case a or b. *Journal of Molecular Spectroscopy* **252,** 5 –8 (2008).

85. Norrgard, E. B. *Magneto-optical trapping of diatomic molecules* PhD thesis (2016).

86. Angel, J. R. P., Sandars, P. G. H. & Bleaney, B. The hyperfine structure Stark effect I. Theory. *Proceedings of the Royal Society of London. Series A. Mathematical and Physical Sciences* **305,** 125–138 (1968).

87. Le Kien, F., Schneeweiss, P. & Rauschenbeutel, A. Dynamical polarizability of atoms in arbitrary light fields: General theory and application to cesium. *Eur. Phys. J. D* **67,** 28–30 (2013).

88. Kuga, T. *et al.* Novel Optical Trap of Atoms with a Doughnut Beam. *Phys. Rev. Lett.* **78,** 4713–4716 (1997).

89. Johnson, R. C. & Merton, T. R. The band spectra of the alkaline earth halides. II.—BaF, MgF. *Proceedings of the Royal Society of London. Series A, Containing Papers of a Mathematical and Physical Character* **122,** 189–200 (1929).

90. Domaille, P. J., Steimle, T. C. & Harris, D. O. The rotational spectrum of the $X^2\Sigma^+$ state of the SrF radical using laser microwave optical double resonance. *J. Mol. Spectrosc.* **68,** 146–155 (1977).

91. Fowler, C. A. New Absorption Spectra of the Alkaline Earth Fluorides. *Phys. Rev.* **59,** 645–652 (1941).

92. Novikov, M. M. & Gurvich, L. V. Electronic Emission Spectrum of SrF. *Optics and Spectroscopy* **22,** 395 (1967).

93. Sheridan, P. M., Wang, J. G., Dick, M. J. & Bernath, P. F. Optical-optical double resonance spectroscopy of the $C^2\Pi - A^2\Pi$ and $D^2\Sigma^+ - A^2\Pi$ Transitions of SrF. *J. Phys. Chem. A* **113,** 13383–13389 (2009).

94. Ernst, W. & Schröder, J. The $B^2\Sigma^+ - X^2\Sigma^+$ system of SrF: Precise spectroscopic constants from a combined fit of microwave and sub-doppler optical spectra. *Chem. Phys.* **78,** 363–368 (1983).

95. Steimle, T. C., Domajlle, P. J. & Harris, D. O. Rotational Analysis of the $B^2\Sigma^+ - X^2\Sigma^+$ System of SrF Using a cw Tunable Dye Laser. *Spectrosc. Lett.* **43,** 207–212 (1977).

96. Samujh Ram, R., Rai, S. B. & Upadhya, K. N. The $C^2\Pi - X^2\Sigma$ system of SrF molecule. *Pramana* **15,** 413–422 (1980).

97. Berg, L. E. *et al.* Time-resolved measurements of the $B^2\Sigma$ state of SrF by laser spectroscopy. *Chem. Phys. Lett.* **248,** 283–288 (1996).

98. De Melo, G. F. & Ornellas, F. R. The $\Lambda + S$ and Ω electronic states of SrF below 40,000 cm1: A theoretical contribution. *J. Quant. Spectrosc. Radiat. Transf.* **237** (2019).

99. *NIST Chemistry WebBook* https://webbook.nist.gov/cgi/inchi?ID=C13569272&Mask=1000.

100. Childs, W. J., Goodman, L. S. & Renhorn, I. Radio-frequency optical double-resonance spectrum of SrF: The $X^2\Sigma^+$ state. *J. Mol. Spectrosc.* **87,** 522–533 (1981).

101. *RKR1 program* http://scienide2.uwaterloo.ca/~rleroy/rkr/.

102. *LEVEL program* http://scienide2.uwaterloo.ca/~rleroy/level/.

103. Kändler, J., Martell, T. & Ernst, W. Electric dipole moments and hyperfine structure of SrF $A^2\Pi$ and $B^2\Sigma^+$. *Chem. Phys. Lett.* **155,** 470–474 (1989).

104. Julienne, P. S., Mies, F. H., Tiesinga, E. & Williams, C. J. Collisional stability of double bose condensates. *Phys. Rev. Lett.* **78,** 1880–1883 (1997).

105. Roberts, J. L. *et al.* Resonant Magnetic Field Control of Elastic Scattering in Cold ^{85}Rb. *Phys. Rev. Lett.* **81,** 1–4 (1998).